TECHNISCHE UNIVERSITÄT MÜNCHEN

Lehrstuhl E23 für Technische Physik

Walther-Meissner-Institut für Tieftemperaturforschung
der Bayerischen Akademie der Wissenschaften

Carrier dynamics of $Ba(Fe_{1-x}Co_x)_2As_2$ as a function of doping

Bernhard Muschler

Vollständiger Abdruck der von der Fakultät für Physik der Technischen Universität München zur Erlangung des akademischen Grades eines

Doktors der Naturwissenschaften

genehmigten Dissertation.

Vorsitzender:	Univ.-Prof. Dr. Wilhelm Zwerger
Prüfer der Dissertation	1. Univ.-Prof. Dr. Rudolf Gross
	2. Univ.-Prof. Dr. Christian Pfleiderer

Die Dissertation wurde am 13.06.2012 bei der Technischen Universität München eingereicht und durch die Fakultät für Physik am 23.07.2012 angenommen.

Abstract

In this thesis a systematic light scattering study of the newly discovered iron-based superconductor $Ba(Fe_{1-x}Co_x)_2As_2$ is presented. The main focus is placed on the study of electronic properties in a doping range x in which magnetism and superconductivity are in close proximity. The experiment affords a window into band and momentum-dependent electronic properties. The magnetic order is predominantly itinerant. The structure of the superconducting gap indicates that the coupling potential may result from magnetic fluctuations.

Zusammenfassung

In dieser Arbeit wird eine systematische Studie des kürzlich entdecktem Eisen-basierten Supraleiters $Ba(Fe_{1-x}Co_x)_2As_2$ mittels inelastischer Lichtstreuung präsentiert. Das Hauptaugenmerk liegt dabei auf der Untersuchung der elektronischen Eigenschaften in dem Dotierungsbereich x, in welchem Magnetismus und Supraleitung nahe beieinanderliegen. Das Experiment bietet einen Einblick in die band- und impulsabhängigen elektronischen Eigenschaften. Der Magnetismus ist vornehmlich itinerant. Die Struktur der Energielücke zeigt, dass die Kopplung von magnetischen Fluktuationen kommen könnte.

Contents

Chapter 1

Introduction

Superconductivity in iron based superconductors (FeSCs) [1, 2] at transition temperatures T_c in excess of 50 K [3] was at least as unexpected and ground breaking as T_c values close to 40 K in MgB_2 [4] or Ba-La-Cu-O [5]. It was not only the perspectives of applications of the FeSCs but also the rich variety of new ordered phases next to superconductivity that triggered an avalanche of research activities comparable to that in the cuprates.

Similarly to the cuprates, the FeSCs are layered materials and exhibit a magnetically ordered phase in close proximity to superconductivity. However, as opposed to undoped cuprates where the antiferromagnetic insulating phase is well described by a Mott-Hubbard model [6], undoped FeSCs stay metallic at low temperatures and exhibit a spin-density-wave. The magnetic ordering temperature T_{SDW} is at or slightly below T_{TO} where a structural tetragonal to orthorhombic phase transition occurs. Both, the magnetic and the structural phase transitions are continuously suppressed upon doping. When T_{SDW} and T_{TO} approach zero, the superconducting transition temperature T_c reaches its maximum [7]. The superconducting phase in the FeSCs is not separated from the magnetically ordered phase, as for cuprates, but there is a doping region where superconductivity and magnetism coexist microscopically [8]. The pairing correlations leading to superconductivity in the cuprates are substantial only in the *d*-wave channel [9], while in the FeSCs they are proposed to be substantial in the *s*-wave as well as in the *d*-wave channel [10].

All these observations make it plausible that magnetism and superconductivity are intertwined, and the exclusive study of the superconducting properties aims too short. For this reason, the evolution of the electronic properties as a function of doping will be studied in detail starting from undoped $Ba(Fe_{1-x}Co_x)_2As_2$ having long-ranged magnetic order below T_{SDW} and will cover the range up to doping levels where no magnetism

exists any further. The magnetism itself is already complicated in that a more itinerant magnetism is expected from the nesting between the electron and hole pockets as also observed by inelastic neutron scattering experiments [11] while Raman experiments are more indicative of localized spins [12].

In any case the magnetic phase below T_{SDW} is more stripe-like, as opposed to the checkerboard-like magnetic phase in the cuprates [13]. The stripe-like magnetic phase is accompanied [14] or even preceded [7] by a nematic phase [15] below T_{TO} where the tetragonal symmetry of the lattice is broken already in the paramagnetic phase [16]. Since the magnetic and structural transitions follow each other closely up to optimal doping [7], an intimate relation between both seems plausible [17]. However, it is unclear whether the nematic order is driven by the orbital order which induces magnetic order [18] or if a breaking of the tetragonal magnetic order (without breaking the spin rotational symmetry) induces orbital order [19]. This might be possible since the electron Fermi surfaces at $(\pi, 0)$ and $(0, \pi)$ consist of different orbitals [20]. Then, the structural transition is induced by magnetic fluctuations [19].

The carrier dynamics in the normal state are reported by several authors to be strongly band dependent [21, 22, 23] although none of the experiments performed so far is bulk sensitive and has a sufficient momentum resolution to observe the carrier properties of the bands separately. Independent of this, the origin of the different carrier dynamics on the electron and hole bands is not yet clear.

Superconductivity is the most intensively studied phase in the FeSCs. Due to multiple bands cutting through the Fermi level different gap symmetries seem possible, and there is general agreement that the gap in most FeSCs has an extended s-wave symmetry. Nevertheless, this does not answer the question about the momentum dependence of the gap at optimal doping, the doping dependence of the gap and the underlying pairing interaction.

Several of these questions can be addressed with light scattering experiments. The importance of electronic Raman scattering (ERS) is mainly based on its finite momentum resolution [24]. In the study of the FeSCs the finite momentum resolution enables one to investigate the hole and electron bands separately [25, 26]. In addition, ERS is less sensitive to surface effects due to the finite penetration depth of visible light and has a good energy resolution. This enabled a detailed study of the electronic properties of the cuprates in the normal [27] and superconducting state [28, 29, 30]. In the case of a localized spin model described via a Heisenberg model it is possible to study the strength of the magnetic interactions via two-magnon excitations [31, 32, 33]. Thus,

ERS is a powerful tool for the investigation of the electronic properties of the FeSCs in the magnetically ordered phase, the normal and the superconducting state. To obtain a complete picture of the carrier dynamics the FeSCs are investigated via ERS as a function of doping, temperature, uniaxial pressure, excitation energy and light polarization.

The work is organized as follows: After an overview over the characteristics of the FeSCs in chapter 2, chapter 3 introduces the theoretical aspects of ERS and the formation of density waves. In chapter 4 the investigated samples as well as the experimental setup are presented. The magnetic properties of $BaFe_2As_2$, as seen via the Raman spectra for high and low energy transfer, are discussed in chapter 5. In chapter 6 electronic properties in the normal state for differently doped $Ba(Fe_{1-x}Co_x)_2As_2$ are presented. The origin of the band dependent carrier dynamics and the nature of the fluctuations will be addressed. The results and the analysis of the spectra in the superconducting state at optimal doping and the evolution of the spectra with doping is presented in chapter 7. Here, a more complete picture of the gap structure at optimal doping and its evolution with doping is obtained.

Chapter 2

The iron based superconductors

In this chapter basic properties of the iron based superconductors (FeSCs) in the normal and superconducting state will be reviewed. Special emphasize is placed on the '122' compounds and their properties relevant for the presented study.

2.1 Basic properties

2.1.1 Materials

There are several different crystal structures of FeSCs [35, 36, 37, 38, 39]. The four most frequently studied crystal structures, the so called '1111', '122', '111' and '11' compounds, are shown in Fig. 2.1.

In 1995 Zimmer *et al.* [40] studied the series of LnFePO (Ln = La - Nd, Sm, Gd) which crystallizes in the ZrCuSiAs type structure. Although superconductivity at 6 K was reported for LaFePO in the thesis of Zimmer [41], the first publication in a scientific journal is that by Kamihara and coworkers in 2006 [1]. These '1111' compounds

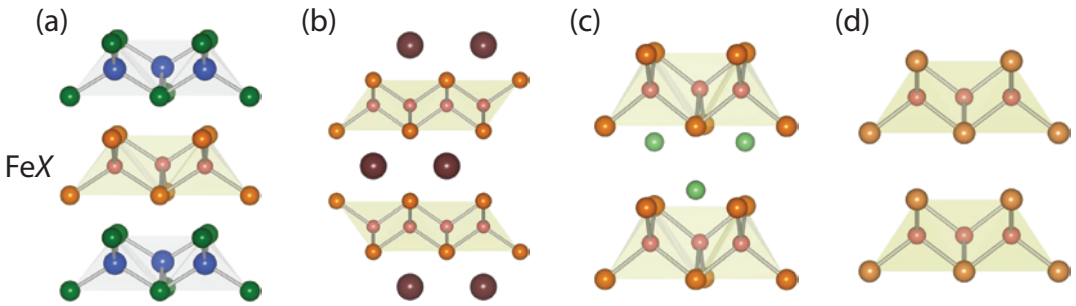

Figure 2.1: Crystal structures of different FeSCs. (a) LaFePO ('1111') (b) $BaFe_2As_2$ ('122') (c) LiFeAs ('111') and (d) FeSe ('11'). The shaded area denote the FeX-layers. From [34].

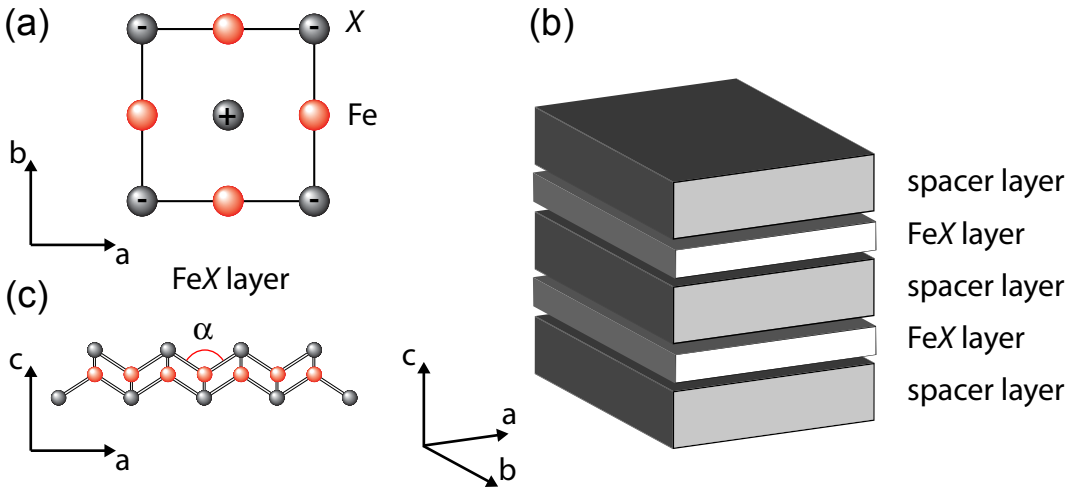

Figure 2.2: Schematic structure of the unit cell of FeSCs. (a) FeX layer. + and − designates the position of the X atom above and below the Fe layer. (b) Layered structure with alternating FeX and spacer layers. (c) b-axis view of the FeX layer. α designates the X-Fe-X bond angle in the FeX_4 tetrahedron.

exhibit the highest transition temperature (T_c) among all FeSCs with T_c = 56 K for $Sr_{1-x}Sm_xFFeAs$ [3]. The '122' compounds crystallize in the $ThCr_2Si_2$ structure and are the best investigated FeSCs due to the availability of relatively large high quality single crystals. The highest T_c in the so called '122' compounds is observed in $Ba_{1-x}K_xFe_2As_2$ with T_c^{max} = 38 K [42]. The '111' compounds crystallize in the tetragonal Cu_2Sb structure. A representative is $Li_{1-\delta}FeAs$ which turns superconducting at T_c^{max} = 18 K [43]. A member of the '11' compounds is $FeSe_{0.5}Te_{0.5}$, which crystallizes in the α-PbO structure. Here, thin films with T_c^{max} = 17 K were grown [44].

2.1.2 Structure

Similarly to the CuO_2 layer of the cuprates, the unit cell of all FeSCs is composed of quasi two dimensional (2D) conducting FeX layers where X is a pnictogen (As or P) or chalcogen (Te, Se or S) [45]. The FeX layers are separated by an oxide ('1111'), an ionic ('122' and '111') or by no layer ('11') [Fig. 2.1, 2.2(a) and 2.2(b)]. Due to the layered structure, the materials are expected to exhibit strongly 2D electronic properties.
The X atoms in the FeX layers are displaced by $c/8$ in c-direction with respect to the Fe layer. This is illustrated in Fig. 2.2(c). If the angle α of the X-Fe-X bonds in the FeX_4 tetrahedron approaches the ideal angle of 109.47°, T_c is reported to be maximal [46].

In the following, $Ba(Fe_{1-x}Co_x)_2As_2$, a member of the '122' compound class, will be

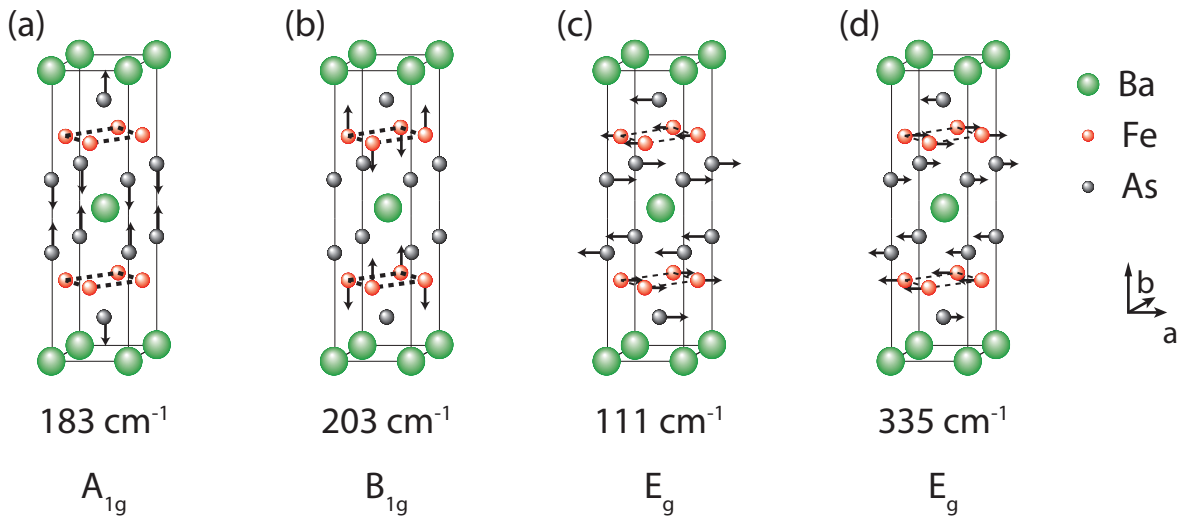

Figure 2.3: Displacement patterns of the Raman active lattice vibrations in $BaFe_2As_2$ with the corresponding vibrational frequency. The two E_g modes in (c) and (d) are strongly mixed.

studied. Only for completeness some properties of the '122' materials will be compared with properties of other FeSCs.

2.1.3 Raman active lattice vibrations in '122' compounds

In the Raman spectra of tetragonal $BaFe_2As_2$, four different phonons are expected with eigenvectors transforming like A_{1g}, B_{1g} (one each) and E_g (two phonons) symmetry [47]. The modes correspond to in-plane (E_g) and out-of-plane vibrations (A_{1g}, B_{1g}) of Fe and As atoms and are displayed in Fig. 2.3. From shell model calculations the expected frequency for the modes are 183 cm^{-1} for the A_{1g} and 203 cm^{-1} for the B_{1g} phonon. The E_g phonons are strongly mixed and expected at frequencies of 111 cm^{-1} and 335 cm^{-1} [47].

2.2 Phase diagram

The control parameter in the phase diagram of the FeSCs can be doping or pressure. Doping is the replacement of, for instance, one Ba atom in $BaFe_2As_2$ by a K atom. The neutral Ba atom has an electronic configuration of $[Xe]6s^2$ while the neutral K atom has an electronic configuration of $[Ar]4s^1$. Hence, one hole is added to the unit cell by this replacement (hole doping, $Ba_{1-x}K_xFe_2As_2$) [42]. The replacement of one Fe atom with configuration $[Ar]3d^64s^2$ by a Co atom with $[Ar]3d^74s^2$ in the conducting FeX

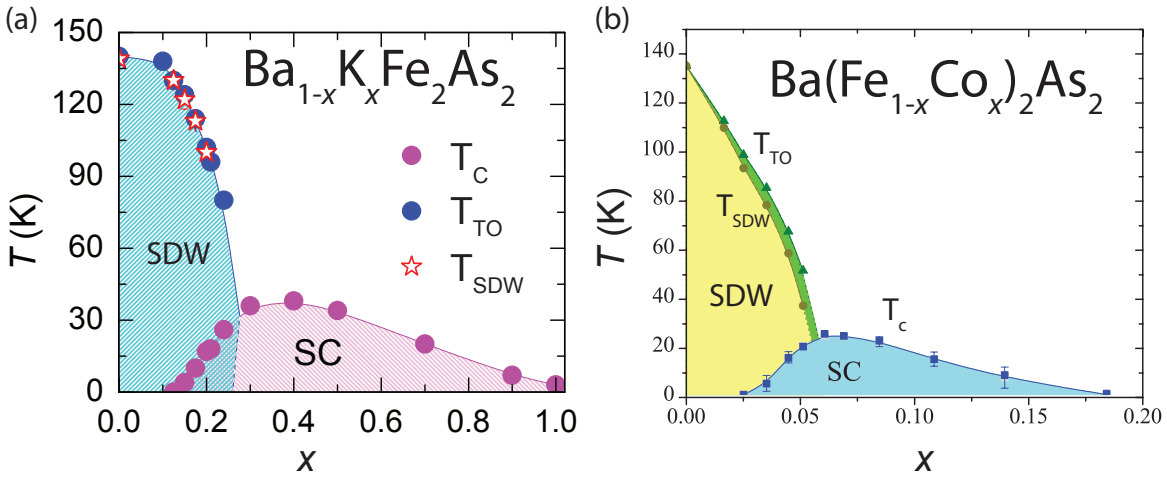

Figure 2.4: Phase diagram of the '122' superconductor (a) $Ba_{1-x}K_xFe_2As_2$ (hole doped) [48] and (b) $Ba(Fe_{1-x}Co_x)_2As_2$ (electron doped) [7]. SC denotes the superconducting and SDW the spin-density-wave phase. T_c, T_{SDW} and T_{TO} indicate the superconducting, SDW and tetragonal to orthorhombic transition temperature, respectively.

layer leads to superconductivity in $Ba(Fe_{1-x}Co_x)_2As_2$ with $T_c^{max} = 26$ K [7]. Here, Co doping should add one electron per Co atom to the conducting $(FeAs)^-$ layers [49, 50]. However, this extra d electron is proposed to be located within the muffin-tin sphere of the substituted site. Then, the main effect of Co doping is to add impurities to the system and the Co atoms acts as an isovalently doped atom [51, 52]. However, also by isovalent doping superconductivity can be introduced: here, an As atom ($[Ar]3d^{10}4s^24p^3$) in $BaFe_2As_2$ is replaced by a P atom ($[Ne]3s^23p^3$) leading to $T_c^{max} = 30$ K [53] or Fe is replaced by Ru ($[Kr]4d^75s^1$) leading to $T_c^{max} = 22$ K [54]. Alternatively, the FeSCs turn superconducting through the application of pressure [55, 56, 57] with $T_c^{max} = 30$ K in $BaFe_2As_2$ at a pressure close to 55 kbar [56].

Figs. 2.4(a) and 2.4(b) show the phase diagrams of hole doped $Ba_{1-x}K_xFe_2As_2$ and electron doped $Ba(Fe_{1-x}Co_x)_2As_2$, respectively. Both phase diagrams are rather similar and resemble those of the cuprates, ruthenates or heavy fermion superconductors for the close proximity of magnetism and superconductivity.

The undoped parent compound is a bad metal and has a tetragonal lattice with a remarkably longer c-axis compared to the nominally equivalent a- and b-axes. At room temperature the ground state is non magnetic [7, 50, 58]. Cooling leads to a small tetragonal-to-orthorhombic (TO) distortion for $T < T_{TO}$ with $a \approx 1.008 \cdot b$ [59] and a spin-density-wave (SDW) ground state for $T < T_{SDW} = T_{TO}$. In the orthorhombic phase the Fe-Fe bonds along the a-axis, a_{Fe}, are slightly longer than along the b-axis, b_{Fe}. Then the sample forms domains where a_{Fe} and b_{Fe} are interchanged. This is illustrated

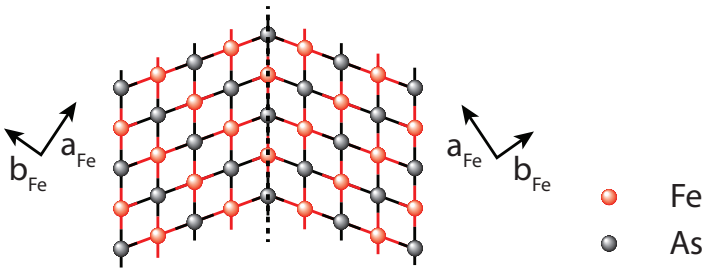

Figure 2.5: Twin boundary between two domains in the orthorhombic phase of $BaFe_2As_2$. The Fe-Fe bonds along a_{Fe} are slightly longer than along b_{Fe}. The sample forms domains where a_{Fe} and b_{Fe} are exchanged. Between the two equivalent domains a twin boundary forms (black dashed line). Adapted from [60].

in Fig. 2.5. The domains have a stripe like phase with a thickness of less than 10 µm and are separated by twin boundaries [60].

With doping the structural and the magnetic transitions are continuously suppressed with still $T_{TO} \geq T_{SDW}$ and superconductivity emerges. The doping level, where T_c is maximal, is called optimal doping, while for lower (underdoped) as well as for higher doping levels (overdoped regime) T_c is reduced and may disappear. Between under- and overdoped samples there is a striking difference in that for overdoped samples no magnetic order is present and T_c decreases slowly with doping as for $Ba(Fe_{1-x}Co_x)_2As_2$ or may even survive as for KFe_2As_2 with $T_c = 3$ K [61]. On the underdoped side there is a coexistence region of magnetism and bulk superconductivity where both phases coexist without phase separation in $Ba(Fe_{1-x}Co_x)_2As_2$ and $Ba_{1-x}K_xFe_2As_2$ [8, 62, 63].

The order of the phase transitions is not yet clear. By early nuclear magnetic resonance (NMR) studies on $BaFe_2As_2$ [64], muon spin relaxation and x-ray studies on $SrFe_2As_2$ [65], and neutron diffraction studies on $CaFe_2As_2$ [66] a discontinuously and often hysteretic structural phase transition was reported suggesting a first order transition. Pratt *et al.* saw via their neutron and x-ray diffraction studies that both transitions are of first order. They occur simultaneously in $BaFe_2As_2$ and split for finite Co doping. At finite doping the magnetic transition is of second order [62]. Wilson *et al.* saw in their neutron diffraction study both phase transitions in $BaFe_2As_2$ to occur simultaneously and without any hysteresis arguing for a second order phase transition [67] while Kim and coworkers observed in their x-ray studies a second order structural transition at 134.5 K followed by a first order magnetic transition at 133.75 K [68].

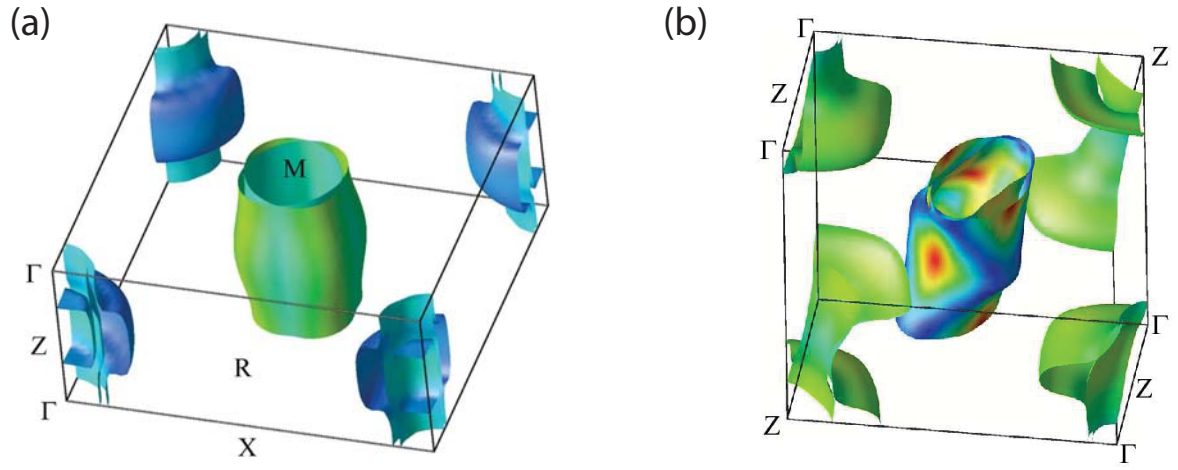

Figure 2.6: 3D view of the Fermi surface (FS) of the (a) '1111' compound $LaFeAsO_{1-x}F_x$ [69] and (b) '122' compound $BaFe_2As_2$ [70]. The FSs consist mainly of two hole barrels at the Γ point and two electron barrels at the M point. The barrels of the '122' compound are stronger warped than the barrels of the '1111' compound. The colors of the FS sheets indicate the different Fermi velocities (blue denotes low velocity).

2.3 Normal state properties

2.3.1 Electronic structure

The electronic properties of the FeSCs are determined by the Fe atoms [69, 71, 72]. The Fermi surface (FS), which has contributions from all five possible Fe $3d$ orbitals [10, 69], is very similar for the different compounds. Figs. 2.6(a) and 2.6(b) show the BZ of '1111' and '122' FeSCs, respectively, as obtained via local density approximation (LDA) [69]. For both materials the BZ contains four cylindrical FS sheets having a similar cross-section. Two barrels around the Γ $[(0,0)]$ point of the BZ have hole character while two barrels at the M $[(\pi,\pi)]$ points have electron character. The 2D character of the FS sheets is more pronounced for the '1111' superconductors where the FS is only little warped along k_z [Fig. 2.6(a)], while for the '122' compounds there is a remarkable dispersion in k_z direction [Fig. 2.6(b)] [69, 70]. The average Fermi velocity on the electron band is remarkably larger than that on the hole bands[1] as illustrated by the colored FSs in Fig. 2.6. This indicates heavier charge carriers on the hole bands [69]. Due to the similar shape of the barrels the hole and electron bands are approximately connected via the nesting vector (π,π) [23, 73]. Also the effect of doping can be investigated

[1]The average Fermi velocities in the '1111' superconductor $LaFeAsO_{1-x}F_x$ are $0.81 \times 10^7\,\mathrm{cm\,s^{-1}}$ (in-plane) and $0.34 \times 10^7\,\mathrm{cm\,s^{-1}}$ (c-axis) for the hole pockets and $2.39 \times 10^7\,\mathrm{cm\,s^{-1}}$ (in-plane) and $0.35 \times 10^7\,\mathrm{cm\,s^{-1}}$ (c-axis) for the electron pockets [69]

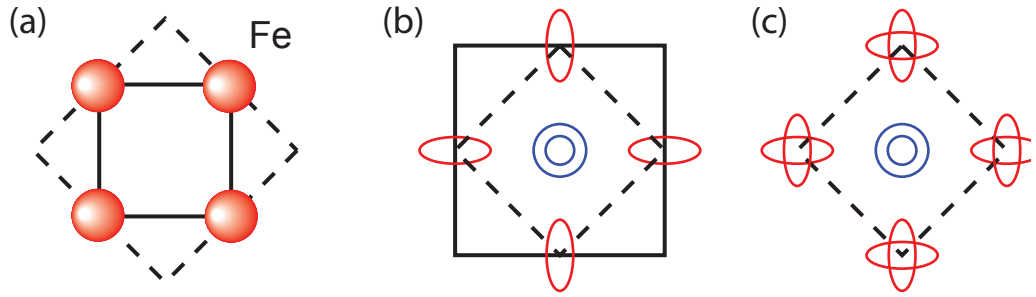

Figure 2.7: 1-Fe and 2-Fe unit cell and BZ of the FeSCs. (a) 1-Fe (solid lines) and 2-Fe unit cell (dashed lines). (b), (c) 1-Fe (solid lines) and 2-Fe BZ (dashed lines). The red ellipses mark the electron and the blue circles the hole bands. Due to backfolding the electron bands intersect each other in the 2-Fe BZ in (c) as opposed to the 1-Fe BZ in (b).

theoretically via LDA [70] and density-functional-theory (DFT) calculations [74]. The density of states (DOS) at the Fermi energy is found to be only weakly doping dependent in contrast to what one expects from the presence of a rigid band model [70]. The main effect of doping is rather a change of the sizes of the electron and hole pockets. Hence, doping leads to a reduction in the degree of nesting of the FSs [70].

The two electron and two hole pockets in the BZ of undoped '1111' and '122' FeSCs as well as the change of the sizes of the FS sheets upon doping is in principle verified by angle-resolved-photo-emission spectroscopy (ARPES) experiments [75, 76, 77, 78, 79]: Upon hole doping, the electron pockets become smaller and the hole pockets are expanded [61] while upon electron doping the central hole pockets are observed to shrink and the electron pockets grow in size [80]. The latter is observed in overdoped $Ba(Fe_{1-x}Co_x)_2As_2$ indicating that Co substitution introduces additional electrons in the unit cell as opposed to the discussion in Sec. 2.2 that the extra d electron of Co is located within the muffin-tin sphere of the substituted site.

2.3.2 Orbital character of the bands

The five bands crossing the Fermi level E_F originate in first order approximation from the five Fe $3d$ orbitals d_{xy}, d_{xz}, d_{yz}, d_{x2-y2} and $d_{3z^2-r^2}$ [10]. This makes the FeSCs more complicated than the cuprates where the only conduction band consists of one single orbital, the copper $d_{x^2-y^2}$ orbital hybridizing with the oxygen $p_{x,y}$ orbitals [81].

Due to the importance of the Fe atoms for the electronic properties of the FeSCs the so called 1-Fe BZ will be applied in this thesis. The 1-Fe BZ [solid line in Fig. 2.7(b)] is derived from the square lattice of the Fe atoms and the corresponding unit cell contains only one Fe atom [solid line in Fig. 2.7(a)]. The 2-Fe BZ in Fig. 2.7(c) is derived from

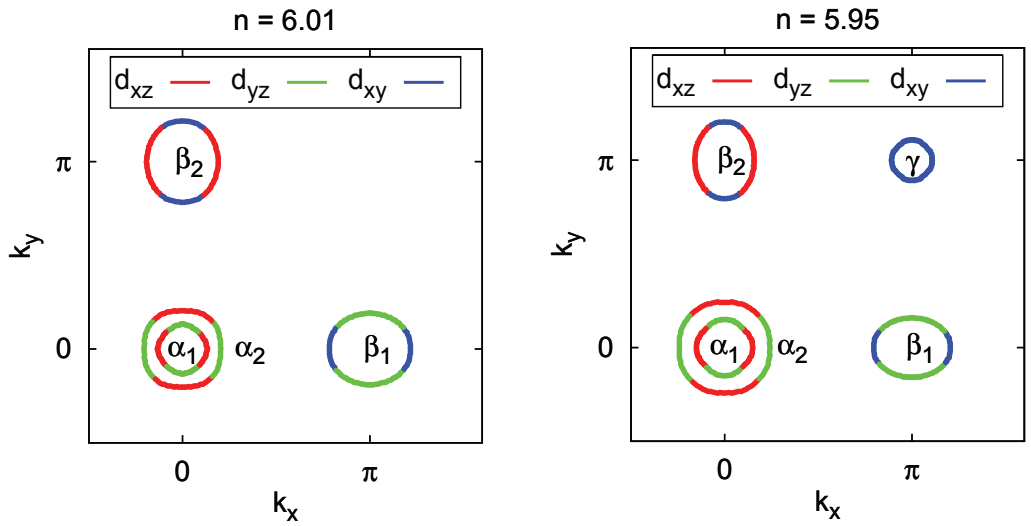

Figure 2.8: Orbital character of the bands. Shown are the electron (β_i) and hole bands (α_i) in the 1-Fe BZ for electron (n=6.01) and hole doping (n=5.95). For hole doping there emerges a third hole band at (π, π) which is referred to as the γ band. From [84].

the crystallographic unit cell containing two Fe atoms [dashed line in Fig. 2.7(a)]. As illustrated in Fig. 2.7(b) the 1-Fe BZ is rotated by 45° and has twice the size of the 2-Fe BZ [dashed line in Fig. 2.7(b)]. In addition, the electron bands in the 1-Fe BZ are unfolded and sit at the X $[(\pi, 0)]$ points of the BZ as opposed to the folded electron bands of the 2-Fe BZ which are located at the corner ($[(\pi, \pi)]$ points) of the BZ [Fig. 2.7(c)].

To illustrate the orbital character of the bands, the results of a five orbital tight-binding model solved in random-phase-approximation (RPA) are presented in the 1-Fe BZ in Fig. 2.8 [20]. In RPA, both hole bands have predominantly d_{xz} and d_{yz} character while the electron bands consist of d_{xy}, d_{xz} and d_{yz} orbitals. This result is by and large corroborated by polarization dependent ARPES studies which reveal little variation in the orbital nature of the hole bands[2] [78, 82]. Due to the orbital character of the bands the relevance of orbital ordering phenomena in the FeSCs has been emphasized early [85]. Additionally, the observed strong anisotropies of the mobilities, Fermi velocities and masses between the hole and electron bands can be explained via the orbital character by intra- and interorbital scattering [86].

2.3.3 Nematic phase

A nematic phase breaks the rotational symmetry of a lattice spontaneously while preserving the translational and mirror symmetry [15, 87]. The nematicity manifests itself

[2] experimentally it was reported that the hole band consist of d_{xy} and d_{xz}/d_{yz} orbitals [78, 82, 83]

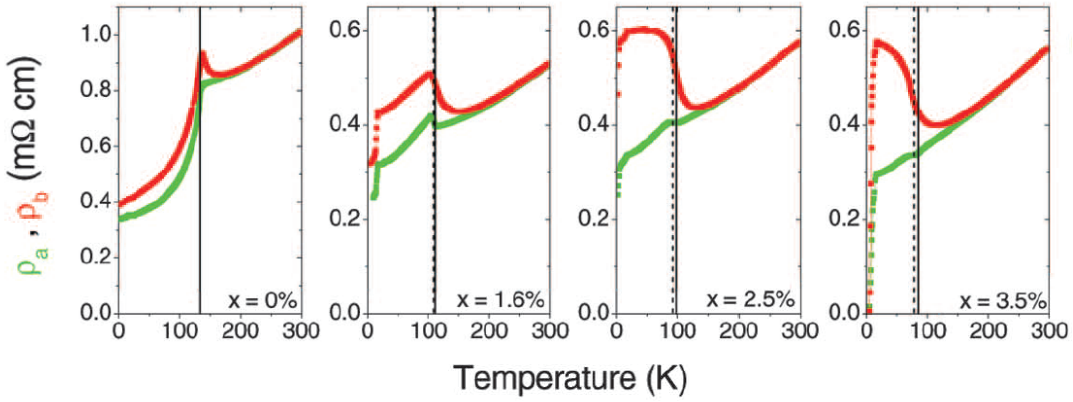

Figure 2.9: Temperature dependence of the in-plane resistivity along the ferromagnetic a (ρ_a, green) and antiferromagnetic b direction (ρ_b, red) of detwinned $Ba(Fe_{1-x}Co_x)_2As_2$. Solid and dashed vertical lines indicate the structural and magnetic transition temperature, respectively. From [60].

in a large and strongly temperature dependent anisotropy of the electronic response to a small symmetry breaking external field [88]. Such an anisotropy is observed in transport measurements where the resistivity along the a- and b-axes, nominally equivalent in a tetragonal lattice, is different for detwinned $Ba(Fe_{1-x}Co_x)_2As_2$ (Fig. 2.9) [60] and $Eu(Fe_{1-x}Co_x)_2As_2$ single crystals [89]. Also by means of neutron scattering [90] and scanning tunneling experiments [91] an in-plane anisotropy along the equivalent a- and b-axes was detected.

Hence, in the FeSCs the phase below T_{TO} breaks the tetragonal C_4 symmetry, and the quantum fluctuations associated with this phase are nematic in character [92]. Nevertheless it is unclear whether the structural phase transition and therefore the nematic order is induced by magnetic fluctuations due to the onset of antiferromagnetic order [19, 93, 94] or by orbital ordering phenomena in the quasi 1D d_{xz} and d_{yz} bands [18, 95, 96].

2.4 Magnetism

Magnetism is not only a candidate for driving the T_{TO} phase transitions. Due to the close proximity of magnetism and superconductivity in the phase diagram, magnetic and spin fluctuations are also believed to be important for the superconducting pairing mechanism [97, 98, 99, 100].

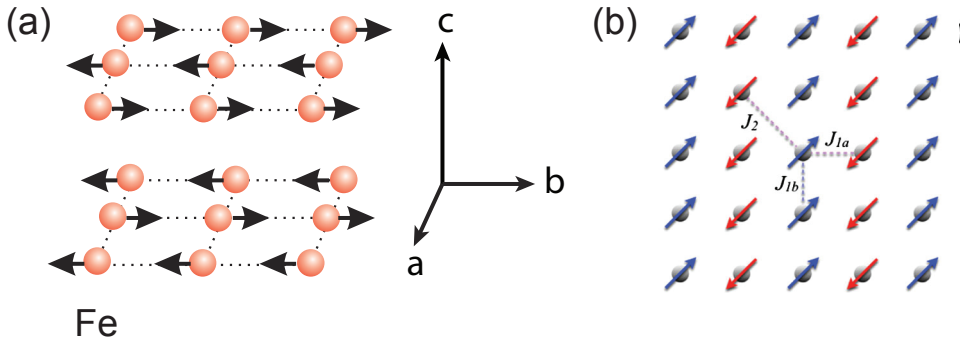

Figure 2.10: Magnetic order and coupling between nearest and next nearest neighbors. (a) The spins of the Fe atoms are antiferromagnetically ordered along the c- and the a-axis and ferromagnetically aligned along the b-axis of the 1-Fe unit cell (from [101]). (b) Coupling between nearest (J_1) and next nearest neighbors (J_2). The coupling between nearest neighbors may be different along the a- and b-axis (from [33]).

2.4.1 Magnetic order

The magnetic order below T_{SDW} is illustrated in Fig. 2.10(a). It is ferromagnetic along the b- and antiferromagnetic along the a- and c-axis as shown by neutron diffraction experiments [101, 102]. The ordered Fe moments in the ab-plane are roughly $0.36\,\mu_B$ in '1111' [101] and $0.9\,\mu_B$ in '122' compounds [102, 103]. This is remarkably smaller than the theoretically expected values of roughly $2.3\,\mu_B$ per Fe atom [104]. The large discrepancy is attributed to the dichotomy between the theoretically calculated moment which is formed due to local Hund's rule spin alignment and the dynamically screened moment which is determined experimentally [105].

The resistivity ρ in detwinned samples is larger along the ferromagnetic b- than along the a-direction as illustrated in Fig. 2.9 [60, 89] contrary to the expectation that scattering from spin fluctuations results in a larger resistivity along the antiferromagnetic direction [89]. The discrepancy of ρ between the a- and b-axis is largest for underdoped samples with $x = 0.025$ while it is small for the undoped sample and weakens toward optimal doping. For overdoped samples it is entirely absent [60].

For the nature of the magnetism in the FeSCs a band-like itinerant [106] and a Mott-like [6] localized model [93], are conceivable. On the one hand, the undoped and underdoped compounds exhibit long range magnetic order at low temperatures. On the other hand, even the undoped FeSCs stay metallic without indications of any insulating behavior. This dichotomy is also observed in an optical study where transport is argued to be between an itinerant and a localized picture [107]. For the explanation of the experimental data an anisotropic in-plane exchange coupling $J_{1a} - J_{1b} - J_2$ model, as

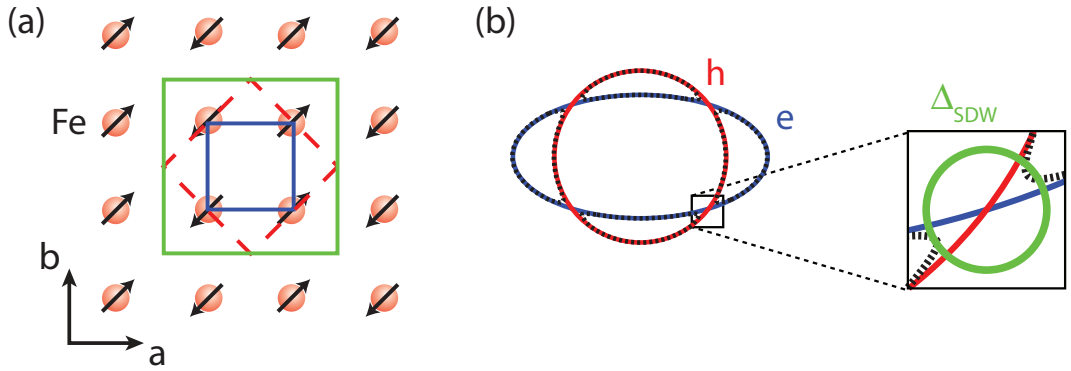

Figure 2.11: Impact of the magnetic order on the unit cell and the BZ. (a) The magnetic order introduces a magnetic unit cell (green line) which is a factor of two larger than the 2-Fe unit cell (red dashed line) and a factor of four larger than the 1-Fe unit cell (blue line). (b) The doubling of the unit cell cuts the first BZ into half. The correlated backfolding of the BZ projects the electron band (blue ellipse) onto the hole bands (red ellipse) and a new FS is formed (doted lines). At the spots where the electron and hole FS intersect the SDW gap (green ellipse) opens up.

shown in Fig. 2.10(b), is theoretically suggested [108, 109]. In an INS study by Zhao *et al.* the magnetism in the parent compounds is reported to be neither purely localized nor purely itinerant [90]. Since the data at low and high energy of an INS study by Ewings *et al.* cannot be fitted with a single parameter set in a local moment model and the spectra only weakly change upon warming through T_{SDW}, an itinerant picture is reported to better explain these data [11].

2.4.2 Fermi surface reconstruction below T_{SDW}

In both, the itinerant and the localized picture, the onset of magnetic order below T_{SDW} doubles the crystallographic unit cell as illustrated in Fig. 2.11(a) [110]. Hence, the antiferromagnetic BZ has only half the size in comparison to the non magnetic 2-Fe BZ. The correlated backfolding of the 2-Fe BZ projects the electron bands onto the hole bands as shown in Fig. 2.11(b). At the intersection points of both FSs an at least nodal [111] SDW gap opens up [112]. Here, ARPES [113] and quantum oscillation (QO) experiments [110, 114, 115] provide evidence that the newly constructed FS consists of several small pockets. While in early ARPES studies the reconstruction of the FS was not observed [116], in later studies it is concluded that there are large exchange splitting phenomena in the SDW state leading to band splittings and possibly gaps [117]. Just recent ARPES studies were capable to fully reproduce the reconstructed FS as seen via QO experiments [118]. However, these studies reveal that the electronic structure cannot be explained by

a band folding and FS nesting picture alone. Rather, the magnetostructural transition accompanies the orbital-dependent modifications in the electronic structure which has been detected by linearly polarized laser ARPES [119]. While the splitting of the bands is a genuine feature of the magnetic phase, the importance of the orbital character of the multiband FeSCs was pointed out in the interpretation of an ARPES study of detwinned $BaFe_2As_2$ single crystals [120].

2.5 Superconducting properties

In close proximity to the magnetic phase superconductivity emerges. Imprints of the magnetism on superconductivity are expected if the two phases are interrelated. This holds particularly true for quantities such as the superconducting gap. The magnitude and symmetry of the gap is one of the most studied properties of the FeSCs. Knowledge about the gap size and symmetry would put some constraints on the nature of the pairing mechanism.

2.5.1 Electron-phonon interaction

The strength of the electron-phonon interaction was calculated early via first principle approaches and found to be too weak to explain the high T_c's [121]. This is corroborated by INS studies. These studies observed for different compounds a phonon density of states which is in good agreement to the theoretical considerations. The analysis of the data indicates only weak electron-phonon coupling [122, 123, 124]. Hence, also the experimental results are not compatible with a conventional electron-phonon mediated superconductivity. Nevertheless, an isotope effect on $Ba_{1-x}K_xFe_2As_2$ samples was reported with values of $\alpha = 0.4$ [125, 126] which is a rather sizable effect close to that of BCS phonon-mediated superconductors ($\alpha = 0.5$). The contradiction between weak electron-phonon coupling and a sizable isotope effect was explained via a spin-fluctuation pairing model [99]. Thus, there is general agreement that alternatives to the phonon mediated superconductivity in the FeSCs are needed.

2.5.2 Gap symmetry and gap structure

In the absence of spin-orbit coupling the total spin S of a Cooper pair is either $S = 0$ or $S = 1$. From measurements of the Knight shift [127, 128, 129, 130, 131, 132] and Josephson tunneling experiments [133] it is well established that the Cooper pairs form

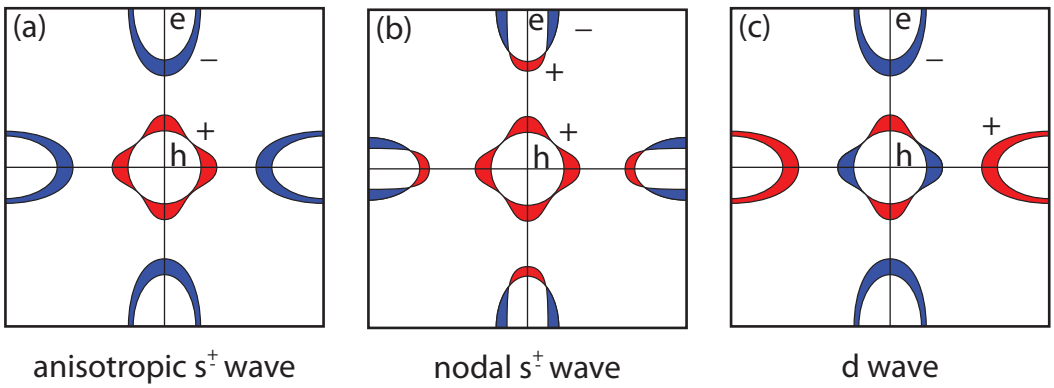

Figure 2.12: Symmetries of the energy gap in momentum space: (a) anisotropic $s^{\pm}$-wave (b) nodal $s^{\pm}$-wave and (c) d-wave. Red (blue) denote a positive (negative) sign of the order parameter. e and h indicate the electron and hole bands, respectively.

a spin singlet state. Hence, in a 3D tetragonal system, there are several possible representations how the order parameter transforms under 90° rotation and other operations of the tetragonal group. This includes A_{1g} (s-wave) and B_{1g} (d-wave) [132]. Fig. 2.12 shows the case of an extended $s^{\pm}$- and a d-wave gap. The extended $s^{\pm}$-wave gap changes sign between the hole and electron bands, but, as opposed to the d-wave, it does not change sign if the crystal axes are rotated by 90°.

Apart from these symmetry considerations, the gap structure $\Delta(\mathbf{k})$, which describes the $\mathbf{k}$-dependent variation of the gap magnitude within a given symmetry class, is a matter of current research in the FeSCs. For an anisotropic $s^{\pm}$ gap [Fig. 2.12(a)] the magnitudes of the gaps on the electron and hole bands change as a function of $\mathbf{k}$ but there is no sign change of the order parameter on one band. Nevertheless, osculating or kissing nodes [134] may occur where the minimal gap approaches zero. This is opposed to the nodal $s^{\pm}$ gap where true nodes occur on the electron bands due to the sign change of the order parameter. Here, the sign on the hole pockets is still opposite to the average sign on the electron bands [132]. Since these so called true nodes are not imposed by symmetry they are often called accidental [132]. A d-wave gap structure is shown in Fig. 2.12(c). Since the d-wave gap transforms like B_{1g} symmetry the gap is $\mathbf{k}$ dependent and changes sign on the hole band. Therefore, true nodes are imposed by symmetry on the hole bands. The sign of the gap on the electron bands changes on the nearest neighbor bands. Here, the gaps may be isotropic as well as anisotropic.

Chapter 3

Theory

In this chapter basics about the theory of electronic Raman scattering are discussed. The main focus is placed on theoretical concepts relevant for this thesis. For details the reader is referred to a comprehensive overview in [135] and references therein.

3.1 The Raman effect

In a Raman scattering experiment photons with energy $\hbar\omega_i$ and momentum $\mathbf{k}_i$ are focused on a sample. Most of the photons are scattered off elastically and only the minor part is scattered inelastically. The energy $\hbar\omega_s$ and momentum $\mathbf{k}_s$ of these inelastically scattered photons is analyzed. Energy and momentum conservation require that

$$\hbar\Omega = \hbar\omega_i - \hbar\omega_s \qquad \text{energy conservation} \tag{3.1}$$

$$\mathbf{q} = \mathbf{k}_i - \mathbf{k}_s \qquad \text{momentum conservation} \tag{3.2}$$

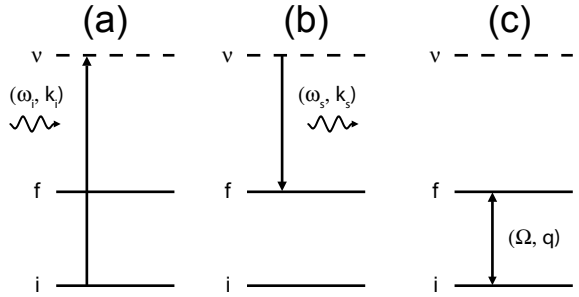

Figure 3.1: Energy scheme of the Raman process. i and f are the initial and final energy level, respectively, and ν is a virtual energy level. $\omega_{i,s}$ and $\mathbf{k}_{i,s}$ are the energy and momentum of the incoming and scattered photon. Only the Stokes process $\Omega > 0$ is shown.

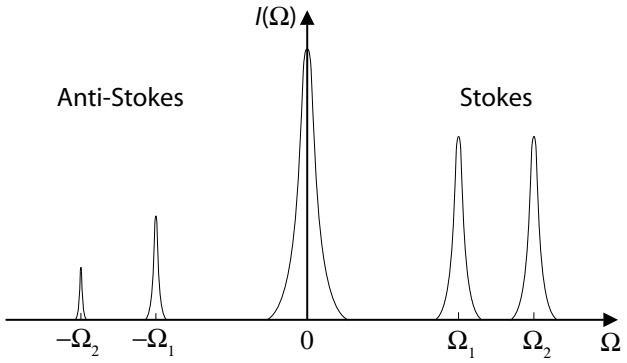

Figure 3.2: Schematic Raman spectrum with excitations on the Stokes ($\Omega > 0$) and Anti-Stokes side ($\Omega < 0$). The Raman intensity $I(\Omega)$ on the Stokes side is higher than on the Anti-Stokes side. The peak at $\Omega = 0$ originates from elastically scattered light.

where $\hbar\Omega$ is the energy and $\mathbf{q}$ the momentum transfered to the electron. In the scattering process an electron absorbs the energy $\hbar\omega_i$ of the incoming photon and is transfered to a higher energy level. From this excited level the electron relaxes and emits a photon with energy $\hbar\omega_s$ as illustrated in Fig. 3.1. In the Raman experiment one distinguishes between the Stokes process (ST, $\omega_i > \omega_s$), where excitations with energy Ω are created, and the Anti-Stokes process (AS, $\omega_i < \omega_s$), where excitations with energy Ω are annihilated.

A schematic Raman spectrum is shown in Fig. 3.2. It displays the number of scattered photons $I(\Omega)$ versus the Raman shift Ω, which is given in units of wavenumbers ($8.065\,\mathrm{cm}^{-1} = 1\,\mathrm{meV}$). The peak at $\Omega = 0$ originates from the elastically scattered photons and the peaks at Ω_1 and Ω_2 from the excitations created in the sample. In the AS spectrum the peaks occur at the same energy but are lower in intensity since the number of excitations in the sample decreases with temperature. Due to time-reversal symmetry and phase space arguments, the intensity of the ST (I_{ST}) and AS spectrum (I_{AS}) are related by the principle of detailed balance via

$$\frac{I_{AS}}{I_{ST}} = \left(\frac{\omega_i + \Omega}{\omega_i - \Omega}\right)^2 \cdot e^{-\frac{\hbar\Omega}{k_B T}} \tag{3.3}$$

with k_B the Boltzmann constant. Via the comparison of I_{ST} and I_{AS} the temperature T of the sample in the laser spot can be estimated.

3.2 Electronic Raman scattering

For a theoretical description of electronic Raman scattering, the interaction part of the N electron Hamiltonian coupled to an electromagnetic field,

$$H_{int} = \frac{e}{2m}\sum_{i}^{N}[\hat{\mathbf{p}}_i \cdot \mathbf{A}(\mathbf{r}_i) + \mathbf{A}(\mathbf{r}_i)\cdot\hat{\mathbf{p}}_i] + \frac{e^2}{2m}\sum_{i}\mathbf{A}(\mathbf{r}_i)\cdot\mathbf{A}(\mathbf{r}_i) \tag{3.4}$$

is introduced where e and m is the charge and mass of the electron, respectively. $\hat{\mathbf{p}}_i$ and $\mathbf{r}_i$ are the momentum and position of the i^{th} electron, respectively, and $\mathbf{A}(\mathbf{r}_i)$ the vector potential.

Raman scattering measures the total cross-section of all electrons illuminated by the light [136]. The scattering intensity $\dot{N}(\Omega, T)$ of inelastically scattered light is proportional to the differential photon cross-section

$$\dot{N}(\Omega, T) \propto \frac{\partial^2\sigma}{\partial\widetilde{\Omega}\partial\omega_s} = \hbar r_0^2\frac{\omega_s}{\omega_i}R \tag{3.5}$$

which gives the probability that the incident photon with energy ω_i is scattered into a solid-angle interval between $\widetilde{\Omega}$ and $\widetilde{\Omega}+d\widetilde{\Omega}$ in an energy window between ω_s and $\omega_s+d\omega_s$. $r_0 = e^2/4\pi\epsilon_0 mc^2$ is the Thompson radius of the electron and

$$R = \frac{1}{Z}\sum_{I,F}\exp(-\beta E_I)|M_{F,I}|^2\delta(E_F - E_I - \hbar\Omega) \tag{3.6}$$

with $\beta = 1/k_BT$, Z the partition function and $M_{F,I} =< F|M|I >$, where $|F >, |I >$ are the initial and final states, respectively. M is the effective light scattering operator and contains the electron-photon interaction. The electron-photon interaction is given by Eq. (3.4) which shows that the contributions to $M_{F,I}$ originates from three terms: the first two terms couple the electron's current to a single photon and the last term couples the electron's charge to two photons [135].

In the limit of small momentum transfer to the electron, $\mathbf{q}$ is small with respect to the Fermi momentum, $|\mathbf{q}| \ll k_F$ and the limit $q \to 0$ is applicable. Then, the evaluation of the matrix elements $M_{F,I}$ is simplified. Assuming that the intermediate many-particle states only differ from the initial and final states by single-electron excitations, which is exact only for non-interacting electrons, the matrix element, simplified using commutator

algebra, can be written as [135, 136]

$$M_{F,I} = \sum_{\alpha,\beta} \gamma_{\alpha,\beta} < F|\hat{c}_\alpha^+ \hat{c}_\beta|I > \tag{3.7}$$

with $\hat{c}^+$ and $\hat{c}$ the electron creation and annihilation operators, respectively, and

$$\gamma_{\alpha,\beta} = \rho_{\alpha,\beta}(\mathbf{q})\hat{\mathbf{e}}_i\hat{\mathbf{e}}_s + \frac{1}{m}\sum_{\beta'}\left(\frac{p^s_{\alpha,\beta'}p^i_{\beta',\beta}}{E_\beta - E_{\beta'} + \hbar\omega_i} + \frac{p^i_{\alpha,\beta'}p^s_{\beta',\beta}}{E_\alpha - E_{\beta'} - \hbar\omega_s}\right). \tag{3.8}$$

$\gamma_{\alpha,\beta}$ is the scattering amplitude indexed by quantum numbers α, β. It depends on the initial, intermediate and final states of the electrons. $p^{i,s}_{\alpha,\beta}(\mathbf{q}_{i,s}) =< \alpha|\mathbf{p}\cdot\mathbf{e}_{i,s}e^{\pm i\mathbf{q}_{i,s}\mathbf{r}}|\beta >$ is the momentum density matrix element with the polarization vectors of incident ($\mathbf{e}_i$) and scattered light ($\mathbf{e}_i$). $\rho_{\alpha,\beta}(\mathbf{q})$ is the matrix element for single-particle density fluctuations. If the energy of the incoming or outgoing photon equals the energy gap separation between the bands for interband transitions, $\gamma_{\alpha,\beta}$ and therefore the matrix element $M_{F,I}$ diverges and the scattering may be resonant.

Hence, R in Eq. (3.6) depends on γ and can be expressed via the dynamical effective density-density correlation function $S_{\gamma\gamma}(\mathbf{q}, \Omega, T)$. With this replacement, Eq. (3.5) reads

$$\dot{N}(\Omega, T) \propto \frac{\partial^2\sigma}{\partial\widetilde{\Omega}\partial\omega_s} = \hbar r_0^2 \frac{\omega_s}{\omega_i} S_{\gamma\gamma}(\mathbf{q}, \Omega, T). \tag{3.9}$$

Via the fluctuation-dissipation theorem $S_{\gamma\gamma}(\mathbf{q}, \Omega, T)$ is related to the imaginary part of the Raman response function $\chi''(\mathbf{q}, \Omega)$ and can be written as

$$S_{\gamma\gamma}(\mathbf{q}, \Omega, T) = -\frac{1}{\pi}\left[1 + n(\Omega, T)\right]\chi''_{\gamma\gamma}(\mathbf{q}, \Omega) \tag{3.10}$$

where $n(\Omega, T)$ is the Bose distribution function

$$n(\Omega, T) = \frac{1}{e^{\frac{\hbar\Omega}{k_B T}} - 1}. \tag{3.11}$$

Hence, via Eq. (3.9) and (3.10) the Raman scattering intensity is related to the Raman response function and reads

$$\dot{N}(\Omega, T) = R_{\gamma\gamma} \cdot \left[1 + n(\Omega, T)\right] \cdot \chi''_{\gamma\gamma}(\mathbf{q}, \Omega) \tag{3.12}$$

with $R_{\gamma\gamma}$ a symmetry-dependent factor absorbing all frequency and temperature inde-

pendent constants. The scattering amplitude γ is proportional to the Raman matrix elements and depends on the incident and scattered light polarization vectors as

$$\gamma(\mathbf{k},\mathbf{q}) = \sum_{\mu,\nu} \gamma_{\mu,\nu}(\mathbf{k},\mathbf{q}) \mathbf{e}_i^\mu \mathbf{e}_s^\nu. \tag{3.13}$$

The Raman vertex $\gamma_{\mu,\nu}(\mathbf{k},\mathbf{q})$, with $\mu,\nu = x,y,z$, itself depends non-trivially on the energy of incoming and scattered photons and the initial, intermediate and final states of the electrons.

The polarization dependence of $\gamma_{\mu,\nu}(\mathbf{k},\mathbf{q})$ can be expressed using group theory arguments. Since the Raman fluctuations vary along the same directions as the polarizations of incoming and outgoing photons which induce the fluctuations, the Raman fluctuations obey the same symmetry rules governing the scattering geometry. Thus, the Raman vertex can be decomposed into basic functions of the irreducible point group of the crystal Φ_L [137, 138, 139, 140, 141]

$$\gamma(\mathbf{k},\mathbf{q}\to 0) = \sum_L \gamma_L(\mathbf{q}\to 0)\Phi_L(\mathbf{k}). \tag{3.14}$$

L is an irreducible representation of the point group of the crystal and the polarization direction of incoming and scattered photons determine which set of L contributes to the sum. Alternatively, assuming that the energies of incoming and outgoing photons are vanishingly small with respect to the distance between conduction band and intermediate state, $\hbar\omega_{i,s} \ll |\epsilon_{\mathbf{k}\nu} - \epsilon_{\mathbf{k}}|$, the scattering amplitude simplifies to the well known effective-mass approximation [142]

$$\gamma(\mathbf{k},\mathbf{q}\to 0) = \sum_{\mu,\nu} e_\mu^i \frac{1}{\hbar^2} \frac{\partial^2 \epsilon_{\mathbf{k}}}{\partial k_\mu \partial k_\nu} e_\nu^s \tag{3.15}$$

In this approach the Raman vertex depends on the curvature of the conduction band and the polarization vectors of incident and scattered light. Thus, the sensibility of the Raman vertex in different $\mathbf{k}$-space regions in the BZ can be calculated given the knowledge of the band dispersion.

3.3 Raman response function

For the calculation of the Raman response the contribution originating from different Feynman diagrams must be added up [135]. The leading contribution comes from the

polarization bubble shown in Fig. 3.3 where the dashed and solid lines correspond to photonic and fermionic propagators, respectively. γ represents the Raman vertex containing the details of the electron-photon interaction. For the determination of the Raman response one generally needs to take the effects of vertex correction into account. Since these corrections are shown to produce only minor corrections in the B_{1g} and B_{2g} spectra [143], they will be neglected in the following. Then, the Raman response function $\chi_{\gamma\gamma}$ in the normal state reads [144]

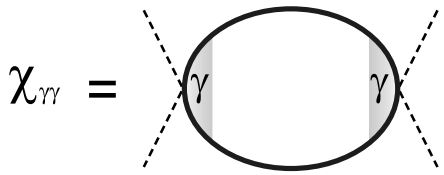

Figure 3.3: Feynman diagram of the polarization bubble. Dashed and solid lines represent photonic and fermionic propagators, respectively. γ denotes the **k**-dependent Raman vertex.

$$\chi^0_{\gamma\gamma}(\mathbf{q}, i\omega) = \frac{1}{\beta}\sum_{\mathbf{k},i\omega'} \gamma_{\mathbf{k}} G(\mathbf{k}, i\omega')\gamma_{\mathbf{k}} G(\mathbf{k}-\mathbf{q}, i\omega' - i\omega). \tag{3.16}$$

with $\hbar = k_B = 1$. $G(\mathbf{k}, i\omega')$ is the fermionic propagator and $i\omega = 2n\pi T$ and $i\omega' = (2n+1)\pi T$ are the bosonic and fermionic Matsubara frequencies. The electronic propagator is renormalized due to impurities or electron-electron interactions. Using the Dyson equation, the renormalized Green's function reads

$$G(\mathbf{k}, i\omega)^{-1} = G^{(0)}(\mathbf{k}, i\omega)^{-1} - \Sigma(\mathbf{k}, i\omega) \tag{3.17}$$

where $G^{(0)}$ is the bare propagator and $\Sigma(\mathbf{k}, i\omega) = \Sigma'(\mathbf{k}, i\omega) + i\Sigma''(\mathbf{k}, i\omega)$ is the self energy, which is generally complex. $\Sigma''(\mathbf{k}, i\omega)$ can be associated with the damping of the particle motion and $\Sigma'(\mathbf{k}, i\omega)$ is the energy shift of the excitation due to interactions. The gauge-invariant and hence charge-conserving form of the total Raman response reads [143]

$$\chi_{\gamma\gamma}(i\omega) = \chi^0_{\gamma\gamma}(i\omega) - \frac{[\chi^0_{\gamma 1}(i\omega)]^2}{\chi^0_{11}(i\omega)}, \tag{3.18}$$

where $\chi_{\gamma 1}$ and χ_{11} are obtained via the replacement $\gamma(\mathbf{k}) = 1$. Since the scattering cross-section is proportional to the imaginary part of the response function, the imaginary part of Eq. (3.18) must be calculated after the analytic continuation to real frequencies.

3.3.1 Normal state

For the calculation of the response in the normal state the bare electronic propagator is expressed via $G^{(0)}(\mathbf{k}, i\Omega)^{-1} = i\Omega - \xi_{\mathbf{k}}$ and therefore the Green's function reads

$$G(\mathbf{k}, i\Omega) = \frac{1}{i\Omega - \xi_{\mathbf{k}} - \Sigma(\mathbf{k}, i\Omega)}. \tag{3.19}$$

$\xi_{\mathbf{k}} = \epsilon_{\mathbf{k}} - \mu$ is the quasiparticle energy and $\epsilon_{\mathbf{k}}$ and μ the band dispersion and chemical potential, respectively. Inserting this expression of the Green's function into Eq. (3.16) and taking the imaginary part, one obtains after performing the sum over the fermionic Matsubara frequencies and the analytic continuation

$$\chi''_{\gamma\gamma}(\mathbf{q}, \Omega) = \frac{1}{N} \sum_{\mathbf{k}} \gamma_{\mathbf{k}}^2 \int_{\infty}^{\infty} \frac{d\omega}{\pi} G''(\omega, \mathbf{k}) G''(\omega + \Omega, \mathbf{k} + \mathbf{q}) \left[n_F(\omega) - n_F(\omega + \Omega) \right] \tag{3.20}$$

with $n_F(\omega)$ the Fermi Dirac distribution function. This equation is usually evaluated in the limit $\mathbf{q} \to 0$.

3.3.2 Superconducting state

In the superconducting state the response is given in Nambu notation [145] in particle-hole space via the 2×2 Pauli matrices $\hat{\tau}_{i=0\ldots3}$. In the BCS approximation and for singlet pairing, the Green's function is written as a matrix and is expressed via

$$\hat{G}(\mathbf{k}, i\Omega) = \frac{i\Omega\hat{\tau}_0 + \xi_{\mathbf{k}}\hat{\tau}_3 + \Delta_{\mathbf{k}}\hat{\tau}_1}{(i\Omega)^2 - E_{\mathbf{k}}^2} \tag{3.21}$$

with $E_{\mathbf{k}}^2 = \xi_{\mathbf{k}}^2 + \Delta_{\mathbf{k}}^2$ the quasiparticle energies, $\xi_{\mathbf{k}}$ the band dispersion and $\Delta_{\mathbf{k}}$ the energy gap. The Raman vertex is given via the replacement $\gamma_{\mathbf{k}} \to \hat{\gamma}_{\mathbf{k}} = \gamma_{\mathbf{k}}\hat{\tau}_3$, and Eq. (3.16) reads

$$\chi^0_{\gamma\gamma}(\mathbf{q}, i\omega) = \frac{1}{\beta} \mathrm{Tr} \sum_{\mathbf{k}, \mathrm{i}\omega'} \hat{\gamma}_{\mathbf{k}} \hat{\mathrm{G}}(\mathbf{k}, \mathrm{i}\omega') \hat{\gamma}_{\mathrm{k}} \hat{\mathrm{G}}(\mathbf{k} - \mathbf{q}, \mathrm{i}\omega' - \mathrm{i}\omega). \tag{3.22}$$

For materials with n bands crossing the Fermi level, the Raman spectra in the absence of Coulomb screening, charge backflow and after performing the Matsubara frequency summation is given in the limit $\mathbf{q} \to 0$ by [146]

$$\chi_{\gamma\gamma}(\Omega) = \frac{1}{N} \sum_{n} \sum_{\mathbf{k}} \gamma_n(\mathbf{k})^2 \lambda_n(\mathbf{k}, \Omega), \tag{3.23}$$

where

$$\lambda_n(\mathbf{k},\Omega) = \tanh\left(\frac{E_n(\mathbf{k})}{2k_BT}\right)\frac{4 \mid \Delta_n(\mathbf{k}) \mid^2 / E_n(\mathbf{k})}{4E_n^2(\mathbf{k}) - (\hbar\Omega + i\delta)^2} \tag{3.24}$$

is the Tsuneto-Maki function for the n^{th} band.

To model the spectra, band structure effects are neglected and all Fermi surface sheets are taken as circles. The imaginary part of Eq. (3.24) at $T = 0$ after integrating over energies reads [147]

$$\chi''_{\gamma\gamma}(\Omega) = \sum_n \chi''_{\gamma\gamma,n}(\Omega) = \sum_n \frac{N_{F,n}}{2\Omega}\int d\theta\gamma_n^2(\theta)\Re\frac{\mid \Delta_n(\theta) \mid^2}{\sqrt{\Omega^2 - 4 \mid \Delta_n(\theta) \mid^2}}, \tag{3.25}$$

with the real parts determined by Kramers-Kronig transformations. This expression indicates the interplay of anisotropies of the Raman vertices and the energy gap on each band.

3.4 Momentum resolution of the Raman response

The importance of ERS is based on the finite momentum resolution of ERS [Eq. (3.14) and (3.15)]. In this section the sensitivity of the Raman vertex in the first BZ of the FeSCs and the proper alignment of the incoming and outgoing photons to access these symmetries is described. Due to the importance of the Fe atoms for the electronic properties, the electronic or 1-Fe BZ is used which is derived from the 1-Fe unit cell (c.f. Sec. 2.3).

3.4.1 The Raman vertex

According to Eq. (3.14), the Raman vertex can be decomposed into basis function of the irreducible point group of the crystal. The FeSCs crystallize in a tetragonal lattice obeying the D_{4h} symmetry group and the leading order contribution to the relevant symmetries are

$$\begin{aligned}
\Phi_{A_{1g}}(\mathbf{k}) &= \text{constant} + \cos(\mathrm{k_x a}) + \cos(\mathrm{k_y a}) + \ldots, \\
\Phi_{B_{1g}}(\mathbf{k}) &= \cos(\mathrm{k_x a}) - \cos(\mathrm{k_y a}) + \ldots, \\
\Phi_{B_{2g}}(\mathbf{k}) &= \sin(\mathrm{k_x a})\sin(\mathrm{k_y a}) + \ldots.
\end{aligned} \tag{3.26}$$

The momentum-dependence of the Raman vertex in the first BZ is illustrated in Fig. 3.4 displaying contour plots of the leading order basis function of Eq. (3.26). The

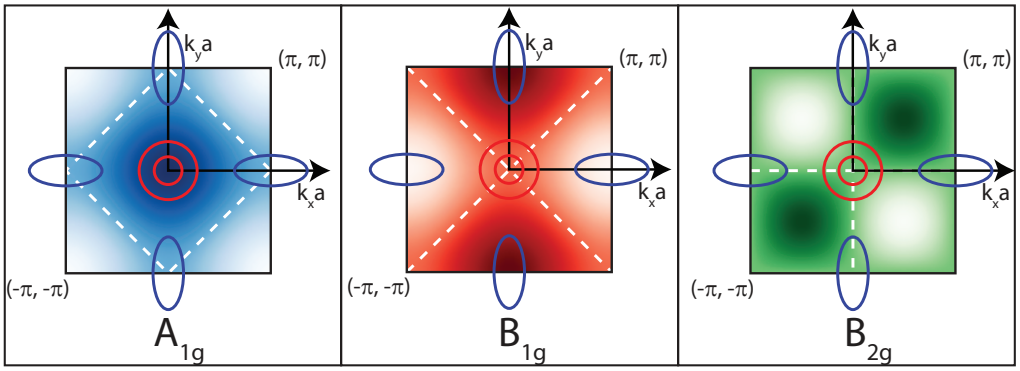

Figure 3.4: Momentum-dependence of the BZ harmonics in the 1-Fe BZ. Color and white regions mark where the vertex is maximal and minimal, respectively. The white dashed lines mark where the vertex is identical zero. Red circles and blue ellipses indicate the position of the hole and electron bands, respectively.

maximal and minimal values are represented by color and white, respectively. The electron and hole bands are indicated as blue and red ellipses, respectively. From the figure it is clear that the A_{1g} vertex is largest in regions of the BZ where the hole bands are located. While the B_{1g} vertex is extremal at the electron bands, the B_{2g} vertex is sensitive in regions where no bands cross the Fermi level.

The symmetry of the Raman vertex is described sufficiently by the symmetry considerations of Eq. (3.14) which will be applied throughout this work. The effective-mass-approximation, as evaluated in Sec. 7.5.2, brings only minor correction to the above symmetry considerations. Thus, in B_{1g} symmetry the electron bands are mainly probed while the A_{1g} vertex is, in principle, sensitive to the electron and hole bands. Since the A_{1g} vertex is modified by charge backflow effects the largest contribution comes from interband scattering involving more the hole bands. B_{2g} symmetry, in contrast, does not probe any band according to the lowest order approximation of the Raman vertex [25].

3.4.2 Selection rules

To probe the response in different symmetries, the polarization states of incoming and outgoing photons need to be adjusted. As reference for the polarization vectors the 1-Fe unit cell is chosen and $\hat{x}$ and $\hat{y}$ polarizations are aligned along the Fe-Fe bonds. $\hat{x}'$ and $\hat{y}'$ polarizations are rotated by 45° with respect to $\hat{x}$ and $\hat{y}$, respectively, and hence point along the axes of the crystallographic unit cell.

The contribution to one single symmetry cannot be accessed individually but always the sum of two symmetries is projected out by one polarization combination of the photons in crystals obeying the D_{4h} symmetry group. This is illustrated in Fig. 3.5, where

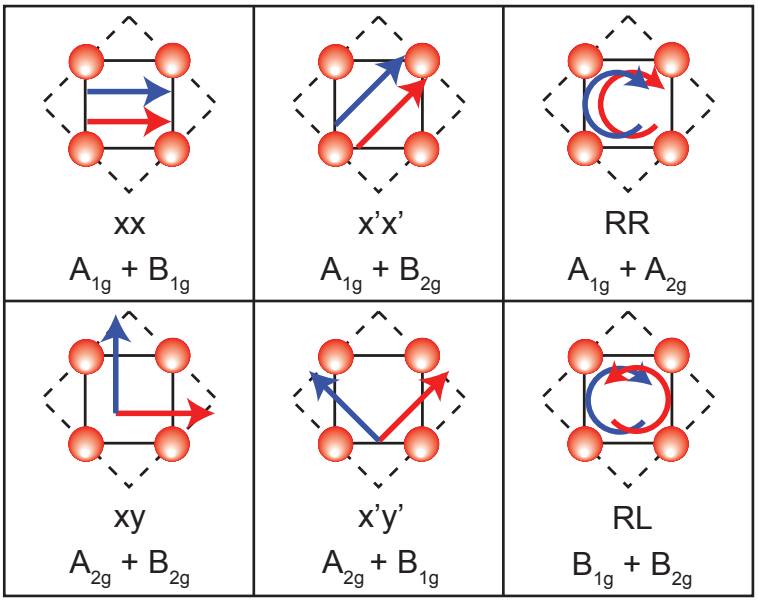

Figure 3.5: Scattering geometry of incoming (blue arrow) and scattered photons (red arrow) and projected symmetries in a tetragonal D_{4h} crystal. The red circles mark the position of the Fe atoms and the solid and dashed lines are the 1-Fe and 2-Fe unit cell.

the polarization states of incoming and outgoing photons are shown and the projected symmetries are indicated. To extract the contribution from one single symmetry one has to measure at least four different polarization combinations including both combinations with circularly polarized photons. For consistency checks and to perform a fully symmetric polarization analysis, a complete set of all six different in-plane light polarization combinations, as shown in Fig. 3.5, is measured in this study. Using the linear combinations

$$\begin{aligned} I_{\mathrm{A1g}} &= \frac{1}{3}\left[(xx + x'x' + RR) - \frac{1}{2}(xy + x'y' + RL)\right], \\ I_{\mathrm{A2g}} &= \frac{1}{3}\left[(xy + x'y' + RR) - \frac{1}{2}(xx + x'x' + RL)\right], \\ I_{\mathrm{B1g}} &= \frac{1}{3}\left[(xy + x'x' + RL) - \frac{1}{2}(xx + x'y' + RR)\right] \text{ and} \\ I_{\mathrm{B2g}} &= \frac{1}{3}\left[(xx + x'y' + RL) - \frac{1}{2}(xy + x'x' + RR)\right], \end{aligned} \tag{3.27}$$

the contributions in individual symmetries are accessed.

3.5 Extended relaxation function analysis

For the quantitative description of the Raman spectra in the normal state an extended relaxation function analysis, which is similar to the memory-function analysis of the optical conductivity [148], can be applied. Via this analysis dynamic mass enhancement factors and Raman relaxation rates are calculated.

For the analysis, the Raman susceptibility is written in terms of a memory-function via

$$\chi_{\gamma\gamma}(\Omega, T) = \frac{M_{\gamma\gamma}(\Omega, T)}{\Omega + M_{\gamma\gamma}(\Omega, T)} \tag{3.28}$$

with

$$M_{\gamma\gamma}(\Omega, T) = i\Gamma(\Omega, T) + \Omega\lambda(\Omega, T). \tag{3.29}$$

Here, $1 + \lambda(\Omega, T) = m^*(\Omega, T)/m$ is the dynamic mass enhancement factor with the bare electron mass m, and $\Gamma(\Omega, T)$ is the dynamic Raman relaxation rate. Thus, the imaginary part of the Raman susceptibility reads

$$\chi''_{\gamma\gamma}(\Omega, T) = \frac{\Omega\Gamma(\Omega, T)}{\Omega^2 \left[1 + \lambda(\Omega, T)\right]^2 + \Gamma(\Omega, T)^2}. \tag{3.30}$$

For the further analysis one uses the functions

$$I(\Omega, T) = -R\frac{\chi''(\Omega, T)}{\Omega} \tag{3.31}$$

and

$$\Omega K(\Omega, T) = -\frac{2\Omega}{\pi}\wp \int_0^{\Omega_c} d\xi \, \frac{I(\xi, T)}{\xi^2 - \Omega^2}. \tag{3.32}$$

Eq. (3.32) is obtained by the Kramers-Kronig transformation of Eq. (3.31). $\wp$ denotes the principle value of the integral. Inserting Eq. (3.31) and Eq. (3.32) into Eq. (3.30) and separating real and imaginary part, one obtains

$$\Gamma(\Omega, T) = R\frac{I(\Omega, T)}{[I(\Omega, T)]^2 + [\Omega K(\Omega, T)]^2}, \tag{3.33}$$

$$1 + \lambda(\Omega, T) = R\frac{K(\Omega, T)}{[I(\Omega, T)]^2 + [\Omega K(\Omega, T)]^2}. \tag{3.34}$$

which are also related by a Kramers-Kronig transformation. The constant R is fixed by

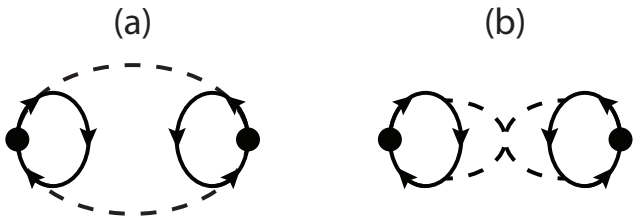

Figure 3.6: (a) Direct and (b) crossed Feynman diagrams for the fluctuation contributions to the Raman response. Dashed and solid lines denote collective modes and fermionic propagators, respectively. The dots represent the Raman vertices.

a sum rule

$$R = \frac{2}{\pi} \int_0^{\Omega_c} d\Omega \; I(\Omega, T) \tag{3.35}$$

originating from the causality of the response function. To guarantee the convergence of Eq. (3.35), a cutoff frequency Ω_c is introduced which is typically of the order of the bandwidth. Whenever $\chi''(\Omega)$ is constant, the dependence of the integral on Ω_c is logarithmic. If $\chi''(\Omega)$ decays, Eq. (3.35) converges. Details of the analysis can be found in earlier publications [149, 150].

In the limit $\Omega \to 0$ Eq. (3.33) gives the static Raman relaxation rate $\Gamma_0(T)$. $\Gamma_0(T)$ is inversely proportional to the initial slope of the Raman spectra and represents the inverse of the two particle lifetime $\tau(T)$. Thus, $\Gamma_0(T) \propto 1/\tau(T) \propto \rho(T)$ holds with $\rho(T)$ the dc resistivity in a metal. Therefore, $\Gamma_0(T)$ can, in principle, be compared to the relaxation rates obtained from transport measurements. For the comparison $\rho(T)$ needs to be converted into units of wavenumbers. In a Drude model $\Gamma_0^{\mu}(T)$ and $\rho(T)$ are related as [149]

$$\Gamma_0^{\rho}(T) = \frac{1}{\tau(T)} = 1.08 \cdot \rho(T) \cdot \omega_{pl}^2 \tag{3.36}$$

with $\rho(T)$ the resistivity in units of $\mu\Omega$cm and ω_{pl} the plasma frequency in units of eV.

3.6 Fluctuation contribution to the Raman response

The importance of fluctuations above T_c was originally emphasized by Aslamazov and Larkin [151]. This work was extended to the particle-hole channel for 1D charge-density-wave systems [152, 153]. The latter work is reconsidered in 2D for the Raman response and the presented model is originally calculated to express the Raman response contribution due to collective charge-order (CO) excitations associated to stripe fluctuations

in the cuprates [154]. According to this work, a Raman active excitation originates from the exchange of two fluctuations with opposite momenta Q_c and $-Q_c$, hence preserving $\mathbf{q}_{\text{total}} = 0$. The Feynman diagrams, contributing to the process, are shown in Fig. 3.6. The CO fluctuations provide an additional channel for the Raman response beside the polarization bubble presented in Sec. 3.3.

Evaluating the diagrams in Fig. 3.6, the contribution from fluctuations can be expressed via

$$\Delta\chi'' = \Lambda^2 \int_0^\infty dz \left[b(z-\Omega/2) - b(z+\Omega/2)\right] \frac{z_+ z_-}{z_+^2 - z_-^2} \left[F(z_-) - F(z_+)\right]. \tag{3.37}$$

Here Λ is a fitting parameter independent of temperature and Raman shift to adjust the intensity of the fit to the intensity of the experimentally obtained data and

$$z_\pm \equiv (z \pm \Omega/2)\left[1 + (z \pm \Omega/2)^2/\Omega_0^2\right]. \tag{3.38}$$

$b(z)$ is the Bose distribution function and

$$F(z) \equiv \frac{1}{z}\left[\arctan\left(\frac{\Omega_0}{z}\right) - \arctan\left(\frac{m}{z}\right)\right]. \tag{3.39}$$

The ultraviolet cutoff Ω_0, generally of the order of a few hundred wavenumbers, is of the order of the phonon energy coupling to the electrons and driving the system near the charge ordering instability [155]. The effective mass of the fluctuation propagator $m(T)$ in Eq. (3.39) depends only on the temperature and is the only fitting parameter in this approach.

3.7 The spin-density-wave

Below T_{SDW} underdoped FeSCs are magnetically ordered and exhibit a SDW ground state. In the SDW ground state the spin density is a spatially varying wave having a period of $d = \pi/k_F$ with k_F the Fermi wavevector as illustrated in Fig. 3.7(a). Since both spin directions modulate with the same phase but are shifted by π, there is no spatial variation of the charge density [156]. Due to the spin density modulation, a new periodicity of the lattice with lattice constant $l_{\text{SDW}} = d > a$ develops with a the lattice constant in the paramagnetic state. The new periodicity leads to a reconstruction of the bands in the BZ as shown in Fig. 3.7(b) for a half filled band. Consequently, the band is intersected and there occurs a new BZ boundary at $\pi/d < \pi/a$. At the new BZ

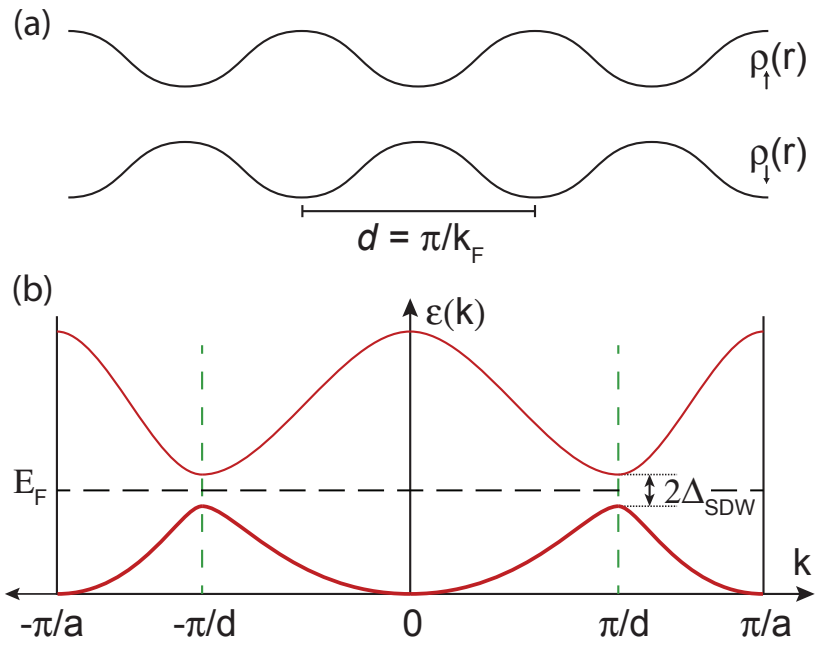

Figure 3.7: Dispersion relation in the SDW ground state for a half filled band (thick red line denotes the filled band). (a) In the SDW state the spin density $\rho(r)$ for both spin directions is spatially varying with a periodicity of $d = \pi/k_F$. d is the new lattice constant. (b) Due to the new periodicity of the lattice in the SDW state the BZ becomes smaller and a gap Δ_{SDW} opens on the new BZ boundary (dashed green lines). $\mathrm{E_F}$ denotes the Fermi level in the SDW state. Adapted from [156]

boundary a SDW gap Δ_{SDW} is introduced which opens on, at least, parts of the FS and leads to a decrease of the kinetic energy. The size of Δ_{SDW} in a mean-field approach can be expressed in the weak coupling BCS relation [156] via

$$2\Delta_{\mathrm{SDW}}^{\mathrm{MF}} = 3.53 \cdot T_{\mathrm{SDW}}^{\mathrm{MF}}. \tag{3.40}$$

This is, strictly speaking, valid only for 1D electronic properties. With increasing 3D character of the electronic properties, $T_{\mathrm{SDW}}^{\mathrm{MF}}$ continuously decreases and the transition may even be completely removed [156].

Chapter 4

Samples and experimental details

In this chapter details of the investigated samples and the experimental setup are presented. Additionally, aspects for the data analysis are introduced.

4.1 Samples

For the investigation of the electronic properties of FeSCs via ERS high quality single crystals with a minimal size of approximately 1 x 1 mm^2 are desired. These requirements are fulfilled by Co doped $BaFe_2As_2$ crystals. The $Ba(Fe_{1-x}Co_x)_2As_2$ samples are prepared and characterized in the group of Ian Fisher at Stanford University [7]. The crystals were grown from self-flux. Ba and FeAs in a molar ratio 1:4 with additional Co were placed in an alumina crucible and sealed in a quartz tube. The mixture was heated up to 1150°C and held at that temperature for 24 h. At 1000°C the remaining flux was removed. The crystals have a platelike morphology with the *c*-axis perpendicular to the plane [7].

4.1.1 $BaFe_2As_2$

	T_{TO} / T_{SDW}	a[Å]	b[Å] (300 K)	c[Å]	a[Å]	b[Å] (20 K)	c[Å]
$BaFe_2As_2$	134 K	3.963	3.963	13.017	5.615	5.574	12.945

Table 4.1: Parameters of the studied $BaFe_2As_2$ sample, with the corresponding structural and magnetic transition temperature T_{TO} and T_{SDW}, respectively. The lattice parameters in the tetragonal and orthorhombic phase are given at 300 and 20 K, respectively. Data are taken from [157].

$BaFe_2As_2$ crystallizes in the body centered tetragonal $ThCr_2Si_2$ structure shown in Fig. 4.1. The lattice parameters are given in Tab. 4.1. The Fe-Fe nearest neighbor distant is $a/\sqrt{2}$. The conducting $(FeAs)^-$ layers are separated by approximately 6.5 Å [158]. Between the $(FeAs)^-$ layers are insulating layers of Ba^{2+} atoms which are believed to transfer electrons to the conducting layers [35, 157]. The tetragonal structure suffers a small orthorhombic distortion below 134 K concomitantly with a transition to an antiferromagnetically ordered SDW ground state. The resistivity of twinned samples is shown in Fig. 4.2. It is mainly constant between 300 and 134 K and suffers a sudden drop at 134 K. At low temperatures the temperature dependence is weak. The residual resistivity ratio is roughly 2.8.

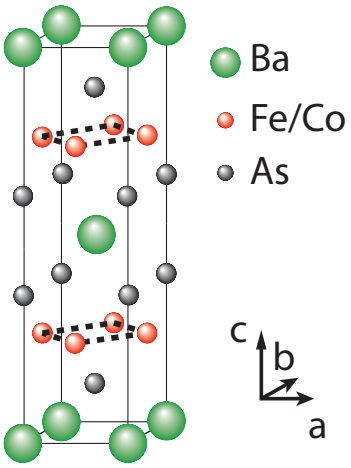

Figure 4.1: Crystal structure of $Ba(Fe_{1-x}Co_x)_2As_2$.

4.1.2 $Ba(Fe_{1-x}Co_x)_2As_2$

The studied $Ba(Fe_{1-x}Co_x)_2As_2$ samples are listed in Tab. 4.2. Doping $BaFe_2As_2$ with Co atoms leads to a random substitution of Fe atoms and reduces the c-axis length slightly while the a-axis length remains mainly unaffected [160]. This results in lattice constants of $a = 3.964$ Å and $c = 12.980$ Å for overdoped $Ba(Fe_{0.9}Co_{0.1})_2As_2$ [50]. The Co concentration was determined by microprobe analysis and the measured dc resistivity

$Ba(Fe_{1-x}Co_x)_2As_2$	T_c	ΔT_c	T_{TO}	T_{SDW}	x	comment	sample ID
$BaFe_2As_2$	-	-	134 K	134 K	0	unstressed	Ba122
$BaFe_2As_2$	-	-	137 K	145 K	0	stressed	Ba122s
$Ba(Fe_{1.955}Co_{0.045})_2As_2$	14 K	2 K	68 K	60 K	0.045	unstressed	UD14
$Ba(Fe_{1.949}Co_{0.051})_2As_2$	18 K	1 K	52 K	37 K	0.051	unstressed	UD18
$Ba(Fe_{1.945}Co_{0.055})_2As_2$	23 K	1 K	33 K	30 K	0.055	unstressed	UD23
$Ba(Fe_{1.939}Co_{0.061})_2As_2$	24 K	0.5 K	-	-	0.061	unstressed	OPT24
$Ba(Fe_{1.915}Co_{0.085})_2As_2$	22 K	1 K	-	-	0.085	unstressed	OD22

Table 4.2: Table of the studied $Ba(Fe_{1-x}Co_x)_2As_2$ samples, with the corresponding superconducting transition temperature T_c and width ΔT_c, structural and magnetic transition temperature T_{TO} and T_{SDW}, respectively, doping level x and sample ID used in the text. The structural and magnetic transition temperature of the stressed sample Ba122s are a guess from the data in [159].

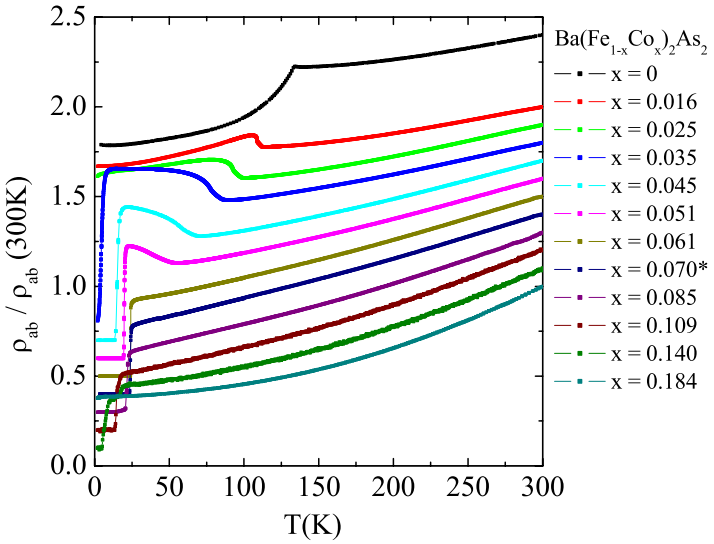

Figure 4.2: DC resistivity of differently doped $Ba(Fe_{1-x}Co_x)_2As_2$ single crystals. The data are offset for clarity. From [7].

of the investigated samples are displayed in Fig. 4.2. While the underdoped samples display a resistivity anomaly where the resistivity increases at low temperature before it falls to zero at T_c, the resistivity of optimally and overdoped samples, where no magnetic order is present, decreases monotonously with the temperature. Hall measurements show that the dominant charge carriers in $Ba(Fe_{1-x}Co_x)_2As_2$ are electrons [22, 50].

Co doping introduces superconductivity for $0.035 \leq x \leq 0.14$ and suppresses the structural and magnetic transitions. The maximal T_c is 24 K for $x = 0.061$. For $x \geq 0.061$ the structural and magnetic transitions have disappeared entirely. The T_c of each sample is determined via the measured resistivity [7] and the third harmonic of the susceptibility which has the advantage to be contactless. The latter method is described elsewhere in detail [161, 162].

The penetration depth of visible light is, according to measurements of the optical constants during this thesis, roughly 30 nm. Thus, also bulk properties of the material are probed via ERS. Nevertheless, it is essential for the experiment to have a flat and shiny surface which is obtained via sample cleavage.

4.2 Experimental Details

The experimental equipment of the ERS setup is described elsewhere in great detail [150, 161, 163, 164]. Here, relevant features of the setup including the detwinning device

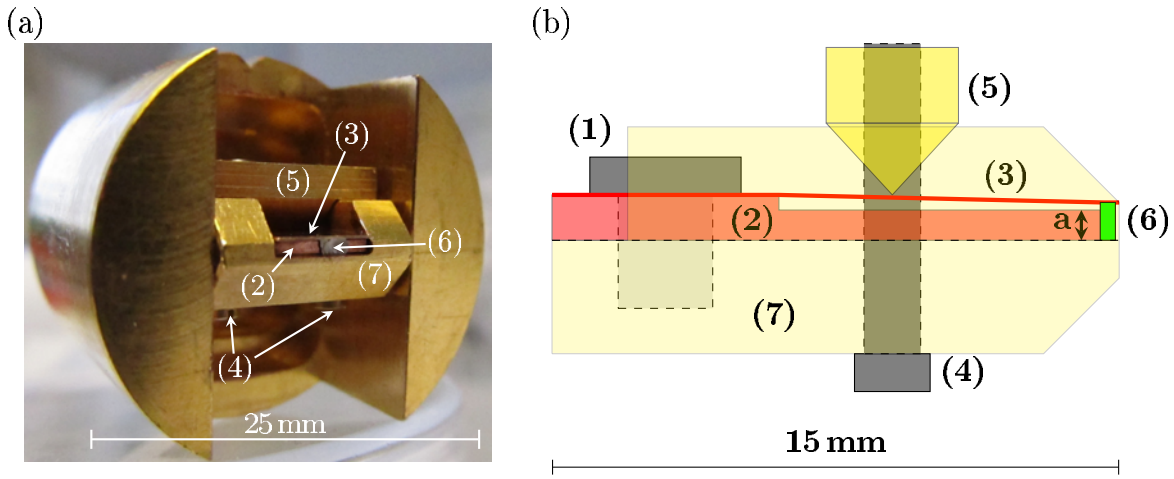

Figure 4.3: (a) Photograph and (b) schematic sketch of the in-situ detwinning device. The sample (6) is sandwiched between the cantilever (3) and he sample holder (7). With screw (1) the cantilever is fixed on the sample holder. Using screws (4) and brace (5) stress can be applied to the sample. The thickness of the space holder (2) is $a = 0.8$ mm. From [166].

for the samples and the light source for the experiment are introduced. Finally, details of the data analysis are presented.

4.2.1 Sample holder

The sample is mounted on the cold finger of a cryopumped ^{4}He flow cryostat with a vacuum of better than 10^{-6} mbar and an accessible temperature range of $1.8 \leq T \leq 340$ K. The temperature of the sample holder is measured via a Si-diode. The orientation of the crystals is determined via a Laue picture [164]. The proper adjustment of the polarization state of incoming photons with respect to the crystal axes is described in a recent work [165]. Details of the cryostat can be found elsewhere [163].

Without uniaxial stress the samples were mounted on a copper block to maintain good thermal contact to the cold finger. For the mounting GE Varnish was used which has a finite elasticity at low temperatures [164]. A finite elasticity at low temperatures is necessary since the FeSCs are rather sensitive to uniaxial stress [57, 166]. Details of the mounting of the sample are described in [150].

In the orthorhombic phase $a_{\mathrm{Fe}} > b_{\mathrm{Fe}}$ holds. Here, the sample is twinned forming domains where a_{Fe} and b_{Fe} are exchanged. These domains are smaller than the laser spot on the sample [60] which has a size of roughly 50×100 µm (see Sec. 2.2). Thus, the spot illuminates several domains and the measured Raman response is an average

over the response of many domains. In order to measure the response from a single domain, uniaxial pressure is applied and the sample is detwinned. The sample holder for applying uniaxial stress is shown in Fig. 4.3 [166]. The applied stress is in the range $15 \leq P \leq 35$ MPa which is sufficient to fully detwin the sample [60]. Details can be found in [166].

4.2.2 Light scattering Setup

The setup for the Raman experiment is schematically shown in Fig. 4.4. Via mirror M1 the light source for the experiment, either a diode-pumped solid state (DPSS) or an Argon ion laser (see Sec. 4.2.3), can be selected. To adjust the beam diameter of the DPSS laser to the larger beam diameter of the ion laser (Tab. 4.3), the beam diameter of the DPSS laser is expanded with two lenses L1 and L2, which have a focal length of 30 and 40 mm, respectively. The first pinhole system eliminates contribution of the plasma radiation from the laser medium with a higher divergence than the coherent laser light. Via the combination of a prism monochromator (PMC) and a spatial filter S2 plasma lines, which differ by more than 30 cm^{-1} from the laser line, are removed. The power and polarization state of the incoming light can be adjusted via the combination of a $\lambda/2$ retardation plate, a Glan-Thompson polarizer and a Soleil-Babinet compensator. To maintain a homogeneous Gaussian beam profile, the light is filtered via the spatial filter S3 before the beam is focused on the sample surface with the achromatic lens L8. The photons scattered off inelastically of the sample are collected with an objective lens (O2) and focused on the entrance slit of the spectrometer.

On its way to the spectrometer the polarization state of the scattered photons is selected by the combination of a $\lambda/4$ retardation plate and a polarizer. A $\lambda/2$ retardation plate rotates the polarization of the scattered photons into the direction of maximal sensitivity of the spectrometer. The spectrometer consists of two stages where the light is dispersed by a grating in the first stage. Via an intermediate slit between the two stages, the bandwidth of the light can be determined before the second grating reverses the dispersion of the first grating. Hence, an image of the entrance slit is generated at the exit slit having a bandwidth determined by the intermediate slit. After the spectrometer the beam is focused on a liquid nitrogen cooled CCD chip [150]. Further details of the setup can be found in [161].

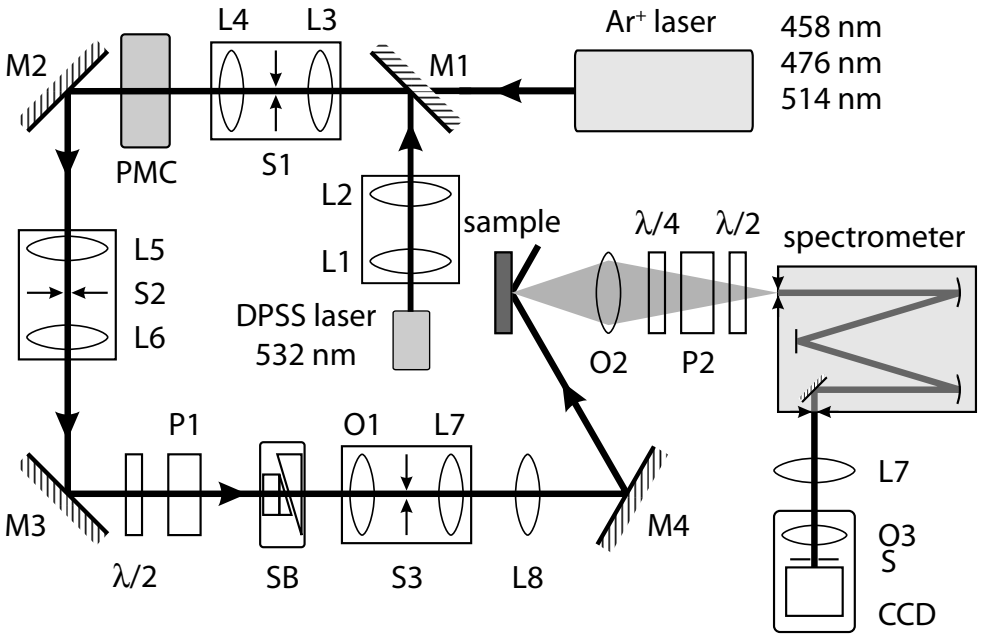

Figure 4.4: Schematic sketch of the Raman experiment. For details see the text. From [161].

4.2.3 Light source

In an ERS experiment one out of 10^{13} incoming photons is scattered inelastically per second, meV bandwidth and steradian. Thus, a light source, which emits a large number of coherent photons at a fixed energy, is required. Additionally, a constant output power and a high beam stability over a long time period is a prerequisite for the light source. These requirements are fulfilled by lasers where up to now an Ar ion laser, Coherent Innova 304, was used. For the rapid evolution of DPSS lasers, nowadays also frequently doubled DPSS lasers are suitable and a Neodymium doped YAG laser, Klastech Scherzo-DENICAFC-532-300, was additionally installed in the lab.

The advantage of the ion laser is that the wavelength of the emitted photons can be tuned to discrete wavelengths in the range $458 \leq \lambda_{\mathrm{exc}} \leq 514$ nm, while the DPSS laser emits at only one fixed wavelength of $\lambda_{\mathrm{exc}} = 532$ nm. The advantage of the DPSS laser is to have a power consumption which is by more than two orders of magnitude lower than that of the ion laser and the absence of a large scale water cooling system while the beam parameters of the ion and the DPSS lasers are similar. The specifications of both lasers are tabulated in Table 4.3. Since a typical measurement of the FeSCs last roughly 14 h there is a remarkable reduction of power consumption with the application of the DPSS laser while the spectra, which are generally measured at only one λ_{exc}, are unchanged to within the experimental resolution.

Specification	Coherent Innova 304	Klastech Scherzo-532-300
output wavelength [nm]	458 nm $\leq \lambda \leq$ 514 nm	532
output power [mW]	$100 \leq P \leq 1500$	300
output power stability	$\pm 0.5\%$	$\leq 2\%$
beam diameter ($1/e^2$) [mm]	1.5	1.0
beam divergence [mrad]	0.5	diffraction limited
beam pointing stability [μrad/K]	< 5	≤ 10
transverse mode structure	TEM_{00}	TEM_{00}
optical noise [rms]	0.2% (10 Hz to 2 MHz)	$\leq 0.3\%$ (10 Hz to 10 MHz)
cooling	water	air
controller size [mm^3]	533 x 543 x 193	164 x 109 x 45
laser head size [mm^3]	1225 x 150 x 179	160 x 109 x 98
weight (all) [kg]	81	< 2
power consumption [kWh]	15	0.1

Table 4.3: Specifications of the Ar ion laser (Coherent Innova 304) and the DPSS laser (Klastech Scherzo-532-300).

4.2.4 Calibration of the setup

For the absolute determination of the Raman spectra over a wide frequency range the experimental setup needs to be calibrated. The experimentally determined number of photons $\dot{N}$, scattered into an energy interval $\Delta\omega_s$ and a solid angle $\Delta\widetilde{\Omega}$, depends on several experimental parameters. It can be expressed as [167] [c.f. Eq. (3.5)]

$$\dot{N}(\omega_s, \Delta\omega_s, \Delta\widetilde{\Omega}) = r I_0 \frac{d^2\sigma}{d\widetilde{\Omega} d\omega_s} T(\omega_s) \Delta\omega_s \Delta\widetilde{\Omega} \tag{4.1}$$

where σ is the light scattering cross-section for certain polarizations. $T(\omega_s)$ is the transmission coefficient of the entire setup including the spectrometer and the CCD camera.

The transmission through the spectrometer and the sensitivity of the CCD camera are measured separately and are shown in Fig. 4.5 together with the energy interval $\Delta\omega_s$ which gives the energy dependent resolution of the spectrometer. $\Delta\omega_s$ can be determined by the intermediate slit. For a given spectrometer geometry the dependence of $\Delta\omega_s$ on ω_s can be calculated. As shown in Fig. 4.5, $\Delta\omega_s$ decreases roughly linearly with decreasing energy of the scattered photons [150].

The spectra throughout this thesis are presented in units of counts per second and Milliwatt (counts s^{-1} mW^{-1}) if not indicated differently. They are divided by $T(\omega_s)$ and normalized to a fixed resolution $\Delta\omega_s = 10$ cm^{-1} at 458 nm. Further details of the calibration procedure are described elsewhere [150].

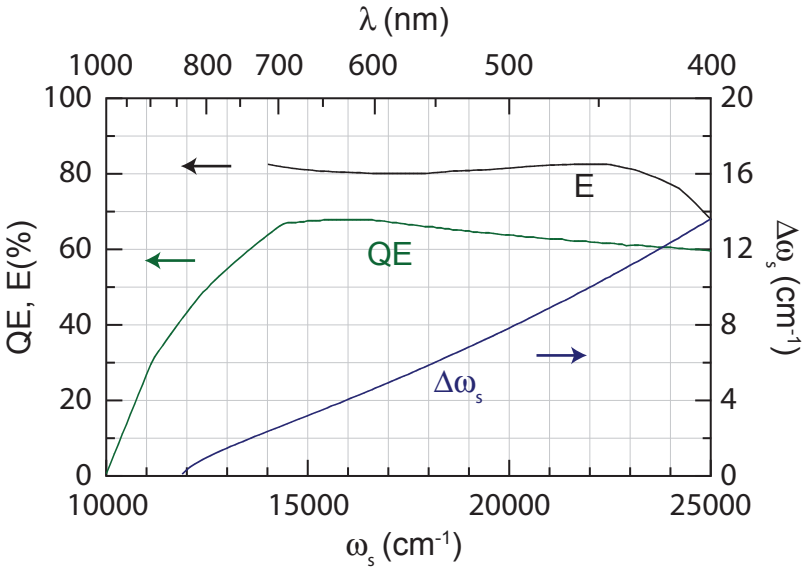

Figure 4.5: Sensitivity calibration of the experimental setup (from [150]). Shown is the efficiency of the gratings E and the quantum efficiency of the CCD camera QE in percent. The bandwidth $\Delta\omega_s$ of the spectrometer is given for a fixed width of the intermediate slit of 550 µm on the right hand scale.

4.2.5 Determination of the spot temperature

The temperature of the sample in the illuminated spot is crucial for the interpretation of the Raman spectra.

Probe temperature in the normal state

For the determination of the sample temperature in the normal state one usually takes advantage of the principle of detailed balance as given in Eq. (3.3) [135] and obtains

$$T(\Omega) = -\frac{\hbar\Omega}{k_\mathrm{B}} \ln\left[\frac{\dot{N}_\mathrm{AS}}{\dot{N}_\mathrm{ST}}\left(\frac{\omega_i - \Omega}{\omega_i + \Omega}\right)^2\right] \tag{4.2}$$

with $\dot{N}_\mathrm{ST}$ and $\dot{N}_\mathrm{AS}$ the intensities of the Stokes and anti-Stokes spectrum, respectively. ω_i is the energy of the incoming light, Ω the Raman shift and k_B the Boltzmann constant. With this relation the temperature of the sample in the laser spot can be estimated to within a few degrees. This is, in general, sufficient [150] although the determination of T via Eq. (4.2) is precise only if $\dot{N}_\mathrm{AS}$ is remarkably greater than zero.

Sample temperature in the superconducting state

For this reason the estimation of the sample temperature via Eq. (4.2) is problematic below T_c. Here, $\dot{N}_{\mathrm{AS}}$ is close to zero. In addition, the temperature increase ΔT per mW absorbed laser power has a remarkably temperature dependence for $T < T_{\mathrm{c}}$ since the heat transport in the samples is strongly temperature dependent [168].

To obtain a reasonable estimate of the sample temperature in the spot position, the spectra are measured at different temperatures T_h of the sample holder and with different absorbed laser powers P [163]. If a spectrum, which is measured at $T_{h1} < T_{\mathrm{c}}$ with an absorbed laser power P_1, is identical to a spectrum measured at $T_{h1} < T_{h2} < T_{\mathrm{c}}$ with laser power $P_2 < P_1$, the temperature increase per mW absorbed laser power, $\Delta T/\Delta P$, can be calculated via

$$T_{h1} + \Delta T/\Delta P \cdot P_1 = T_{h2} + \Delta T/\Delta P \cdot P_2. \tag{4.3}$$

This immediately leads to

$$\Delta T/\Delta P = \frac{T_{h2} - T_{h1}}{P_1 - P_2} \tag{4.4}$$

which is the temperature increase of the sample in the illuminated spot for a given absorbed laser power ΔP.

This method is applicable only if there are strongly temperature dependent features in the spectrum. Since the superconductivity induced features have, in general, a pronounced temperature dependence, it gives a relatively precise estimate of the sample temperature in the spot position. It is applied also in the normal state if there are strongly temperature dependent features in the spectra necessitating the knowledge of the exact temperature of the sample at the spot position, for instance in close proximity to a phase transitions.

4.2.6 Subtraction of the laser line

For the study of the superconducting gap structure it is essential to measure data points close to the laser line at $\Omega = 0$. For these low energies the relevant superconductivity induced features occur and the response may be close to zero for a fully gapped superconductor. However, the analysis of the low energy spectra is impeded by a finite contribution to the spectra from the laser line. This contribution sits on top of the response and originates from Rayleigh scattering and absorbed molecules of the residual gas on the sample surface. Not surprisingly, this effect is most pronounced at low

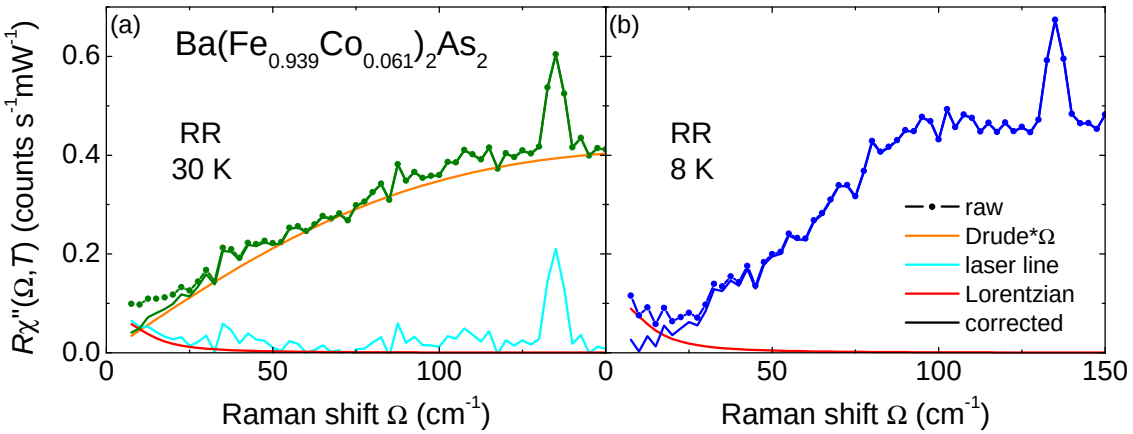

Figure 4.6: Subtraction of the laser line contribution from the spectra. From the raw data (symbols) in (a) the normal and (b) superconducting state a Drude function multiplied by Ω (orange) is subtracted. This spectrum represents the contribution of the laser line The red full line is a Lorentzian fit to the laser line contribution. The symbols and full lines are the spectra before and after the subtraction of the Lorentzian fit to laser line, respectively.

temperature.

Since the normal state Raman spectra for $\Omega \to 0$ can be approximated as [169, 170],

$$\chi''(\Omega, T) \approx A \frac{\Omega \cdot \Gamma^2}{\Gamma^2 + \Omega^2}, \tag{4.5}$$

the low energy contribution of the laser line can be estimated. This is illustrated in Fig. 4.6(a). To separate the contribution of elastically scattered light, the Drude like response is subtracted from the spectra. The resulting contribution of the laser line is fitted by a Lorentzian which is subtracted from the Raman spectra above and below T_c. The spectra before (symbols) and after the subtraction of the laser line (solid lines) for $T > T_c$ and $T < T_c$ are shown in Fig. 4.6(a) and 4.6(b), respectively.

4.2.7 Extraction of the electronic continuum

For the analysis of the dynamic carrier properties the bare response from the carriers is required meaning that the contribution of the phonons needs to be subtracted [150, 164].

The subtraction of the phonons from the spectra is demonstrated in Fig. 4.7. For the subtraction, the spectra measured at different temperatures are averaged (black line). The electronic contribution to the obtained average spectrum is fitted by an analytic approximation (red). After the subtraction of this function from the average spectrum, the contribution originating solely from phononic excitations (blue) is obtained. This phonon

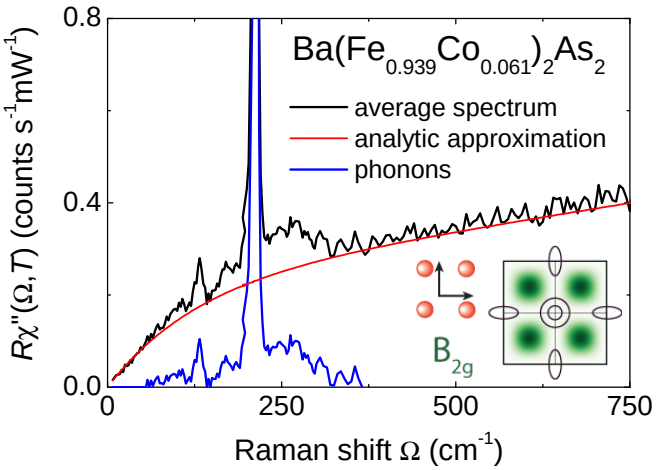

Figure 4.7: Subtraction of the phononic modes from the spectra. The spectrum represented by the black solid line is the average of the spectra measured at different temperatures. It is fitted by an analytic approximation (red solid line). The contribution from phonons to the spectrum (blue solid line) is the difference of the average spectrum and the analytic approximation.

spectrum is subtracted from the Raman spectra at different temperatures yielding the purely electronic Raman response. Since the lineshapes and central positions of some phonons have a remarkable temperature dependence, this is not always a straightforward procedure and some artifacts resulting from contributions of phonons may survive in the spectra. Nevertheless, the procedure turns out to be useful and reliable in most of the cases.

Chapter 5

Magnetic properties of $BaFe_2As_2$

In this chapter results on $BaFe_2As_2$ will be presented. The main focus is placed on the magnetic properties and the phase transition to the spin-density-wave (SDW) state at 134 K.

5.1 Experimental results

The experiments were performed on samples Ba122 and Ba122s (Tab. 4.2). For comparison spectra of $Ba(Fe_{1-x}Co_x)_2As_2$ samples at finite doping (UD23, OPT24 and OD22 in Tab. 4.2) are presented in order to explore the boundary of the magnetic phase.

5.1.1 Raman active phonons in $Ba(Fe_{1-x}Co_x)_2As_2$

In Fig. 5.1 the experimentally observed phonon modes in the Raman spectrum of $BaFe_2As_2$ are shown. The spectrum is measured at a temperature of 130 K, excitation at $\lambda_{exc} = 532$ nm and a spectral resolution of roughly 7 cm^{-1}. Incoming and outgoing photons are align parallel to the axis of the crystallographic unit cell. In the spectra all four Raman active phonons, introduced in Fig. 2.3, are visible. The E_g phonons are observed since the incoming photons have a finite projection onto the c-axis of the crystal in the scattering geometry of the experimental setup similar to [171]. One E_g phonon is located at 270 cm^{-1} and has only small intensity. The other E_g phonon has an energy of 135 cm^{-1}. Thus, for both E_g modes there is a relatively large discrepancy of approximately 20% between the shell model calculations (c.f. Sec. 4.1) and the experiment. This is also observed in other Raman studies [47, 171, 172]. The A_{1g} phonon is observed at a frequency of 180 cm^{-1}, while the B_{1g} phonon is at a frequency of 215 cm^{-1} for $T = 130$ K. Hence, the A_{1g} and B_{1g} phonons are in good agreement

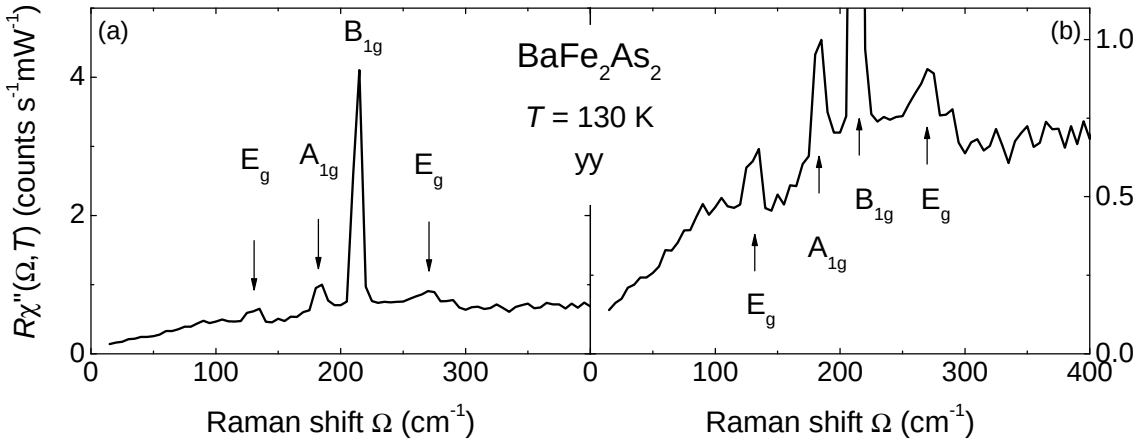

Figure 5.1: Experimentally observed phonon modes of $BaFe_2As_2$ at 130 K in yy polarization. (a) The positions and symmetries of all four phonon modes are indicated. The symmetries correspond to the crystallographic unit cell. (b) Zoom in of panel (a).

with the theoretical predictions (Sec. 4.1) as also observed in other experimental Raman studies [47, 171, 172, 173].

5.1.2 Electronic Raman spectra

For the reasons discussed in Sec. 2.3, the 1-Fe unit cell is applied in the following. In this notation B_{1g} and B_{2g} symmetry are exchanged and the B_{1g} phonon is observed in the B_{2g} spectra. The fully symmetry-resolved (see Sec. 3.4) low energy Raman response of pseudo-tetragonal $BaFe_2As_2$ with $T_{SDW} = 134$ K for $\Omega \leq 1000$ cm^{-1} is presented in Fig. 5.2. Spectra at temperatures above (150 K) and below T_{SDW} (130 K and 50 K) are shown. They are measured with a step width of 5 cm^{-1} and the spectral resolution is set to 6.5 cm^{-1}. The temperatures indicated in the figure correspond to those in the laser spot. For $T > T_{SDW}$, the phonons superposed on the spectra appear only in the A_{1g} and B_{2g} symmetry of the 1-Fe unit cell as expected from symmetry considerations (see Sec. 5.1.1). Due to the orthorhombic distortion of the lattice below T_{TO}, the A_{1g} phonon at 185 cm^{-1} is also observed in the B_{1g} spectra.

Apart from the phonons, there is a strong redistribution of the electronic continuum upon crossing T_{SDW}. This is seen most clearly in B_{1g} symmetry [Fig. 5.2(c)], for which it has been discussed before [174, 175]. At $T = 150$ K the spectrum exhibits a peak centered at roughly 120 cm^{-1}. At $T = 130$ K, the low energy intensity is strongly reduced along with an increased intensity at higher energy. In the 50 K spectrum the response below 400 cm^{-1} is further suppressed resulting in a step-like feature at $\Omega \approx 400$ cm^{-1}. At higher energy around 850 cm^{-1} the intensity has increased further.

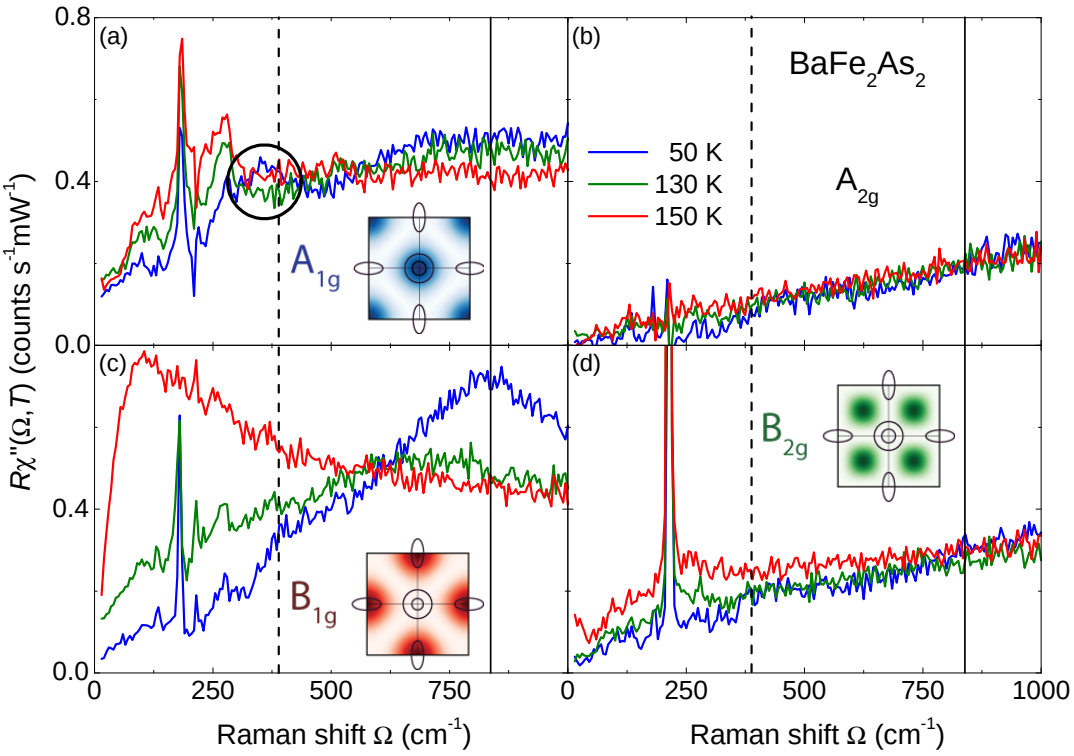

Figure 5.2: Low energy Raman response of $BaFe_2As_2$ as a function of symmetry and temperature. The spectra are measured above, below and well below $T_{SDW} = T_{TO} = 134$ K. The dashed and solid vertical lines at 390 cm^{-1} and 850 cm^{-1}, respectively, mark the energy where the step and the peak maximum in the B_{1g} spectra at 50 K are located. The ellipse in (a) emphasizes the enhanced intensity in the A_{1g} spectrum.

A similar but less pronounced redistribution of spectral weight is observed in the A_{1g} and B_{2g} spectra upon crossing T_{SDW} [Fig. 5.2(a) and 5.2(d), respectively]. However, the B_{2g} spectrum at $T = 50$ K exhibits enhanced intensity for $\Omega \geq 800$ cm^{-1}. The A_{2g} response suffers an even weaker change upon crossing T_{SDW} [Fig. 5.2(b)]. The intensity gets remarkably suppressed only at 50 K resulting in a response very close to zero below 250 cm^{-1}. There is no enhanced intensity observed for $\Omega \leq 1000$ cm^{-1}. In general, the A_{2g}, B_{1g} and B_{2g} spectra exhibit all suppressed intensity below 400 cm^{-1} as indicated by the dashed lines at 390 cm^{-1} in Fig. 5.2. The A_{1g} spectrum, in contrast, exhibits a peak between 300 and 400 cm^{-1} [black ellipse in Fig. 5.2(a)] and is reduced only for $\Omega \leq 300$ cm^{-1}. The solid lines at 850 cm^{-1} in Fig. 5.2 indicate the energy of the B_{1g} peak for $T = 50$ K. This is at roughly the same energy as the A_{1g} peak at 50 K while the peak in the B_{2g} spectrum is shifted to higher energy.

The temperature dependence of the RR (A_{1g} +A_{2g}) and xy (B_{1g} +A_{2g}) spectra of Ba122 for $T \leq T_{SDW}$ is displayed in Fig. 5.3. Since the A_{2g} response is weak and ex-

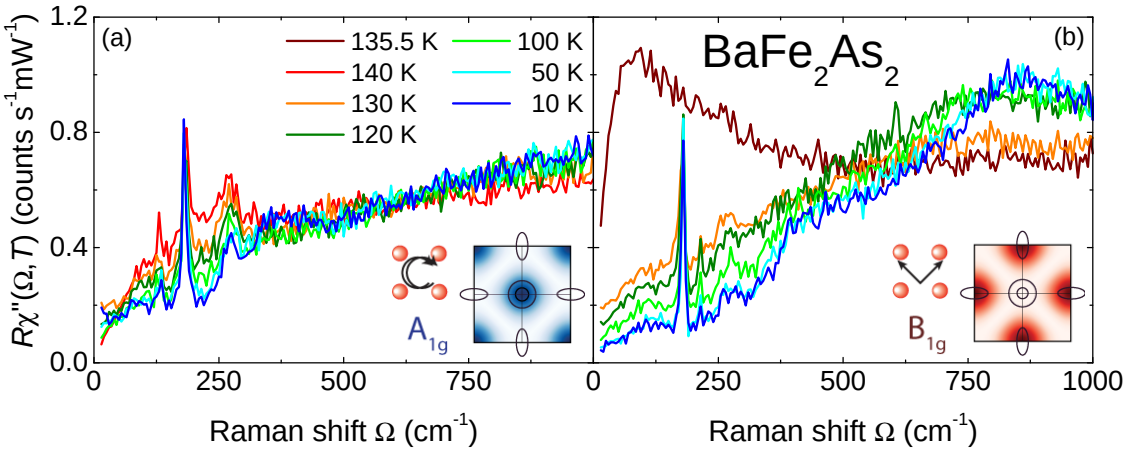

Figure 5.3: Raman response of $BaFe_2As_2$ below and above T_{SDW} in (a) A_{1g} and (b) B_{1g} symmetry. Upon cooling the low energy B_{1g} intensity decreases rapidly crossing $T_{SDW} = 134$ K. In A_{1g} symmetry there is only a weak temperature dependence of the spectra.

hibits only little temperature dependence, it is not subtracted from the spectra. The A_{1g} response [Fig. 5.3(a)] changes only slightly with temperature. Here, the intensity decreases for $\Omega < 300$ cm^{-1} upon crossing $T_{SDW} = 134$ K. The loss of intensity in this energy range saturates for the lowest temperatures and the spectrum at 10 K is almost energy independent below 250 cm^{-1} with an intensity of roughly 0.2 counts s^{-1}mW^{-1}. The increase of the A_{1g} spectra for $\Omega \to 0$ indicates the insufficient suppression of elastically scattered light at low temperature. Above approximately 600 cm^{-1} the intensity increases with decreasing temperature developing a peak centered at roughly 850 cm^{-1} for $T \leq 50$ K. Qualitatively the same just with a stronger redistribution of spectral weight is observed in the B_{1g} spectra [Fig. 5.3(b)]. Here, the response at $T = 135.5$ K is peaked at around 100 cm^{-1} for reasons which will be discussed in Sec. 5.3. At $T = 130$ K the low energy response is considerably smaller than at 135.5 K for $\Omega \leq 500$ cm^{-1} and the intensity below roughly 150 cm^{-1} is reduced by more than 60%. Thus, crossing T_{SDW} leads to a collapse of the low energy B_{1g} response within 5.5 K. The low energy spectral intensity saturates for $T \leq 50$ K and is practically energy independent below 250 cm^{-1}. This results in a step in the spectrum at 390 cm^{-1} and an intensity of roughly 0.1 counts s^{-1}mW^{-1} corresponding to approximately half of the intensity of the A_{1g} spectra at this temperature and energy. For $\Omega \geq 500$ cm^{-1} the intensity increases with the temperature decreasing below T_{SDW} exhibiting a maximum at around 750 cm^{-1} at 130 K. For $T \leq 50$ K this peak has shifted to 850 cm^{-1}.

The above spectra are measured on a twinned sample. Thus, they are an average over many twin domains in the orthorhombic state. Since the electronic response from

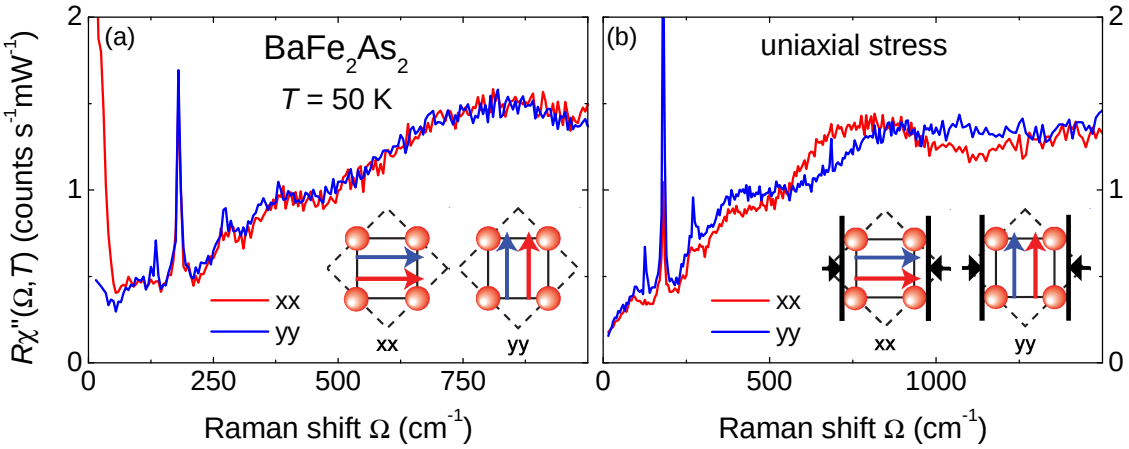

Figure 5.4: Raman spectra on $BaFe_2As_2$ at $T = 50$ K with (a) and without uniaxial stress (b) along the Fe-Fe bonds. The light polarizations are aligned parallel (xx) and perpendicular (yy) to the direction of applied stress as illustrated in the insets. While the xx and yy spectra measured without uniaxial stress are identical within the experimental error, the spectra measured with light polarizations parallel (xx) and perpendicular (yy) to the applied stress differ strongly between $250 \leq \Omega \leq 1250$ cm^{-1}. Data taken from [166].

a single domain measured in direction and perpendicular to the direction of applied stress is reported to be different [60, 176, 177, 178], the samples are detwinned via the application of uniaxial stress along the Fe-Fe bonds. The spectra measured without and with applied uniaxial stress are shown in Fig. 5.4(a) and 5.4(b), respectively. They are measured with light polarizations parallel and perpendicular to the direction of applied stress[1] as indicated in the figure. Fig. 5.4(a) shows that, apart from the low energy response which is superposed by elastically scattered light, the xx and the yy spectra are identical without uniaxial stress. As opposed, the response for these two polarization combinations differs remarkably in the range $250 \leq \Omega \leq 1250\,\text{cm}^{-1}$ if the sample is detwinned via the application of uniaxial stress [Fig. 5.4(b)]. While the step-like feature around 390 cm^{-1} appears at the same energy for both polarization combinations, the peak around 850 cm^{-1} shifts to lower energy in the xx spectra while it shifts to higher energy in the yy spectra. This anisotropy of the response measured parallel and perpendicular to the direction of applied stress is robust if the sample is rotated by 45° [166]. This provides evidence that the anisotropy is not related to extrinsic effects such as the experimental setup but is an intrinsic property of the sample.

Fig. 5.5 displays the A_{1g} and B_{1g} spectra of Ba122 for $T > T_{SDW}$ in small temperature steps. The A_{1g} spectra [Fig. 5.5(a)] exhibit only a very weak temperature dependence

[1] xx and yy designates measurements parallel and perpendicular to the direction of applied stress, respectively

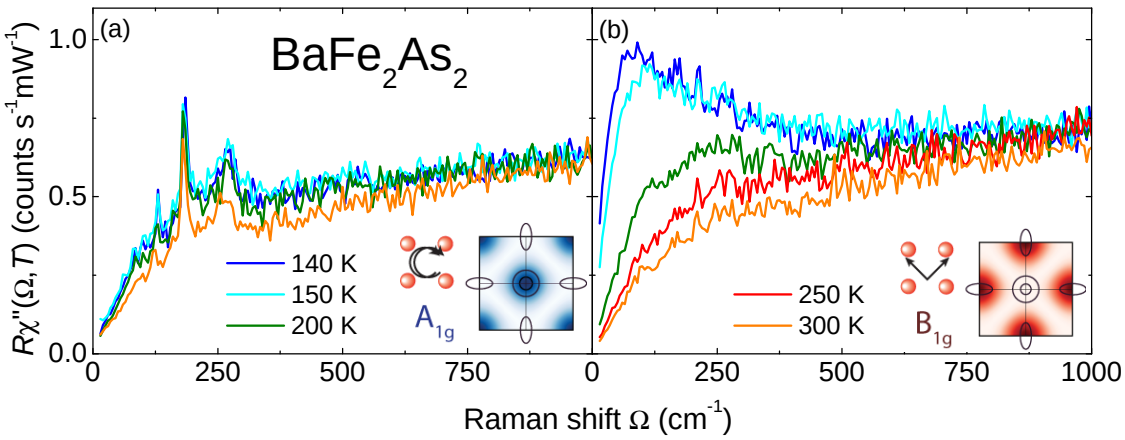

Figure 5.5: Temperature dependent Raman response of $BaFe_2As_2$ above T_{SDW} in (a) A_{1g} and (b) B_{1g} symmetry. The low energy B_{1g} response increases rapidly with decreasing temperature approaching $T_{SDW} = 134$ K. In the A_{1g} spectra there is only a weak temperature dependence observable.

above T_{SDW}. Between 300 and 200 K the intensity grows weakly for $\Omega \leq 500\,\mathrm{cm}^{-1}$ while for $T \leq 200$ K neither the spectral shape nor the intensity changes as a function of temperature. This is in contrast to the B_{1g} response [Fig. 5.5(b)]. Upon lowering the temperature the spectra gain continuously in intensity for $\Omega \leq 500\,\mathrm{cm}^{-1}$. This results in a peak at $\Omega \approx 120\,\mathrm{cm}^{-1}$ in the 150 K spectrum. At 140 K this peak has grown in intensity and shifted to lower energy. For $\Omega \geq 500\,\mathrm{cm}^{-1}$ the spectra are only moderately altered with temperature and fall on top of each other between 900 and 1000 cm^{-1}.

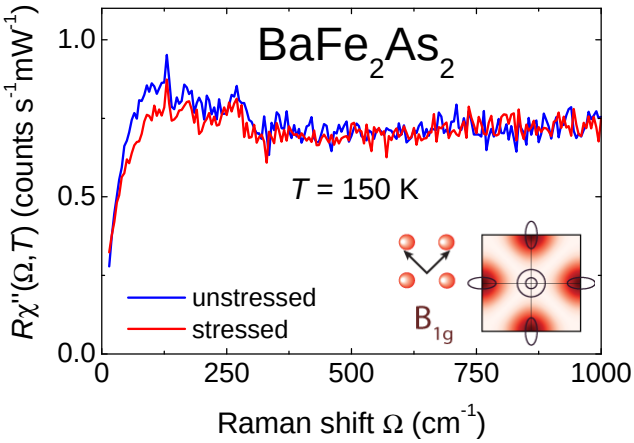

Figure 5.6: Pressure dependence of the 150 K spectra of $BaFe_2As_2$. The spectra of samples Ba122 and Ba122s, both measured without uniaxial pressure, are almost identical. The spectrum of sample Ba122s measured with uniaxial pressure exhibits reduced intensity for $\Omega \leq 200\,\mathrm{cm}^{-1}$. Data from [166].

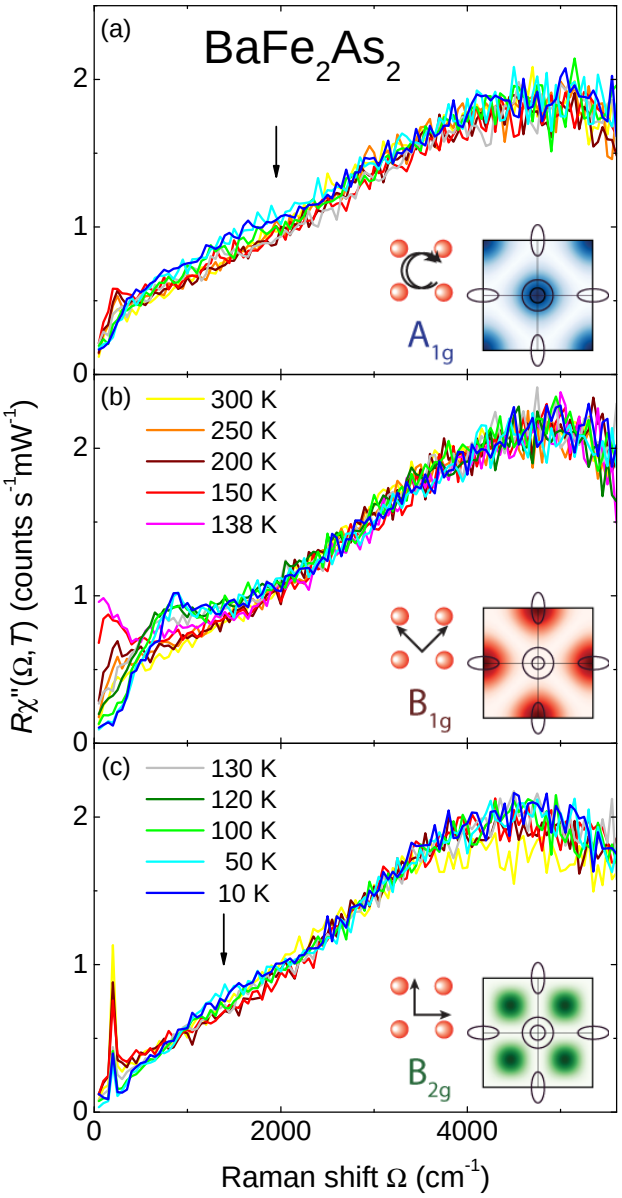

Figure 5.7: High energy Raman response as a function of temperature for the polarizations indicated symbolically. From (a) to (c) the symmetries are $A_{1g} + A_{2g}$, $B_{1g} + A_{2g}$ and $B_{2g} + A_{2g}$. The spectral shape is similar in each symmetry. The down pointing arrows emphasize the enhanced intensity in the 50 K spectra compared to the spectra at higher temperature.

The dependence of the B_{1g} response upon uniaxial pressure at $T = 150\,\mathrm{K} > T_{\mathrm{SDW}}$ is shown in Fig. 5.6 [166]. The spectra are measured with and without uniaxial pressure at the same temperature and spot position on the sample. The figure shows that the response in the range $15 \leq \Omega \leq 300\,\mathrm{cm}^{-1}$ decreases little in intensity upon applying uniaxial pressure.

Fig. 5.7 exhibits the temperature evolution of the A_{1g}, B_{1g} and B_{2g} response at high energy up to $5600\,\mathrm{cm}^{-1}$. Here, the A_{2g} response is not subtracted. For $\Omega > 1000\,\mathrm{cm}^{-1}$ the spectra are measured with excitation at 514.5 nm, a step width of $50\,\mathrm{cm}^{-1}$ and a spectral resolution of $27\,\mathrm{cm}^{-1}$ close to the laser line and $10\,\mathrm{cm}^{-1}$ at 700 nm. In

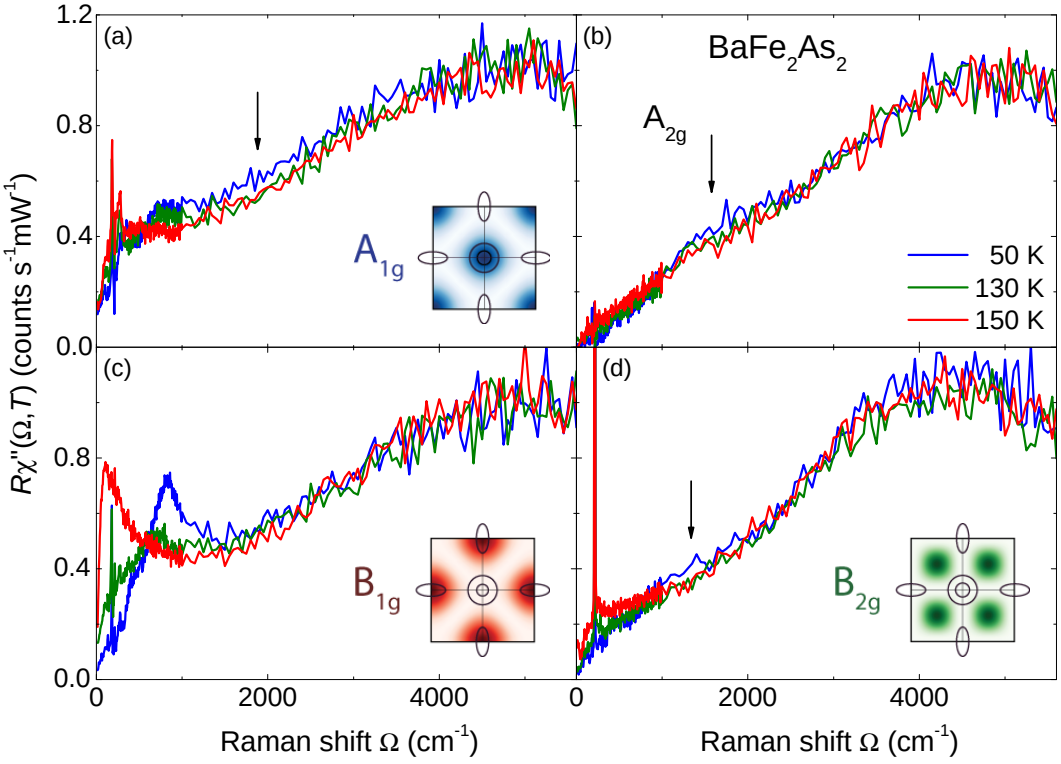

Figure 5.8: High energy Raman response of $BaFe_2As_2$ as a function of symmetry and temperature. The spectra are measured above, below and well below $T_{SDW} = 134$ K. The down pointing arrows indicate the energy where the 50 K response is enhanced with respect to the response at higher temperature.

contrast to the changes below 1000 cm^{-1}, there is only weak variation in the spectra above 1000 cm^{-1}. Around 5000 cm^{-1} the B_{1g} spectra as well as the A_{1g} and B_{2g} spectra exhibit intensities of roughly 2 counts $s^{-1}mW^{-1}$. The A_{1g} spectra fall on top of each other for $T > 100$ K in the entire energy range while for $T \leq 100$ K there is enhanced intensity in the range $600 \leq \Omega \leq 2200$ cm^{-1} [Fig. 5.7(a)]. The B_{2g} spectra [Fig. 5.7(c)] are also identical above roughly 2200 cm^{-1} and exhibit an enhanced intensity for $800 \leq \Omega \leq 2200$ cm^{-1} below 50 K. In contrast, the enhanced intensity in the B_{1g} spectra in the range $600 \leq \Omega \leq 2000$ cm^{-1} is observable already just below T_{SDW} at 130 K and gets more pronounced with decreasing temperature.

To study the contribution of the A_{2g} response to the spectra at high energy, a complete symmetry analysis of the spectra was performed. Fig. 5.8 shows the symmetry resolved Raman spectra of sample Ba122. The spectra are presented at 50, 100 and 150 K and are more noisy than the spectra displayed in Fig. 5.7 due to the subtraction procedure in Eq. (3.27). The high energy spectra are nearly symmetry independent with a maximum of approximately 1 count $s^{-1}mW^{-1}$ at roughly 5000 cm^{-1}. The A_{1g} response is enhanced

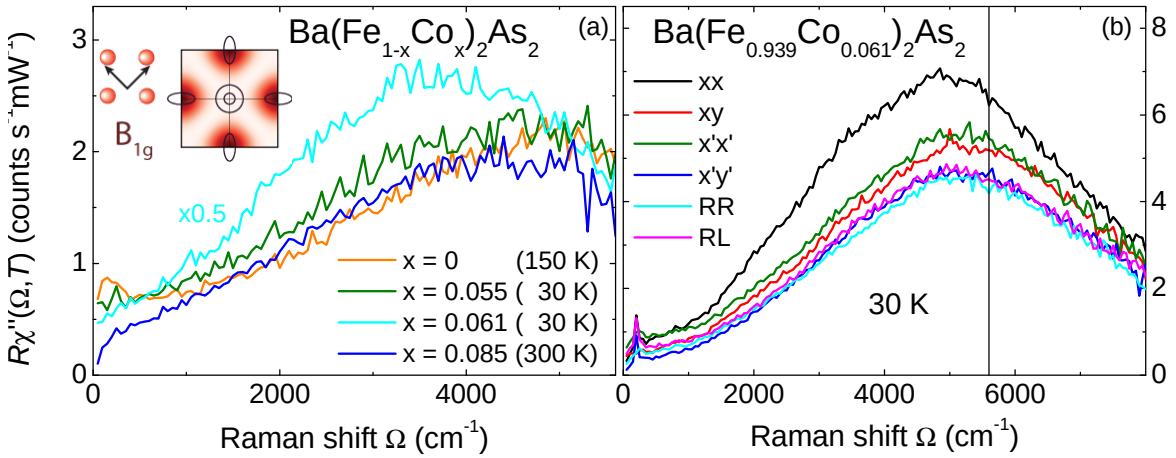

Figure 5.9: High energy Raman spectra of $Ba(Fe_{1-x}Co_x)_2As_2$. (a) Spectra at different doping levels measured with $\lambda_{exc} = 514.5$ nm. The doping levels cover a range from undoped to overdoped samples. The spectrum of the optimally doped sample is multiplied by 0.5. (b) Spectra of OPT24 in six different light polarizations. The spectra are measured at 30 K with $\lambda_{exc} = 458$ nm and exhibit a weakly polarization dependent shape and a relatively high intensity compared to the spectra at other doping levels in (a). The vertical line indicates the highest energy transfer of (a).

for $1200 \leq \Omega \leq 2200$ cm^{-1} and the B_{2g} response in the range $800 \leq \Omega \leq 2200$ cm^{-1} only at 50 K as shown by the down pointing arrows in Figs. 5.8(a) and 5.8(d), respectively, while the B_{1g} intensity increases already for $T \leq 130$ K. The A_{2g} response changes weakly above 1000 cm^{-1} [Fig. 5.8(b)] and shows an enhanced intensity in the range $1400 \leq \Omega \leq 2300$ cm^{-1} at 50 K. For none of the spectra a peak in the high energy response is observed.

Fig. 5.9(a) displays the high energy Raman spectra in $A_{2g} + B_{1g}$ symmetry as a function of doping for $0 \leq x \leq 0.085$. The spectra are measured up to a Raman shift of 5600 cm^{-1} with excitation at 514.5 nm. The intensity of the spectrum of sample OPT24 is multiplied by 0.5 to enable a comparison of the spectral shape. Apart from the response below 1000 cm^{-1} the spectra of the samples Ba122, UD23 and OD22 are very similar. These spectra increase roughly linearly in the range $1000 \leq \Omega \leq 4000$ cm^{-1} and saturate at higher energy at an intensity of approximately 2 count s^{-1}mW^{-1}. There is no peak-like structure in the studied energy range. This is opposed to the spectrum of optimally doped $Ba(Fe_{1-x}Co_x)_2As_2$ (OPT24). Here, a peak at approximately 3500 cm^{-1} is observed. Fig. 5.9(b) shows the spectra of sample OPT24 for all six polarization combinations measured with an excitation wavelength of 458 nm up to a Raman shift of 8000 cm^{-1} (1 eV). The high energy spectra have approximately twice the intensity of the spectra presented in Fig. 5.9(a). The intensity and the spectral shape of the high

energy response change only little as a function of light polarizations, and there is a broad peak with a maximum at roughly 5000 cm^{-1}.

5.2 Nature of the magnetism

Due to the close proximity of magnetism and superconductivity in the phase diagram, spin fluctuations are believed to play a key role for the superconducting pairing mechanism in the FeSCs [97, 98, 99, 100, 179, 180]. While the relevance of spin excitations is generally accepted, the nature of magnetism remains a fundamental open question. Raman scattering may help to discriminate between a local and an itinerant model.

5.2.1 Indications of localized spins?

It is clear at first glance that the high energy response in Ba122 is different from that in undoped cuprates [135]. This is not completely unexpected since Ba122 is still a metal while undoped cuprates are antiferromagnetic insulators. However, some similarities exist with spectra of doped cuprates [167, 181]. Therefore, the Raman response of localized spins with a strongly frustrated J_1-J_2 and an unfrustrated but anisotropic J_{1a}-J_{1b}-J_2 interaction [Fig. 2.10] for nearest (J_1) and next-nearest neighbors (J_2) interactions was calculated in a Heisenberg model. The results of this study are reproduced in Fig. 5.10(a). For frustrated as well as unfrustrated interactions sharp features are predicted to appear in the A_{1g} and B_{1g} spectra [33]. The energy of these peaks depends on the coupling strength J_1 and J_2 and is generally expected in the energy range $2000 \leq \Omega \leq 3000$ cm^{-1}.

In the spectra presented here [Figs. 5.7, 5.8 and 5.9(a)] no sharp peaks are observed in this energy range. This is at variance with the results of Sugai *et al.* who find broad peaks around 2300 cm^{-1} with a FWHM of 500 cm^{-1} in the spectra of $BaFe_2As_2$ [Fig. 5.10(b)] as well as of $Ba(Fe_{1-x}Co_x)_2As_2$ and $Fe_{1+y}Te_{1-x}Se_x$ [12, 182, 184, 185] for all light polarizations. These peaks are claimed to originate from spin excitations, and, in a study by Okazaki *et al.* [12] of the same group, it is argued that the peak energy of the two-magnon peaks is explained reasonably using the coupling constants J_{1a}, J_{1b} and J_2 derived from inelastic neutron scattering (INS) studies [90, 109, 186].

The only high energy spectra which are compatible with the study of Sugai *et al.* are the spectra of sample OPT24. These spectra exhibit a broad and pronounced peak which is mainly polarization independent [Fig. 5.9(b)]. If this peak should indeed originate from two-magnon excitations one would expect that the energy hardens and the intensity

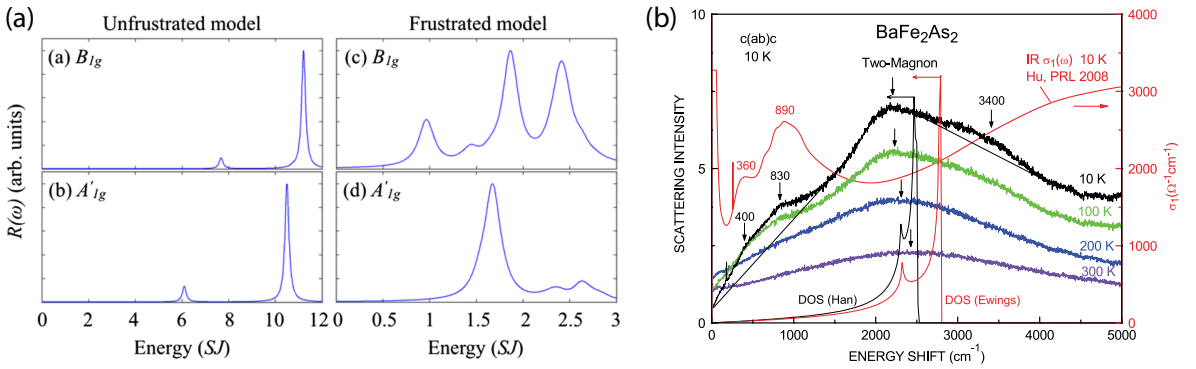

Figure 5.10: Theoretically calculated high energy Raman response of two-magnon excitations and experimentally observed response of $BaFe_2As_2$. (a) Two-magnon response of localized spins calculated for an unfrustrated and a frustrated model (see text) using a Heisenberg model. From [33]. (b) Experimentally observed high energy B_{1g} response of $BaFe_2As_2$. From [182]. For comparison, the optical conductivity $\sigma_1(\omega)$ at 10 K obtained by Hu *et el.* [183] and the DOS of the spin waves obtained by Han *et al.* [109] and Ewings *et al.* [179] are shown. The left pointing arrows demonstrate the reduction of the two-magnon peak energy due to the magnon-magnon interaction energy according to the study of [182].

increases towards lower doping levels where the magnetic order is more long ranged such as observed for the cuprates [167, 187]. Since for Ba122 (Figs. 5.7 and 5.8) no peak in the high energy spectra is observed, the occurrence of a pronounced peak in the spectra at optimal doping is rather surprising. Moreover, the broad peak in the spectra of sample OPT24 has shifted to lower energy when the energy of the exciting laser light is increased from 2.4 eV [$\lambda_{\mathrm{exc}} = 514.5$ nm, Fig. 5.9(a)] to 2.7 eV [$\lambda_{\mathrm{exc}} = 458$ nm, Fig. 5.9(b)]. While the energy of the exciting light has changed by $\Delta\Omega_{\mathrm{exc}} = 2400\ \mathrm{cm}^{-1}$, the peak shifts by $\Delta\Omega_{\mathrm{peak}} = 1500\ \mathrm{cm}^{-1}$ to a Raman shift of $\Omega_{\mathrm{peak}} = 3500\ \mathrm{cm}^{-1}$. Thus, the absolute energy of the peak structure stays almost constant at roughly $\Omega^{\mathrm{abs}}_{\mathrm{peak}} = 16300\ \mathrm{cm}^{-1}$. This suggests that the observed peak is not related to the Raman effect but to fluorescence [163]. The fluorescence affects mainly the high energy spectra and may originate from the sample or, possibly, from the glue which is used to mount the sample on the copper block (Sec. 4.2). The fluorescence can, in addition, explain the high intensity and the weak polarization dependence of the spectra [c.f. Fig. 5.9(b)]. Hence, the spectra of sample OPT24 are most likely superposed by fluorescence which exceeds the response of the charge carriers.

Another possible origin of the peak in the spectra of Sugai and coworkers may be traced back to artifacts of the sensitivity correction [167]. According to Eq. (4.1), the presented spectra are divided by the transmission of the setup $T(\omega_s)$ and the energy

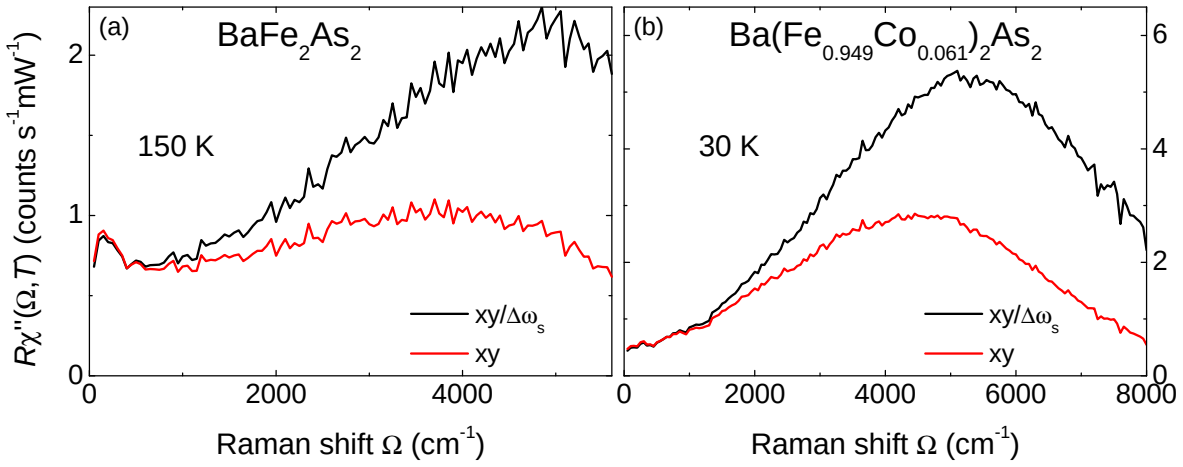

Figure 5.11: High energy Raman spectra with (black) and without (red) correction for the energy dependent resolution of the spectra $\Delta\omega_s$. (a) The spectrum of $BaFe_2As_2$ is measured with $\lambda_{exc} = 514.5$ nm to a Raman shift of 5600 cm^{-1} and (b) the spectrum of optimally doped $Ba(Fe_{1-x}Co_x)_2As_2$ with $\lambda_{exc} = 458$ nm to a Raman shift of 8000 cm^{-1}.

dependent resolution $\Delta\omega_s$ of the spectra. If the spectra are not divided by $\Delta\omega_s$, one obtains the red spectra shown in Fig. 5.11. Here, the spectra of undoped [Fig. 5.11(a)] and optimally doped $Ba(Fe_{1-x}Co_x)_2As_2$ [Fig. 5.11(b)] are presented with (black) and without (red) correction for $\Delta\omega_s$. In the spectrum of $BaFe_2As_2$ a broad feature at roughly 4000 cm^{-1} is generated by omitting the correction for $\Delta\omega_s$. In the spectrum of the optimally doped sample, where the response is measured up to 8000 cm^{-1}, a peak is present already in the corrected spectrum and moves substantially to lower energy in the uncorrected spectrum. This could explain the broad peaks in the spectra of Sugai and coworkers.

Summarizing, in the spectra presented in Figs. 5.7 and 5.8 neither above nor below T_{SDW} a structure, which could be assigned to two-magnon excitations, is found below 0.7 eV. However, even for the largest magnetic couplings reported in the literature [11, 179, 188, 189] two-magnon excitations are expected in this energy range. Thus, based on the presented data the existence of two-magnon excitations can be excluded signaling the failure of the Heisenberg model in the description of the magnetism. This is an argument in favor of itinerant rather than localized spins in the iron pnictides. In the case of itinerant spins it is worth analyzing the rapid loss of spectral weight, shown in Fig. 5.2, in terms of the opening of a SDW gap below T_{SDW}.

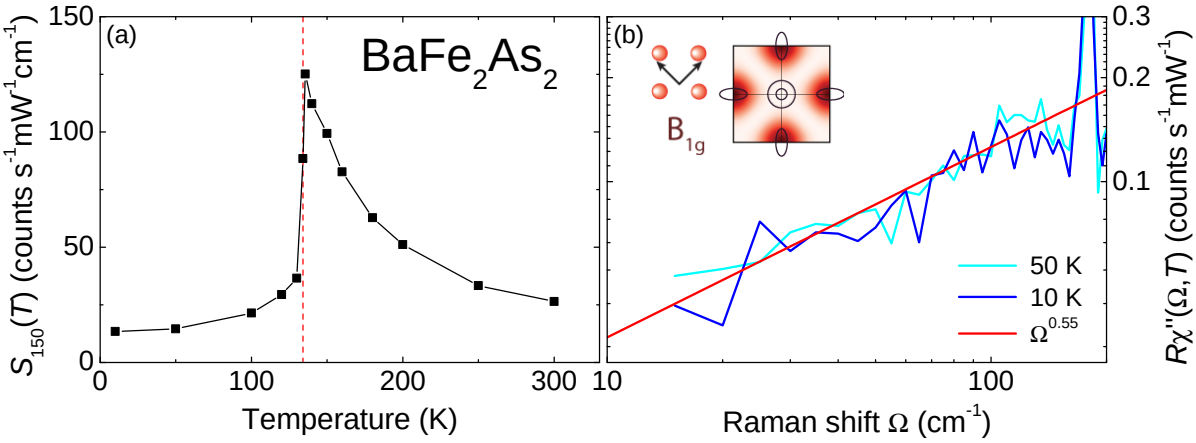

Figure 5.12: Loss of low energy spectral intensity and initial slope of the $BaFe_2As_2$ spectra in B_{1g} symmetry. (a) Loss of spectral intensity in a range up to 150 cm^{-1} as a function of temperature. $S_{150}(T)$ denotes the integrated intensity in the range between 15 and 150 cm^{-1}. The structural and magnetic transition at $T_{SDW} = 134$ K is indicated by the dashed vertical line. (b) Initial slope of the B_{1g} spectra of $BaFe_2As_2$ at the lowest measured temperatures. The red line is a simulation of the spectra with an $\Omega^{0.55}$ variation of the slope.

5.2.2 Signatures of the spin-density-wave

In Fig. 5.12(a) the loss of spectral weight in B_{1g} symmetry below T_{SDW} is demonstrated. Here, the integrated B_{1g} intensity between 15 and 150 cm^{-1},

$$S_{150}(T) = \int_{15\ cm^{-1}}^{150\ cm^{-1}} \chi''_{B1g}(\Omega, T) d\Omega, \tag{5.1}$$

is shown as a function of temperature. Between 300 and 135.5 K, $S_{150}(T)$ increases strongly as will be discussed in the next section. As soon as $T_{SDW} = 134$ K is crossed [red dashed line in Fig. 5.12(a)], $S_{150}(T)$ decreases by almost 70% from $T = 135.5$ to 130 K, i.e. in a temperature interval as small as $\Delta T = 5.5$ K. At lower temperatures $S_{150}(T)$ decreases moderately and finally saturates for $T < 100$ K retaining roughly 10% of $S_{150}(135.5\ K)$. This is in agreement with the small B_{1g} intensity in the range $15 \leq \Omega \leq 250\ cm^{-1}$ [Fig. 5.3(b)] for $T \leq 50$ K with values of roughly 0.1 counts $s^{-1}mW^{-1}$. In addition, Fig. 5.12(b) shows that the spectra for $T \leq 50$ K follow nearly a $\sqrt{\Omega}$ dependence over roughly 100 cm^{-1}. This means that the Raman spectrum at the lowest temperatures extrapolates to zero for $\Omega \to 0$ and therefore argues for an energy gap with deep minima or nodes on the electron bands instead of a small but finite gap. Such a partial energy gap in the SDW state is in agreement with theoretical considerations that the SDW gap cannot acquire a full gap [111]. Via QO [110, 114], ARPES [113]

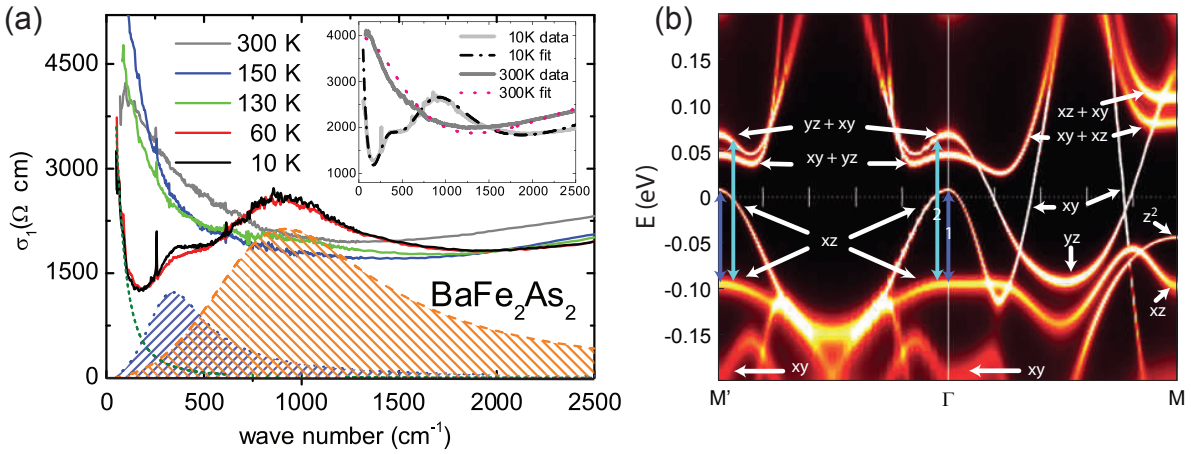

Figure 5.13: Dynamic conductivity spectra of $BaFe_2As_2$ and orbital character of the bands near the Fermi level. (a) Dynamic conductivity below 2500 cm^{-1} for different temperatures (from [183]). The figure shows the clear suppression of spectral intensity upon entering the SDW state. (b) Orbital character of the bands near the Fermi level. The blue (1) and cyan arrow (2) indicate the intraorbital and interorbital transitions that give, according to [190], rise to the step at 400 cm^{-1} and the peak at 890 cm^{-1}, respectively.

and optical conductivity studies [183] a partial gap in the SDW state is experimentally observed. Thus, the low energy Raman response is suppressed due to the opening of a SDW gap.

Along with the depletion of low energy spectral weight, a pronounced structure occurs in the spectra for $T \leq 50$ K. Independent of pressure, a step at roughly $\Omega = 400$ cm^{-1} ($\Omega^{400}_{\mathrm{step}}$), in the A_{2g}, B_{1g}, and B_{2g} spectra and a peak at 850 cm^{-1} ($\Omega^{850}_{\mathrm{peak}}$) in the A_{1g} and B_{1g} spectra is observed [Figs. 5.2(c) and 5.3(b)]. Similar features below T_{SDW} are also reported from other authors but the origin is unclear: In a Raman study of Chauviere *et al.* on $BaFe_2As_2$ with a similar B_{1g} spectrum the features at 400 and 850 cm^{-1} are attributed to two different SDW transitions [174]. In optical spectroscopy studies on samples of undoped MFe_2As_2 (M = Ba, Eu) and underdoped $Ba(Fe_{1-x}Co_x)_2As_2$ [21, 183, 190, 191, 192] a similarly pronounced redistribution of spectral weight below T_{SDW} is observed. The spectra of an optical study on $BaFe_2As_2$ by Hu *et al.* [183] are reproduced in Fig. 5.13(a). In this study the first peak is located at 360 cm^{-1} and the second peak at 890 cm^{-1} corresponding to gap values of $2\Delta/k_B T_{\mathrm{SDW}} = 3.5-3.6$ and $9-9.6$, respectively. This double peak structure was identified with two SDW gaps opening on different bands below T_{SDW}. In this study it could be derived that about 88% itinerant carriers were removed by the gapping of the FS. In another optical conductivity study on $BaFe_2As_2$ by Yin *et al.* both features are attributed to orbital transitions as predicted by DMFT calculations [190]. The corresponding transitions are shown in Fig. 5.13(b).

For uncovering the origin of $\Omega_{\text{step}}^{400}$ it is important to note that $\Omega_{\text{step}}^{400}$ is independent of the applied uniaxial stress [Fig. 5.4(a)], gets rapidly smeared out with increasing temperature and is unobservable for $T \geq 130$ K [Fig. 5.3(b)]. Below 400 cm^{-1}, the response is only suppressed in the A_{2g}, B_{1g} and B_{2g} spectra as demonstrated by the dashed lines in Fig. 5.2. In the A_{1g} spectra the intensity is reduced for $\Omega \leq 300$ cm^{-1}, while for $300 \leq \Omega \leq 400$ cm^{-1} a peak appears. If the steps in the spectra of different symmetries are associated with orbital transitions, the enhanced intensity in the B_{1g} spectra can only originate from transitions between the x^2-y^2 and the $3z^2-r^2$ orbitals. The A_{1g} step can only be induced by intraorbital transitions while the step in B_{2g} symmetry can be induced by $xy \rightarrow 3z^2-r^2$ and $xz \leftrightarrow yz$ transitions [174]. Thus, many participating orbitals are needed to explain why the features occur in all four symmetries. Additionally, if $\Omega_{\text{step}}^{400}$ is of orbital nature, it is unlikely that it occurs at a similar energy in the spectra of different symmetries. This makes an orbital transition as the origin of $\Omega_{\text{step}}^{400}$ unlikely. Rather, orbital transitions might be at the origin of relatively weak and broad peak structures between 1000 and 3000 cm^{-1} in the A_{1g}, A_{2g} and B_{2g} spectra at 50 K although it is not yet clear why these peaks are observed only for $T \leq 50$ K. Those peaks are shown by the down pointing arrows in Fig. 5.8. For instance, it is found that there are transition from the $3z^2-r^2$ to the xy orbitals [193]. The excitations originate from charge modes and have an energy of 150 meV at the zone center if a renormalization factor of two is taken into account to adjust the single particle LDA calculations to the interacting electrons as observed in the experiments [80, 194, 195, 196]. These transitions are Raman active and have B_{2g} symmetry. Therefore, they can explain the increased B_{2g} intensity observed for 850 cm$^{-1} \leq \Omega \leq 1600$ cm^{-1} at 50 K.

If $\Omega_{\text{step}}^{400}$ originates from a SDW gap, which is in agreement with the robustness of the peak against uniaxial pressure (Fig. 5.4) [166, 197] and a recent ARPES study [113], the excess A_{1g} intensity between 300 and 400 cm^{-1} for $T \leq 50$ K, needs an explanation [Fig. 5.3(a)]. Here, the optical study of Yin *et al.* on $BaFe_2As_2$ helps. In this study the peak in the optical spectrum at 370 cm^{-1} is assigned to intraorbital transitions between the d_{xz} orbitals [dark blue arrow in Fig. 5.13(b)] [190]. Since such intraorbital transitions are observable in A_{1g} symmetry, they may allow an explanation of the increased intensity between 300 and 400 cm^{-1} in the A_{1g} spectra. Therefore, $\Omega_{\text{step}}^{400}$ can be assigned to the SDW. The A_{1g} response for 300 cm$^{-1} \leq \Omega \leq 400$ cm^{-1} is superposed by intraorbital transitions which enhance the response in this energy range.

$\Omega_{\text{peak}}^{850}$ is found in B_{1g} and in A_{1g} symmetry at 50 K (Fig. 5.2). A possible way to explain the origin of $\Omega_{\text{peak}}^{850}$, which is not yet observed in ARPES data [113, 118, 119], is to

investigate the temperature dependence of the peak. In B_{1g} symmetry the peak is located at $\Omega = 850\ \mathrm{cm}^{-1}$ for $T \leq 50$ K [Fig. 5.3(b)]. With increasing temperature $\Omega^{850}_{\mathrm{peak}}$ loses slightly intensity and moves toward lower energy. At $T = 130$ K the peak is clearly visible but is located at roughly $750\ \mathrm{cm}^{-1}$. Such a temperature dependence is expected for a mean-field transition and is an argument in favor of the SDW origin of the peak. If $\Omega^{850}_{\mathrm{peak}}$ indeed originates from the SDW, the size of this SDW induced peak $\Omega^{\mathrm{SDW}}_{\mathrm{peak}}$ normalized to T_{SDW}, $\Omega^{\mathrm{SDW}}_{\mathrm{peak}}/k_B T_{\mathrm{SDW}} = 9.1$, exceeds by far the BCS weak coupling value of 3.53 for an isotropic gap in a mean-field approach [Eq. (3.40)]. This suggests that the transition temperature $T_{\mathrm{SDW}} = T_{\mathrm{TO}}$ in $BaFe_2As_2$ is largely reduced from the respective mean-field transition temperature T_{MF}. Such a reduction of the phase transition below T_{MF} may primarily arise from fluctuations in the range $T_{\mathrm{MF}} > T > T_{\mathrm{SDW}} = T_{\mathrm{TO}}$ [155, 198, 199]. These fluctuations will be studied in the following section. In addition to the temperature dependence, the pressure dependence of this peak can help elucidating its origin. Fig. 5.4 shows that the peak in $A_{1g} + B_{1g}$ symmetry splits upon applying uniaxial stress. In the xx spectra, measured with polarizations in direction of the uniaxial stress, enhanced intensity is observed with a maximum in the range $800 \leq \Omega \leq 820\ \mathrm{cm}^{-1}$ while the yy response, measured with polarizations perpendicular to the direction of the applied stress, is enhanced with a maximum in the range $870 \leq \Omega \leq 920\ \mathrm{cm}^{-1}$. This pronounced pressure dependence of $\Omega^{850}_{\mathrm{peak}}$ favors band folding effects as the origin of the peak since the electronic bands are expected to shift differently in the direction and perpendicular to the direction of applied stress [176]. Thus, the temperature and pressure dependence of $\Omega^{850}_{\mathrm{peak}}$ argues for a SDW origin of this feature.

5.2.3 Conclusion

The lack of spectral features corresponding to two-magnon excitations of localized spins in the high energy spectra of $BaFe_2As_2$ (Figs. 5.7 and 5.8) argues more for the itinerant than for the localized nature of the spins. The itinerant nature of the spins is consistent with the opening of a SDW gap which only partially gaps the FS. For higher energy two features occur in the spectra where both of them can be assigned to the SDW via the analysis of the spectra under uniaxial stress. The observation of itinerant spins in $Ba(Fe_{1-x}Co_x)_2As_2$ is in agreement with LDA calculations [113] and INS experiments [11, 106].

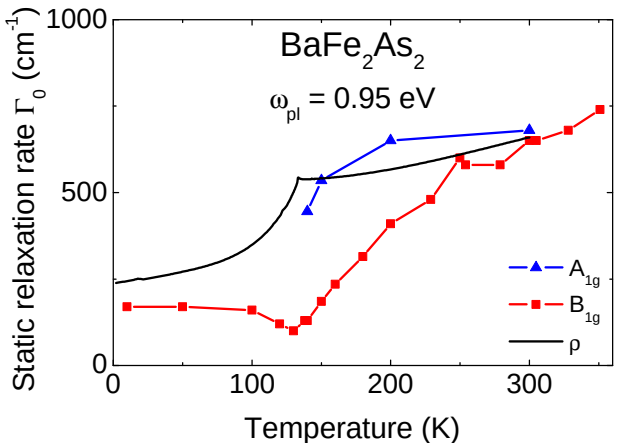

Figure 5.14: Raman relaxation rates of $BaFe_2As_2$ in the static limit and resistivity data obtained from the same sample. The plasma frequency ω_{pl} and the value of the static rates at 300 K are in good agreement with data from optical spectroscopy [183].

5.3 Evidence for fluctuations above $T_{\mathrm{SDW}} = T_{\mathrm{TO}}$

The presence of fluctuations in the reponse for $T > T_{\mathrm{SDW}} = T_{\mathrm{TO}}$ will be investigated. Such fluctuations are suggested by the data shown in Fig. 5.12(a) where $S_{150}(T)$ grows by a factor of approximately 5 in the temperature range $300 \geq T \geq 135.5$ K with a tendency to diverge toward T_{SDW}.

5.3.1 Indications of fluctuations

An increase of the initial slope of the Raman spectra translates into a decrease of the carrier relaxation rates via the Shastry-Shraiman relation [169]. Therefore, static Raman relaxation rates $\Gamma_0(T)$ in the limit $\Omega \to 0$ (Sec. 3.5), are derived from the spectra and compared to the resistivity measured on similar crystals [7]. The results are displayed in Fig. 5.14. For $T < T_{\mathrm{TO}} = T_{\mathrm{SDW}}$ the B_{1g} spectra are superposed by the A_{1g} phonon at 185 cm^{-1} due to the structural distortion of the lattice. Additionally, the intensity of the spectra is reduced due to the SDW gap. Here, $\Gamma_0^{\mathrm{B1g}}(T)$ is determined from the spectra for $\Omega \leq 150$ cm^{-1}. This low energy response can be associated with the carriers which are not gapped by the nodal SDW gap. The resistivity can be expressed in units of wavenumbers via Eq. (3.36). The plasma frequency is 1 eV and acts as fitting parameter to adjust the resistivity data to the Raman relaxation rates and is in agreement with ω_{pl} obtained from optical conductivity at room temperature [183].

Fig. 5.14 displays $\Gamma_0^{\mu}(T)$ for $\mu = \mathrm{A_{1g}}, \mathrm{B_{1g}}$ and $\Gamma_0^{\rho}(T)$. Below T_{SDW} $\Gamma_0^{\mathrm{B1g}}(T)$ increases slightly with decreasing temperature and therefore has a trend opposite to $\Gamma_0^{\rho}(T)$. For

$T > T_{\mathrm{SDW}}$ $\Gamma_0^{\mu}(T)$ exhibits a remarkable temperature dependence approaching T_{SDW} in both symmetries. While $\Gamma_0^{\mathrm{A1g}}(T)$ decreases moderately between 300 and 140 K by about 30%, $\Gamma_0^{\mathrm{B1g}}(T)$ decreases by a factor of 5.5 in the same temperature range. Such a symmetry dependence of $\Gamma_0^{\mu}(T)$ is in agreement with the distinct temperature dependences of the spectra [Fig. 5.5]. Hence, from Fig. 5.14 it is clear that $\Gamma_0^{\mathrm{B1g}}(T)$ heavily overestimates the temperature dependence of $\Gamma_0^{\rho}(T)$ which decreases by roughly 20% between 300 K and T_{SDW}. This observation is reminiscent of Raman studies of underdoped $La_{2-x}Sr_xCuO_4$ where fluctuating stripe order [200] leads to a low energy peak in the Raman spectra [154, 161, 201, 202, 203].

The interpretation of the increased low energy Raman response in terms of fluctuations is also in agreement with a theoretical study [199]. There, it was proposed that, if the electron-phonon interaction λ is small but exceeds a critical value λ_c, nematic order and fluctuations (Sec. 2.3.3) occur in a material having a charge-density-wave (CDW) at low temperature. In a Raman spectrum λ can in principle be extracted from an asymmetric Fano lineshape [204] of the phonons [205, 206, 207]. The observation that the lineshape of all four Raman active phonons occurring in the spectra (Fig. 5.1) is symmetric, as also observed in other ERS studies [47, 171, 172, 173], argues for a vanishingly weak λ in agreement with theoretical considerations [121]. Nevertheless, changes of the frequency and linewidth of the B_{1g} phonon upon crossing T_c [208, 209] and of the A_{1g} phonon upon crossing T_{SDW} are observed [174]. Thus, the change of the phonons linewidth and frequency indicate that there is a small but finite λ, as proposed theoretically [210].

An anomalously low energy response above T_{SDW} is also reported in other Raman studies and interpreted in terms of the response from magnetic fluctuations which superpose the response from the electronic continuum [174, 182, 211, 208] as observed in magnetic insulators [212]. In the earlier studies the response from fluctuations was not further analyzed. It turns out that the response can be understood quantitatively.

5.3.2 Theoretical model of fluctuations

Due to the absence of the f-sum rule in Raman spectroscopy [137, 142], scattering from fluctuations can open a new channel. The related response is superposed on the continuum of particle-hole excitations [213] which is expected to resemble transport properties [149]. Assuming that the resistivity is temperature independent between 300 K and T_{SDW}, which is approximately justified by transport data [7], the electronic continuum is expected to change only weakly for $T > T_{\mathrm{SDW}}$. Therefore, an analytic approximation of the 300 K spectrum, $\chi_a''(\Omega, 300\ \mathrm{K})$, is subtracted from the response

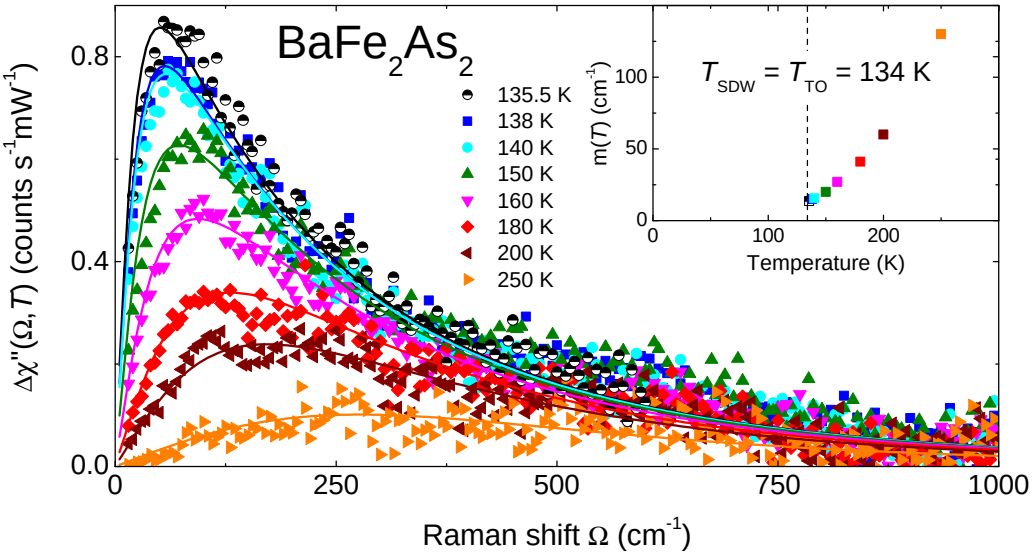

Figure 5.15: Difference spectra $\Delta\chi''(\Omega, T) = \chi''(\Omega, T) - \chi''_a(\Omega, 300\ \mathrm{K})$ (symbols) and calculated response from fluctuations (solid lines) for $BaFe_2As_2$. The inset shows the temperature dependence of the effective mass which acts as the only fitting parameter. For details see the text.

at lower temperatures to extract the low energy response superposed on the electronic continuum. The resulting difference spectra $\Delta\chi''(\Omega, T)$ are shown as symbols in Fig. 5.15 with $\Delta\chi''(\Omega, T) = \chi''(\Omega, T) - \chi''_a(\Omega, 300\ \mathrm{K})$. $\Delta\chi''(\Omega, T)$ is close to zero at 1000 cm^{-1} where the Raman spectra $\chi''(\Omega, T)$ for different temperature merge. For $T = 250$ K the difference spectrum exhibits a broad but weak peak around 300 cm^{-1}. For decreasing temperature the low energy peak gains continuously intensity and shifts to lower energy while the high energy part of $\Delta\chi''(\Omega, T)$ is practically unaffected. At 140 K the intensity of the low energy peak at 60 cm^{-1} has increased by approximately a factor of 7 with respect to that of the peak of $\Delta\chi''(\Omega, 250\ \mathrm{K})$.

For the analysis of the response a theoretical model of dynamic charge order or charge fluctuations is applied [154]. The response from fluctuations can be expressed as (see Sec. 3.6)

$$\Delta\chi''(\Omega, T) = \Lambda^2 \int_0^\infty dz\, [b(z - \Omega/2) - b(z + \Omega/2)]\, \frac{z_+ z_-}{z_+^2 - z_-^2}\, [F(z_-) - F(z_+)]\,. \qquad (5.2)$$

Here, Λ is a fit parameter independent of temperature and Ω to adjust the intensity of the spectra, $b(z)$ is the Bose function. $F(z)$ depends on ω_0 and $m(T)$ where ω_0 is an ultraviolet cutoff and $m(T)$ is the mass of the fluctuation propagator. The results of the fitting procedure are shown as solid lines in Fig. 5.15. The free parameters for

the calculation of the theoretical spectra are obtained from an optimal fit to the 180 K spectrum yielding $\omega_0 = 400\,\mathrm{cm}^{-1}$ and $\Lambda = 0.2$. These parameters are kept constant for all temperatures. At high energy the calculated spectra have a small intensity of roughly $0.05\,\mathrm{counts\,s^{-1}mW^{-1}}$ at 1000 cm^{-1} mainly independent of the temperature. The increasing intensity and decreasing energy of the peak maximum with decreasing temperature is well reproduced by the theoretical spectra. The only fitting parameter, tuned to mimic the temperature dependence and intensity of the spectra, is the mass of the fluctuation propagator $m(T)$. It is shown in the inset of Fig. 5.15 to decrease approximately linearly at high temperatures before it tends to saturate at very small values for $T_{\mathrm{SDW}} \leq T \leq 150$ K. The agreement of the calculated spectra with the experimental data is almost quantitative. The strong temperature dependence is basically described by the temperature dependences of $m(T)$ and the Bose function $b(z)$. This justifies the approximation made to separate $\Delta\chi''$ and strongly supports the interpretation of the low-energy Raman response in terms of fluctuations.

Thus, it is demonstrated explicitly that the anomalous low energy Raman response is a superposition of a mainly temperature independent electron-hole continuum, as suggested by the weak temperature dependence of $\rho(T)$, and a strongly temperature dependent response of a fluctuating order. Here, the observation of fluctuations indicates that the combined structural and magnetic transition at 134 K is a second order phase transition. Yet, the nature of the fluctuations has still to be determined.

5.3.3 Nature of the fluctuations

As the origin of the ordering fluctuations in principle two different possibilities are discussed: Via transport studies a resistivity anisotropy for stressed $Ba(Fe_{1-x}Co_x)_2As_2$ single crystals along the nominally identical a- and b-axis is observed. This resistivity anisotropy increases approaching T_{TO} from above. This is suggested to reflect fluctuations which are associated with the structural phase transition in unstressed samples [60]. In an ARPES study [176] on detwinned $Ba(Fe_{1-x}Co_x)_2As_2$ single crystals an electronic anisotropy in the orbital degree of freedom between the a- and b-axis develops well above T_{TO}. The temperature regime above T_{TO} indicates the involvement of fluctuations of possibly orbital origin [176]. In both studies this anisotropy has disappeared above maximally 150 K. Via INS Diallo *et al.* [214] studied paramagnetic excitations in $CaFe_2As_2$ above T_{SDW}. For $T < 300$ K they observed in-plane anisotropic spin-wave excitations which are assigned to the anisotropy of the in-plane spin fluctuations in the paramagnetic state. Harringer *et al.* [188] observed anisotropic short range magnetic exchange

couplings in $BaFe_2As_2$ without an external driving field. These couplings are unchanged upon crossing T_{SDW} indicating a spin nematic fluid. Since the magnetic anisotropy and the fluctuations in $BaFe_2As_2$ can be observed above $T_{\mathrm{SDW}} = T_{\mathrm{TO}}$ and therefore in the tetragonal lattice of the paramagnetic state, Harriger *et al.* proposed that the magnetic fluctuations are intrinsically nematic [188]. Thus, the influence of magnetic interaction in the FeSCs persists up to room temperature. Therefore, magnetic fluctuations could explain the strong increase of the low energy Raman spectra better than orbital fluctuations which are related to the structural transitions. Nevertheless, the observations that the fluctuations are reduced upon the application of uniaxial stress (Fig. 5.6) is an argument in favor of orbital rather than magnetic fluctuations. This will be further analyzed in Sec. 6.5 via the analysis of Co-doped samples where T_{TO} and T_{SDW} are separated in temperature.

However, the abrupt loss of low energy spectral weight crossing T_{SDW}, as demonstrated in Fig. 5.12(a), can now be attributed to two different effects. On the one hand, the scattering on fluctuations disappears as one enters the ordered state meaning the enhancement of the low energy Raman response disappears as soon as the temperature is lowered below $T_{\mathrm{SDW}} = T_{\mathrm{TO}}$. On the other hand, there opens a nodal SDW gap below T_{SDW} which results in the depletion of the low energy Raman response (see Sec. 5.2.2). Both effects in combination lead to the strong and abrupt loss of spectral weight upon crossing T_{SDW}.

Chapter 6

Normal state properties at finite doping

In this chapter, light scattering results of $Ba(Fe_{1-x}Co_x)_2As_2$ at finite doping are presented. The data are recorded in the normal state. For the discussion of the phonons the reader is referred to Sec. 5.1.1.

The symmetry dependence of the spectra is analyzed via the momentum dependence of the Raman form factors and discussed along with other experimental techniques. In the last section the nature of the fluctuations, which have been observed in the low energy response of Ba122 (Sec. 5.3), will be addressed via the detailed analysis of the spectra of an underdoped sample.

6.1 Experimental Results

Experiments on $Ba(Fe_{1-x}Co_x)_2As_2$ were performed in the doping range $0.045 \leq x \leq 0.085$ around optimal doping (samples UD14, UD18, UD23, OPT24 and OD22 in Tab. 4.2). Fig. 6.1 shows a compilation of the A_{1g} and B_{1g} spectra as a function of doping just above T_c at roughly 25 K [Figs. 6.1(a) and 6.1(b), respectively] and at 300 K [Figs. 6.1(c) and 6.1(d), respectively]. All spectra include the A_{2g} response which is small at energies below 1000 cm^{-1} [Fig. 5.2(b)]. At $T = 25$ K the spectra are measured with a step width of 5 cm^{-1}, a resolution of 6.5 cm^{-1} and excitation at $\lambda_{exc} = 514.5$ (UD14, UD18 and UD23) and 532 nm (OD22). The optimally doped sample is measured with a step width of 2.5 cm^{-1} and a spectral resolution of 5 cm^{-1} at $\lambda_{exc} = 514.5$ nm. At 300 K the spectra are measured with a spectral resolution of 6.5 cm^{-1} and a step width of 5 cm^{-1} except for OPT24, where the measurement parameters are the same as at low temperature.

The A_{1g} spectra at low temperature [Fig. 6.1(a)] exhibit a weak doping dependence

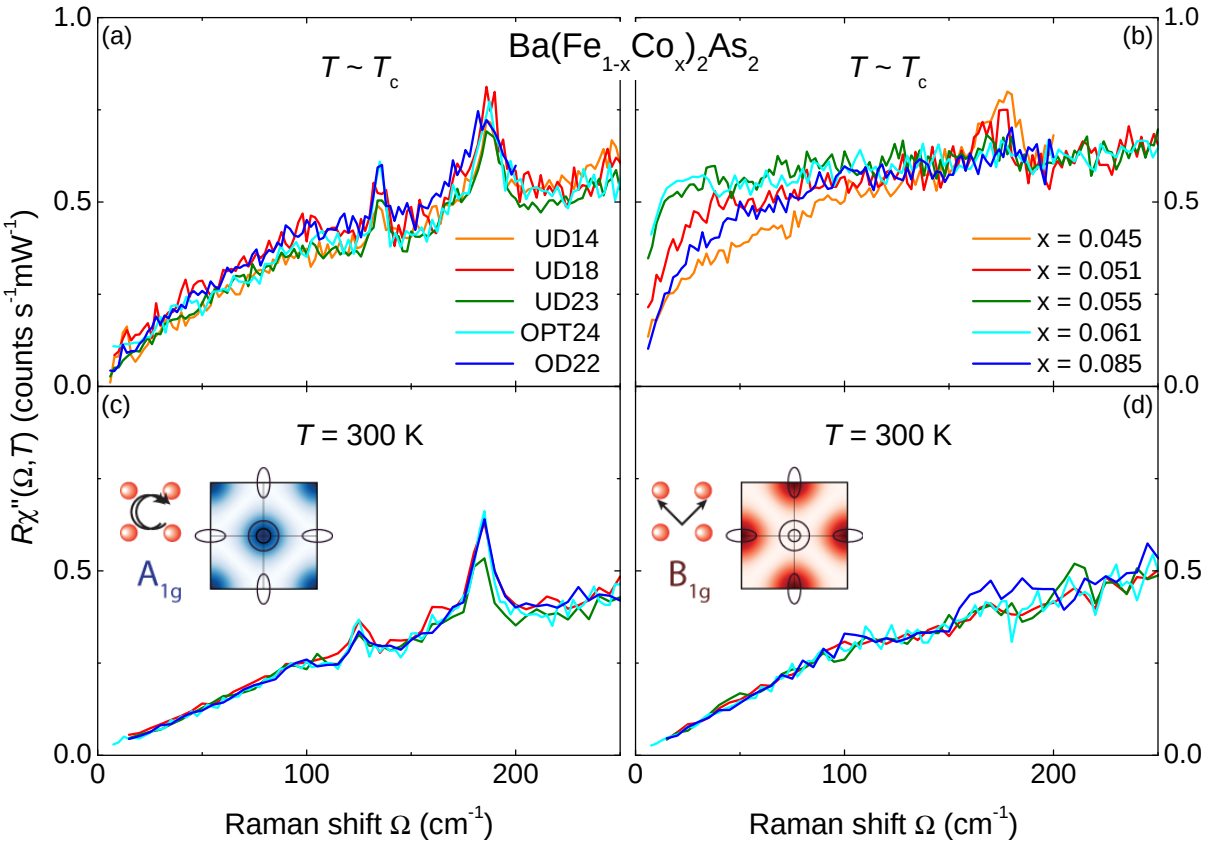

Figure 6.1: Doping dependence of the A_{1g} [(a), (c)] and B_{1g} Raman spectra [(b), (d)] of $Ba(Fe_{1-x}Co_x)_2As_2$. The spectra are shown for $T \to T_c$ at roughly 25 and at 300 K. The spectra in (b), (c) and (d) are adjusted to each other in the range $180 \leq \Omega \leq 200$ cm^{-1} to emphasize the low energy evolution of the spectra with doping. The raw data in (a) indicate that even the overall intensity of the spectra is doping independent. For details see the text.

below $\Omega \leq 250\,\mathrm{cm}^{-1}$. Shown are raw data emphasizing that the intensity as well as the spectral shape is doping independent for $T \to T_c$. At $\Omega = 250\,\mathrm{cm}^{-1}$ the electronic continuum has a maximal intensity of roughly $0.5\,\mathrm{counts\,s^{-1}mW^{-1}}$, which is one order of magnitude less than for cuprates. The variations in the response as a function of doping for $\Omega \leq 25\,\mathrm{cm}^{-1}$ are due to accumulating surface layers and, as a result, an insufficient suppression of elastically scattered light. At 300 K [Fig. 6.1(c)], the A_{1g} spectra of samples UD23 ($x = 0.055$), OPT24 ($x = 0.061$) and OD22 ($x = 0.085$) are adjusted to that of sample UD18 ($x = 0.051$) by constant scaling factors of 0.87, 1.04 and 0.82, respectively. Doping independently the spectra vary linearly with Ω and exhibit a little smaller intensity around 250 cm^{-1} than at 25 K. These universal A_{1g} spectra at low and at high temperature indicate mainly doping independent properties of the carriers on the central hole bands in the normal state.

In contrast to the A_{1g} spectra, the B_{1g} spectra for $T \to T_c$ [Fig. 6.1(b)] show a pronounced doping dependence. The spectra of sample UD14 ($x = 0.045$), UD23, OPT24 and OD22 are adjusted to that of sample UD18 between 180 and 200 cm^{-1} by constant scaling factors of 1.4, 0.9, 0.8 and 0.9, respectively. This emphasizes the evolution of the spectral shape with doping. The enhanced intensity around 185 cm^{-1} in the spectra of samples UD14 and UD18 is due to the A_{1g} phonon which is visible in B_{1g} symmetry due to the orthorhombic distortion of the lattice below T_{TO} (c.f. Sec. 5.1.2). The initial slope of the spectra varies non-monotonically with doping and is small for underdoped samples (UD14 and UD18), increases strongly towards optimal doping (UD23 and OPT24) and abruptly decreases for the overdoped sample (OD22). Here, especially the strong doping evolution of the spectra between the optimally doped sample OPT24 and the overdoped sample OD22 is remarkable. For these two doping levels, T_c differs by only 2 K with $T_c = 24$ and 22 K for sample OPT24 and OD22, respectively. Nevertheless, the normalized initial slope is remarkably reduced for sample OD22. This occurs although neither sample OPT24 nor OD22 exhibits a transition to a magnetically ordered state at low temperature. Thus, the possibility that the changes in the spectra are related to the onset of magnetic order can be excluded for $x \geq 0.061$. At 300 K [Fig. 6.1(d)] the spectra of sample UD23, OPT24 and OD22 are adjusted to that of sample UD18 by constant scaling factors of 1.35, 1.35 and 1, respectively. Here, the spectra are independent of the actual doping level.
These symmetry and temperature dependent variations in the spectra are observed for at least two different samples at each doping level. Additionally, the differences between the A_{1g} and B_{1g} spectra are observed with the spectra in both symmetries measured on the same sample spot and within a short time period. Therefore, extrinsic reasons such as inhomogeneities of the sample can be excluded.

In the following, the temperature dependence of the spectra at a fixed doping level will be studied. Fig. 6.2 displays the spectra at different temperatures in A_{1g} [6.2(a) - (e)], B_{1g} [6.2(f) - (j)] and B_{2g} symmetry [6.2(k) - (o)] for $0.045 \leq x \leq 0.085$. The doping and temperature evolution of the phonons is in agreement with published data and analyzed elsewhere [172, 215]. The B_{2g} spectra at optimal doping, where most data are collected, have very low spectral intensity and increase approximately linearly with Ω. At 300 cm^{-1} the intensity is still below 0.5 counts $s^{-1}mW^{-1}$ at low temperature and decreases further with increasing temperature. A similarly small intensity and weak temperature dependence is observed for all other doping levels. The low intensity of the B_{2g} spectra can be explained with the B_{2g} Raman vertex which projects regions

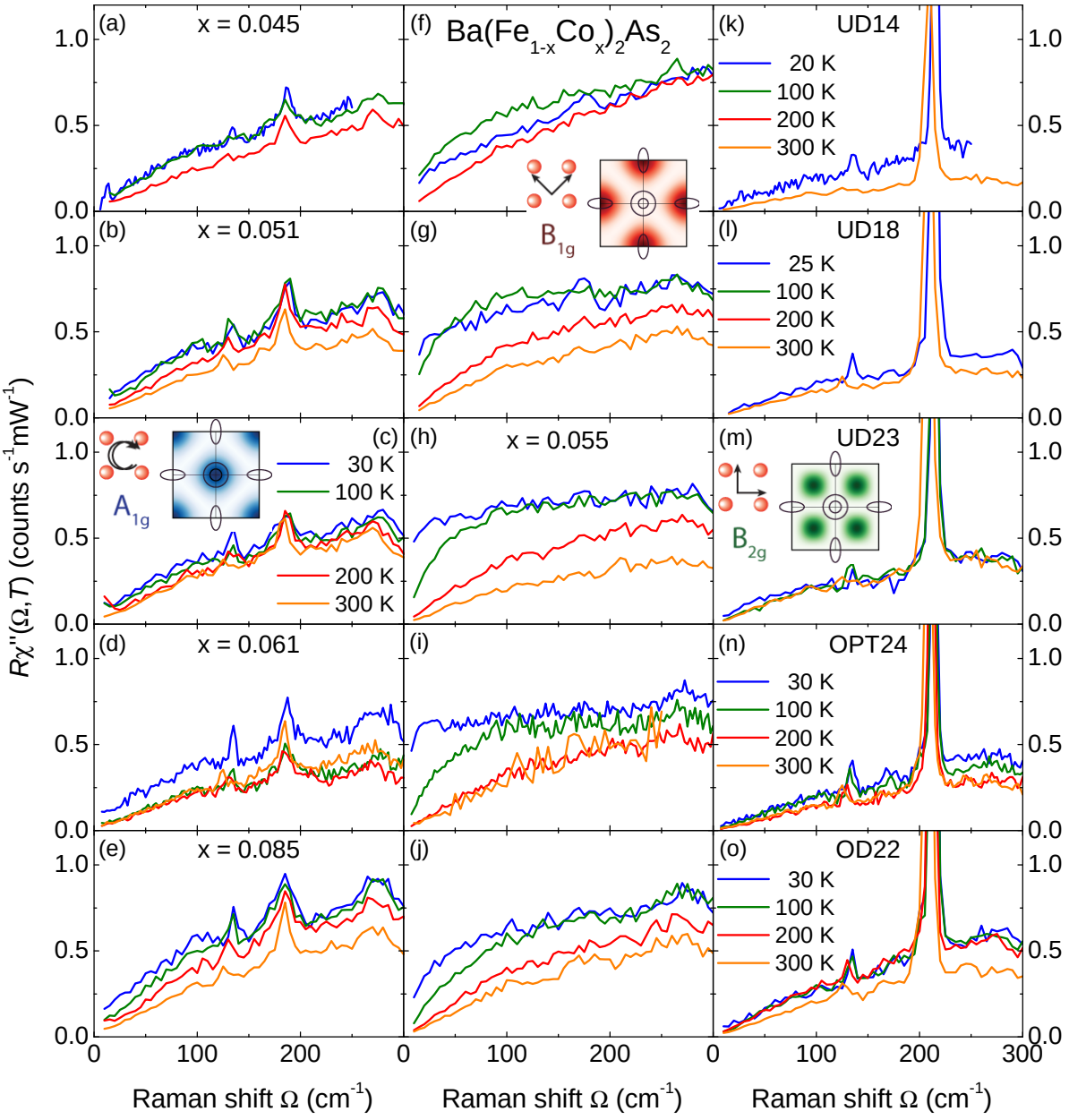

Figure 6.2: Temperature dependent Raman spectra of $Ba(Fe_{1-x}Co_x)_2As_2$ for different doping levels as indicated. (a)-(e) A_{1g}, (f)-(j) B_{1g} and (k)-(o) B_{2g} symmetry. The sample temperature in the spot position is indicated once per line.

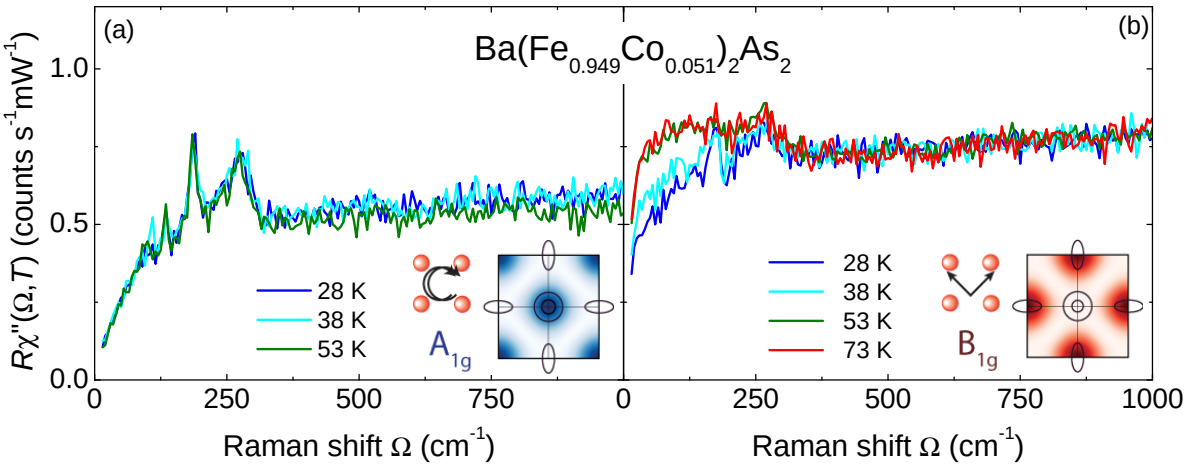

Figure 6.3: Temperature dependent Raman response of sample UD18 with $T_{\mathrm{SDW}} = 37$ K and $T_{\mathrm{TO}} = 52$ K. (a) The A_{1g} spectra are temperature independent while (b) the B_{1g} spectra lose spectral weight below 250 cm^{-1} for $T < 53$ K.

of the BZ where no bands cross E_F (see Sec. 3.4). The A_{1g} spectra, where mainly the hole bands are probed, exhibit more intensity than the B_{2g} spectra and exceed 0.5 counts $\mathrm{s}^{-1}\mathrm{mW}^{-1}$ for low temperature around 300 cm^{-1} [Fig. 6.2(a)-(e)]. At optimal doping [Fig. 6.2(d)] the spectra lie on top of each other for $T \geq 100$ K. The strongest variation in the spectra is due to phonons. At 30 K, the intensity abruptly increases by approximately 20% while the overall shape is preserved. The same is observed for the 50 K spectrum (not shown here). The spectra at the other doping levels exhibit a similar shape but there is a stronger and more continuous evolution of the spectra as a function of temperature on the overdoped side [Fig. 6.2(e)]. For underdoped samples [Fig. 6.2(a)-(c)] the temperature dependence of the spectra is weak.

The B_{1g} spectra are shown in Fig. 6.2(f) - (j). The spectra have a similar energy dependence as those in B_{2g} symmetry for $200 \leq T \leq 300$ K but exhibit a little more intensity. For lower temperatures the response changes drastically: at optimal doping [Fig. 6.2(i)] the intensity grows little around 300 cm^{-1}, while for $\Omega \leq 100\,\mathrm{cm}^{-1}$ it increases remarkably leading to a much steeper initial slope of the spectra at lower temperature. The 30 K spectrum is measured down to $\Omega = 7.5\,\mathrm{cm}^{-1}$ and is nearly constant over the entire energy range down to 10 cm^{-1}. The decrease in intensity for $\Omega \to 0$, expected from the antisymmetry of $\chi''(\Omega)$, is seen just for the lowest measured energy. This causes a very steep initial slope of the 30 K spectrum. A similar trend with temperature is observed for the slightly underdoped sample UD23 [Fig. 6.2(h)]. For the overdoped sample OD22 [Fig. 6.2(j)] the initial slope of the spectra increases also monotonically with decreasing temperature but the change of the spectral shape is less

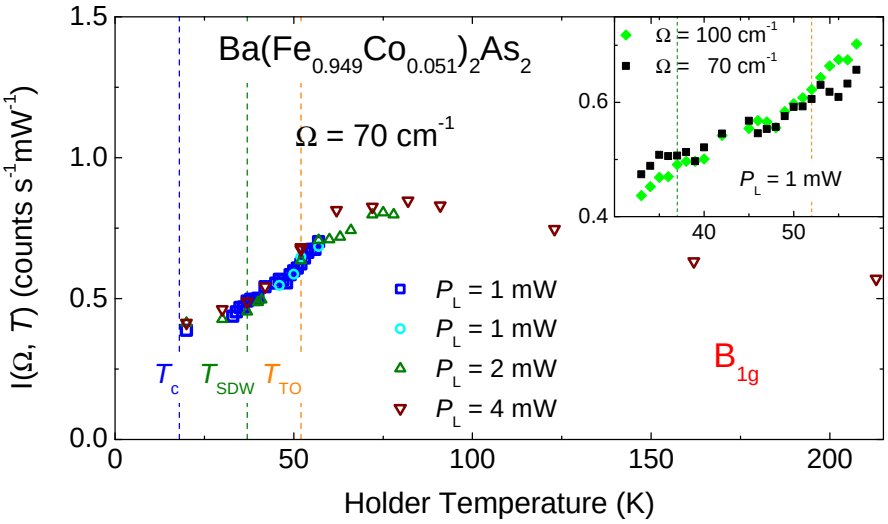

Figure 6.4: Temperature evolution of the B_{1g} Raman intensity of the underdoped sample UD18 at $\Omega = 70$ cm^{-1}. The data is measured with the absorbed laser power indicated and a spectral resolution of $\Delta\Omega = 50$ cm^{-1}. The indicated temperature is the temperature of the sample holder. The inset shows a zoom into the data around T_{SDW} and T_{TO}. The data points are taken at 70 cm^{-1} (black) and 100 cm^{-1} (green) and measured with 1 mW absorbed laser power.

pronounced. Here, the overall temperature dependence of the B_{1g} spectra is similar to the A_{1g} spectra [Fig. 6.2(e)]. For underdoped samples UD14 and UD18 [Fig. 6.2(f) and 6.2(g), respectively], the initial slope changes lesser with temperature. In addition, the spectra have an energy range where the intensity for $T \to T_{\mathrm{c}}$ is lower than the intensity at $T = 100$ K.

This anomalous temperature dependence of the spectra of underdoped samples is illustrated in more detail in Fig. 6.3 which presents the A_{1g} and B_{1g} spectra of sample UD18 for temperatures around $T_{\mathrm{SDW}} = 37$ K and $T_{\mathrm{TO}} = 52$ K. While the A_{1g} response is temperature independent in the range $28 \leq T \leq 73$ K [Fig. 6.3(a)], the B_{1g} spectra suffer a loss of spectral weight for $T < 53$ K and $\Omega \leq 250$ cm^{-1} [Fig. 6.3(b)]. In contrast to the undoped sample Ba122, the loss of low energy spectral weight sets in less abruptly and no enhanced intensity at higher energy is observed. In addition, the spectral intensity is already reduced at $T > T_{\mathrm{TO}} > T_{\mathrm{SDW}}$.

For the further investigation of the temperature evolution of the spectra close to T_{SDW} and T_{TO}, the Raman intensity $I(\Omega, T)$ at $\Omega = 70$ and 100 cm^{-1} is measured with a spectral resolution of $\Delta\Omega = 50$ cm^{-1} on a second sample. Fig. 6.4 presents $I(70\ \mathrm{cm}^{-1}, T)$ measured with different absorbed laser powers. The presented data are not divided by the Bose factor and the temperature increase due to the absorbed laser power is not taken

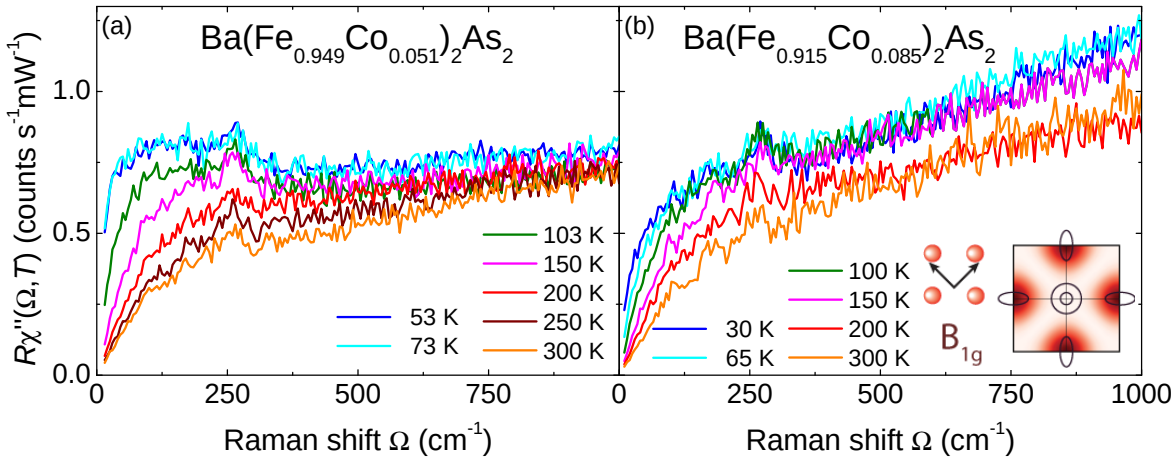

Figure 6.5: Temperature dependent Raman response in B_{1g} symmetry for (a) underdoped (UD18, $x = 0.051$) and (b) overdoped $Ba(Fe_{1-x}Co_x)_2As_2$ (OD22, $x = 0.085$). Only the low energy response of sample UD18 increases for decreasing temperature down to 70 K leading to a clear change of the spectral shape with doping. The spectra of sample OD22 increase in the entire energy range with only little variation in the spectral shape.

into account. Rather, the temperature of the sample holder is indicated. $I(70\ \mathrm{cm}^{-1}, T)$ saturates for $50 \leq T \leq 70$ K clearly above T_{TO} in agreement with the data presented in Fig. 6.3(b). For lower temperature $I(70\ \mathrm{cm}^{-1}, T)$ decreases roughly linearly down to $T = 40$ K. Around T_{SDW}, $I(\Omega, T)$ is constant and decreases again for $T \leq 35$ K as shown in detail in the inset of Fig. 6.4 where the spectra measured at $\Omega = 70$ and $100\ \mathrm{cm}^{-1}$, both measured with 1 mW absorbed laser power, are compared. For $20 \leq T \leq 30$ K, $I(70\ \mathrm{cm}^{-1}, T)$ and $I(100\ \mathrm{cm}^{-1}, T)$ saturate.

The B_{1g} response of sample UD18 for $T \geq 53\ \mathrm{K} > T_{\mathrm{TO}} > T_{\mathrm{SDW}}$ is displayed in Fig. 6.5(a) in small temperature steps. In this temperature range the spectral shape changes strongly with temperature due to the continuous increase of the low energy response with decreasing temperature. For $T \leq 150$ K the spectra have enhanced intensity below $300\ \mathrm{cm}^{-1}$ while for $\Omega > 300\ \mathrm{cm}^{-1}$ the spectra are nearly constant. This is similar to the spectra of sample Ba122 but the low energy peak is a less pronounced [see Fig. 5.5(b)]. For comparison Fig. 6.5(b) shows the B_{1g} spectra of the overdoped sample OD22 above T_c in small temperature steps. This sample shows neither a structural nor a magnetic transition. In contrast to the response of sample UD18 [Fig. 6.5(a)], the spectral intensity increases with decreasing temperature in the entire energy range exhibiting a temperature independent linear energy dependence for $\Omega \geq 400\ \mathrm{cm}^{-1}$.

6.2 Anisotropic carrier properties in the normal state

For a quantitative description of the carrier dynamics as a function of temperature and doping, the Raman spectra (Fig. 6.2) are analyzed using a memory function analysis. This analysis has been introduced in Sec. 3.5. For the analysis solely the response from the electronic continuum is relevant. Hence, the phononic contribution to the response needs to be subtracted from the spectra (c.f. Sec. 4.2.7). Since this is not a straightforward procedure due to the temperature dependence of some phonons, there may occur sharp features in the derived spectra of the mass enhancement factors and relaxation rates. For small Ω the quality of the derived spectra may be reduced due to the low intensity of the Raman spectra at small Ω. This low energy response is strongly weighted in the Kramers-Kronig analysis. Nevertheless, a good quantitative description of the Raman spectra is possible via this analysis. The reliability of the analysis is demonstrated by the comparison of the Raman scattering rates, as obtained from the Raman spectra, and the measured dc resistivity.

6.2.1 Dynamic Raman relaxation rates and mass renormalization

The dynamic Raman mass enhancement factors $1 + \lambda^{\mu}(\Omega, T)$, $\mu = \mathrm{A_{1g}}, \mathrm{B_{1g}}$, for samples UD18, OPT24 and OD22, representative for the underdoped, optimally and overdoped range, respectively, are displayed as a function of temperature in Fig. 6.6. For large energies, $1 + \lambda^{\mu}(\Omega, T)$ approaches values between 1 and 2. Thus, $\lambda^{\mu}(\Omega, T) > 0$ holds as expected since interactions enhance the band mass of the carriers. Toward lower energy $1 + \lambda^{\mu}(\Omega, T)$ increases roughly linearly and is independent of temperature for $\Omega > 300$ cm^{-1}. Only for $\Omega \leq 250$ cm^{-1} $1 + \lambda^{\mu}(\Omega, T)$ exhibits a temperature dependence. In this energy range $1 + \lambda^{\mathrm{A1g}}(\Omega, T)$ increases continuously with decreasing Ω having generally steeper slopes at lower temperatures. In contrast, $1 + \lambda^{\mathrm{B1g}}(\Omega, T)$ varies non-monotonically with decreasing Ω and displays a maximum around 150 cm^{-1} for $T \geq 200$ K [(d)-(f)]. For lower temperatures the maximum disappears and $1 + \lambda^{\mathrm{B1g}}(\Omega, T)$ increases monotonously with decreasing Ω. In the static limit, $1 + \lambda^{\mu}(\Omega, T)$ reaches values between 3 and 6 with larger values for lower temperatures, which is usually attributed to correlation effects, and is in good agreement to published data from optical studies [216]. The divergence for $T \geq 200$ K is most likely an artifact due to the reduced data

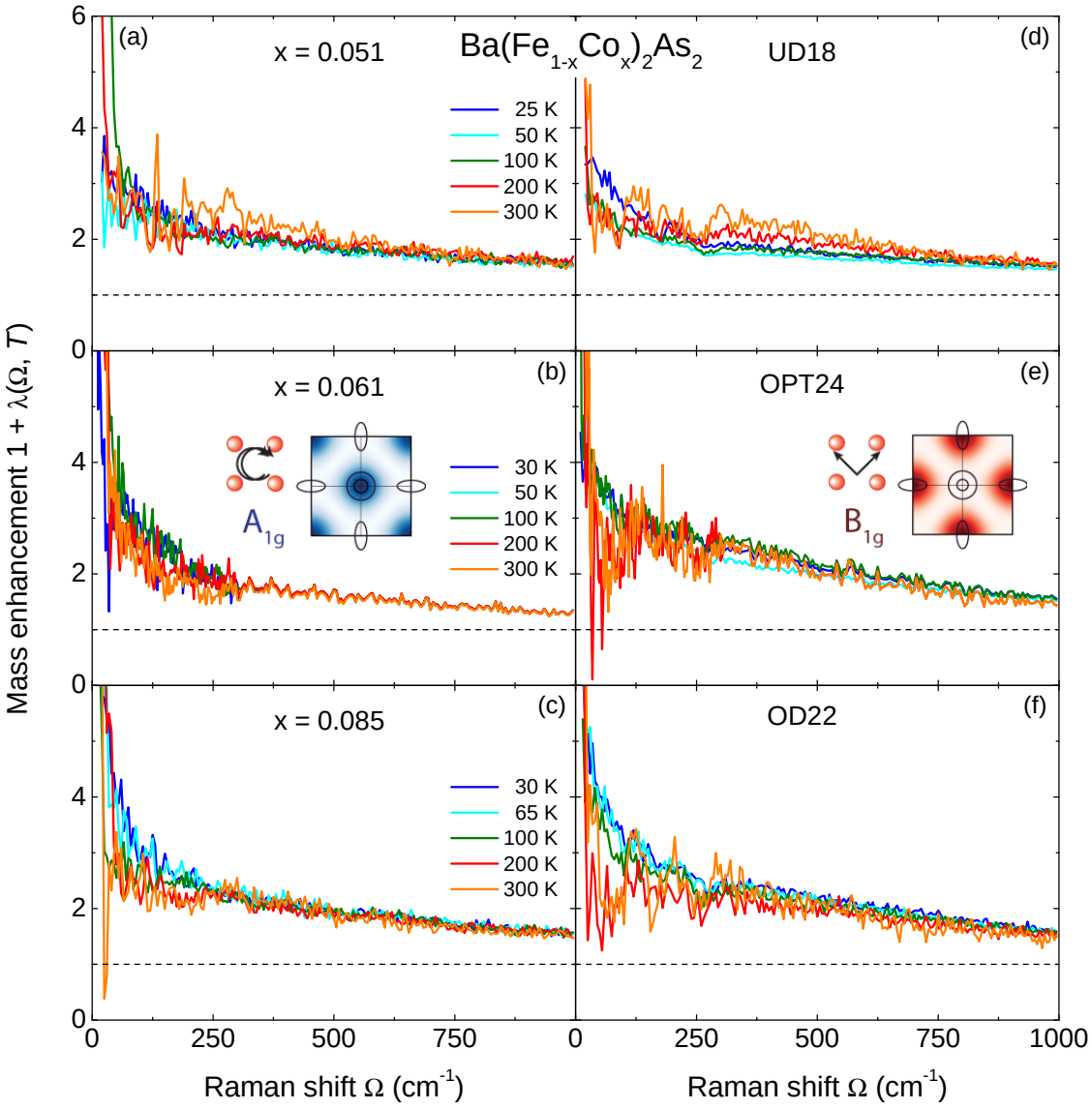

Figure 6.6: Dynamic Raman mass enhancement factors in A_{1g} and B_{1g} symmetry for underdoped [(a), (d)], optimal [(b), (e)] and overdoped [(c), (f)] $Ba(Fe_{1-x}Co_x)_2As_2$. The Raman spectrum for the calculation of the data in (b) and (e) is measured at only one temperature above 300 cm^{-1}. Hence, there is only a weak temperature dependence of the data in this energy range.

quality for $\Omega \to 0$.

The temperature dependent dynamic Raman relaxation rates $\Gamma^{\mu}(\Omega, T)$ in A_{1g} and B_{1g} symmetry are displayed in Figs. 6.7(a)-(c) and 6.7(d)-(f), respectively. As expected from the Raman spectra, $\Gamma^{A1g}(\Omega, T)$ exhibits a much weaker temperature dependence than $\Gamma^{B1g}(\Omega, T)$. For samples UD18 and OPT24 $\Gamma^{A1g}(\Omega, T) \propto \Omega$ holds in almost the entire energy range and for all temperatures [Fig. 6.7(a) and 6.7(b), respec-

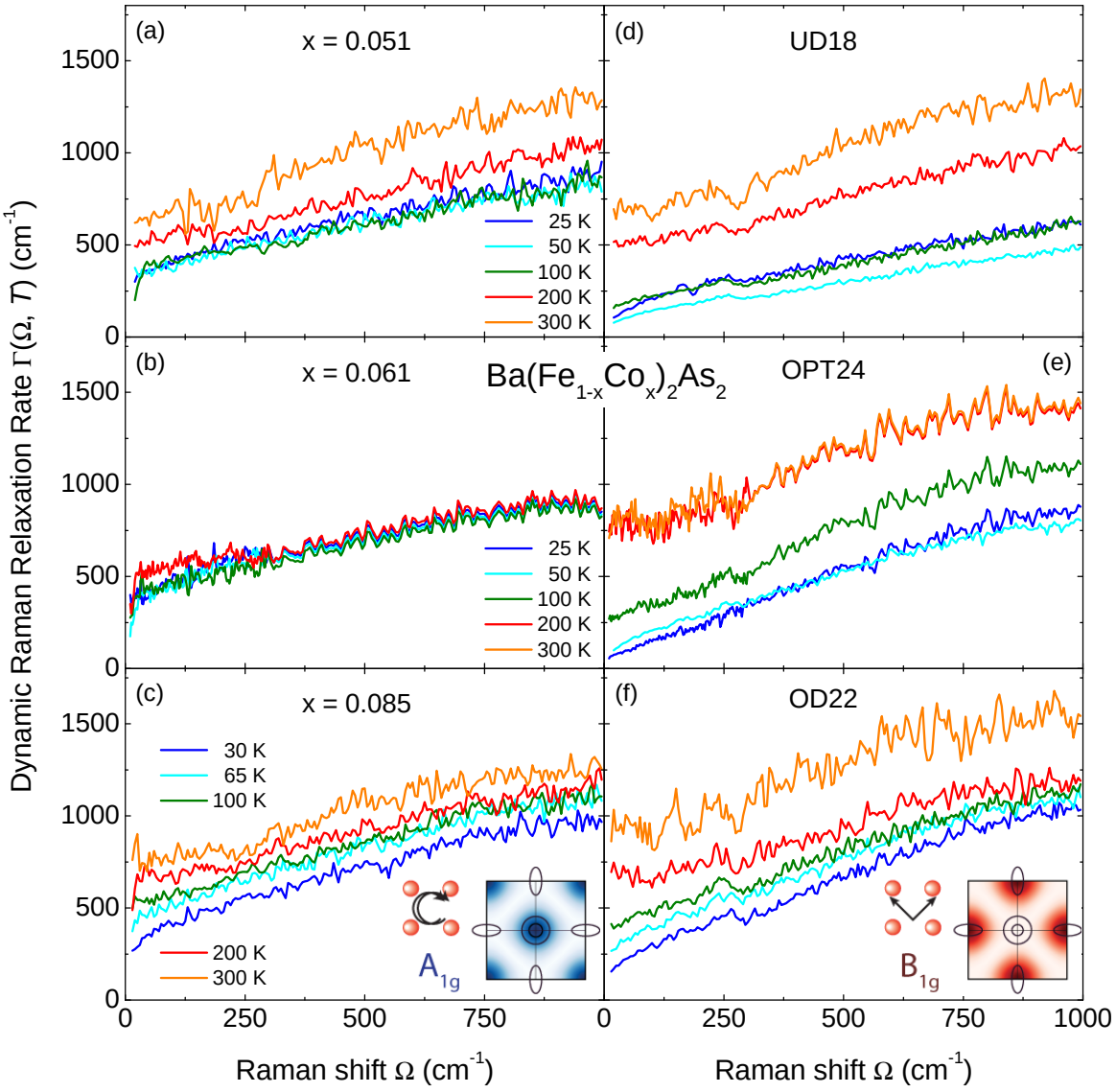

Figure 6.7: Dynamic Raman relaxation rates in A_{1g} and B_{1g} symmetry for underdoped [(a), (d)], optimal [(b), (e)] and overdoped [(c), (f)] $Ba(Fe_{1-x}Co_x)_2As_2$. The Raman spectrum for the calculation of the data in (b) and (e) is measured at only one temperature above 300 cm^{-1}. Hence, there is only a weak temperature dependence of the data in this energy range.

tively]. The overdoped sample OD22 displays deviations from this frequency dependence and $\Gamma^{A1g}(\Omega, T) \propto \Omega$ holds only for $\Omega \geq 250$ cm^{-1}. Below 250 cm^{-1}, $\Gamma^{A1g}(\Omega, T)$ tends to saturate for $T \geq 100$ K [Fig. 6.7(c)]. At lower temperatures the rates continue to decrease linearly with frequency. $\Gamma^{B1g}(\Omega, T) \propto \Omega$ holds below 250 cm^{-1} and $\Gamma^{B1g}(\Omega, T)$ tends to saturate for smaller Ω for all doping levels and $T \geq 200$ K. For $T < 100$ K, $\Gamma^{B1g}(\Omega, T)$ is linear over the entire energy range. The non-monotonic temperature de-

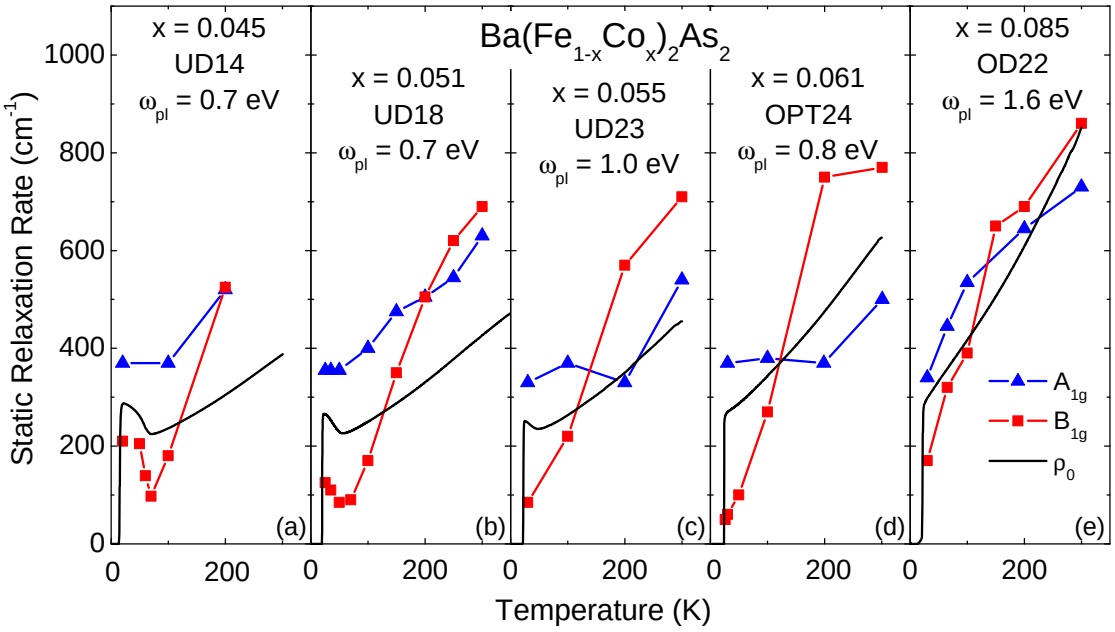

Figure 6.8: Temperature dependent static Raman relaxation rates of $Ba(Fe_{1-x}Co_x)_2As_2$ for different doping levels in A_{1g} (blue triangles) and B_{1g} symmetry (red squares). The solid black lines denote the dc resistivity measured on similar crystals. The plasma frequency ω_{pl} for the conversion of the resistivity data into units of wavenumbers is indicated in each panel.

pendence of $\Gamma(\Omega, T \leq 100\ \mathrm{K})$ is a consequence of the reduced low energy spectral weight at the lowest temperature as will be discussed in Sec. 6.5.1.

6.2.2 Static Raman relaxation rates

Fig. 6.8 displays the relaxation rates in the static limit $\Omega \to 0$, $\Gamma_0^{\mu}(T)$, as a function of temperature for different doping levels. Also shown are the relaxation rates $\Gamma_0^{\rho}(T)$ derived via Eq. (3.36) from the dc resistivity $\rho(T)$, which is measured on similar crystals. The plasma frequency ω_{pl}, as indicated in the figure, is a fitting parameter here and chosen to be temperature independent. It is taken to satisfy

$$\Gamma_0^{\rho}(T \to T_c) \approx \frac{1}{2}\left[\Gamma_0^{\mathrm{A1g}}(T \to T_c) + \Gamma_0^{\mathrm{B1g}}(T \to T_c)\right] \tag{6.1}$$

holds. ω_{pl} is of the same order of magnitude as the plasma frequency obtained from optical spectroscopy studies [21, 183, 217].

The temperature evolution of $\Gamma_0^{\mu}(T)$ depends strongly on the doping level. For the overdoped sample [Fig. 6.8(e)], $\Gamma_0^{\mu}(T)$ exhibits roughly a linear temperature dependence

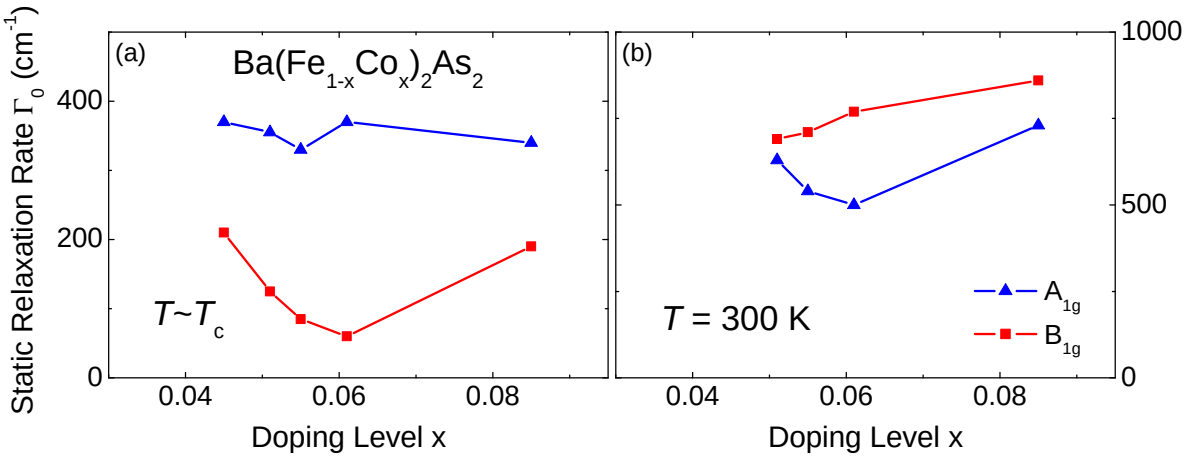

Figure 6.9: Doping dependent Raman relaxation rates of $Ba(Fe_{1-x}Co_x)_2As_2$ in A_{1g} and B_{1g} symmetry at fixed temperatures. (a) For $T \to T_c$ the A_{1g} rates are constant and the B_{1g} rates exhibit a minimum at optimal doping. (b) For $T = 300$ K the A_{1g} rates exhibit a minimum at optimal doping and the B_{1g} rates continuously increase with doping.

in both symmetries. This holds also true for $\Gamma_0^{\rho}(T)$. Hence, for sample OD22 $\Gamma_0^{A1g}(T)$ and $\Gamma_0^{B1g}(T)$ are similar and in good agreement to $\Gamma_0^{\rho}(T)$. This is different at and near optimal doping [Fig. 6.8(d) and (c), respectively]. Here, $\Gamma_0^{\mathrm{A1g}}(T)$ is constant up to roughly 200 K before it increases for higher temperatures while $\Gamma_0^{B1g}(T)$ increases monotonically with temperature exhibiting an almost linear temperature dependence. At optimal doping [Fig. 6.8(d)] $\Gamma_0^{\rho}(T)$ is roughly the average of $\Gamma_0^{\mathrm{A1g}}(T)$ and $\Gamma_0^{\mathrm{B1g}}(T)$. $\Gamma_0^{\mathrm{B1g}}(T)$ varies by an order of magnitude between low and and high temperature exhibiting values of $\Gamma_0^{\mathrm{B1g}}(30\ \mathrm{K}) = 30\ \mathrm{cm}^{-1}$ and $\Gamma_0^{\mathrm{B1g}}(300\ \mathrm{K}) = 770\ \mathrm{cm}^{-1}$, respectively. The small value of $\Gamma_0^{\mathrm{B1g}}(T)$ close to T_c and the strong temperature dependence indicate that the electrons scatter dynamically from still to be identified excitation rather than from impurities. Hence, it argues for the excellent quality of the investigated sample. For underdoped samples [Fig. 6.8(a) and 6.8(b), respectively] the dichotomy between $\Gamma_0^{\mathrm{A1g}}(T)$ and $\Gamma_0^{\mathrm{B1g}}(T)$ grows further. At lower temperature $\Gamma_0^{\mathrm{B1g}}(T)$ of both underdoped samples exhibits a minimum around $T = 70$ and 50 K, respectively. A similar minimum as a function of temperature is observed in transport measurements [black solid lines in Fig. 6.8] on underdoped $Ba(Fe_{1-x}Co_x)_2As_2$ [7] and is associated with the magnetic/structural transition. Via Raman spectroscopy this anomaly is found only in B_{1g} symmetry (electron bands), while the rates in A_{1g} symmetry (hole bands) exhibit constant rates in this temperature regime as investigated in detail for sample UD18 [Fig. 6.8(b)].

The anisotropy of the carrier properties in A_{1g} and B_{1g} symmetry is an interesting similarity of the cuprates and FeSCs. However, for the cuprates, antinodal (B_{1g} sym-

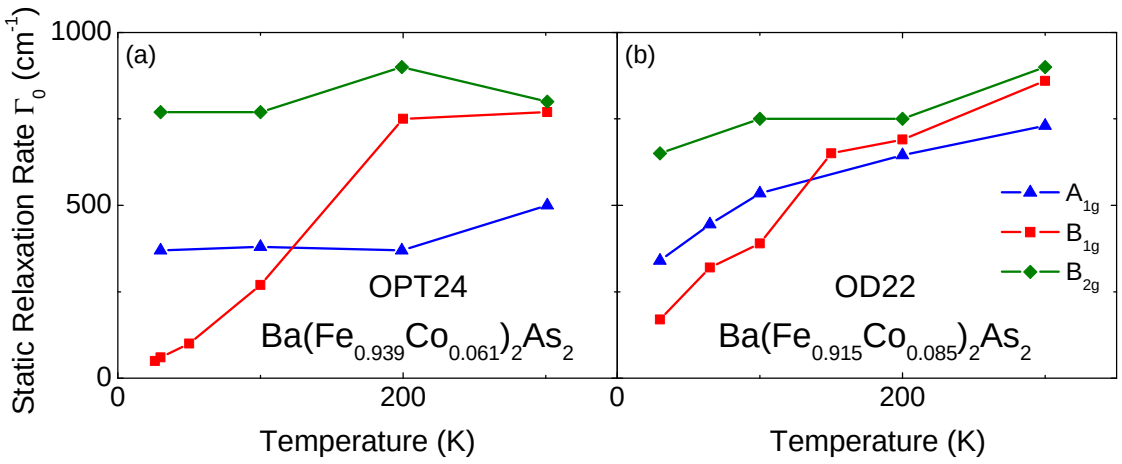

Figure 6.10: Raman relaxation rates in A_{1g} (blue triangles), B_{1g} (red squares) and B_{2g} symmetry (green diamonds) for (a) optimally and (b) overdoped $Ba(Fe_{1-x}Co_x)_2As_2$.

metry) and nodal quasiparticles (B_{2g} symmetry) are probed separately [135], while for the FeSCs the hole bands (A_{1g} symmetry) and the electron bands (B_{1g} symmetry) are probed separately. In both cases there is a dichotomy of the relaxation rates for low doping levels near the magnetically ordered state while for higher doping levels, where the materials become more conventional, the dichotomy is lifted and the carrier properties are more or less isotropic [27, 167]. Thus, both, the cuprates and the FeSCs show their Janus face in Raman scattering experiments [218] exhibiting doping dependent strongly anisotropic relaxation rates.

Fig. 6.9 presents the doping evolution of $\Gamma_0^{\mu}(T)$ at low and for high temperature. Just above T_c, $\Gamma_0^{\mathrm{A1g}}(T \to T_c)$ is doping independent with values between 350 and 400 cm^{-1}. $\Gamma_0^{\mathrm{B1g}}(T \to T_c)$ is substantially smaller and shows a non-monotonic variation with doping exhibiting a minimum right at optimal doping [Fig. 6.9(a)]. The monotonic doping dependence of $\Gamma_0^{\mathrm{A1g}}(T \to T_c)$ and the non-monotonic doping dependence of $\Gamma_0^{\mathrm{B1g}}(T \to T_c)$ are direct consequences of the Raman spectra displayed in Fig. 6.1(a) and 6.1(b) where it is shown that the A_{1g} response is doping independent while the B_{1g} response exhibits a doping dependent variation of the low energy response close to T_c. At 300 K [Fig. 6.9(b)], the trend is reversed. Here, the B_{1g} rates are larger than the A_{1g} rates. Additionally, $\Gamma_0^{\mathrm{A1g}}(300\ \mathrm{K})$ varies non-monotonically exhibiting a minimum close to 500 cm^{-1} at optimal doping, while $\Gamma_0^{\mathrm{B1g}}(300\ \mathrm{K})$ increases monotonically with doping from 700 to 800 cm^{-1}. This is not directly clear from Fig. 6.1(c) and 6.1(d), respectively, but results from the variation of the Raman intensity at higher Ω.

Fig. 6.10 shows the temperature dependent relaxation rates of samples OPT24 and

OD22 in A_{1g}, B_{1g} and B_{2g} symmetry. At 300 K the B_{1g} and B_{2g} rates of both samples exhibit values exceeding 800 cm^{-1}. As expected from the spectra shown in Fig. 6.2(n) and 6.2(o), $\Gamma_0^{B2g}(T)$ of OPT24 exhibits only a weak temperature dependence [Fig. 6.10(a)] while the temperature dependence of $\Gamma_0^{B2g}(T)$ of OD22 is slightly stronger [Fig. 6.10(b)]. The same holds for $\Gamma_0^{A1g}(T)$: while $\Gamma_0^{A1g}(T)$ of OPT24 is nearly constant, the temperature dependence of $\Gamma_0^{A1g}(T)$ of OD22 is similar to $\Gamma_0^{B1g}(T)$. This suggests that the electronic properties become more isotropic with increasing doping level.

6.2.3 Comparison to transport

Finally, the relation of the static Raman relaxation rates to the resistivity as a function of doping at a fixed temperature is studied. Fig. 6.11 displays the doping evolution of the resistivity at $T = 25$, 100 and 200 K, normalized to the corresponding value at 300 K, $\rho(T)/\rho(300\text{ K})$, to avoid uncertainties in the geometric factor [219]. For comparison, the doping evolution of $\Gamma_0^{\mu}(T)/\Gamma_0^{\mu}(300\text{ K})$ with $\mu = A_{1g}, B_{1g}$ for similar temperatures is shown. The average of the A_{1g} and B_{1g} relaxation rates, as suggested by Matthiessen's rule in the presence of distinct $\mathbf{k}$ independent scattering mechanisms [220], normalized to their room-temperature values,

$$\gamma_0^{av}(T) = \frac{\Gamma_0(T)}{\Gamma_0(300\text{ K})} = \frac{1}{2}\left[\frac{\Gamma_0^{A1g}(T)}{\Gamma_0^{A1g}(300\text{ K})} + \frac{\Gamma_0^{B1g}(T)}{\Gamma_0^{B1g}(300\text{ K})}\right] \tag{6.2}$$

is shown by the orange symbols. The presented data are independent of fitting parameters, in particular, of the plasma frequency.

Fig. 6.11(c) shows that $\Gamma_0^{\mu}(200\text{ K})/\Gamma_0^{\mu}(300\text{ K})$ varies little and non-monotonically as a function of doping and is close to $\rho(200\text{ K})/\rho(300\text{ K})$. Hence, $\gamma_0^{av}(200\text{ K})$ is comparable to $\rho(200\text{ K})/\rho(300\text{ K})$ for all doping levels. This holds also true at 100 K [Fig. 6.11(b)] although $\Gamma_0^{\mu}(100\text{ K})/\Gamma_0^{\mu}(300\text{ K})$ increase monotonically with doping and $\gamma_0^{av}(100\text{ K})$ deviates from $\rho(100\text{ K})/\rho(300\text{ K})$ especially at low doping. For $T \to T_c$ [Fig. 6.11(a)], where $T < T_{SDW}$ for underdoped samples, $\Gamma_0^{B1g}(T \to T_c)/\Gamma_0^{B1g}(300\text{ K})$ is remarkably smaller than $\rho(25\text{ K})/\rho(300\text{ K})$ in the entire doping range and exhibits a minimum at optimal doping while $\Gamma_0^{A1g}(T \to T_c)/\Gamma_0^{A1g}(300\text{ K})$ is larger than $\rho(25\text{ K})/\rho(300\text{ K})$ and is maximal at optimal doping. Both effects compensate each other for $x \geq 0.061$ and the absolute values of $\gamma_0^{av}(T \to T_c)$ are in good agreement to $\rho(25\text{ K})/\rho(300\text{ K})$ for both doping levels. For $x < 0.061$, the doping evolution of $\rho(25\text{ K})/\rho(300\text{ K})$ is better mimicked by $\Gamma_0^{B1g}(T \to T_c)/\Gamma_0^{B1g}(300\text{ K})$ although the latter exhibits much smaller values.

This demonstrates that the relaxation rates obtained from the Raman spectra are,

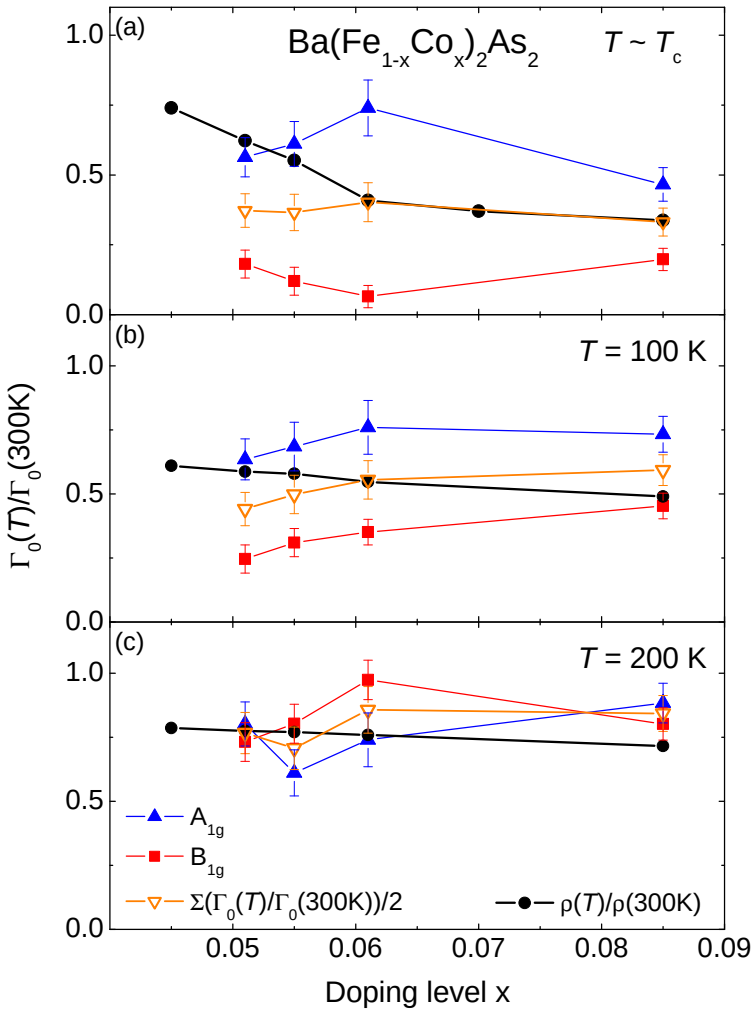

Figure 6.11: Doping evolution of the Raman relaxation rates and in-plane resistivity of twinned $Ba(Fe_{1-x}Co_x)_2As_2$ single crystals at (a) 25 K (b) 100 K and (c) 200 K. The quantities are normalized to their 300 K value. The A_{1g}, B_{1g} rates are shown by blue and red symbols, respectively, and the transport data are indicated by black symbols. The orange symbols indicate the average of the rates in A_{1g} and B_{1g} symmetry. Resistivity data from [7] and [219].

apart from the low doping low temperature regime, in good agreement to the relaxation rates obtained from resistivity measurement. The difference of $\gamma_0^{\mathrm{av}}(T \rightarrow T_c)$ and $\rho(25\,\mathrm{K})/\rho(300\,\mathrm{K})$ in the low doping regime could be explained by the strongly anisotropic mobilities and effective masses of the electron and hole bands [23, 115, 221, 222] and the strong mass enhancement toward low doping [223] reported by quantum oscillation (QO) experiments. This may stronger weight the carriers seen via the B_{1g} Raman response in transport measurements. Alternatively, this could be consistent with the observation that the hole contribution to transport is only relevant at high tempera-

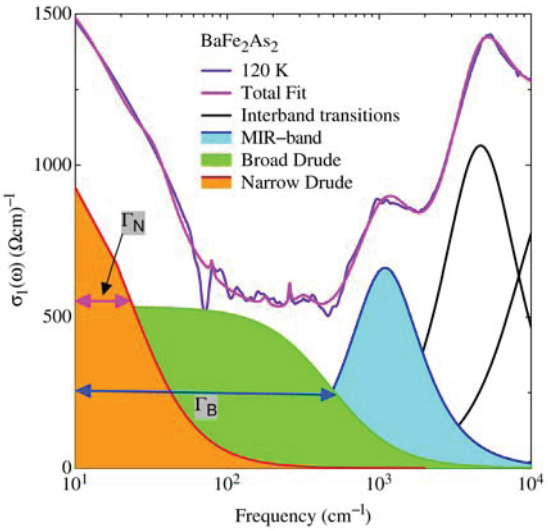

Figure 6.12: Decomposition of the optical conductivity of $BaFe_2As_2$ into a narrow (Γ_N) and a broad (Γ_B) Drude term. Together with some Lorentz terms at higher energy the total fit reproduces the optical spectrum in all detail. From [224].

ture for low doping [22]. Thus, for $x \geq 0.061$ holes and electrons contribute similarly to the transport for all temperatures. For $x < 0.061$ there is a reliable contribution from holes to transport only at high temperatures while at low temperatures the transport is dominated by the contribution of electrons.

6.3 Influence of the orbital character of the bands

Via ERS strongly band dependent carrier dynamics are observed (Fig. 6.8). This is compared to the results of other experimental and theoretical studies and the origin of the anisotropic carrier relaxation rates is discussed.

Carrier dynamics in optical spectroscopy

The analysis of optical reflectivity measurements on FeSCs [21, 183, 225] reveals that $\sigma'(\omega, T)$ can be well modeled within a Drude-Lorentz approach. Via this approach $\sigma'(\omega, T)$ for small ω is purely phenomenologically decomposed into two Drude responses as shown in Fig. 6.12: a narrow Drude term with a high conductivity and a small relaxation rate and a broad Drude term with a small conductivity and a large relaxation rate. Since optical spectroscopy measures a weakly weighted momentum average of the carrier dynamics over the whole BZ, one may assume that the optical spectrum can be decomposed into a sum of the A_{1g} and B_{1g} Raman spectra. In this approach the narrow

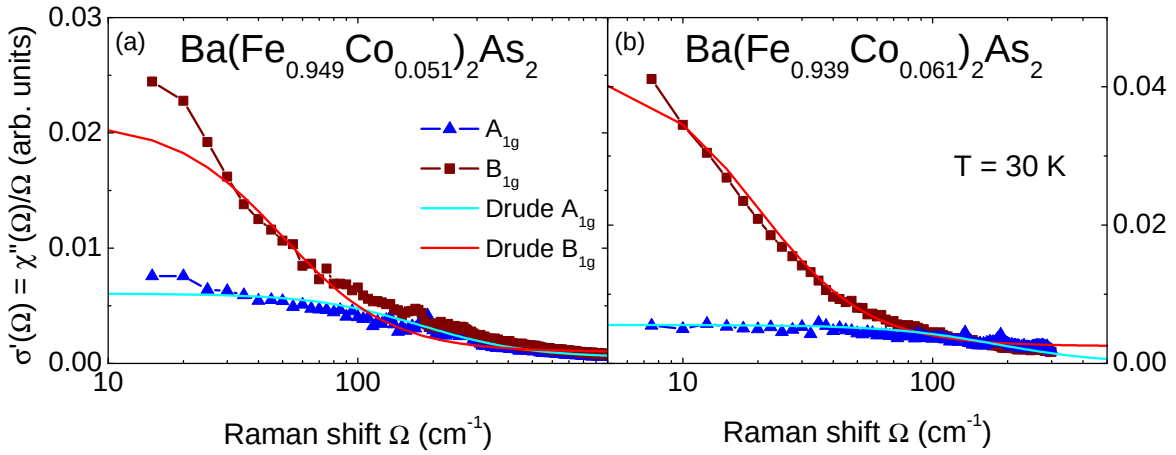

Figure 6.13: Real part of the Raman conductivity $\sigma'_\mu(\Omega)$ as a function of symmetry as calculated from the measured Raman response of $Ba(Fe_{1-x}Co_x)_2As_2$ via Eq. (6.3) (symbols) and Drude fit to the data (solid lines) for (a) $x = 0.051$ and (b) $x = 0.061$. The deviations from the Drude fit at low Ω come from an insufficient suppression of elastically scattered light. All data are recorded at 30 K.

Drude term of the optical spectrum corresponds to the B_{1g} Raman response where mainly the charge carriers on the electron bands are probed and low relaxation rates are found at low temperatures. On the other hand, the broad Drude term corresponds to the A_{1g} Raman response, where the carriers from the hole bands are mainly probed and relatively large relaxation rates at low temperature are found.

To investigate this idea, the real part of the conductivity $\sigma'(\Omega, T)$ is calculated from the measured Raman response in A_{1g} and B_{1g} symmetry via the Shastry-Shraiman relation [169, 170]

$$\chi''(\Omega, T) \propto \Omega \cdot \sigma'(\Omega, T). \tag{6.3}$$

The resulting Raman conductivities $\sigma'_\mu(\Omega, T)$ ($\mu = A_{1g}, B_{1g}$) with $T \to T_c$ of underdoped (UD18) and optimally doped $Ba(Fe_{1-x}Co_x)_2As_2$ (OPT24) are shown in Fig. 6.13(a) and 6.13(b), respectively, together with the corresponding Drude fits. While the results from optical measurements with a narrow and a broad Drude term can indeed be reproduced qualitatively, the analysis is impeded by the elastically scattered light, which sits on top of the Raman response for $\Omega \to 0$ and results in deviations of $\sigma'_\mu(\Omega)$ from the Drude fit at low energy. Nevertheless, the comparison of the Raman relaxation rates and the relaxation rates obtained in optical studies is possible.

In a study by Lucarelli *et al.* [21] the relaxation rates from the narrow, Γ_N, and broad Drude term, Γ_B, were explicitly derived as functions of temperature for different doping levels. The results of this analysis are shown in Fig. 6.14. Γ_N is a factor of 20 smaller

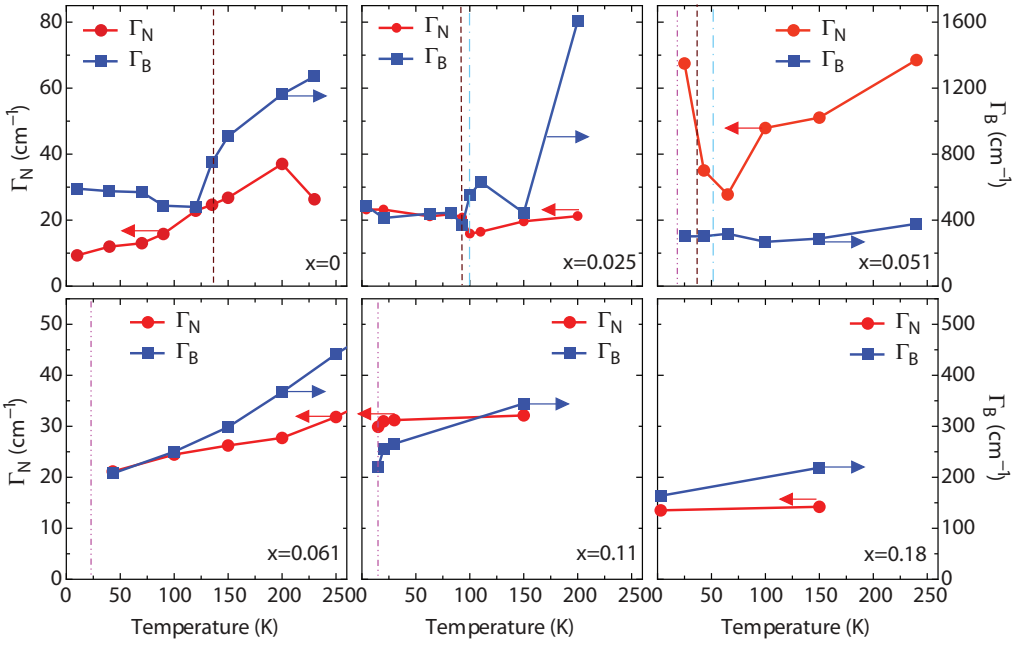

Figure 6.14: Temperature dependence of the scattering rates of the narrow (Γ_N) and broad (Γ_B) Drude terms obtained from optical spectroscopy. The dashed-dotted, dashed and dashed-dotted-dotted lines mark the structural, magnetic and superconducting transitions, respectively. From [21]

than Γ_B for underdoped samples while the anisotropy decreases with increasing doping level. For optimally doped and overdoped samples Γ_N is a factor of 10 smaller than Γ_B. Therefore, optical spectroscopy observes a similar anisotropy of the relaxation rates at low temperatures as Raman spectroscopy. However, there is a significant discrepancy in the temperature evolution. In Raman spectroscopy, $\Gamma_0^{\mathrm{A1g}}(T) > \Gamma_0^{\mathrm{B1g}}(T)$ holds only at low temperature, while at high temperature $\Gamma_0^{\mathrm{A1g}}(T)$ is smaller than $\Gamma_0^{\mathrm{B1g}}(T)$ for all doping levels [Fig. 6.9]. In addition, the anisotropy almost disappears on the overdoped side [Fig. 6.10(b)]. In the optical study Γ_N and Γ_B have a much weaker temperature dependence over the doping range studied, and the anisotropy is still as large as one order of magnitude for overdoped samples at high temperature.

Anisotropies in transport studies

In magneto-transport studies on $Ba(Fe_{1-x}Co_x)_2As_2$, the Hall coefficient is decomposed into one contribution from the electron and one from the hole bands and it was found that mainly the electrons contribute to the transport. The contribution of holes to transport is negligible at low temperature for most doping levels [22]. At higher doping levels the scattering rates extracted from the data are assigned to the electron bands

and the T^2 dependence of the rates $1/\tau$ is consistent with a Fermi liquid picture. In a magneto-transport study by Fang *et al.* [226] it was observed that the mobilities of the electrons are about six times larger than those of the holes above the magnetic transition of undoped $BaFe_2As_2$. With increasing doping, the mobilities of electrons and holes become comparable but are still larger for electrons than for holes. This supports a theoretical study where anisotropies of the charge carriers on the electron and hole bands were proposed for the FeSCs [69]. DFT calculations predict a factor of three difference in the Fermi velocities where that on the electron bands larger than that on the hole bands [69].

Anisotropies in quantum oscillation measurements

Different charge dynamics on the electron and hole bands are also reported from QO measurements. In measurements on '122' [23, 223] and '1111' FeSCs [221] the mass enhancement factors are strongly band dependent. Additionally, a pronounced de Haas-van Alphen signal is reported which is attributed to the electron bands. The mean free paths of the carriers is calculated to be longer on the electron bands than on the hole bands [222].

Anisotropic carrier lifetimes in ARPES

Via the analysis of ARPES data the carrier dynamics on the hole and electron bands can be investigated separately. Additionally, the selection rules of ARPES enable one to determine the orbital character of the bands [78, 227]. Although the details of the orbital characters of the bands differ slightly from theory (see Sec. 2.3), different carrier properties are found on the electron and hole bands. This originates from the anisotropy between the d_{xy} and d_{xz}/d_{yz} orbitals where the lifetimes on the d_{xy} are longer than those on the d_{xz}/d_{yz} orbitals [83]. The shorter lifetime of the d_{xz}/d_{yz} orbitals is attributed to a stronger interaction with spin fluctuations.

Anisotropic lifetimes in theoretical models

The ARPES results are in good agreement with an LDA calculation of Kemper *et al.* [86]. In this study the effect of the multiorbital character of the electron and hole bands is calculated and the scattering rates and the effect of quasiparticle scattering due to spin fluctuations in a multiorbital model are investigated. The results are presented in Fig. 6.15. According to this study the scattering rate on the d_{xy} portions of the

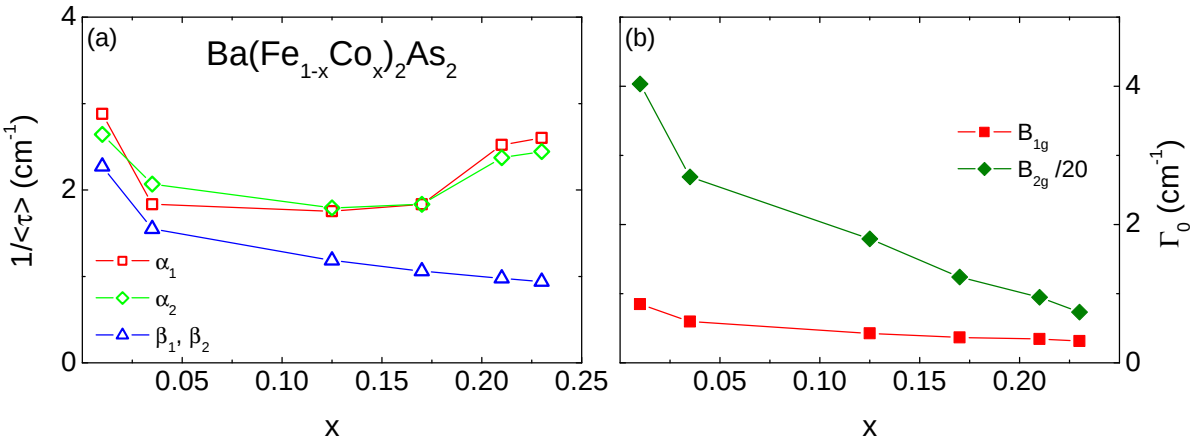

Figure 6.15: Theoretical predictions of the carrier dynamics in Ba122 in the limit $\Omega \to 0$. (a) Inverse of the average scattering times for holes (α_1, α_2) and electrons (β, β_2) in a multiorbital model. (b) Raman scattering rate as function of doping in B_{1g} and B_{2g} symmetry. The B_{2g} curve is divided by 20 to enable a comparison. Data taken from [86].

FS is small, while the d_{xz} and d_{xy} orbitals experience a larger scattering rate. This is attributed to the fact that only the electron bands have contribution from d_{xy} orbitals and therefore the phase space for scattering events is smaller for the electron bands. Thus, the lifetimes are longer on the electron bands (β_1, β_2) than on the hole bands (α_1, α_2) [Fig. 6.15(a)].

The predicted B_{1g} and B_{2g} Raman relaxation rates are displayed in Fig. 6.15(b). The rates in A_{1g} symmetry were not calculated since the calculation is very complicated due to backflow effects. According to the model $\Gamma_0^{B2g} \gg \Gamma_0^{B1g}$ in the entire doping range and the anisotropy becomes smaller with increasing doping level in good qualitative agreement with the experimental results (Fig. 6.10).

Summarizing, anisotropic scattering rates are observed in several experimental and theoretical studies and there is growing evidence that the multiband and multiorbital character of the FeSCs is at the origin of the large anisotropies of the carrier properties. Although there is not yet an agreement concerning the orbital character of the bands, the lifetimes on the electron bands are larger than on the hole bands at least for low temperature. Hence, the difference in the A_{1g} and B_{1g} Raman scattering rates originates from the orbital character of the bands and the scattering between the orbitals. It is important to mention that in the theoretical model the interactions are kept low and impurities are neglected [86]. Thus, a quantitative improvement between the theoretical and experimental values of the relaxation rates by a factor of five is easily possible [228]. The doping dependence of the theoretically obtained relaxation rates, which are

predicted to decrease with increasing doping level [86], is in good agreement with the Raman results presented here. Even if the magnitude of the relaxation rates agrees only qualitatively, the Raman results support an interpretation in terms of magnetic scattering.

6.4 Interplay of magnetic order and impurities

Yet, the non-monotonic doping dependence of $\Gamma_0^{\mathrm{B1g}}(25\ \mathrm{K})$ and $\Gamma_0^{\mathrm{A1g}}(300\ \mathrm{K})$ remains unclear. Naively, one expects that the scattering time $\tau(T)$ becomes shorter by the addition of impurities. Since doping generally adds impurities one would expect that $\Gamma_0^{\mu}(T) \propto 1/\tau(T)$ increases monotonously with doping, at least, for low temperatures, although in-plane Co doping acts only as a weak scatterer [22]. This is observed only for $\Gamma_0^{\mathrm{B1g}}(300\ \mathrm{K})$ [Fig. 6.9(b)].

To explain the non-monotonic doping dependence of $\Gamma_0^{\mu}(T)$ the interplay of magnetism and impurities is studied. When the magnetic order is continuously suppressed by doping, the scattering from magnetic excitations is reduced. On the other hand the increasing doping level enhances the impurity concentration and hence the scattering from impurities. Both aspects are most relevant at low temperatures. Then, from underdoped to optimally doped samples $\Gamma_0^{\mathrm{B1g}}(T \rightarrow T_{\mathrm{c}})$ decreases since the increased scattering from impurities is overcompensated by the decreased scattering from magnetic excitations. At optimal doping the influence of magnetism and the scattering from magnetic excitations has disappeared. Then, scattering from impurities remains the only contribution to $\Gamma_0^{\mathrm{B1g}}(T \rightarrow T_{\mathrm{c}})$ which is smallest at optimal doping. With further doping the number of impurities increases leading to an enhanced scattering from impurities and therefore of $\Gamma_0^{\mathrm{B1g}}(T \rightarrow T_{\mathrm{c}})$. Since the influence of magnetic order is mainly observed in $\mathrm{B_{1g}}$ symmetry, and the $\mathrm{A_{1g}}$ spectra are only weakly affected by magnetism (Fig. 5.3), the described effects on $\Gamma_0^{\mathrm{A1g}}(T \rightarrow T_{\mathrm{c}})$ can obviously be neglected.

Thus, the non-monotonic doping dependence of $\Gamma_0^{\mathrm{B1g}}(T \rightarrow T_{\mathrm{c}})$ with a minimum at optimal doping [Fig. 6.9] is compatible with the interplay of magnetism and impurities. At high temperatures magnetism has no influence on the carriers, and $\Gamma_0^{\mathrm{B1g}}(300\ \mathrm{K})$ increases monotonically with doping.

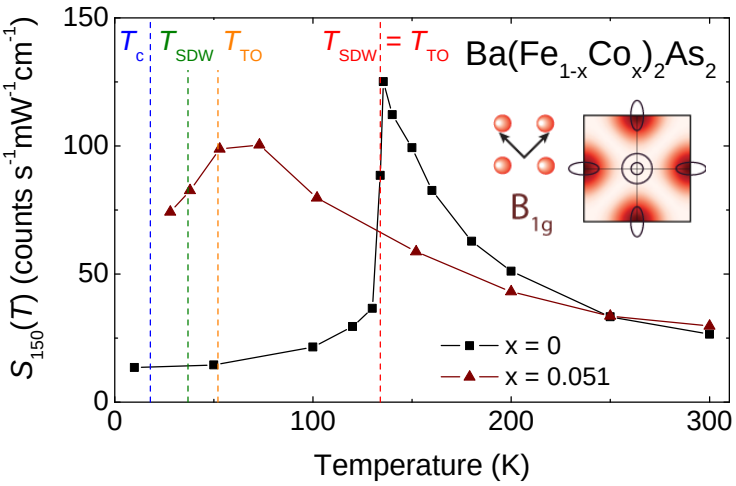

Figure 6.16: Loss of spectral intensity below 150 cm^{-1} as a function of temperature for undoped (squares) and underdoped Ba(Fe$_{1-x}$Co$_x$)$_2$As$_2$ (triangles). $S_{150}(T)$ denotes the integrated intensity in the range between 15 and 150 cm^{-1}. The structural and magnetic transition for BaFe$_2$As$_2$ at $T_{TO} = T_{SDW} = 134$ K are indicated by the red dashed line. The blue, green and orange dashed lines indicate the superconducting, magnetic and structural transition temperature, respectively, of underdoped Ba(Fe$_{1-x}$Co$_x$)$_2$As$_2$.

6.5 Nature of the fluctuations in Ba(Fe$_{1-x}$Co$_x$)$_2$As$_2$

The nature of the fluctuations, which manifest themselves in an increased low energy intensity in the B$_{1g}$ spectra of Ba122 upon approaching T_{SDW} from above [Fig. 5.5(b)], is not yet clear. A similar although less pronounced increase of the low energy spectral weight with decreasing temperature for $T > T_{TO} > T_{SDW}$ is observed in the B$_{1g}$ spectra of sample UD18 [Fig. 6.5(a)]. Here, the low energy B$_{1g}$ response is less abruptly suppressed below T_{SDW} (37 K) and T_{TO} (52 K) [Fig. 6.3(b)] than for sample Ba122 [Fig. 5.3(b)]. To illustrated this observation, Fig. 6.16 shows the integrated intensity of the spectra between 15 and 150 cm^{-1}, $S_{150}(T)$ [Eq. (5.1)], of both samples. Similarly to $S_{150}^{\mathrm{Ba122}}(T)$, $S_{150}^{\mathrm{UD18}}(T)$ increases remarkably with decreasing temperature. However, as opposed to $S_{150}^{\mathrm{Ba122}}(T)$, which increases continuously for $T > 134$ K and abruptly collapses for $T < 134$ K, $S_{150}^{\mathrm{UD18}}(T)$ is nearly constant between 73 and 53 K and decreases linearly below 53 K without a clear signature of a suppressed intensity below T_{SDW}.

This naturally raises the question of the relevance of fluctuations at finite doping and a possible interplay with the SDW gap.

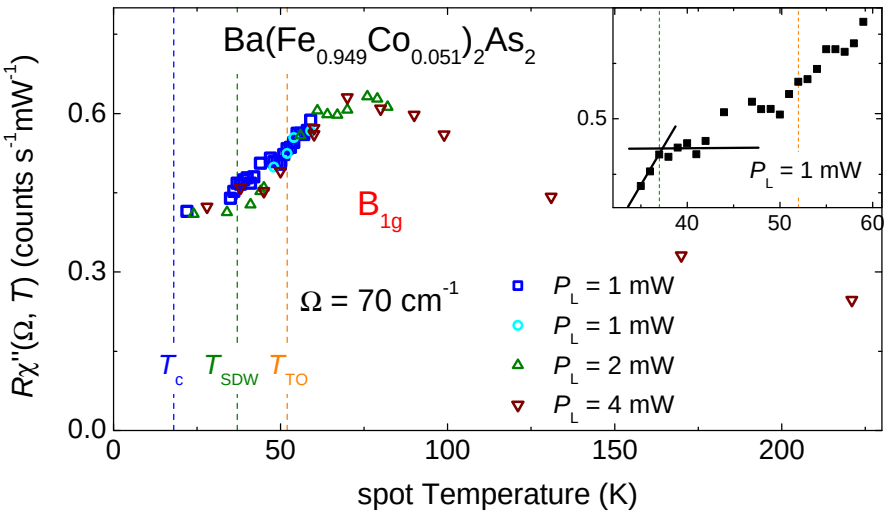

Figure 6.17: Temperature evolution of the B_{1g} Raman intensity of sample UD18. The data are measured with a spectral resolution of $\Delta\Omega = 50$ cm^{-1} and different absorbed laser powers as indicated. The data are an average of the data points at 70 and 100 cm^{-1}. The inset shows a zoom in to the data, measured at temperatures around T_{SDW} and T_{TO} and with 1 mW absorbed laser power. The solid lines are guides to the eye.

6.5.1 Opening of a SDW induced gap

From Figs. 6.3(b) and 6.16 it is clear that the intensity of the low energy B_{1g} response of sample UD18 is already reduced for $T = 38$ K $> T_{SDW}$. Below $T_{SDW} = 35$ K no sign of a further reduction of the spectral weight due to the opening of a SDW gap is observed. Rather, $S_{150}^{UD18}(T)$ decreases roughly linearly below T_{TO}. For the search of indications for the opening of a SDW gap, Fig. 6.4 exhibits data points at 70 and 100 cm^{-1} measured around T_{SDW} and T_{TO} in 1 K temperature steps. Due to the large spectral resolution, $I(\Omega, T)$ is essentially sensitive to the change of the spectra in the range $20 \leq \Omega \leq 120$ cm^{-1} and $50 \leq \Omega \leq 150$ cm^{-1}, respectively. In this energy range the strongest changes with temperature are expected. $I(\Omega, T)$ is shown in Fig. 6.4. Since the temperature increase due to the absorbed laser power is unknown, the data in Fig. 6.4 are shown as a function of the temperature of the sample holder and are not divided by the Bose factor. From the inset of Fig. 6.4 it is clear that $I(\Omega, T)$ is constant above and reduced below $T = 35$ K. This suppression can be associated with the opening of a SDW gap below $T_{SDW} = 37$ K and translates into a temperature increase in the illuminated spot of 2 K per mW absorbed laser power. This is a reasonable value that compares well with the analysis of the energy gain and loss spectra via Eq. (4.2).

Fig. 6.17 presents the Bose corrected data points of Fig. 6.4 versus the sample tem-

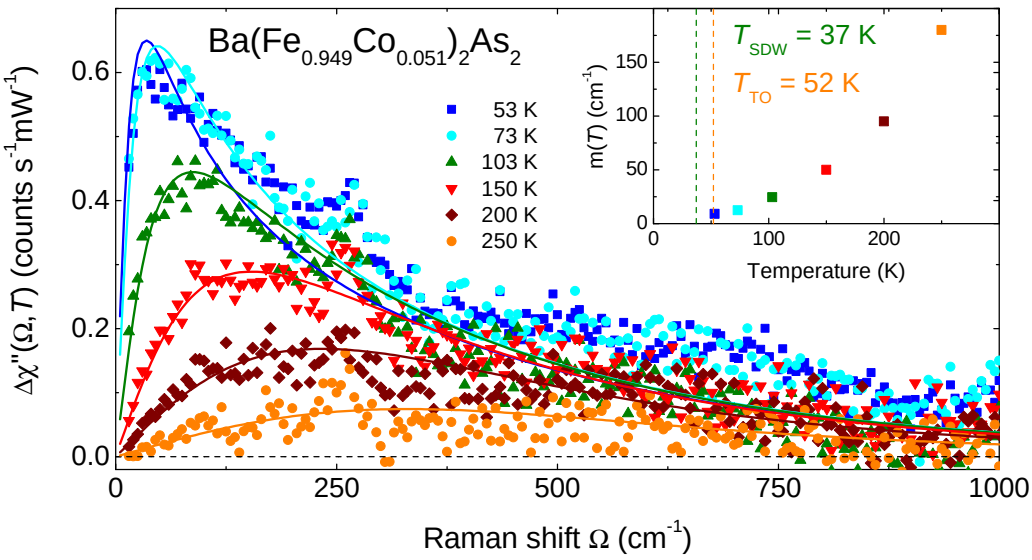

Figure 6.18: Difference spectra $\Delta\chi''(T,\Omega) = \chi''(T,\Omega) - \chi''_a(300\,\mathrm{K},\Omega)$ (symbols) and calculated response from fluctuations (solid lines) of underdoped $Ba(Fe_{1-x}Co_x)_2As_2$. The inset shows the temperature dependence of the effective mass which acts as the only fitting parameter. For details see the text.

perature. Shown is the average of $I(\Omega,T)$ measured at $\Omega = 70$ and 100 cm^{-1} to improve the signal to noise ratio. Here, $I(\Omega,T)$ decreases below $T_{\mathrm{SDW}} = 37$ K due to the opening of a SDW induced gap. Hence, although $S_{150}^{\mathrm{UD18}}(T)$ is less abruptly suppressed below T_{SDW} than $S_{150}^{\mathrm{Ba122}}(T)$ (compare Fig. 6.16), the opening of an SDW induced gap below T_{SDW} can be also observed at finite doping.

6.5.2 Evidence against magnetic fluctuations

The presence of fluctuations at finite doping is studied via the response of an underdoped as well as of an overdoped sample. For finite doping levels both, the magnetic and structural transition are separated enabling the study of the nature of these fluctuations.

Fluctuations in the underdoped sample

To separate the response from fluctuations and the response from the particle-hole continuum, the same method as for Ba122 is applied (Sec. 5.3) and an analytic approximation of the 300 K spectrum is subtracted from the spectra at lower temperatures. The procedure is applicable if $\rho(T)$ varies little in this temperature range. This is only approximately justified by the transport data [7] [Fig. 6.8(b)]. The difference spectra $\Delta\chi''(\Omega,T) = \chi''(\Omega,T) - \chi''_a(\Omega,300\,\mathrm{K})$ are presented in Fig. 6.18 as symbols. For

$\Delta\chi''(\Omega, T)$ the spectral weight for $\Omega \leq 500\,\mathrm{cm}^{-1}$ increases upon cooling and the peak at low energy grows while the intensity for $\Omega \geq 500\,\mathrm{cm}^{-1}$ is small.

The theoretical response from charge fluctuations, calculated via Eq. (5.2), is shown in Fig. 6.18 by solid lines. The fits to the experimental data are obtained with $\Lambda = 0.26$ and $\omega_0 = 400\,\mathrm{cm}^{-1}$. Λ as well as ω_0 are adjusted for the 150 K spectrum and are kept constant for all other temperatures. Only the mass of the fluctuation propagator $m(T)$ is varied to mimic the temperature dependence of the spectra. $m(T)$ is shown in the inset of Fig. 6.18 and, similarly as for Ba122, $m(T)$ decreases linearly at high temperature and tends to saturate below 100 K. The agreement between theory and experiment is satisfactory over the entire energy range of $15 \leq \Omega \leq 1000\,\mathrm{cm}^{-1}$ for $73 \leq T \leq 250$ K showing that the increased low energy response of underdoped samples can be explained by Eq. (5.2). For $T = 53$ K the fit via Eq. (5.2) traces $\Delta\chi''(\Omega)$ only in the low energy range. Above 70 cm^{-1} $\Delta\chi''(\Omega, T = 53\,\mathrm{K})$ is remarkably reduced suggesting that already for $T = 53\,\mathrm{K} > T_{\mathrm{TO}}$ the spectra cannot be explained via the response from fluctuations.

Fluctuations in the overdoped sample

Fig. 6.5(b) displays the B_{1g} response of OD22 for $\Omega \leq 1000\,\mathrm{cm}^{-1}$ as a function of temperature. At first glance there are two main features in the spectra: (i) in contrast to Ba122 [Fig. 5.5(b)] the spectral intensity increases with decreasing temperature over the entire energy range without exhibiting a low energy peak as observed in the spectra of sample UD18 [Fig. 6.5(a)]. In addition, the low energy response increases much weaker than for the undoped and underdoped sample. (ii) in the entire energy range the spectra measured at $T \geq 200$ K lie below those measured at $T \leq 150$ K. The spectra are separated from each other by an intensity gap of roughly $0.2\,\mathrm{counts\,s^{-1}mW^{-1}}$. Thus, $\Delta\chi''(\Omega, T) = \chi''(\Omega, T) - \chi''_a(\Omega, 300\,\mathrm{K})$, which is presented in Fig. 6.19, is larger than zero around 1000 cm^{-1} for $T < 200$ K. In addition, $\Delta\chi''(\Omega, 200\,\mathrm{K})$ is smaller than zero for $\Omega > 500\,\mathrm{cm}^{-1}$. All these facts suggest that the data cannot be fitted by a Raman response of fluctuations. This is demonstrated in Fig. 6.19. The parameters for the fit, which is adjusted to the 200 K spectrum, are $\omega_0 = 150\,\mathrm{cm}^{-1}$ and $\Lambda = 3.2$. Both are unexpected values compared to the fitting parameters of samples Ba122 and UD18. Conspicuously and less surprisingly, Fig. 6.19 shows that $\Delta\chi''(\Omega, 200\,\mathrm{K})$, for which all parameters are optimized, is well reproduced by the fluctuation fit via Eq. (5.2) (solid lines) except for the response around 1000 cm^{-1}. Once the parameters are fixed the fit cannot reproduce the spectra measured at $T = 100$ and 65 K.

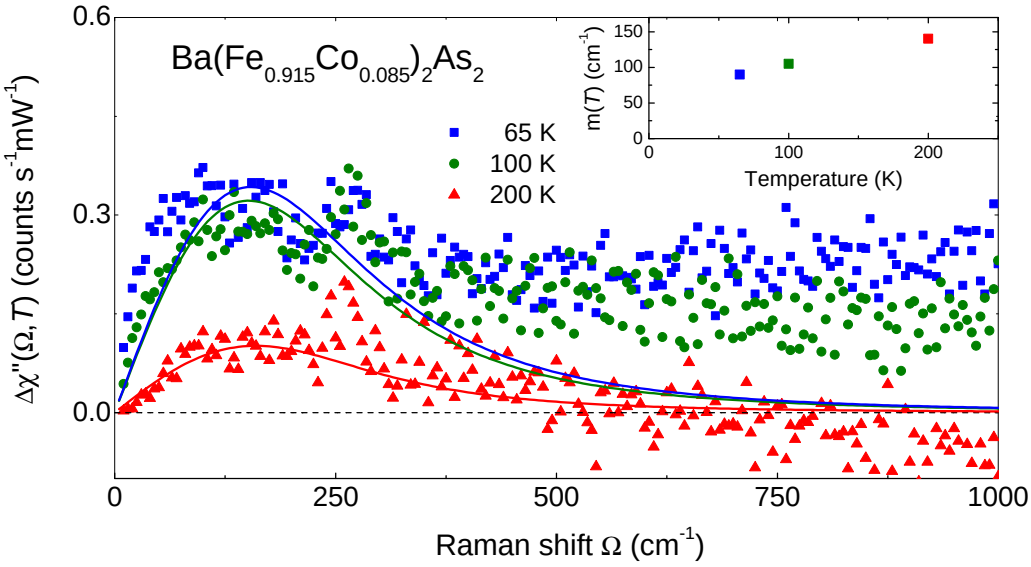

Figure 6.19: Difference spectra $\Delta\chi''(T,\Omega) = \chi''(T,\Omega) - \chi''_a(300\,\mathrm{K},\Omega)$ (symbols) and calculated response from fluctuations (solid lines) of overdoped $Ba(Fe_{1-x}Co_x)_2As_2$. The inset shows the temperature dependence of the effective mass which acts as the only fitting parameter. For details see the text.

Nature of the fluctuations

Thus, the increased low energy response observed in the spectra of undoped and underdoped samples, is compatible with the response from fluctuations in Eq. (5.2). The fluctuations are only present for $x < 0.061$ while fluctuations in the spectra of an overdoped sample can be excluded. This provides evidence that the fluctuations are related to the magnetic and/or structural transition.

The poor agreement of $\Delta\chi''(\Omega, T = 53\,\mathrm{K})$ with the theoretical fit (Fig. 6.18) suggests that the response from fluctuations is reduced already at 53 K. This is in agreement with the data presented in Fig. 6.17. Here, $I(\Omega, T)$ starts to decrease already above T_{TO} while it saturates in the temperature range above T_{SDW}. Hence, only the structural transition is accompanied by fluctuations suggesting a second order phase transition at T_{TO}. This provides compelling evidence that the fluctuations cannot be magnetic in origin since the strongest fluctuations are expected close to the transition temperature. Thus, one can conclude that the fluctuations observed for undoped and underdoped $Ba(Fe_{1-x}Co_x)_2As_2$ single crystals precede the structural transition and are most likely of orbital nature.

Chapter 7

The superconducting energy gap

In this chapter Raman results of $Ba(Fe_{1-x}Co_x)_2As_2$ in the superconducting state are presented for different doping levels.

The quantitative analysis of the spectra reveals the size and momentum dependence of the gap at optimal doping and its doping dependence. In the last section the location of the gap maxima and minima on the electron bands is investigated.

7.1 Raman spectra of optimally doped $Ba(Fe_{1-x}Co_x)_2As_2$

The spectra of the optimally doped $Ba(Fe_{1-x}Co_x)_2As_2$ sample (OPT24, $T_c = 24$ K) below T_c are presented. For the search for superconductivity induced features the samples is illuminated with different excitation energy.

7.1.1 Resonance properties

For calculating the Raman vertices via the effective-mass-approximation in Eq. (3.15) the occurrence of resonances in the response needs to be excluded. Resonance effects occur if interband transitions are excited by the incoming photons. Then, the response varies greatly as a function of the photon energy as observed for hole and electron doped cuprates [161, 229, 230]. To study the presence of resonances, the optimally doped $Ba(Fe_{1-x}Co_x)_2As_2$ sample was excited with photons of energies of 2.7, 2.5 and 2.4 eV corresponding to $\lambda_{exc} = 458$, 501 and 514 nm, respectively. Fig. 7.1 displays raw data measured with parallel and perpendicular light polarizations of incoming and outgoing photons below T_c. The measurement parameters are given in Sec. 6.1. For the studied photon energies neither the intensity nor the lineshape of the spectra changes

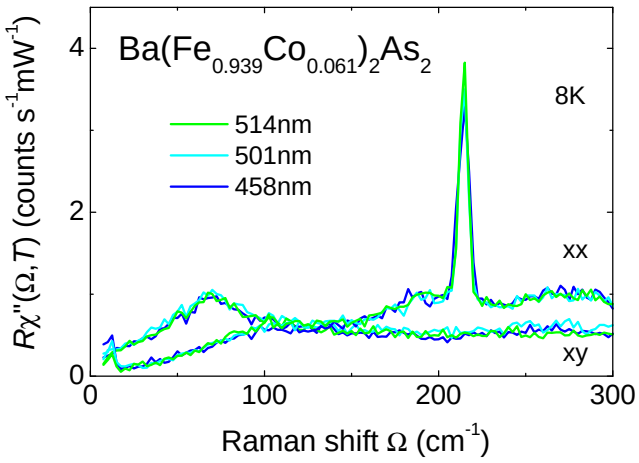

Figure 7.1: Study of resonance properties of optimally doped $Ba(Fe_{1-x}Co_x)_2As_2$ in the superconducting state. The excitation energies and polarization combinations of the light are indicated. From [26].

as a function of the excitation energy. Thus, the Raman response of optimally doped $Ba(Fe_{1-x}Co_x)_2As_2$ exhibits no indications of resonance properties in the superconducting state between 2.7 and 2.4 eV. Similar results were obtained by Chauviere *et al.* [211] for energies between 1.9 and 2.4 eV. Hence, the effective-mass-approximation is applicable and the Raman vertices can be calculated via Eq. (3.15) (Sec. 7.5.2).

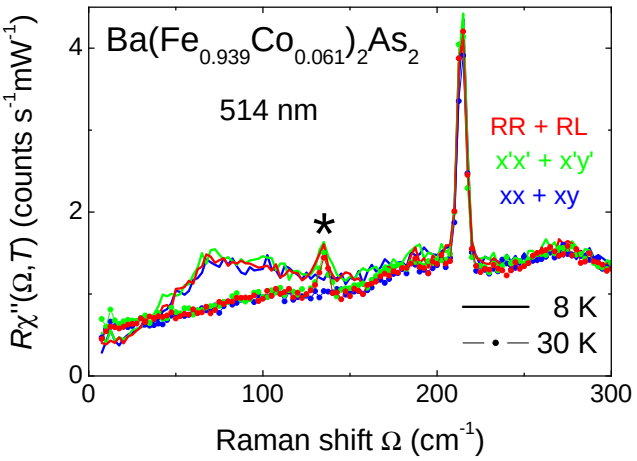

Figure 7.2: Polarization analysis of optimally doped $Ba(Fe_{1-x}Co_x)_2As_2$. The sample was studied with six different light polarization combinations. The asterisk marks the position of the E_g phonon. This phonon is detectable only if the polarization of the incoming photon has a finite projection onto the *c*-axis of the crystal.

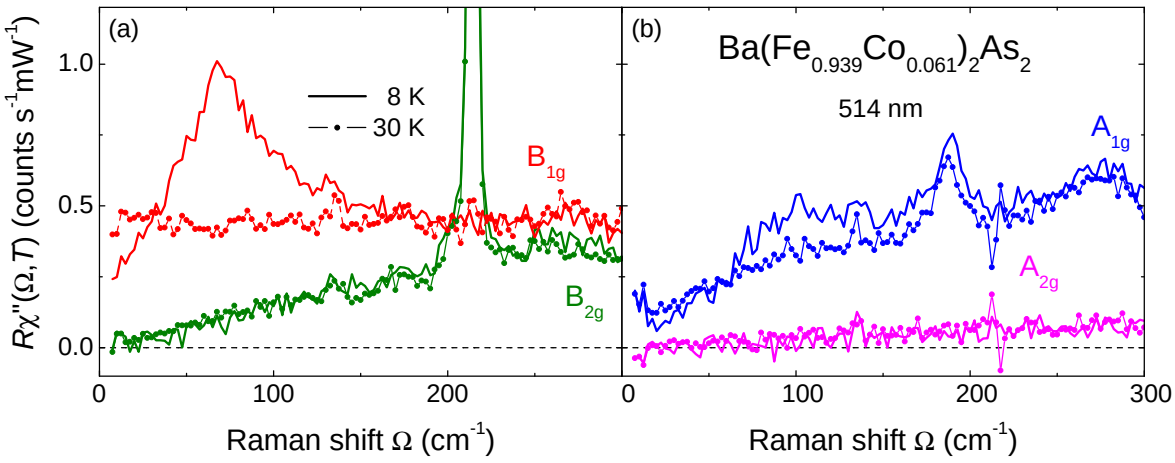

Figure 7.3: Symmetry dependent Raman spectra just above (30 K, symbols) and well below T_c (8 K, solid lines). The response shows clear superconductivity induced features in B_{1g} and A_{1g} symmetry. The A_{2g} response is negligibly small in the investigated energy range. From [25].

7.1.2 Complete symmetry analysis of the Raman spectra

To extract the contribution of each symmetry to the Raman response, a complete symmetry analysis of the spectra is performed. As introduced in Sec. 3.4, linearly and circularly polarized light is necessary to extract the pure symmetry components. Fig. 7.2 shows a quantitative check of the consistency of the measurement. The spectra with the same polarization state of the incoming photons are summed. According to Fig. 3.5, this sum contains all four symmetry components

$$\left.\begin{array}{c} xx+xy \\ x'x'+x'y' \\ RR+RL \end{array}\right\} = \mathrm{A_{1g}} + \mathrm{A_{2g}} + \mathrm{B_{1g}} + \mathrm{B_{2g}}. \tag{7.1}$$

The sums of the spectra below (8 K) and above T_c (30 K) have identical lineshape and intensity for $\Omega \leq 300$ cm^{-1} to within the experimental error. This provides evidence for the proper adjustment of the power and polarization state of the photons. The peak at 135 cm^{-1}, marked by an asterisk, originates from an E_g phonon and is observed only for x' and R polarized incoming photons having a finite projection onto the c-axis of the crystal (c.f. Sec. 5.1.1).

The symmetry resolved Raman response, calculated via Eq. (3.27), is presented in Fig. 7.3 below (solid lines) and above T_c (symbols). Among all four in-plane symmetries the strongest superconductivity induced features are observed in the B_{1g} spectrum. The

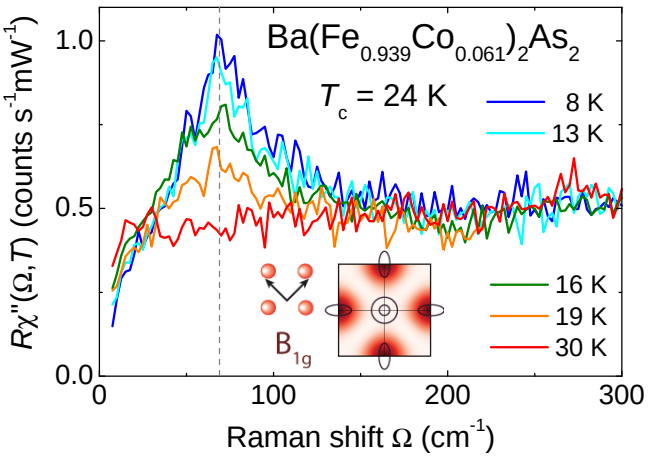

Figure 7.4: Temperature dependence of the B_{1g} response in the superconducting state for optimally doped $Ba(Fe_{1-x}Co_x)_2As_2$. The vertical gray dashed line marks the energy of the pair breaking peak at the lowest temperature.

spectrum shows a clear redistribution of spectral weight as expected for the opening of a superconducting gap and the existence of a condensate [24, 137, 231]. The pair breaking peak is centered at roughly 70 cm^{-1}. In B_{2g} symmetry there is no significant difference between the spectra below and above T_c. The A_{1g} spectrum [Fig. 7.3(b)] shows a superconductivity induced redistribution of spectral weight and has a pair breaking peak at roughly 100 cm^{-1}. As compared to the B_{1g} and B_{2g} response, there is an increasing contribution for $\Omega \leq 20$ cm^{-1} originating from the less effective suppression of stray light in A_{1g} symmetry. The contribution in A_{2g} symmetry is not affected by superconductivity. It increases linearly with Ω and is very small below 300 cm^{-1}. At 300 cm^{-1} the A_{2g} intensity is approximately 1/4 of the intensity in the other symmetries. This is in agreement with theoretical considerations, where the electronic contribution to the A_{2g} response should vanish in a non-magnetic material [232].

This demonstrates that the main features in the response below T_c occur in A_{1g} and B_{1g} symmetry while the low energy A_{2g} response is negligible small. Therefore, also in the superconducting state the A_{2g} contribution to the response will not be subtracted from the spectra in other symmetries in the following. This saves a factor of two in measurement time.

7.1.3 Temperature dependence below T_c

Fig. 7.4 displays the B_{1g} spectra at several temperatures in the superconducting state. The clear redistribution of spectral weight with the pair breaking peak centered at

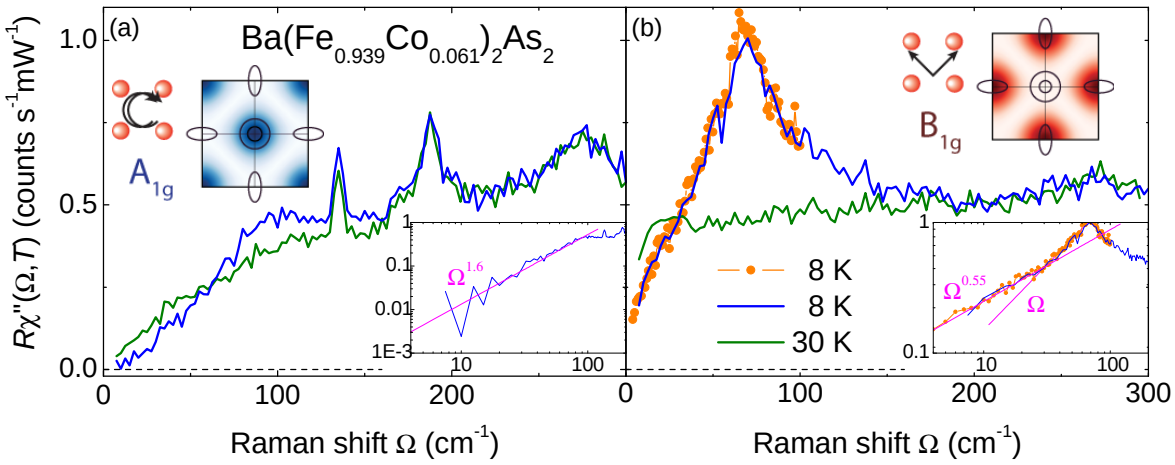

Figure 7.5: Raman spectra of optimally doped $Ba(Fe_{1-x}Co_x)_2As_2$ below (blue, 8 K) and above (green, 30 K) $T_c = 24$ K in (a) A_{1g} +A_{2g} and (b) B_{1g} +A_{2g} symmetry. Due to the vanishing contribution to the spectra the A_{2g} response is not subtracted. The insets show the low energy response on a log-log scale. The orange symbols are measured at 8 K with a resolution of 3.6 cm^{-1} and a step width of 1 cm^{-1} down to $\Omega = 4$ cm^{-1}.

approximately 70 cm^{-1} and the reduced intensity for $\Omega \leq 30$ cm^{-1} at 8 K is continuously weakened with increasing temperature. Above $T_c = 24$ K no superconductivity induced features are observed. Within the experimental resolution no shift of the position of the peak is detectable. This is in good agreement with another Raman study on $Ba(Fe_{1-x}Co_x)_2As_2$ [211].

The temperature independence of the superconducting peak energy is similar to the observations in optimally doped cuprates [233, 234] and opposed to what is observed in the weak coupling BCS superconductor V_3Si [235]. For the latter material the peak energy decreases with increasing temperature as expected for the energy gap in the BCS theory [236, 237].

7.2 The energy gap of optimally doped $Ba(Fe_{1-x}Co_x)_2As_2$

The A_{1g} and B_{1g} response of optimally doped $Ba(Fe_{1-x}Co_x)_2As_2$ is analyzed in detail. From this analysis the momentum dependence and size of the energy gap of optimally doped $Ba(Fe_{1-x}Co_x)_2As_2$ will be deduced.

7.2.1 Details of the Raman response

Fig. 7.5 displays the A_{1g} and B_{1g} Raman response below (8 K, blue solid lines) and above T_c (30 K, green solid lines). The insets show the response on a log-log scale. The low energy A_{1g} response [Fig. 7.5(a)] varies as $\Omega^{1.6}$ below 80 cm^{-1}. Here, the data quality may be reduced due to surface layers which enhance the low energy response. If there is an activation threshold it is smaller than 30 cm^{-1}. In the B_{1g} spectra [Fig. 7.5(b)] no clear activation threshold can be found but there is finite intensity down to the lowest measured energy. The B_{1g} spectrum varies linearly with frequency above 30 cm^{-1} and changes to a $\sqrt{\Omega}$ dependence for $\Omega \leq 30$ cm^{-1} [inset of Fig. 7.5(b)].

To search for an activation threshold in the B_{1g} response smaller than 7.5 cm^{-1}, the spectra are measured with a resolution of 3.6 cm^{-1} and a step width of 1 cm^{-1} down to energies as low as $\Omega = 4$ cm^{-1} which corresponds to a temperature of 6 K [orange symbols in the inset of Fig. 7.5(b)]. Even for $\Omega = 4$ cm^{-1} a finite Raman intensity is observed. Since 4 cm^{-1} are already smaller than the thermal energy at the measurement temperature of 8 K, the study of the response at lower energy cannot uncover a minimal gap at smaller energy.

The pair breaking peaks, as displayed in Fig. 7.5, turn out to have a rather strong symmetry dependence. The A_{1g} peak is relatively weak and broad with a maximum at $\Omega_{\mathrm{peak}}^{\mathrm{A1g}} \approx 100$ cm^{-1} corresponding to $\Omega_{\mathrm{peak}}^{\mathrm{A1g}}/k_{\mathrm{B}}T_{\mathrm{c}} = 6$. The B_{1g} spectrum exhibits a sharp superconducting peak with the maximum located at $\Omega_{\mathrm{peak}}^{\mathrm{B1g}} = 69$ cm^{-1}, corresponding to $\Omega_{\mathrm{peak}}^{\mathrm{B1g}}/k_{\mathrm{B}}T_{\mathrm{c}} = 4.2$. For $\Omega < \Omega_{\mathrm{peak}}^{\mathrm{B1g}}$, the B_{1g} spectrum has a shoulder or even a peak at 52 cm^{-1} [Fig. 7.5(b)]. This shoulder has a width of only 2 cm^{-1}. Since the presented spectra are the sum of three single spectra each measured with an integration time of 400 s per data point, it is unlikely that this shoulder is due to a statistical error. Additionally, a very similar structure at the same energy and a similar doping level is observed but not commented in the study of Chauviere *et al.* [211]. A possible origin of this peak will be discussed in Sec. 7.4.2.

The sharpness of the superconducting B_{1g} peak underlines the high purity and order of the investigated sample since impurities are expected to smear out these sharp features [238]. To illustrate the sharpness of the superconducting B_{1g} peak, the data in Fig. 7.5(b) are plotted on a logarithmic scale as a function of $|1 - \Omega/\Omega_{\mathrm{max}}|$ with $\Omega_{\mathrm{max}} = 69$ cm^{-1}. The resulting spectra are shown in Fig. 7.6. There is an universal linear variation on either side of Ω_{max}, which extends over 1 and 1/2 decade on the low- [Fig. 7.6(a)] and high-energy side [Fig. 7.6(b)], respectively, indicating a logarithmic divergence of the superconducting B_{1g} peak. The peak is cut only by the resolution of the

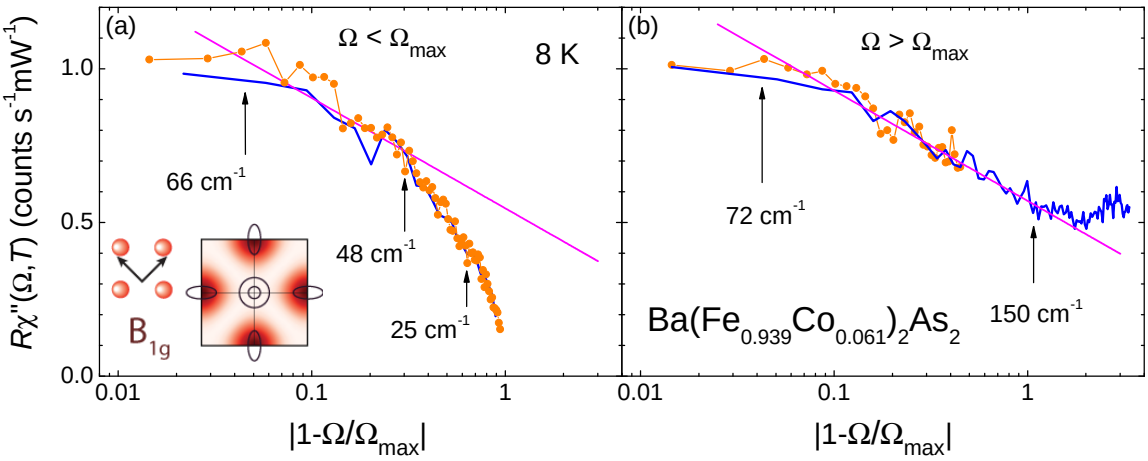

Figure 7.6: Pair breaking peak in B_{1g} symmetry of optimally doped $Ba(Fe_{1-x}Co_x)_2As_2$. The figure shows the variation of the peak on a scale of $|1-\Omega/\Omega_{max}|$ on the (a) low and (b) high energy side of the peak maximum at $\Omega_{max} = 69$ cm^{-1}. The orange symbols are measured with a resolution of 2.5 cm^{-1} and a step width of 1 cm^{-1}. The magenta lines indicate the spectral shape for a logarithmic divergence of the peak.

spectrometer. Such a logarithmic divergence in a Raman spectrum is only possible if either the electronic properties or the Raman vertex are strongly 2D [147, 239]. Since the FS of '122' compounds has a remarkable dispersion along k_z [c.f. Fig. 2.6(b)], the B_{1g} Raman vertex seems to be rather 2D.

7.2.2 Evidence for nodal gaps

For the interpretation of the Raman scattering results there are two important points concerning the initial slope and the pair breaking peak: (i) The low-energy response is generally expected to follow from the low-energy DOS [137, 138]. Hence, the finite intensity for $\Omega \to 0$ without an activation threshold [inset of Fig. 7.5(b)] is an argument in favor of a finite DOS down to very low energy and therefore for a vanishingly small or vanishing minimal gap Δ_{min}. The $\sqrt{\Omega}$ dependence of the B_{1g} response favors a superconducting gap vanishing quadratically with momentum near the nodes [25]. If there is a threshold in the A_{1g} spectra, the threshold is smaller than 30 cm^{-1} and is smeared by inelastic processes. Since the FSs of the hole bands have a similar shape and cross-section as those of the electron bands (Sec. 2.3), a gap with a small threshold plus inelastic scattering can plausibly explain the $\Omega^{1.6}$ dependence of the Raman slope [147]. (ii) The logarithmic divergence of the superconducting B_{1g} peak indicates the high purity and order of the sample [238] and that the electronic properties probed in B_{1g} symmetry have a strongly 2D character [147]. The reduced peak intensity in A_{1g}

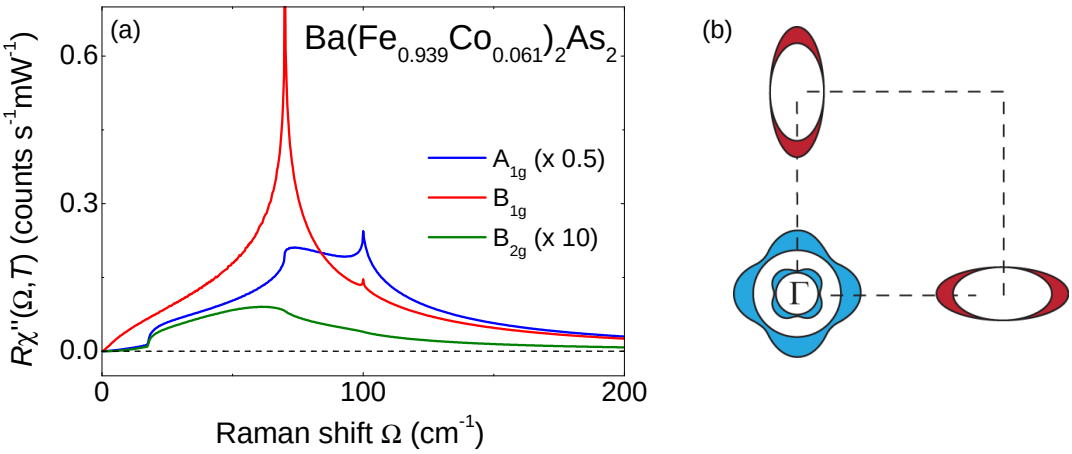

Figure 7.7: (a) Theoretically calculated Raman response in the superconducting state for A_{1g}, B_{1g} and B_{2g} symmetry. The spectra in A_{1g} and B_{2g} symmetry are multiplied by 0.5 and 10, respectively, to make it visible in the graph. (b) Multi gap behavior on the two hole bands around the Γ point and two electron bands at the M points of the BZ used for the calculation of the response. Different colors of the gaps on the hole and electron bands indicate the different sign of the order parameter. From [25].

symmetry is in agreement with theoretical considerations where the A_{1g} response is more smeared out than the B_{1g} response, since backflow terms and Coulomb screening cut the sharp structures and divergences in A_{1g} symmetry [135].

Theoretically calculated Raman spectra are shown in Fig. 7.7(a) together with the underlying gap structure in Fig. 7.7(b) [25]. For the calculations of the spectra, the position of Ω_{peak} is adjusted to the experimental data in both symmetries. The results in B_{1g} symmetry compare almost quantitatively with the data since the clean limit applies here [147]. The calculation is performed with a Raman vertex which is constant on the electron bands and zero everywhere else in the BZ (Sec. 3.4). The $\sqrt{\Omega}$ dependence of the initial slope provides evidence for the presence of accidental nodes on the electron bands since for a finite gap there would be a threshold observable in the spectra. In contrast, for true nodes, i.e. a sign change of the order parameter on the electron bands, one would lose the sublinear energy dependence of the low-energy B_{1g} spectra [146, 147]. For the examination of the gap structure underlying the A_{1g} spectra it is assumed that the A_{1g} vertex measures mainly the hole bands, as suggested by the symmetry considerations in Sec. 3.4. Then, the broad superconducting peak with the $\Omega^{1.6}$ variation of the low-energy response is well reproduced with an anisotropic gap structure on the hole bands and a very small Δ_{min}.

The best fitting choices for the gaps on the electron and hole bands are compiled in Fig. 7.7(b). Different colors of the gaps on the electron and hole bands correspond to

different signs of the order parameter. This, according to Sec. 2.5, corresponds to a $s_\pm$ gap of optimally doped $Ba(Fe_{1-x}Co_x)_2As_2$. The details of the gaps are as follows [25]: (i) the inner hole band has a gap which is maximal along (π, π) and minimal along $(\pi, 0)$ and corresponding directions. The minimal gap is larger than zero. (ii) The outer hole band has the same gap structure as the inner hole band but the momentum dependence of the gap structure is rotated by 45° with respect to the inner hole band. (iii) the electron bands have accidental nodes, i.e. the minimal gap is zero. The maximal gap is facing the maximal gap of the outer hole band.

The presented results of nodal gaps for optimally doped $Ba(Fe_{1-x}Co_x)_2As_2$ are at variance with several other experimental techniques, which find more or less isotropic gaps for optimally doped $Ba(Fe_{1-x}Co_x)_2As_2$ as will be discussed in Sec. 7.5.1. However, the size of the gaps on the electron ($\Omega^{B1g}_{peak}/k_BT_c = 4.2$) and hole bands ($\Omega^{A1g}_{peak}/k_BT_c = 6$) is in good agreement with other studies [77, 240].

7.3 Doping dependence of the $Ba(Fe_{1-x}Co_x)_2As_2$ Raman spectra

The results at optimal doping are supplemented by systematic studies in the doping range $0.045 \leq x \leq 0.085$. In this range magnetic order disappears, so that possible interactions of magnetism and superconductivity can be scrutinized.

7.3.1 Experimental results

Fig. 7.8 presents the Raman spectra of $Ba(Fe_{1-x}Co_x)_2As_2$ single crystals as a function of doping in all three in-plane symmetries. The spectra in the superconducting state at 8 K (blue solid lines) and in the normal state just above T_c at roughly 30 K (green solid lines) are measured up to a Raman shift of 200 cm^{-1} below which the relevant superconductivity induced features occur in the spectra of OPT24. The measurement parameters are the same as in the normal state for $T \to T_c$ (c.f. Sec. 6.1).

The B_{2g} spectra presented in Fig. 7.8(k)-(o) exhibit a roughly linear energy dependence with a small slope and, within the resolution of the experimental setup, no superconductivity induced features. There is only a vanishingly weak doping dependence of the spectra. In the A_{1g} spectra there are clear superconductivity induced features [Fig. 7.8(a)-(e)]. A depletion of low-energy spectral weight is observed for doping levels $0.051 \leq x \leq 0.085$, while a pair breaking peak is visible only for $0.055 \leq x \leq 0.085$

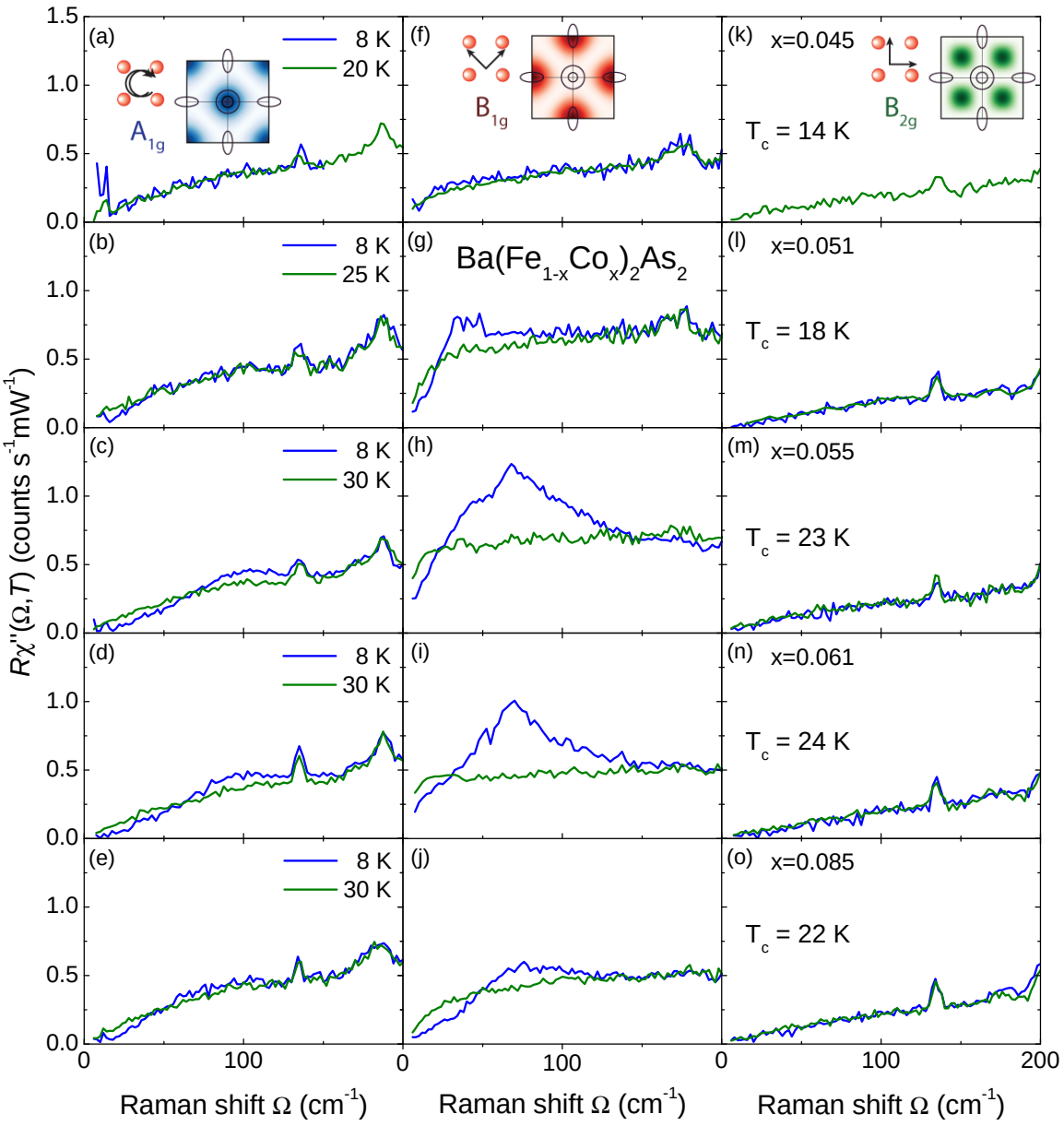

Figure 7.8: Doping dependent Raman spectra of $Ba(Fe_{1-x}Co_x)_2As_2$ above (green) and below (blue) T_c in A_{1g} [(a)-(e)], B_{1g} [(f)-(j)] and B_{2g} symmetry [(k)-(o)] around optimal doping.

[Fig. 7.8(c)-(e)]. For sample UD14 ($x = 0.045$) no superconductivity induced features occur in the A_{1g} spectra [Fig. 7.8(a)].

The B_{1g} spectra exhibit a redistribution of spectral weight below T_c for all doping levels [Fig. 7.8(f)-(j)]. Similar to the normal state spectra at low temperature [Fig. 6.1(b)], the spectral shape changes strongly with doping. While there is hardly any suppression of low energy spectral weight observable for sample UD14 [Fig. 7.8(f)], the depletion gets more pronounced with increasing doping level [Fig. 7.8(g)-(j)]. The shape of the pair-

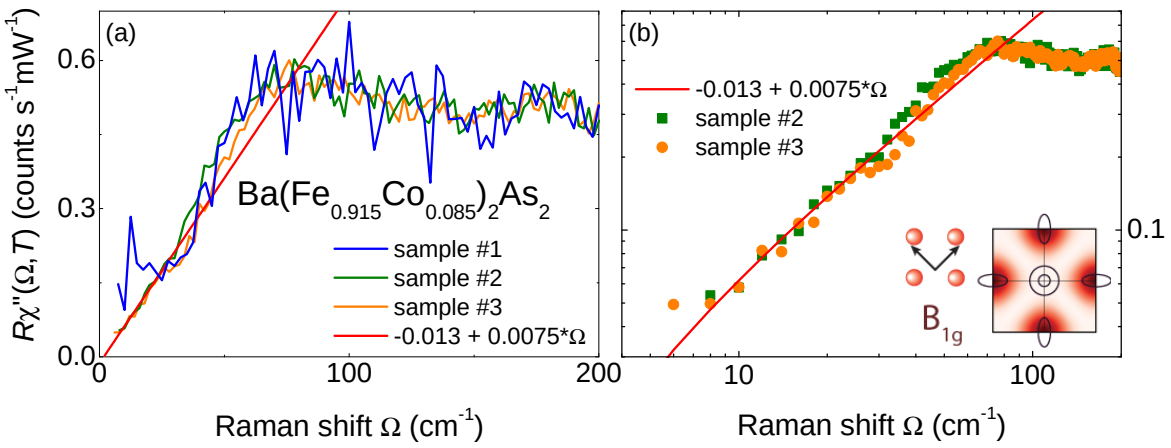

Figure 7.9: Comparison of the Raman spectra of overdoped $Ba(Fe_{1-x}Co_x)_2As_2$ ($x = 0.085$) samples #2 (blue) and #3 (orange). (a) Raman spectra on a linear scale and (b) on a double logarithmic scale. The symbols represent the experimental spectra. The red solid line is a linear fit to the data extrapolating to a finite value of the Raman shift.

breaking peak changes strongly as a function of doping. For underdoped and overdoped samples [Fig. 7.8(f), (g), (j)] the superconducting peak is weaker than for samples close to and at optimal doping [Fig. 7.8(h), (i)]. Even for the three samples UD23, OPT24 and OD22 with nearly the same T_c there is a remarkable change of the spectra.

In the following, it is investigated how the spectra develop with an aging of the sample. For the study of the low energy B_{1g} response the elastically scattered light, superposed on the spectra, needs to be subtracted.

7.3.2 Low-energy Raman response of samples UD18 and OD22

To investigate the dependence of the Raman spectra on sample age, three different overdoped samples from the same batch were studied. Fig. 7.9(a) shows the spectra of the samples with $x = 0.085$ and $T_c = 22$ K. The samples #1 and #2 are measured within a short time period and sample #3 is measured more than one year later. For $\Omega \geq 65$ cm^{-1} the spectra of all three samples are identical within the statistical error. The spectrum of sample #1 is more noisy due to the poor statistics. For $30 \leq \Omega \leq 65$ cm^{-1} sample #3 exhibits a reduced yet unexplained spectral weight compared to the spectrum of sample #2. In this energy range the spectrum of sample #1 lies between the spectra of the other two samples.

For $\Omega \leq 30$ cm^{-1} the spectra of samples #2 and #3 are identical while the response of sample #1 is superposed by elastically scattered light. The low energy response of samples #2 and #3 is presented on a logarithmic scale in Fig. 7.9(b). It can be fitted

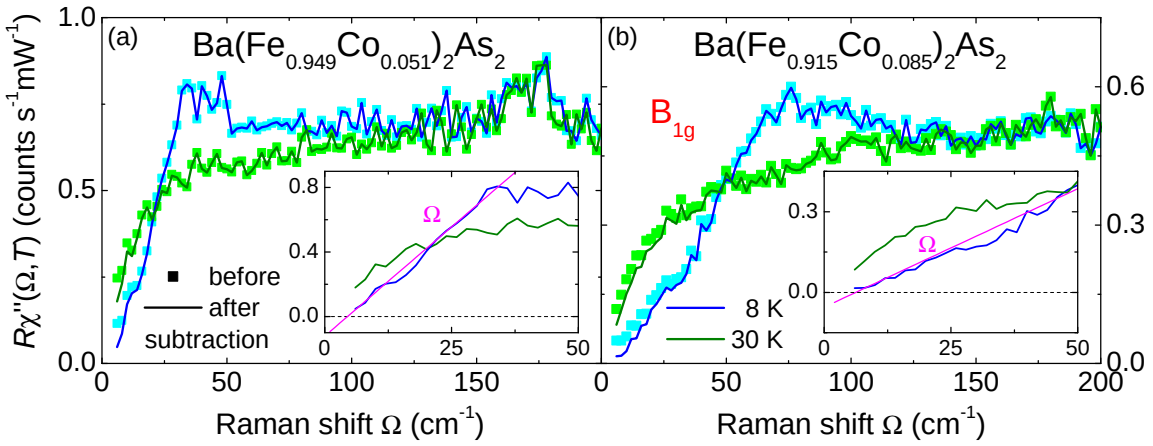

Figure 7.10: B_{1g} Raman response of overdoped and underdoped $Ba(Fe_{1-x}Co_x)_2As_2$ below (blue) and above T_c (green). The spectra are shown before (bright symbols) and after (dark full lines) subtraction of the contribution of elastically scattered light. (a) Spectra of the overdoped sample OD22. (b) Spectra of the underdoped sample UD23. The insets show that the response below T_c varies linearly with Ω for both doping levels and cuts through zero at finite Ω. The magenta line is a fit to the data.

via

$$\chi''(\Omega) = -0.013 + 0.0075 \cdot \Omega. \tag{7.2}$$

Thus, for $\Omega \leq 2$ cm^{-1} the response is zero demonstrating that the spectra exhibit a finite activation threshold [Fig. 7.9(a)]. Note that the spectra are presented as measured.

Since the normal state spectra are superposed by elastically scattered light for $\Omega \to 0$, further processing of the data as described in Sec. 4.2.6 is necessary. The spectra of sample #3 before and after the subtraction of the laser line in the normal and superconducting state are displayed in Fig. 7.10(b). After the subtraction of the elastically scattered light, the response cuts through zero at $\Omega \approx 6.5$ cm^{-1}.

Also the spectra of the underdoped sample UD18 increase for $\Omega \to 0$ due to the contribution from elastically scattered light. The spectra in the normal and superconducting state before and after subtraction of this contribution are presented in Fig. 7.10(a). The subtraction of elastically scattered light affects the low energy spectrum below T_c qualitatively. While the "as measured" low energy spectrum varies linearly in Ω and extrapolates to zero, the spectrum after subtraction of the laser line varies still linearly with Ω but cuts through zero at a finite Raman shift of $\Omega \approx 4$ cm^{-1} [inset of Fig. 7.10(a)].

For samples OD22 and UD23 the contribution of elastically scattered light was determined in the normal state. In the superconducting state the same contribution as in the normal state was subtracted. Since the contribution of the elastically scattered light to

Doping level x	A_{1g}	B_{1g}
0.045	$\propto \Omega^{1.8}$	$0.0090 \cdot \Omega^{1.1}$
0.051	$\propto \Omega^{1.8}$	$-0.12+0.0270 \cdot \Omega^{1.0}$
0.055	$\propto \Omega^{1.6}$	$0.0510 \cdot \Omega^{0.8}$
0.061	$\propto \Omega^{1.6}$	$0.0700 \cdot \Omega^{0.55}$
0.085	$\propto \Omega^{1.8}$	$-0.06+0.0088 \cdot \Omega^{1.0}$

Table 7.1: Parameters for the power law fit of the low energy Raman response in A_{1g} and B_{1g} symmetry.

the response is generally expected to grow for lower temperatures, the applied method should underestimate the stray light contribution to the spectra below T_c. Hence, for the overdoped sample OD22 with $x = 0.085$ as well as for the underdoped sample UD18 with $x = 0.051$ there is a activation threshold observed in the Raman spectra.

7.3.3 Analysis of the spectra

The Raman spectra at all doping levels are fitted by low-energy power laws. The results are tabulated in Tab. 7.1. The determination of the low energy fits in A_{1g} symmetry is complicated below 20 cm^{-1} due to stray light from the laser at low energy. Nevertheless, the power law behavior found for sample OPT24 with an $\Omega^{1.6}$ variation is observed in the spectra at all other doping levels indicating only little variations of the A_{1g} response as a function of doping.

In Fig. 7.11(a) the A_{1g} spectra for $T < T_c$ at all doping levels are compiled. The overall shape of the superconducting A_{1g} spectra is only weakly doping dependent. The strongest intrinsic changes occur between 15 and 80 cm^{-1}. The changes originate from the opening of the superconducting gap and the corresponding suppression of low energy spectral weight, where the suppression is predominantly observed for doping levels $x \geq 0.055$. At roughly 100 cm^{-1} a weak maximum develops in the spectra before two phonons are superposed on the electronic continuum at higher energies. This maximum can be assigned to the pair breaking peak only for $x \geq 0.055$. It is better seen in Fig. 7.8(c)-(e) via the comparison with the normal state spectra. Below the maximum, the shape is more convex for samples UD14, UD18 and OD22, while the spectra of samples UD23 and OPT24 exhibit a concave shape in this energy range.

Fig. 7.11(b) presents the same data with the energy axes normalized to the corresponding T_c of each sample. T_c is a directly measured quantity and varies in the range between 14 K ($x = 0.045$) and 24 K ($x = 0.061$). Below $2.5\, k_B T_c$ the spectra at all

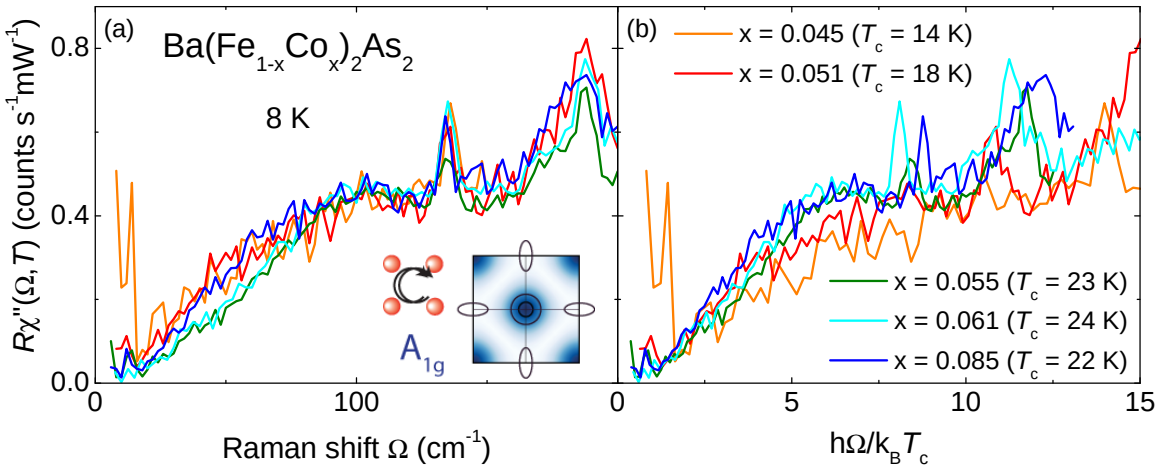

Figure 7.11: Doping dependence of the A_{1g} Raman response of $Ba(Fe_{1-x}Co_x)_2As_2$ at 8 K (a). The spectrum of sample with $x = 0.045$ is adjusted to the other spectra by a constant scaling factor of 1.2 to make the spectral shape better comparable. (b) The same spectra as in (a) but normalized to the corresponding T_c of the samples. The sharp feature in the spectrum of sample UD14 at roughly 20 cm^{-1} results from an insufficient suppression of the laser line.

doping levels are identical to within the experimental error. While the spectrum of sample OD22 is slightly enhanced between 3 and 5 $k_B T_c$, all spectra with pair breaking peak ($x \geq 0.055$) collapse on top of each other between 5 and 7 $k_B T_c$ where the spectra without peak have a reduced intensity. Above 7.5 $k_B T_c$ the spectra are nearly identical for all doping levels.

The fitting results for the low energy B_{1g} spectra vary remarkably with doping. They are presented in Tab. 7.1. The sublinear variation of the Raman response of OPT24 is also found for UD23 with $\chi''(\Omega) \propto \Omega^{0.8}$ while the spectra of the underdoped sample UD18 as well as of the overdoped OD22 vary linearly with Ω and have a finite activation threshold. For the analysis of the response in a larger energy range, Fig. 7.12(a) presents the doping evolution of the spectra below T_c. The spectra are adjusted in the range $170 \leq \Omega \leq 200$ cm^{-1} to the spectrum of sample UD18 by constant scaling factors of 1.4, 0.9, 0.8 and 0.9 for samples UD14, UD23, OPT24 and OD22, respectively, to make the doping dependence of the spectral features better comparable. The spectra of both underdoped samples UD14 and UD18 exhibit a steep linear increase up to roughly 20 cm^{-1} where the spectra are almost identical. With increasing Ω, a broad peak between 25 and 50 cm^{-1} develops for sample UD18, while the spectrum of sample UD14 increases moderately without exhibiting a peak in this energy range. A remarkable change of the spectra is observed approaching optimal doping. For the slightly

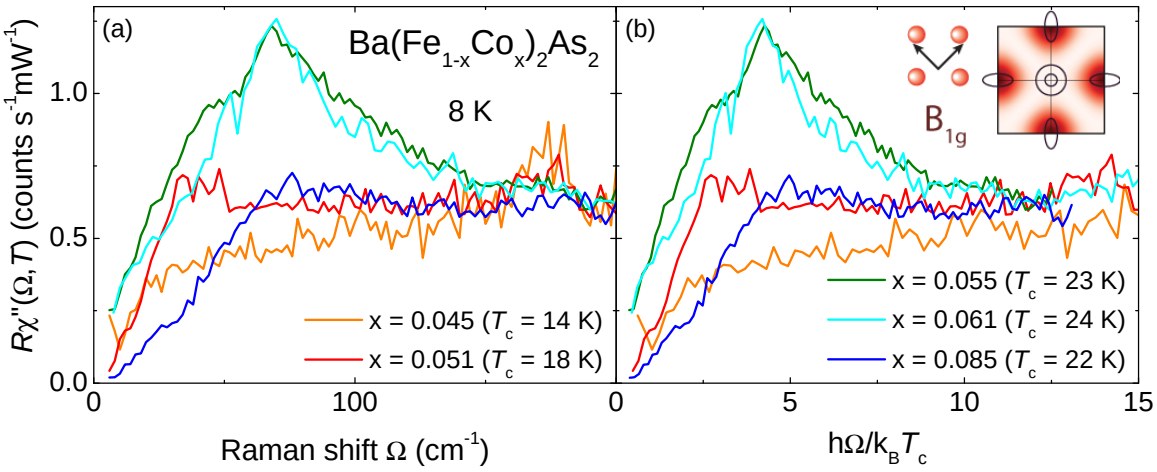

Figure 7.12: Doping dependence of the B_{1g} Raman response of $Ba(Fe_{1-x}Co_x)_2As_2$ at $T = 8$ K (a). The spectra are adjusted between 170 and 200 cm^{-1} to the spectrum with $x = 0.055$ to make the spectral shape better comparable. (b) The same as in (a) but the spectra are normalized to the corresponding T_c of the sample.

underdoped sample UD23 the spectrum starts with an $\Omega^{0.8}$ variation of the initial slope. Between 40 and 55 cm^{-1} a shoulder-like structure is observable, and the maximum is centered at 68 cm^{-1} and relatively sharp. For larger Ω, the spectrum decays roughly linearly over a wide energy range. At optimal doping the superconducting peak loses intensity on the low energy side between 15 and 50 cm^{-1} as well as on the high energy side between 80 and 135 cm^{-1}. Therefore, the peak becomes narrower with respect to the peak observed for sample UD23. The shoulder between 40 and 55 cm^{-1} in the spectrum of sample UD23 becomes narrower and is centered at 52 cm^{-1} while the pair breaking peak stays at 69 cm^{-1}. In the spectrum of the overdoped sample OD22 the overall intensity is strongly reduced. The position of the superconducting peak shifts to higher energy and the peak is centered at roughly 80 cm^{-1}. At this doping level no indications of a structure for $\Omega \leq 80$ cm^{-1} are observed.

In Fig. 7.12(b) the energy axes of the spectra are normalized to the corresponding T_c of each sample. However, the spectra do not fall on top of each other as observed for the A_{1g} spectra indicating that the B_{1g} spectra do not scale with T_c.

At this point the remarkable change of the normal state B_{1g} spectra with doping just above T_c [Fig. 6.1] should be recalled. To study solely the superconductivity induced features, Fig. 7.13(a) displays the difference spectra below and above T_c, $\Delta\chi''(\Omega) = \chi''_{\rm sc}(\Omega, 8\,{\rm K}) - \chi''_{\rm nc}(\Omega, T \approx T_{\rm c})$ where three features are observed: (i) The energy where $\Delta\chi''(\Omega)$ cuts through zero becomes monotonously larger with increasing doping level.

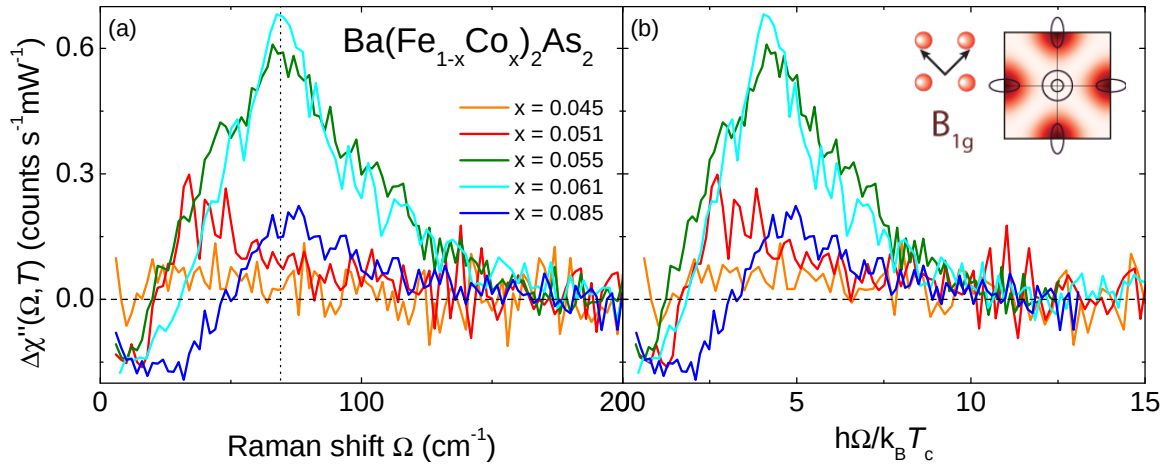

Figure 7.13: Difference spectra of the superconducting and normal state for different doping levels in B_{1g} symmetry, $\Delta\chi''(\Omega) = \chi''_{sc}(\Omega, 8\text{ K}) - \chi''_{nc}(\Omega, T \to T_c)$(a). (b) Same as in (a) but the energy axis is normalized to the T_c of each sample.

(ii) For sample UD14 the maximal internsity appears between 20 and 50 cm^{-1}. The peak continuously narrows and shifts to higher energy with doping. (iii) The intensity of the superconducting peak increases with doping. The peak has its maximal intensity and smallest width at optimal doping. For the overdoped sample the peak height is remarkably reduced and the peak is shifted to higher energy although T_c is reduced by less than 10%. These features change only little when the energy axis is normalized to the corresponding T_c of each samples [Fig. 7.13(b)].

Summarizing this analysis, the superconducting A_{1g} spectra of $Ba(Fe_{1-x}Co_x)_2As_2$ change only little with doping and scale with T_c as opposed to the B_{1g} spectra. Here, the superconducting peak continuously shifts to higher energy with increasing doping level and has its maximal intensity at optimal doping. The dichotomy of the superconducting A_{1g} and B_{1g} spectra is reminiscent on the superconducting spectra of the cuprates. These spectra scale with T_c in B_{2g} symmetry (nodal regions), while the spectra in B_{1g} symmetry (antinodal regions) are strongly doping dependent [241].

7.4 Discussion

In the following, the doping evolution of the superconducting gap on the electron bands is studied. Then, a possible origin of the shoulder-like structure below the pair breaking peak is suggested.

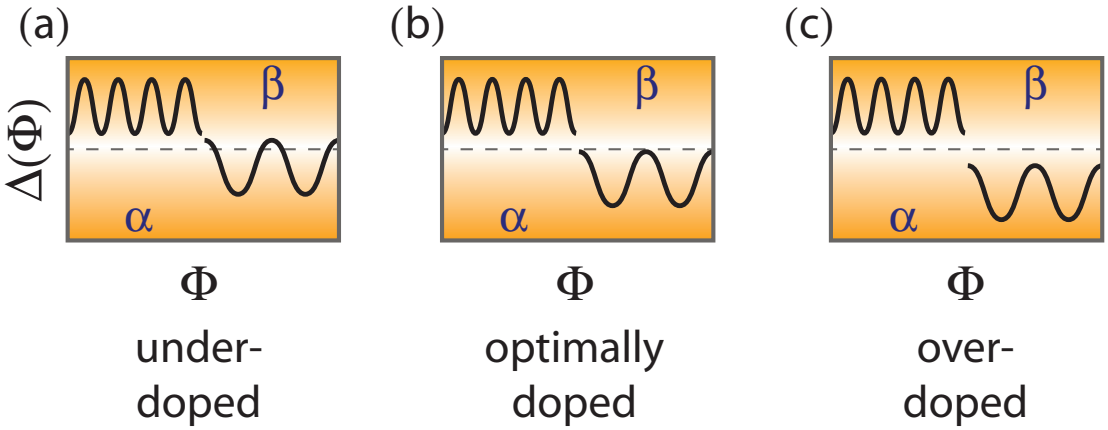

Figure 7.14: Schematic representation of the variation of the $s_{\pm}$ energy gap as a function of the angle Φ encircling the FS on the hole (α) and electron bands (β). While the gap on the hole bands is doping independent, the Fermi level shifts trough the gap on the electron bands as a function of doping.

7.4.1 Doping dependent variation of the gaps on the electron bands

The Raman spectra have a finite activation threshold on the overdoped as well as on the underdoped side. This provides evidence for a finite minimal gap. At optimal doping the low energy response varies as $\Omega^{0.55}$ which is indicative for osculating nodes. For the explanation of the doping dependent changes of the response the gap structure sketched in Fig. 7.14 is suggested. For simplicity, it is assumed that there exists only one hole band (α band) around the Γ point and one electron band (β band) around the M point and corresponding positions in the BZ. Below T_c a gap opens on each of the bands and the gap has opposite signs on the hole and electron bands [98]. While on the hole band the gap is anisotropic, as found in Sec. 7.2, with the maximum scaling with T_c, the gap on the electron band changes remarkably with doping.

On the overdoped side there is a finite Δ_{min} on the electron bands. Thus, the Raman spectra have a finite activation threshold. The finite minimal gap for the overdoped sample OD22 is compatible with the idea that the main effect of Co doping is to introduce impurities [51] which are proposed to lead to a lifting of the near- or osculating nodes if the nodes are not imposed by symmetry [238, 242, 243]. Towards optimal doping Δ_{min} becomes smaller without a significant change in the amplitude of $\Delta(\Phi)$. Then, at optimal doping Δ_{max} has shifted to lower energy, as observed in the spectra (Fig. 7.12 and 7.13), and $\Delta_{\mathrm{min}} = 0$ holds. Thus, there are so called osculating or kissing nodes [25, 134]. The kissing nodes lead to finite intensity down to the lowest energies as found

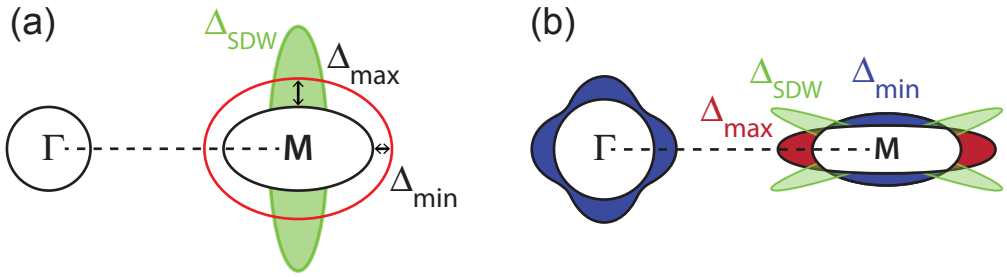

Figure 7.15: Schematic gap structure of underdoped $Ba(Fe_{1-x}Co_x)_2As_2$. Gap structure as obtained in (a) [211] and (b) the presented study. Shown is one hole band at the Γ- and one electron band at the M-point of the 1-Fe BZ with the minimal (Δ_{min}) and maximal gap (Δ_{max}). In (a) Δ_{SDW} (green ellipse) is proposed to open where Δ_{max} occurs. According to the presented study Δ_{SDW} (green ellipse) opens at these spot where the superconducting gap Δ has true nodes. The different colors of Δ indicate different signs of Δ.

in the experiment where $\chi''(\Omega) \propto \Omega^{0.55}$ holds for low energy.

For the explanation of the gap structure on the underdoped side, the influence of the SDW on superconductivity is important. This is suggested by the phase diagram, where both phases coexist homogeneously for underdoped samples. The coexistence of SDW order and superconductivity was studied early for a simple one band BCS superconductor [244]. Applied to the $s_\pm$ gap (see Sec. 2.5) of optimally doped $Ba(Fe_{1-x}Co_x)_2As_2$ (Sec. 7.2), an anisotropic gap with true nodes would be expected [112] since the doubling of the unit cell in the SDW state leads to a backfolding of the 2-Fe BZ as discussed in Sec. 2.4.2. This projects the electron FS with the negative sign of the order parameter onto the hole FS with the positive sign of the order parameter which introduces a sign change of the order parameter and therefore true nodes on the electron bands [112].

Due to the true nodes, the low energy response is expected to vary linearly with Ω without exhibiting an activation threshold. In the presented data the low energy response varies indeed linearly with Ω but there is an activation threshold in the spectrum of UD18 [Tab. 7.1] arguing against true nodes. This discrepancy can be solved keeping in mind that for $BaFe_2As_2$ a SDW gap Δ_{SDW} opens up on the electron bands (Sec. 5.2.2) at these spots where the electron and hole FS intersect in the downfolded BZ (Sec. 2.4.2) [Fig. 2.11(b)]. Since, similarly, a SDW gap is opening up on parts of the electron FS of underdoped $Ba(Fe_{1-x}Co_x)_2As_2$ for $T \leq T_c \leq T_{SDW}$ (Sec. 6.5.1), superconductivity and magnetism might compete for the DOS at E_F as suggested theoretically [112].

Such a competition of superconductivity and magnetism for the DOS at E_F is proposed to explain the data of another Raman scattering study [211]. In that study the spectra

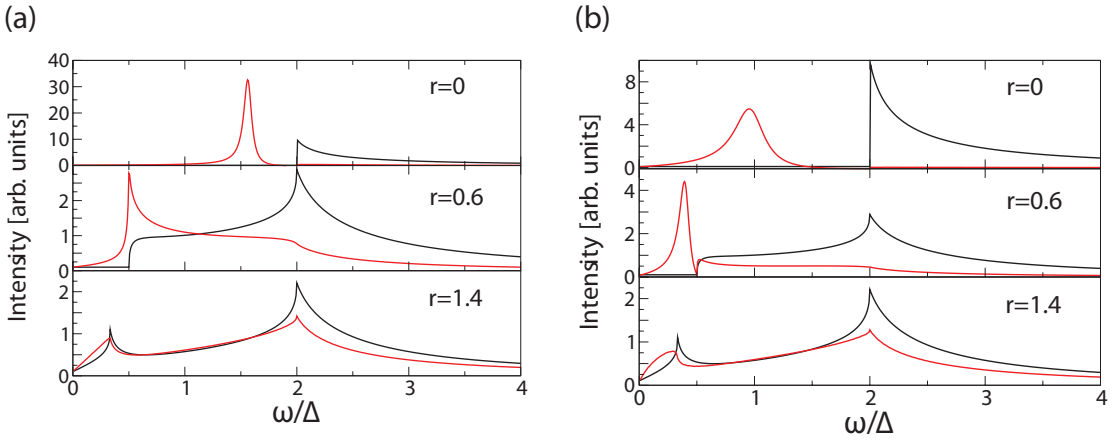

Figure 7.16: Theoretically calculated B_{1g} Raman spectra in the presence of collective modes (red) and for the bare response (black). The response is calculated for different s-wave and d-wave pairing interactions λ_s and λ_d, respectively. r denotes the anisotropy of the gap which is defined in Eq. (7.3). (a) $\lambda_s = 1$ and $\lambda_d = 0.5$. (b) $\lambda_s = 1$ and $\lambda_d = 0.8$. From [245].

are interpreted in terms of a gap structure on the electron bands rotated by 90° with respect to the gap structure reported in the presented study. Hence, Δ_{min} faces the hole bands as illustrated in Fig. 7.15(a). Then, for underdoped crystals Δ_{SDW} opens up on the electron bands and gaps out Δ_{max} [211]. However, according to the presented study, Δ_{SDW} is expected to open up at those $\mathbf{k}$-space regions where $|\Delta(\mathbf{k})|$ is smallest, i.e. has its nodes [c.f. Fig. 2.11(b)]. This is illustrated in Fig. 7.15(b). In this case, Δ_{SDW} gaps those regions on the electron bands where the true nodes occur. This results in a finite activation threshold in the B_{1g} Raman spectra of underdoped samples and is in good agreement to the idea that the magnetism does not destruct superconductivity but competes with superconductivity for the DOS at E_{F} [112].

Thus, with the doping evolution of the gap structure presented in Fig. 7.14, the Raman spectra over the entire studied doping range can be explained consistently. In particular, the finite activation threshold, observed in the spectrum of the underdoped $Ba(Fe_{1-x}Co_x)_2As_2$ sample UD18 (Tab. 7.1), occurs due to Δ_{SDW} which opens up for underdoped $Ba(Fe_{1-x}Co_x)_2As_2$ and gaps out the nodes of $\Delta(\mathbf{k})$.

7.4.2 Signatures of collective modes

One feature in the spectra of samples UD23 and OPT24 still lacking an explanation is the shoulder in the range $40\ \mathrm{cm}^{-1} \leq \Omega \leq 55\ \mathrm{cm}^{-1}$ (Fig. 7.13). This shoulder narrows and shifts slightly to higher energy with increasing doping level. The energy is roughly

25% smaller than the energy of the pair breaking peak at 69 cm^{-1} and the occurrence of the peak cannot be explained by the above gap structure (see Fig. 7.7).

The origin of this peak could be related to the pairing interactions in the FeSCs. The pairing interactions are proposed to be substantial in the *s*- and *d*-wave channel [10, 245, 246, 247] enabling the occurrence of *s*- and *d*-wave instabilities in these multiband superconductors [10, 20, 248]. This leads to excitonic modes [249, 250] visible in the Raman spectra [137, 138]. If the *s*-wave and *d*-wave pairing interaction λ_s and λ_d, respectively, are nearly degenerate, but still $\lambda_s > \lambda_d$ [246], a *d*-wave excitonic collective mode can appear [245]. The signatures of these collective modes are visible in the B_{1g} Raman response [245, 246]. Fig. 7.16 presents the resulting spectra calculated with different *s*- and *d*-wave pairing interactions (see caption of Fig. 7.16) and for a gap structure of

$$\Delta(\Theta) = \Delta_0(1 + r\cos 2\Theta)/(1 + r). \tag{7.3}$$

Here, Θ is the FS angle and r denotes the anisotropy of the gap. For comparison, the bare response without collective modes is also shown in Fig. 7.16. While for an isotropic gap ($r = 0$) the collective mode is essentially undamped and appears below 2Δ as a sharp peak [137, 138], for an anisotropic but true gap ($r = 0.6$), the collective mode appears below $2\Delta_{\mathrm{min}}$ as a sharp peak removing the singularity of the bare response. In both cases the collective mode draws most of the spectral weight from the bare response. For a gap with true nodes ($r = 1.4$), the mode appears below $|2\Delta_{\mathrm{min}}|$ cutting essentially the singularities of the bare response. For increasing λ_d, but still with $\lambda_d < \lambda_s$, the distance in energy between the collective mode, which shifts to lower energy, and the pair breaking peak increases [Fig. 7.16(b)].

Thus, the shoulder in the spectra of samples UD23 and OPT24 around 50 cm^{-1} may originate from a collective mode in the $Ba(Fe_{1-x}Co_x)_2As_2$ superconductor, which exhibits a nodal gap at optimal doping [143]. The close proximity of the shoulder to the superconducting peak at 69 cm^{-1} indicates that λ_d is remarkably smaller than λ_s.

7.5 Location of the gap nodes on the 3D FS of $Ba(Fe_{1-x}Co_x)_2As_2$

In this last section, the results of the superconducting gap, obtained via ERS, will be compared to the results obtained via other experimental techniques. For the better understanding of the distinct results concerning the momentum dependence of $\Delta(\mathbf{k})$,

the Raman vertex will be calculated in detail. Then, it is possible to obtain a complete picture of the momentum dependence of $\Delta(\mathbf{k})$ on the electron bands at least at optimal doping.

7.5.1 Comparison to other experimental techniques

In ARPES studies, where the bands and $\Delta(\mathbf{k})$ can be directly probed, more or less isotropic gaps with different sizes on different bands are observed [75, 77, 251, 252, 253]. In a study of Nakayama *et al.* a gap which scales with T_c over a wide doping range was reported [254]. Also the data of THz reflectance measurements of optimally doped $Ba(Fe_{1-x}Co_x)_2As_2$ are compatible with a two-band scenario where an isotropic gap opens on each band [255]. The spectra of optical conductivity studies are compatible with multiple isotropic gaps [256, 257]. In another optical study by Wu *et al.* the data of nearly optimally doped $Ba(Fe_{1-x}Co_x)_2As_2$ are best fitted via an isotropic gap on one band and an anisotropic gap on another band [258]. Via in-plane thermal conductivity measurements Dong and coworkers observed nodeless gaps for overdoped $Ba(Fe_{1-x}Co_x)_2As_2$ [259]. Another thermal conductivity study reports a gap which changes from isotropic to strongly **k**-dependent from the under- to the overdoped side. Nevertheless, $\Delta(\mathbf{k})$ has no nodes in the *ab*-plane anywhere in the phase diagram [260]. In *c*-axis heat transport studies on $Ba(Fe_{1-x}Co_x)_2As_2$ the same group observed that the gap has nodes on the under- as well as on the overdoped side while there is a nodeless gap at optimal doping [261]. The residual specific heat in the superconducting state of a calorimetric study by Hardy *et al.* [262] is best described via a two-band model with isotropic *s*-wave superconducting gaps. Gofryk *et al.* reported that the superconducting characteristics of $Ba(Fe_{1-x}Co_x)_2As_2$ are significantly improved by annealing [263]. Then, these data are best compatible with a full gap at optimal doping while the data for under- and overdoped samples may be compatible with nodes. In contrast, the specific heat measurement by Mu *et al.* [264] indicates line nodes only for overdoped samples while for under- and optimally doped samples there may be a small anisotropy of the superconducting gap. The results of a London penetration depth study of Martin *et al.* [265] suggests a highly anisotropic nodal 3D gap for overdoped samples. Additionally they conclude that $\Delta(\mathbf{k})$ changes over an extended doping range. The data of a penetration depth study by Luan and coworkers [240] indicate an isotropic gap at optimal doping while on the under- and overdoped side the gaps become anisotropic. A doping dependence of $\Delta(\mathbf{k})$ is also in agreement with theoretical considerations [247, 266, 267].

This demonstrates that, while a pronounced doping evolution of $\Delta(\mathbf{k})$ as obtained

from the presented ERS data, is in general agreement with other theoretical and experimental studies, the detailed **k**-dependence of $\Delta(\mathbf{k})$ for different doping levels is still hotly debated. For the following analysis, I will focus on the gap structure of optimally doped $Ba(Fe_{1-x}Co_x)_2As_2$ where the results obtained via ERS contradict the results of most other experimental techniques which cannot distinguish between electron and hole bands.

The discrepancies in $\Delta(\mathbf{k})$ at optimal doping may, on the one hand, originate from the sensitivity of superconductivity to details of the sample quality, as observed in the specific heat study of Gofryk *et al.* [263], and the related change of the gap structure through impurities [242, 243]. This includes ARPES studies [75, 77, 252, 253], where the contradicting results may originate from a significantly reconstructed surface with respect to the bulk structure [268]. This gives rise to surface related bands which are seen in ARPES studies [268]. On the other hand, the contradicting results of bulk sensitive thermal conductivity [260, 261], specific heat [262, 263, 264] and penetration depth studies [240, 265] need a different explanation.

To solve this discrepancy, the sensitivity of the Raman vertex on the bands at optimal doping is calculated via the effective-mass-approximation. This gives deeper insight into the carrier dynamics as seen via ERS.

7.5.2 Analysis of the Raman vertex

The effective-mass approximation is valid in the limit of vanishingly small momentum transfer $q \to 0$ and a small energy of the photons with respect to interband transitions [135]. In Fig. 7.1 it is shown that the Raman response in the superconducting state is independent of the energy of the exciting photon. This enables one to apply the effective-mass approximation [Eq. (3.15)] [26] where the Raman vertex γ_n is expressed via the curvature of the conduction bands. The different bands $\varepsilon_n(\mathbf{k})$ are obtained via all-electron band-structure calculations [269]. For the calculations of the vertex the 2-Fe BZ is used since downfolding the BZ leads to hybridizations and anticrossings of the electron bands which alters the Raman vertex considerably [26]. Nevertheless, the results in the following are presented in the 1-Fe BZ employed in this work to avoid confusion. The vertices in the three different main symmetries of a tetragonal lattice

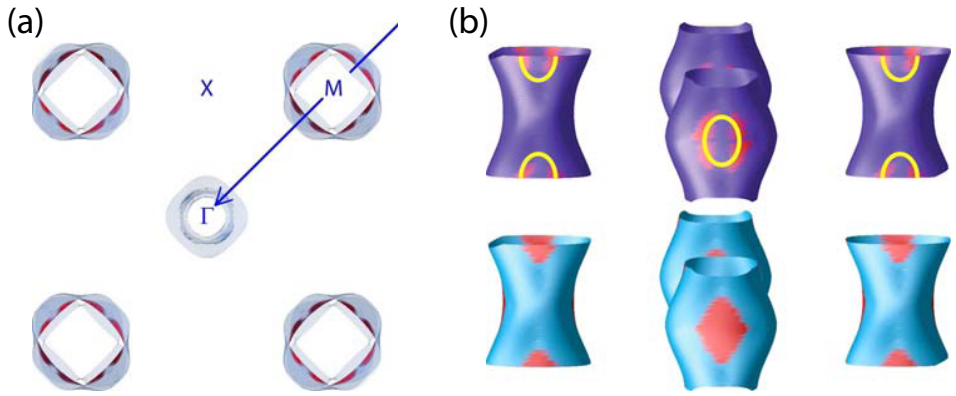

Figure 7.17: B_{2g} Raman vertex calculated via the effective-mass approximation. The electron bands are presented in the 2-Fe BZ. (a) Top view on the ab-plane. The spots where the B_{2g} vertex is maximal are indicated in red. (b) Top: Outer electron bands viewed along $M - \Gamma$ line as indicated by the arrow in the left panel. The red shaded areas mark the region where the B_{2g} vertex is maximal and the gold ellipses the regions where the nodes appear. Bottom: Outer electron bands. The region where the Fermi velocity is largest are shaded red. From [26]

can be expresses via [26]

$$\begin{aligned} A_{1g} : \gamma_n(\mathbf{k}) &= [\partial^2\varepsilon_n(\mathbf{k})/\partial^2 k_x + \partial^2\varepsilon_n(\mathbf{k})/\partial^2 k_y]/2, \\ B_{1g} : \gamma_n(\mathbf{k}) &= \partial^2\varepsilon_n(\mathbf{k})/\partial k_x \partial k_y, \\ B_{2g} : \gamma_n(\mathbf{k}) &= [\partial^2\varepsilon_n(\mathbf{k})/\partial^2 k_x - \partial^2\varepsilon_n(\mathbf{k})/\partial^2 k_y]/2. \end{aligned} \tag{7.4}$$

In Tab. 7.2 average sensitivities over the single FSs are tabulated. Via the effective-mass-approximation the symmetry considerations of Sec. 3.4, where the B_{1g} Raman vertex is most sensitive on the electron bands, are in principle corroborated. The sensitivity of the B_{2g} vertex on the electron bands is shown in Fig. 7.17. The vertex is weak on the hole bands but, in contrast to the symmetry-based vertices (Sec. 3.4), it has a rather sizable contribution from the outer electron band as illustrated by the red spots in the upper part of Fig. 7.17(b). Since the intraband contributions to the A_{1g} vertex are largely screened by backflow terms, the main contributions to the A_{1g} vertex comes from interband transitions between the outer hole and inner electron band. Thus, it follows from Tab. 7.2 that the A_{1g} response has significant contribution from the hole bands and probes the hole bands more than the B_{1g} and B_{2g} response [26].

Symmetry	h1	h2	h3	e1	e2
A_{1g} (intraband)	2.9	2.6	7.8	12.7	15.1
A_{1g} (interband)	7.7	3.6	28.6	38.9	8.6
B_{1g} (averaged)	5.2	8.5	4.8	13.8	21.8
B_{2g}	6.3	4.3	2.2	8.5	32.8

Table 7.2: Values of the Raman vertices around the hole ($h1$, $h2$, $h3$) and electron bands ($e1$, $e2$) in units of Ry. Here, $h1 \ldots h3/e1 \ldots e2$ denote the innermost...outermost hole/electron band on the FS. From [26]

7.5.3 3D gap structure on the electron bands at optimal doping

With the knowledge about the details of the sensitivity of the B_{2g} Raman vertex on the electron bands, a complete picture of the 3D gap structure of optimally doped $Ba(Fe_{1-x}Co_x)_2As_2$ can be provided. The result is illustrated in Fig. 7.18.

The analysis of the B_{1g} spectra described in Sec. 7.2 supports the occurrence of gap nodes on the electron bands. Since the B_{2g} vertex is sensitive at some hot spots on the electron bands (green ellipses in Fig. 7.18), the nodes on the electron bands [gold ellipses in Figs. 7.17(b) and 7.18(a)], must appear at exactly these spots where the B_{2g} vertex is maximal [26]. Only in this way the lack of superconductivity induced features in the B_{2g} response [Figs. 7.3(a) and 7.8(n)] can be explained. Then, the nodes on the electron bands appear where the Fermi velocity on the electron bands is highest [Fig. 7.17(b) lower part].

Moreover, according to Sec. 7.2, the logarithmic divergence of the B_{1g} superconducting peak (Fig. 7.6) provides evidence for the 2D character of the electronic properties as seen in the B_{1g} response. Since the electron bands have a substantial dispersion along k_z and therefore argue against 2D electronic properties, a B_{1g} Raman vertex with an enhanced sensitivity on 2D slices on the electron bands is required. A B_{1g} vertex compatible with the presented data is shown in Fig. 7.18(a) by the red solid circles on the equator. This vertex is two-dimensional and largest at the flared regions of the electron FS while it is small in the other regions along k_z. At exactly these 2D cuts perpendicular to k_z, the electron bands have the maximal as well as the minimal gaps [Fig. 7.18(b)]. Since in other k_z regions neither the B_{1g} nor the B_{2g} Raman vertex is sensitive at optimal doping, in these regions a more or less isotropic gap on the electron bands may occur [blue regions in the 2D cuts of Fig. 7.18(b)]. These regions in momentum space are probed by most other experimental techniques.

Thus, the strong 3D character of the anisotropic FS of '122' compounds may be at

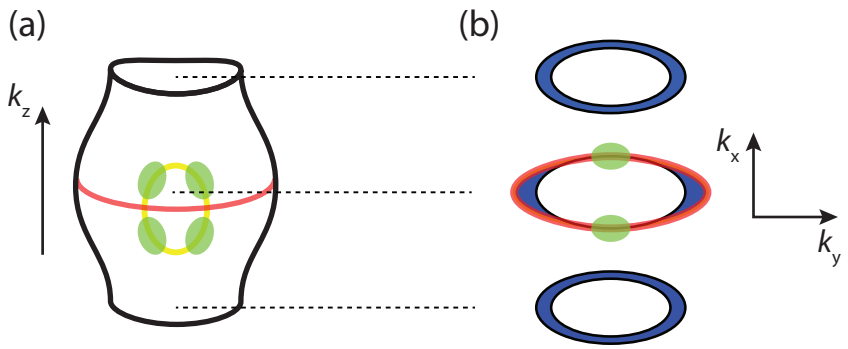

Figure 7.18: 3D Gap structure on the electron bands for optimally doped $Ba(Fe_{1-x}Co_x)_2As_2$. The green ellipses mark the position where the B_{2g} Raman vertex is largest and the red solid line shows the position where the B_{1g} vertex is most sensitive. (a) 3D view of one electron band with warping along the k_z direction. The gold ellipse indicates the position of the nodes. (b) 2D cuts through (a) at three different k_z positions. The inner white ellipses indicate the FS, while the blue portions indicate the gap size on the electron bands.

the origin of the distinct results obtained from different experimental techniques. Hence, the different results not only originate from the difference in probing the hole FS versus probing the electron FS, as suggested earlier [270], but from probing different k_z regions on the same FS [271]. In the latter study, various gap structures were considered to analyze the contradicting results of the superconducting gap obtained via penetration depth and thermal conductivity studies. The theoretically obtained gap structure to explain the discrepancies is best compatible with nodes on the flared sections of the FSs where the Fermi velocity is largest in perfect agreement with the above analysis.

Chapter 8

Summary

In this thesis a systematic study of the electronic properties of $Ba(Fe_{1-x}Co_x)_2As_2$ is described. The aim of this work was the investigation of the electronic properties in the magnetically ordered, the normal and the superconducting state as a function of doping. The doping level spans the range from the parent compound $BaFe_2As_2$ ($x = 0$) to overdoped $Ba(Fe_{1-x}Co_x)_2As_2$ ($x = 0.085$). In the superconducting state especially the electronic properties below the transition temperature are subject of interest. Therefore, the samples are investigated via inelastic light (Raman) scattering as a function of temperature, photon energy, light polarization, uniaxial pressure and doping level.

For the investigation of $Ba(Fe_{1-x}Co_x)_2As_2$ an existing Raman scattering setup was extended to the requirements mainly defined by the low scattering intensity of the iron based superconductors. This includes the installation and successful operation of a solid state laser which has a remarkably reduced power consumption compared to the Ar ion laser, which was formerly used for the data acquisition. Additionally, a detwinning device to apply uniaxial pressure was successfully constructed and used.

The undoped $Ba(Fe_{1-x}Co_x)_2As_2$ compound allows the detailed investigation of the carrier properties for different light polarizations in the low and high energy region. It could be shown that orbital transitions are present in the Raman spectra. The analysis of the high energy spectra reveals no indications of two-magnon excitations neither above nor below T_{SDW}. This argues against localized spins which are the basis of the Heisenberg model. Instead, the occurrence of a spin-density-wave (SDW) with the related opening of a nodal gap and the occurrence of a coherence peak around 390 cm^{-1} provides evidence for a more itinerant than localized spin model. The polarization dependence of the peak around 850 cm^{-1} for light polarizations parallel and perpendicular to the direction of the applied stress suggests the SDW origin of these features.

In the normal state for finite doping a pronounced polarization dependence of the

spectra is observed. Via the analysis of the Raman selection rules and form factors and their application to the band structure of $Ba(Fe_{1-x}Co_x)_2As_2$, the polarization dependent Raman spectra translate into band dependent carrier dynamics. Such band dependent carrier dynamics are similarly observed via other experiments, but without the possibility to study the contributions from the hole and electron bands separately. It could be shown that the band dependent carrier dynamics originate from the orbital character of the bands and the results of a theoretical study are in good agreement with the experimental results including the doping dependence of the calculated Raman scattering rates. The non-monotonic doping dependence of the carrier dynamics on the electron bands can be assigned to the interplay of magnetism and impurities.

The fluctuations, which occur in the Raman response of $BaFe_2As_2$ above the magnetic and structural phase transition, could be unequivocally assigned to fluctuations preceding the structural phase transition via the analysis of the temperature dependence of an underdoped $Ba(Fe_{1-x}Co_x)_2As_2$ sample. Hence, the fluctuations cannot be magnetic in origin. Rather, the comparison with other experiments strongly suggests that the fluctuations are of orbital nature.

In the superconducting state the spectra provide clear evidence for a nodal gap on the electron bands at optimal doping as opposed to what is reported by many other experiments. The analysis of the spectra as a function of doping reveals a superconducting gap, which scales with T_c on the hole bands. The gap on the electron bands exhibits a pronounced doping dependence: on the overdoped side an activation threshold in the spectrum is found indicating a finite minimal gap. On the underdoped side the gap has true nodes. The finite activation threshold in the spectra of the underdoped sample is assigned to the opening of a SDW gap.

To address the inconsistent superconducting gap structure as obtained via ERS and other experimental techniques at optimal doping, the Raman vertex is analyzed via the effective-mass-approximation. Via the following analysis of the B_{1g} and B_{2g} spectra, the gap nodes and the gap maxima on the electron bands are located. Thus, the discrepancies of the Raman results to the results of other experimental techniques at optimal doping originates from the distinct sensitivity of the experimental techniques to different regions of the rather three dimensional Fermi surface on the electron bands.

List of publications

- M. Grilli, S. Caprara, C. D. Castro, T. Enss, R. Hackl, B. Muschler, and W. Prestel, *Spectral signatures of critical charge and spin fluctuations in cuprates*, Physica B **404**, 3070 (2009), proceedings of the International Conference on Strongly Correlated Electron Systems

- B. Muschler, W. Prestel, R. Hackl, T. P. Devereaux, J. G. Analytis, J.-H. Chu, and I. R. Fisher, *Band- and momentum-dependent electron dynamics in superconducting* $Ba(Fe_{1-x}Co_x)_2As_2$ *as seen via electronic Raman scattering*, Phys. Rev. B **80**, 180510 (2009)

- M. Lavagnini, H.-M. Eiter, L. Tassini, B. Muschler, R. Hackl, R. Monnier, J.-H. Chu, I. R. Fisher, and L. Degiorgi, *Raman scattering evidence for a cascade evolution of the charge-density-wave collective amplitude mode*, Phys. Rev. B **81**, 081101 (2010)

- B. Muschler, W. Prestel, E. Schachinger, J. P. Carbotte, R. Hackl, S. Ono, and Y. Ando, *An electron-boson glue function derived from electronic Raman scattering*, J. Phys. Condens. Matter **22**, 375702 (2010)

- W. Prestel, F. Venturini, B. Muschler, I. Tüttő, R. Hackl, M. Lambacher, A. Erb, S. Komiya, S. Ono, Y. Ando, D. Inosov, V. Zabolotnyy, and S. Borisenko, *Quantitative comparison of single- and two-particle properties in the cuprates*, Eur. Phys. J. ST **188**, 163 (2010

- B. Muschler, W. Prestel, L. Tassini, R. Hackl, M. Lambacher, A. Erb, S. Komiya, Y. Ando, D. Peets, W. Hardy, R. Liang, and D. Bonn, *Electron interactions and charge ordering in* CuO_2 *compounds*, Eur. Phys. J. ST **188**, 131 (2010)

- I. I. Mazin, T. P. Devereaux, J. G. Analytis, J.-H. Chu, I. R. Fisher, B. Muschler, and R. Hackl, *Pinpointing gap minima in* $Ba(Fe_{0.94}Co_{0.06})_2As_2$ *via band-structure calculations and electronic Raman scattering*, Phys. Rev. B **82**, 180502 (2010)

- S. Caprara, C. Di Castro, B. Muschler, W. Prestel, R. Hackl, M. Lambacher, A. Erb, S. Komiya, Y. Ando, and M. Grilli, *Extracting the dynamical effective interaction and competing order from an analysis of Raman spectra of the high-temperature $La_{2-x}Sr_xCuO_4$ superconductor*, Phys. Rev. B **84**, 054508 (2011)

- B. Muschler, I. Tüttő, A. Zawadowski, J. Balogh, and R. Hackl, *Light scattering study of low-energy vibrational excitations in the metallic glass $Ni_{67}Zr_{33}$ using electronic Raman scattering*, Phys. Rev. B **84**, 104104 (2011)

- N. Munnikes, B. Muschler, F. Venturini, L. Tassini, W. Prestel, S. Ono, Y. Ando, D. C. Peets, W. N. Hardy, R. Liang, D. A. Bonn, A. Damascelli, H. Eisaki, M. Greven, A. Erb, and R. Hackl, *Pair breaking versus symmetry breaking: Origin of the Raman modes in superconducting cuprates*, Phys. Rev. B **84**, 144523 (2011)

- B. Moritz, S. Johnston, T. P. Devereaux, B. Muschler, W. Prestel, R. Hackl, M. Lambacher, A. Erb, S. Komiya, and Y. Ando, *Investigation of particle-hole asymmetry in the cuprates via electronic Raman scattering*, Phys. Rev. B **84**, 235114 (2011)

- F. Kretzschmar, B. Muschler, T. Böhm, A. Baum, R. Hackl, Hai-Hu Wen, V. Tsurkan, J. Deisenhofer, and A. Loidl, *Observation of s and d-wave pairing channels in iron-based superconductors*, submitted for publication (2012)

Bibliography

[1] Y. Kamihara, H. Hiramatsu, M. Hirano, R. Kawamura, H. Yanagi, T. Kamiya, and H. Hosono, *Iron-Based Layered Superconductor: LaOFeP*, J. Am. Chem. Soc.. **128**, 10012 (2006).

[2] Y. Kamihara, T. Watanabe, M. Hirano, and H. Hosono, *Iron-Based Layered Superconductor La[$O_{1-x}F_x$]FeAs (x = 0.05-0.12) with T_c = 26 K*, J. Am. Chem. Soc. **130**, 3296 (2008).

[3] G. Wu, Y. L. Xie, H. Chen, M. Zhong, R. H. Liu, B. C. Shi, Q. J. Li, X. F. Wang, T. Wu, Y. J. Yan, J. J. Ying, and X. H. Chen, *Superconductivity at 56 K in samarium-doped SrFeAsF*, Condens. Matter **21**, 142203 (2009).

[4] J. Nagamatsu, N. Nakagawa, T. Muranaka, Y. Zenitani, and J. Akimitsu, *Superconductivity at 39 K in magnesium diboride*, Nature **410**, 63 (2001).

[5] J. G. Bednorz and K. A. Müller, *Possible high T_c superconductivity in the Ba-La-Cu-O System*, Z. Phys. B **64**, 189 (1986).

[6] N. F. Mott, *Metal-Insulator Transition*, Rev. Mod. Phys. **40**, 677 (1968).

[7] J.-H. Chu, J. G. Analytis, C. Kucharczyk, and I. R. Fisher, *Determination of the phase diagram of the electron-doped superconductor $Ba(Fe_{1-x}Co_x)_2As_2$*, Phys. Rev. B **79**, 014506 (2009).

[8] M.-H. Julien, H. Mayaffre, M. Horvatic, C. Berthier, X. Zhang, W. Wu, G. Chen, N. Wang, and J. Luo, *Homogeneous vs. inhomogeneous coexistence of magnetic order and superconductivity probed by NMR in Co- and K-doped iron pnictides*, Eur. Phys. Lett. **87**, 37001 (2009).

[9] C. C. Tsuei and J. R. Kirtley, *Pairing symmetry in cuprate superconductors*, Rev. Mod. Phys. **72**, 969 (2000).

[10] K. Kuroki, S. Onari, R. Arita, H. Usui, Y. Tanaka, H. Kontani, and H. Aoki, *Unconventional Pairing Originating from the Disconnected Fermi Surfaces of Superconducting $LaFeAsO_{1-x}F_x$*, Phys. Rev. Lett. **101**, 087004 (2008).

[11] R. A. Ewings, T. G. Perring, J. Gillett, S. D. Das, S. E. Sebastian, A. E. Taylor, T. Guidi, and A. T. Boothroyd, *Itinerant spin excitations in $SrFe_2As_2$ measured by inelastic neutron scattering*, Phys. Rev. B **83**, 214519 (2011).

[12] K. Okazaki, S. Sugai, S. Niitaka, and H. Takagi, *Phonon, two-magnon, and electronic Raman scattering of $Fe_{1+y}Te_{1-x}Se_x$*, Phys. Rev. B **83**, 035103 (2011).

[13] J. Tranquada, in *Treatise of High Temperature Superconductivity*, edited by J. Schrieffer (Springer, ADDRESS, 2007).

[14] K. Prokeš, S. Mat'aš, L. Harnagea, S. Singh, S. Wurmehl, D. N. Argyriou, and B. Büchner, *Effect of Co substitution on the magnetic order in $\mathbf{Ca}(\mathbf{Fe}_{1-x}Co_x)_2As_2$ single crystals studied by neutron diffraction*, Phys. Rev. B **83**, 104414 (2011).

[15] S. A. Kivelson, E. Fradkin, and V. J. Emery, *Electronic liquid-crystal phases of a doped Mott insulator*, Nature **393**, 550 (1998).

[16] R. M. Fernandes, E. Abrahams, and J. Schmalian, *Anisotropic In-Plane Resistivity in the Nematic Phase of the Iron Pnictides*, Phys. Rev. Lett. **107**, 217002 (2011).

[17] R. M. Fernandes, A. V. Chubukov, J. Knolle, I. Eremin, and J. Schmalian, *Preemptive nematic order, pseudogap, and orbital order in the iron pnictides*, Phys. Rev. B **85**, 024534 (2012).

[18] F. Krüger, S. Kumar, J. Zaanen, and J. van den Brink, *Spin-orbital frustrations and anomalous metallic state in iron-pnictide superconductors*, Phys. Rev. B **79**, 054504 (2009).

[19] R. M. Fernandes, L. H. VanBebber, S. Bhattacharya, P. Chandra, V. Keppens, D. Mandrus, M. A. McGuire, B. C. Sales, A. S. Sefat, and J. Schmalian, *Effects of Nematic Fluctuations on the Elastic Properties of Iron Arsenide Superconductors*, Phys. Rev. Lett. **105**, 157003 (2010).

[20] S. Graser, T. Maier, P. Hirschfeld, and D. Scalapino, *Near-degeneracy of several pairing channels in multiorbital models for the Fe pnictides*, New J. Phys. **11**, 025016 (2009).

[21] A. Lucarelli, A. Dusza, F. Pfuner, P. Lerch, J. G. Analytis, J.-H. Chu, I. R. Fisher, and L. Degiorgi, *Charge dynamics of Co-doped $BaFe_2As_2$*, New J. Phys. **12**, 073036 (2010).

[22] F. Rullier-Albenque, D. Colson, A. Forget, and H. Alloul, *Hall Effect and Resistivity Study of the Magnetic Transition, Carrier Content, and Fermi-Liquid Behavior in $Ba(Fe_{1-x}Co_x)_2As_2$*, Phys. Rev. Lett. **103**, 057001 (2009).

[23] A. I. Coldea, J. D. Fletcher, A. Carrington, J. G. Analytis, A. F. Bangura, J.-H. Chu, A. S. Erickson, I. R. Fisher, N. E. Hussey, and R. D. McDonald, *Fermi Surface of Superconducting LaFePO Determined from Quantum Oscillations*, Phys. Rev. Lett. **101**, 216402 (2008).

[24] T. P. Devereaux, D. Einzel, B. Stadlober, R. Hackl, D. H. Leach, and J. J. Neumeier, *Electronic Raman scattering in high–T_c superconductors: A probe of d_{x2-y2} pairing*, Phys. Rev. Lett. **72**, 396 (1994).

[25] B. Muschler, W. Prestel, R. Hackl, T. P. Devereaux, J. G. Analytis, J.-H. Chu, and I. R. Fisher, *Band- and momentum-dependent electron dynamics in superconducting $Ba(Fe_{1-x}Co_x)_2As_2$ as seen via electronic Raman scattering*, Phys. Rev. B **80**, 180510 (2009).

[26] I. I. Mazin, T. P. Devereaux, J. G. Analytis, J.-H. Chu, I. R. Fisher, B. Muschler, and R. Hackl, *Pinpointing gap minima in $Ba(Fe_{0.94}Co_{0.06})_2As_2$ via band-structure calculations and electronic Raman scattering*, Phys. Rev. B **82**, 180502 (2010).

[27] F. Venturini, M. Opel, T. P. Devereaux, J. K. Freericks, I. Tüttő, B. Revaz, E. Walker, H. Berger, L. Forró, and R. Hackl, *Observation of an Unconventional Metal-Insulator Transition in Overdoped CuO_2 Compounds*, Phys. Rev. Lett. **89**, 107003 (2002).

[28] R. Hackl, W. Gläser, P. Müller, D. Einzel, and K. Andres, *Light-scattering study of the superconducting energy gap in $YBa_2Cu_3O_7$ single crystals*, Phys. Rev. B **38**, 7133 (1988).

[29] H. Monien and A. Zawadowski, *Theory of interband electron Raman scattering in $YBa_2Cu_3O_7$: A probe of unconventional superconductivity*, Phys. Rev. Lett. **63**, 911 (1989).

[30] L. Falkovsky and S. Klama, *Electronic Raman light scattering in zero-gap anisotropic superconductors*, Physica C **172**, 242 (1990).

[31] K. B. Lyons, P. A. Fleury, J. P. Remeika, A. S. Cooper, and T. J. Negran, *Dynamics of spin fluctuations in lanthanum cuprate*, Phys. Rev. B **37**, 2353 (1988).

[32] P. J. Freitas and R. R. P. Singh, *Two-magnon Raman scattering in insulating cuprates: Modifications of the effective Raman operator*, Phys. Rev. B **62**, 5525 (2000).

[33] C.-C. Chen, C. J. Jia, A. F. Kemper, R. R. P. Singh, and T. P. Devereaux, *Theory of Two-Magnon Raman Scattering in Iron Pnictides and Chalcogenides*, Phys. Rev. Lett. **106**, 067002 (2011).

[34] K. Ishida, Y. Nakai, and H. Hosono, *To What Extent Iron-Pnictide New Superconductors Have Been Clarified: A Progress Report*, J. Phys. Soc. Jpn **78**, 062001 (2009).

[35] D. Johrendt, *Structure - property relationships of iron arsenide superconductors*, J. Mater. Chem. **21**, 13726 (2011).

[36] P. M. Shirage, K. Kihou, C.-H. Lee, H. Kito, H. Eisaki, and A. Iyo, *Emergence of Superconductivity in "32522" Structure of $(Ca_3Al_2O_{5-y})(Fe_2Pn_2)$ (Pn = As and P)*, J. Am. Chem. Soc. **133**, 9630 (2011).

[37] N. Ni, Jared, M. Allred, B. C. Chan, and R. J. Cava, *Electron doped $Ca_{10}(Pt_3As_8)(Fe_2As_2)_5$ and $Ca_{10}(Pt_4As_8)(Fe_2As_2)_5$ - High Tc superconductors with skutterudite intermediary layers*, Proc. Natl. Acad. Sci, **108**, E1019 (2011).

[38] S. Kakiya, K. Kudo, Y. Nishikubo, K. Oku, E. Nishibori, H. Sawa, T. Yamamoto, T. Nozaka, and M. Nohara, *Superconductivity at 38 K in Iron-Based Compound with Platinum–Arsenide Layers $Ca_{10}(Pt_4As_8)(Fe_{2-x}Pt_xAs_2)_5$*, J. Phys. Soc. Jpn. **80**, 093704 (2011).

[39] C. Löhnert, T. Stürzer, M. Tegel, R. Frankovsky, G. Friederichs, and D. Johrendt, *Superconductivity up to 35 K in the Iron Platinum Arsenides $(CaFe_{1-x}Pt_xAs)_{10}Pt_{4-y}As_8$ with Layered Structures*, Angew. Chem. Int. Ed. **50**, 9195 (2011).

[40] B. I. Zimmer, W. Jeitschko, J. H. Albering, R. Glaum, and M. Reehuis, *The rare earth transition metal phosphide oxides LnFePO, LnRuPO and LnCoPO with ZrCuSiAs type structure*, J. Alloys Compd. **229**, 238 (1995).

[41] B. I. Zimmer, Dissertation, Universität Münster, 1996.

[42] M. Rotter, M. Tegel, and D. Johrendt, *Superconductivity at 38 K in the Iron Arsenide $(Ba_{1-x}K_x)Fe_2As_2$*, Phys. Rev. Lett. **101**, 107006 (2008).

[43] X. Wang, Q. Liu, Y. Lv, W. Gao, L. Yang, R. Yu, F. Li, and C. Jin, *The superconductivity at 18 K in LiFeAs system*, Solid State Commun. **148**, 538 (2008).

[44] W. Si, Z.-W. Lin, Q. Jie, W.-G. Yin, J. Zhou, G. Gu, P. D. Johnson, and Q. Li, *Enhanced superconducting transition temperature in $FeSe_{0.5}Te_{0.5}$ thin films*, Appl. Phys. Lett. **95**, 052504 (2009).

[45] J. E. Hoffman, *Spectroscopic scanning tunneling microscopy insights into Fe-based superconductors*, Rep. Prog. Phys. **74**, 124513 (2011).

[46] C.-H. Lee, A. Iyo, H. Eisaki, H. Kito, M. T. Fernandez-Diaz, T. Ito, K. Kihou, H. Matsuhata, M. Braden, and K. Yamada, *Effect of Structural Parameters on Superconductivity in Fluorine-Free $LnFeAsO_{1-y}$ (Ln = La, Nd)*, J. Phys. Soc. Jpn **77**, 083704 (2008).

[47] A. P. Litvinchuk, V. G. Hadjiev, M. N. Iliev, B. Lv, A. M. Guloy, and C. W. Chu, *Raman-scattering study of $K_xSr_{1-x}Fe_2As_2$ (x = 0.0,0.4)*, Phys. Rev. B **78**, 060503 (2008).

[48] S. Avci, O. Chmaissem, E. A. Goremychkin, S. Rosenkranz, J.-P. Castellan, D. Y. Chung, I. S. Todorov, J. A. Schlueter, H. Claus, M. G. Kanatzidis, A. Daoud-Aladine, D. Khalyavin, and R. Osborn, *Magnetoelastic coupling in the phase diagram of $Ba_{1-x}K_xFe_2As_2$ as seen via neutron diffraction*, Phys. Rev. B **83**, 172503 (2011).

[49] K. Nakamura, R. Arita, and H. Ikeda, *First-principles calculation of transition-metal impurities in LaFeAsO*, Phys. Rev. B **83**, 144512 (2011).

[50] A. S. Sefat, R. Jin, M. A. McGuire, B. C. Sales, D. J. Singh, and D. Mandrus, *Superconductivity at 22 K in Co-Doped $BaFe_2As_2$ Crystals*, Phys. Rev. Lett. **101**, 117004 (2008).

[51] H. Wadati, I. Elfimov, and G. A. Sawatzky, *Where Are the Extra d Electrons in Transition-Metal-Substituted Iron Pnictides?*, Phys. Rev. Lett. **105**, 157004 (2010).

[52] E. M. Bittar, C. Adriano, T. M. Garitezi, P. F. S. Rosa, L. Mendon ça Ferreira, F. Garcia, G. d. M. Azevedo, P. G. Pagliuso, and E. Granado, *Co-Substitution Effects on the Fe Valence in the $BaFe_2As_2$ Superconducting Compound: A Study of Hard X-Ray Absorption Spectroscopy*, Phys. Rev. Lett. **107**, 267402 (2011).

[53] S. Jiang, H. Xing, G. Xuan, C. Wang, Z. Ren, C. Feng, J. Dai, Z. Xu, and G. Cao, *Superconductivity up to 30 K in the vicinity of the quantum critical point in $BaFe_2(As_{1-x}P_x)_2$*, Condens. Matter **21**, 382203 (2009).

[54] S. Sharma, A. Bharathi, S. Chandra, V. R. Reddy, S. Paulraj, A. T. Satya, V. S. Sastry, A. Gupta, and C. S. Sundar, *Superconductivity in Ru-substituted polycrystalline $BaFe_{2-x}Ru_xAs_2$*, Phys. Rev. B **81**, 174512 (2010).

[55] P. L. Alireza, Y. T. C. Ko, J. Gillett, C. M. Petrone, J. M. Cole, G. G. Lonzarich, and S. E. Sebastian, *Superconductivity up to 29 K in $SrFe_2As_2$ and $BaFe_2As_2$ at high pressures*, J. Phys. Condens. Matter **21**, 012208 (2009).

[56] E. Colombier, S. L. Bud'ko, N. Ni, and P. C. Canfield, *Complete pressure-dependent phase diagrams for $SrFe_2As_2$ and $BaFe_2As_2$*, Phys. Rev. B **79**, 224518 (2009).

[57] T. Yamazaki, N. Takeshita, R. Kobayashi, H. Fukazawa, Y. Kohori, K. Kihou, C.-H. Lee, H. Kito, A. Iyo, and H. Eisaki, *Appearance of pressure-induced superconductivity in $BaFe_2As_2$ under hydrostatic conditions and its extremely high sensitivity to uniaxial stress*, Phys. Rev. B **81**, 224511 (2010).

[58] H. Luetkens, H.-H. Klauss, M. Kraken, F. J. Litterst, T. Dellmann, R. Klingeler, C. Hess, R. Khasanov, A. Amato, C. Baines, M. Kosmala, O. J. Schumann, M. Braden, J. Hamann-Borrero, N. Leps, A. Kondrat, G. Behr, J. Werner, and B. Buchner, *The electronic phase diagram of the $LaO_{1-x}F_xFeAs$ superconductor*, Nat. Mater. **8**, 305 (2009).

[59] D. Johnston, *The Puzzle of High Temperature Superconductivity in Layered Iron Pnictides and Chalcogenides* , Adv. Phys. **59**, 803 (2010).

[60] J.-H. Chu, J. G. Analytis, K. D. Greve, P. L. McMahon, Z. Islam, Y. Yamamoto, and I. R. Fisher, *In-Plane Resistivity Anisotropy in an Underdoped Iron Arsenide Superconductor*, Science **329**, 824 (2010).

[61] T. Sato, K. Nakayama, Y. Sekiba, P. Richard, Y.-M. Xu, S. Souma, T. Takahashi, G. F. Chen, J. L. Luo, N. L. Wang, and H. Ding, *Band Structure and Fermi Surface of an Extremely Overdoped Iron-Based Superconductor KFe_2As_2*, Phys. Rev. Lett. **103**, 047002 (2009).

[62] D. K. Pratt, W. Tian, A. Kreyssig, J. L. Zarestky, S. Nandi, N. Ni, S. L. Bud'ko, P. C. Canfield, A. I. Goldman, and R. J. McQueeney, *Coexistence of Competing Antiferromagnetic and Superconducting Phases in the Underdoped $Ba(Fe_{0.953}Co_{0.047})_2As_2$ Compound Using X-ray and Neutron Scattering Techniques*, Phys. Rev. Lett. **103**, 087001 (2009).

[63] E. Wiesenmayer, H. Luetkens, G. Pascua, R. Khasanov, A. Amato, H. Potts, B. Banusch, H.-H. Klauss, and D. Johrendt, *Microscopic Coexistence of Superconductivity and Magnetism in $Ba_{1-x}K_xFe_2As_2$*, Phys. Rev. Lett. **107**, 237001 (2011).

[64] K. Kitagawa, N. Katayama, K. Ohgushi, M. Yoshida, and M. Takigawa, *Commensurate Itinerant Antiferromagnetism in $BaFe_2As_2$: ^{75}As-NMR Studies on a Self-Flux Grown Single Crystal*, J. Phys. Soc. Jpn **77**, 114709 (2008).

[65] A. Jesche, N. Caroca-Canales, H. Rosner, H. Borrmann, A. Ormeci, D. Kasinathan, H. H. Klauss, H. Luetkens, R. Khasanov, A. Amato, A. Hoser, K. Kaneko, C. Krellner, and C. Geibel, *Strong coupling between magnetic and structural order parameters in $SrFe_2As_2$*, Phys. Rev. B **78**, 180504 (2008).

[66] A. I. Goldman, D. N. Argyriou, B. Ouladdiaf, T. Chatterji, A. Kreyssig, S. Nandi, N. Ni, S. L. Bud'ko, P. C. Canfield, and R. J. McQueeney, *Lattice and magnetic instabilities in $CaFe_2As_2$: A single-crystal neutron diffraction study*, Phys. Rev. B **78**, 100506 (2008).

[67] S. D. Wilson, Z. Yamani, C. R. Rotundu, B. Freelon, E. Bourret-Courchesne, and R. J. Birgeneau, *Neutron diffraction study of the magnetic and structural phase transitions in $BaFe_2As_2$*, Phys. Rev. B **79**, 184519 (2009).

[68] M. G. Kim, R. M. Fernandes, A. Kreyssig, J. W. Kim, A. Thaler, S. L. Bud'ko, P. C. Canfield, R. J. McQueeney, J. Schmalian, and A. I. Goldman, *Character of the structural and magnetic phase transitions in the parent and electron-doped $BaFe_2As_2$ compounds*, Phys. Rev. B **83**, 134522 (2011).

[69] D. J. Singh and M.-H. Du, *Density Functional Study of $LaFeAsO_{1-x}F_x$: A Low Carrier Density Superconductor Near Itinerant Magnetism*, Phys. Rev. Lett. **100**, 237003 (2008).

[70] D. J. Singh, *Electronic structure and doping in $BaFe_2As_2$ and LiFeAs: Density functional calculations*, Phys. Rev. B **78**, 094511 (2008).

[71] C. Cao, P. J. Hirschfeld, and H.-P. Cheng, *Proximity of antiferromagnetism and superconductivity in $LaFeAsO_{1-x}F$: Effective Hamiltonian from ab initio studies*, Phys. Rev. B **77**, 220506 (2008).

[72] K. Haule, J. H. Shim, and G. Kotliar, *Correlated Electronic Structure of* $LaO_{1-x}F_xFeAs$, Phys. Rev. Lett. **100**, 226402 (2008).

[73] Y.-M. Xu, P. Richard, K. Nakayama, T. Kawahara, Y. Sekiba, T. Qian, M. Neupane, S. Souma, T. Sato, T. Takahashi, H.-Q. Luo, H.-H. Wen, G.-F. Chen, N.-L. Wang, Z. Wang, Z. Fang, X. Dai, and H. Ding, *Fermi surface dichotomy of the superconducting gap and pseudogap in underdoped pnictides*, Nat. Comm. **2**, 392 (2011).

[74] I. I. Mazin and J. Schmalian, *Pairing symmetry and pairing state in ferropnictides: Theoretical overview* , Physica C **469**, 614 (2009).

[75] H. Ding, P. Richard, K. Nakayama, K. Sugawara, T. Arakane, Y. Sekiba, A. Takayama, S. Souma, T. Sato, T. Takahashi, Z. Wang, X. Dai, Z. Fang, G. F. Chen, J. L. Luo, and N. L. Wang, *Observation of Fermi-surface–dependent nodeless superconducting gaps in* $Ba_{0.6}K_{0.4}Fe_2As_2$, Europhys. Lett. **83**, 47001 (2008).

[76] V. B. Zabolotnyy, D. S. Inosov, D. Evtushinsky, A. Koitzsch, A. A. Kordyuk, G. L. Sun, J. T. Park, D. Haug, V. Hinkov, A. V. Boris, C. T. Lin, M. Knupfer, A. N. Yaresko, B. Büchner, A. Varykhalov, R. Follath, and S. V. Borisenko, (π, π) *electronic order in iron arsenide superconductors*, Nature **457**, 569 (2009).

[77] K. Terashima, Y. Sekiba, J. H. Bowen, K. Nakayama, T. Kawahara, T. Sato, P. Richard, Y.-M. Xu, L. J. Li, G. H. Cao, Z.-A. Xu, H. Ding, and T. Takahashi, *Fermi surface nesting induced strong pairing in iron-based superconductors*, Proceed. Nat. Acad. Sci. **106**, 7330 (2009).

[78] Y. Zhang, F. Chen, C. He, B. Zhou, B. P. Xie, C. Fang, W. F. Tsai, X. H. Chen, H. Hayashi, J. Jiang, H. Iwasawa, K. Shimada, H. Namatame, M. Taniguchi, J. P. Hu, and D. L. Feng, *Orbital characters of bands in the iron-based superconductor* $BaFe_{1.85}Co_{0.15}As_2$, Phys. Rev. B **83**, 054510 (2011).

[79] T. Sudayama, Y. Wakisaka, K. Takubo, R. Morinaga, T. J. Sato, M. Arita, H. Namatame, M. Taniguchi, and T. Mizokawa, *Band Structure of the Heavily-Electron-Doped FeAs-Based* $Ba(Fe,Co)_2As_2$ *Superconductor Suppresses Antiferromagnetic Correlations*, Phys. Rev. Lett. **104**, 177002 (2010).

[80] Y. Sekiba, T. Sato, K. Nakayama, K. Terashima, P. Richard, J. H. Bowen, H. Ding, Y.-M. Xu, L. J. Li, G. H. Cao, Z.-A. Xu, and T. Takahashi, *Electronic structure of heavily electron-doped* $BaFe_{1.7}Co_{0.3}As_2$ *studied by angle-resolved photoemission*, New J. Phys. **11**, 025020 (2009).

[81] R. Hackl, *Superconductivity in copper-oxygen compounds*, Z. Kristallogr. **226**, 323 (2011).

[82] B. Mansart, V. Brouet, E. Papalazarou, M. Fuglsang Jensen, L. Petaccia, S. Gorovikov, A. N. Grum-Grzhimailo, F. Rullier-Albenque, A. Forget, D. Colson,

and M. Marsi, *Orbital nature of the hole-like Fermi surface in superconducting* $Ba(Fe_{1-x}Co_x)_2As_2$, Phys. Rev. B **83**, 064516 (2011).

[83] V. Brouet, M. Fuglsang Jensen, A. Nicolaou, A. Taleb-Ibrahimi, P. Le Fèvre, F. Bertran, A. Forget, and Cols, arXiv:1105.5604 (unpublished).

[84] A. Kemper, T. Maier, S. Graser, H.-P. Cheng, P. Hirschfeld, and D. Scalapino, *Sensitivity of the superconducting state and magnetic susceptibility to key aspects of electronic structure in ferropnictides* , New J. Phys. **12**, 073030 (2010).

[85] C.-C. Chen, B. Moritz, J. van den Brink, T. P. Devereaux, and R. R. P. Singh, *Finite-temperature spin dynamics and phase transitions in spin-orbital models*, Phys. Rev. B **80**, 180418 (2009).

[86] A. F. Kemper, M. M. Korshunov, T. P. Devereaux, J. N. Fry, H.-P. Cheng, and P. J. Hirschfeld, *Anisotropic quasiparticle lifetimes in Fe-based superconductors*, Phys. Rev. B **83**, 184516 (2011).

[87] E. Fradkin, S. A. Kivelson, M. J. Lawler, J. P. Eisenstein, and A. P. Mackenzie, *Nematic Fermi Fluids in Condensed Matter Physics*, Annu. Rev. Cond. Mat. Phys. **1**, 153 (2010).

[88] S. A. Kivelson, I. P. Bindloss, E. Fradkin, V. Oganesyan, J. M. Tranquada, A. Kapitulnik, and C. Howald, *How to detect fluctuating stripes in the high-temperature superconductors*, Rev. Mod. Phys. **75**, 1201 (2003).

[89] J. J. Ying, X. F. Wang, T. Wu, Z. J. Xiang, R. H. Liu, Y. J. Yan, A. F. Wang, M. Zhang, G. J. Ye, P. Cheng, J. P. Hu, and X. H. Chen, *Measurements of the Anisotropic In-Plane Resistivity of Underdoped FeAs-Based Pnictide Superconductors*, Phys. Rev. Lett. **107**, 067001 (2011).

[90] J. Zhao, D. T. Adroja, D.-X. Yao, R. Bewley, S. Li, X. F. Wang, G. Wu, X. H. Chen, J. Hu, and P. Dai, *Spin waves and magnetic exchange interactions in* $CaFe_2As_2$, Nat. Phys. **5**, 555 (2009).

[91] T.-M. Chuang, M. Allan, J. Lee, Y. Xie, N. Ni, S. Budko, G. Boebinger, P. Canfield, and J. C. Davis, *Nematic Electronic Structure in the "Parent" State of the Iron-Based Superconductor* $Ca(Fe_{1-x}Co_x)_2As_2$, Science **327**, 181 (2010).

[92] W.-C. Lee and P. W. Phillips, arXiv:1110.5917 (unpublished).

[93] C. Fang, H. Yao, W.-F. Tsai, J. Hu, and S. A. Kivelson, *Theory of electron nematic order in LaFeAsO*, Phys. Rev. B **77**, 224509 (2008).

[94] C. Xu, M. Müller, and S. Sachdev, *Ising and spin orders in the iron-based superconductors*, Phys. Rev. B **78**, 020501 (2008).

[95] C.-C. Chen, J. Maciejko, A. P. Sorini, B. Moritz, R. R. P. Singh, and T. P. Devereaux, *Orbital order and spontaneous orthorhombicity in iron pnictides*, Phys. Rev. B **82**, 100504 (2010).

[96] W. Lv, J. Wu, and P. Phillips, *Orbital ordering induces structural phase transition and the resistivity anomaly in iron pnictides*, Phys. Rev. B **80**, 224506 (2009).

[97] F. Ning, K. Ahilan, T. Imai, A. S. Sefat, R. Jin, M. A. McGuire, B. C. Sales, and D. Mandrus, *Spin Susceptibility, Phase Diagram, and Quantum Criticality in the Eelctron-Doped High T_c Superconductor $Ba(Fe_{1-x}Co_x)_2As_2$*, J. Phys. Soc. Jpn **78**, 013711 (2009).

[98] I. I. Mazin, D. J. Singh, M. D. Johannes, and M. H. Du, *Unconventional Superconductivity with a Sign Reversal in the Order Parameter of $LaFeAsO_{1-x}F_x$*, Phys. Rev. Lett. **101**, 057003 (2008).

[99] J. Wu and P. Phillips, *Magnon-mediated pairing and isotope effect in iron-based superconductors*, J.Phys. Cond. Matt. **23**, 094203 (2011).

[100] T. A. Maier, D. Poilblanc, and D. J. Scalapino, *Dynamics of the Pairing Interaction in the Hubbard and $t-J$ Models of High-Temperature Superconductors*, Phys. Rev. Lett. **100**, 237001 (2008).

[101] C. de la Cruz, Q. Huang, J. Lynn, J. Li, W. R. II, J. Zarestky, H. Mook, G. Chen, J. Luo, N. Wang, and P. Dai, *Magnetic order close to superconductivity in the iron-based layered $LaO_{1-x}F_xFeAs$ systems*, Nature **453**, 899 (2008).

[102] Q. Huang, Y. Qiu, W. Bao, M. A. Green, J. W. Lynn, Y. C. Gasparovic, T. Wu, G. Wu, and X. H. Chen, *Neutron–Diffraction Measurements of Magnetic Order and a Structural Transition in the Parent $BaFe_2As_2$ Compound of FeAs-Based High–Temperature Superconductors*, Phys. Rev. Lett. **101**, 257003 (2008).

[103] K. Matan, R. Morinaga, K. Iida, and T. J. Sato, *Anisotropic itinerant magnetism and spin fluctuations in $BaFe_2As_2$: A neutron scattering study*, Phys. Rev. B **79**, 054526 (2009).

[104] S. Ishibashi, K. Terakura, and H. Hosono, *A Possible Ground State and Its Electronic Structure of a Mother Material (LaOFeAs) of New Superconductors*, J. Phys. Soc. Jpn **77**, 053709 (2008).

[105] P. Hansmann, R. Arita, A. Toschi, S. Sakai, G. Sangiovanni, and K. Held, *Dichotomy between Large Local and Small Ordered Magnetic Moments in Iron-Based Superconductors*, Phys. Rev. Lett. **104**, 197002 (2010).

[106] D. K. Pratt, M. G. Kim, A. Kreyssig, Y. B. Lee, G. S. Tucker, A. Thaler, W. Tian, J. L. Zarestky, S. L. Bud'ko, P. C. Canfield, B. N. Harmon, A. I. Goldman, and R. J. McQueeney, *Incommensurate Spin-Density Wave Order in Electron-Doped $BaFe_2As_2$ Superconductors*, Phys. Rev. Lett. **106**, 257001 (2011).

[107] M. M. Qazilbash, J. J. Hamlin, R. E. Baumbach, L. Zhang, D. J. Singh, M. B. Maple, and D. N. Basov, *Electronic correlations in the iron pnictides*, Nat. Phys. **5**, 647 (2009).

[108] Z. P. Yin, S. Lebègue, M. J. Han, B. P. Neal, S. Y. Savrasov, and W. E. Pickett, *Electron-Hole Symmetry and Magnetic Coupling in Antiferromagnetic LaFeAsO*, Phys. Rev. Lett. **101**, 047001 (2008).

[109] M. J. Han, Q. Yin, W. E. Pickett, and S. Y. Savrasov, *Anisotropy, Itineracy, and Magnetic Frustration in High-T_c Iron Pnictides*, Phys. Rev. Lett. **102**, 107003 (2009).

[110] S. E. Sebastian, J. Gillett, N. Harrison, P. H. C. Lau, D. J. Singh, C. H. Mielke, and G. G. Lonzarich, *Quantum oscillations in the parent magnetic phase of an iron arsenide high temperature superconductor*, J. Phys. Condens. Matter **20**, 422203 (2008).

[111] Y. Ran, F. Wang, H. Zhai, A. Vishwanath, and D.-H. Lee, *Nodal spin density wave and band topology of the FeAs-based materials*, Phys. Rev. B **79**, 014505 (2009).

[112] D. Parker, M. G. Vavilov, A. V. Chubukov, and I. I. Mazin, *Coexistence of superconductivity and a spin-density wave in pnictide superconductors: Gap symmetry and nodal lines*, Phys. Rev. B **80**, 100508 (2009).

[113] M. Yi, D. H. Lu, J. G. Analytis, J.-H. Chu, S.-K. Mo, R.-H. He, M. Hashimoto, R. G. Moore, I. I. Mazin, D. J. Singh, Z. Hussain, I. R. Fisher, and Z.-X. Shen, *Unconventional electronic reconstruction in undoped (Ba,Sr)Fe_2As_2 across the spin density wave transition*, Phys. Rev. B **80**, 174510 (2009).

[114] J. G. Analytis, R. D. McDonald, J.-H. Chu, S. C. Riggs, A. F. Bangura, C. Kucharczyk, M. Johannes, and I. R. Fisher, *Quantum oscillations in the parent pnictide $BaFe_2As_2$: Itinerant electrons in the reconstructed state*, Phys. Rev. B **80**, 064507 (2009).

[115] T. Terashima, N. Kurita, M. Tomita, K. Kihou, C.-H. Lee, Y. Tomioka, T. Ito, A. Iyo, H. Eisaki, T. Liang, M. Nakajima, S. Ishida, S.-i. Uchida, H. Harima, and S. Uji, *Complete Fermi Surface in $BaFe_2As_2$ Observed via Shubnikov˘de Haas Oscillation Measurements on Detwinned Single Crystals*, Phys. Rev. Lett. **107**, 176402 (2011).

[116] C. Liu, G. D. Samolyuk, Y. Lee, N. Ni, T. Kondo, A. F. Santander-Syro, S. L. Bud'ko, J. L. McChesney, E. Rotenberg, T. Valla, A. V. Fedorov, P. C. Canfield, B. N. Harmon, and A. Kaminski, *K-Doping Dependence of the Fermi Surface of the Iron-Arsenic $Ba_{1-x}K_xFe_2As_2$ Superconductor Using Angle-Resolved Photoemission Spectroscopy*, Phys. Rev. Lett. **101**, 177005 (2008).

[117] L. X. Yang *et al.*, *Electronic Structure and Unusual Exchange Splitting in the Spin-Density-Wave State of the $BaFe_2As_2$ Parent Compound of Iron-Based Superconductors*, Phys. Rev. Lett. **102**, 107002 (2009).

[118] F. Chen, Y. Zhang, J. Wei, B. Zhou, L. Yang, F. Wu, G. Wu, X. Chen, and D. Feng, *Electronic structure reconstruction of $CaFe_2As_2$ in the spin density wave state*, J. Phys. Chem. Solids **72**, 469 (2011).

[119] T. Shimojima, K. Ishizaka, Y. Ishida, N. Katayama, K. Ohgushi, T. Kiss, M. Okawa, T. Togashi, X.-Y. Wang, C.-T. Chen, S. Watanabe, R. Kadota, T. Oguchi, A. Chainani, and S. Shin, *Orbital-Dependent Modifications of Electronic Structure across the Magnetostructural Transition in $BaFe_2As_2$*, Phys. Rev. Lett. **104**, 057002 (2010).

[120] Y. Kim, H. Oh, C. Kim, D. Song, W. Jung, B. Kim, H. J. Choi, C. Kim, B. Lee, S. Khim, H. Kim, K. Kim, J. Hong, and Y. Kwon, *Electronic structure of detwinned $BaFe_2As_2$ from photoemission and first principles*, Phys. Rev. B **83**, 064509 (2011).

[121] L. Boeri, O. V. Dolgov, and A. A. Golubov, *Is $LaFeAsO_{1-x}F_x$ an Electron-Phonon Superconductor?*, Phys. Rev. Lett. **101**, 026403 (2008).

[122] S. Higashitaniguchi, M. Seto, S. Kitao, Y. Kobayashi, M. Saito, R. Masuda, T. Mitsui, Y. Yoda, Y. Kamihara, M. Hirano, and H. Hosono, *Iron-specific phonon density of states in the superconductors $LaFeAsO_{1-x}F_x$ and $La_{1-x}Ca_xFePO$*, Phys. Rev. B **78**, 174507 (2008).

[123] D. Phelan, J. N. Millican, E. L. Thomas, J. B. Leão, Y. Qiu, and R. Paul, *Neutron scattering measurements of the phonon density of states of $FeSe_{1-x}$ superconductors*, Phys. Rev. B **79**, 014519 (2009).

[124] A. D. Christianson, M. D. Lumsden, O. Delaire, M. B. Stone, D. L. Abernathy, M. A. McGuire, A. S. Sefat, R. Jin, B. C. Sales, D. Mandrus, E. D. Mun, P. C. Canfield, J. Y. Y. Lin, M. Lucas, M. Kresch, J. B. Keith, B. Fultz, E. A. Goremychkin, and R. J. McQueeney, *Phonon Density of States of $LaFeAsO_{1-x}F_x$*, Phys. Rev. Lett. **101**, 157004 (2008).

[125] R. H. Liu, T. Wu, G. Wu, H. Chen, X. F. Wang, Y. L. Xie, J. J. Ying, Y. J. Yan, Q. J. Li, B. C. Shi, W. S. Chu, Z. Y. Wu, and X. H. Chen, *A large iron isotope effect in $SmFeAsO_{1-x}F_x$ and $Ba_{1-x}K_xFe_2As_2$*, Nature **459**, 64 (2009).

[126] R. Khasanov, M. Bendele, A. Bussmann-Holder, and H. Keller, *Intrinsic and structural isotope effects in iron-based superconductors*, Phys. Rev. B **82**, 212505 (2010).

[127] K. Matano, Z. Ren, X. Dong, L. Sun, Z. Zhao, and G. qing Zheng, *Spin-singlet superconductivity with multiple gaps in $PrFeAsO_{0.89}F_{0.11}$*, Europhys. Lett. **83**, 57001 (2008).

[128] N. Terasaki, H. Mukuda, M. Yashima, Y. Kitaoka, K. Miyazawa, P. M. Shirage, H. Kito, H. Eisaki, and A. Iyo, *Spin Fluctuations and Unconventional Superconductivity in the Fe-Based Oxypnictide Superconductor $LaFeAsO_{0.7}$ Probed by ^{57}Fe-NMR*, J. Phys. Soc. Jpn **78**, 013701 (2009).

[129] F. Ning, K. Ahilan, T. Imai, A. S. Sefat, R. Jin, M. A. McGuire, B. C. Sales, and D. Mandrus, *^{59}Co and ^{75}As NMR Investigation of Electron-Doped High T_c Superconductor $BaFe_{1.8}Co_{0.2}As_2$ ($T_c = 22$ K)*, J. Phys. Soc. Jpn **77**, 103705 (2008).

[130] Y.-R. Zhou, Y.-R. Li, J.-W. Zuo, R.-Y. Liu, S.-K. Su, G. Chen, J. Lu, N. Wang, and Y.-P. Wang, arXiv:0812.3295v1 (unpublished).

[131] M. Yashima, H. Nishimura, H. Mukuda, Y. Kitaoka, K. Miyazawa, P. M. Shirage, K. Kihou, H. Kito, H. Eisaki, and A. Iyo, *Strong-Coupling Spin-Singlet Superconductivity with Multiple Full Gaps in Hole-Doped $Ba_{0.6}K_{0.4}Fe_2As_2$ Probed by ^{57}Fe-NMR*, J. Phys. Soc. Jpn **78**, 103702 (2009).

[132] P. J. Hirschfeld, M. M. Korshunov, and I. I. Mazin, *Gap symmetry and structure of Fe-based superconductors*, Rep. Prog. Phys. **74**, 124508 (2011).

[133] C.-T. Chen, C. Tsuei, M. Ketchen, Z.-A. Ren, and Z. Zhao, *Integer and half-integer flux-quantum transitions in a niobium?iron pnictide loop*, Nat. Phys. **6**, 260 (2010).

[134] P. J. Hirschfeld, *Nodes to the grindstone*, Physics **2**, 100 (2009).

[135] T. Devereaux and R. Hackl, *Inelastic light scattering from correlated electrons*, Rev. Mod. Phys. **79**, 175 (2007).

[136] F. A. Blum, *Inelastic Light Scattering from Semiconductor Plasmas in a Magnetic Field*, Phys. Rev. B **1**, 1125 (1970).

[137] M. V. Klein and S. B. Dierker, *Theory of Raman scattering in superconductors*, Phys. Rev. B **29**, 4976 (1984).

[138] H. Monien and A. Zawadowski, *Theory of Raman scattering with final-state interaction in high-T_c BCS superconductors: Collective modes*, Phys. Rev. B **41**, 8798 (1990).

[139] B. S. Shastry and B. I. Shraiman, *Raman Scattering in Mott-Hubbard Systems*, Int. J. Mod. Phys. B **5**, 365 (1991).

[140] T. P. Devereaux, *Theory for the effects of impurities on the Raman spectra of superconductors*, Phys. Rev. B **45**, 12965 (1992).

[141] W. Hayes and R. Loudon, *Scattering of Light by Crystals* (Dover, New York, 2005).

[142] A. Abrikosov and V. Genkin, *On the theory of Raman scattering of light in superconductors*, Zh. Eksp. Teor. Fiz. **65**, 842 (1973).

[143] T. P. Devereaux and D. Einzel, *Electronic Raman scattering in superconductors as a probe of anisotropic electron pairing*, Phys. Rev. B **51**, 16336 (1995).

[144] G. D. Mahan, *Many-Particle Physics* (Plenum Press, New York, 1993).

[145] Y. Nambu, *Quasi-Particles and Gauge Invariance in the Theory of Superconductivity*, Phys. Rev. **117**, 648 (1960).

[146] G. R. Boyd, T. P. Devereaux, P. J. Hirschfeld, V. Mishra, and D. J. Scalapino, *Probing the pairing symmetry of the iron pnictides with electronic Raman scattering*, Phys. Rev. B **79**, 174521 (2009).

[147] T. Devereaux, private communication, 2011.

[148] W. Götze and P. Wölfle, *Homogeneous Dynamical Conductivity of Simple Metals*, Phys. Rev. B **6**, 1226 (1972).

[149] M. Opel, R. Nemetschek, C. Hoffmann, R. Philipp, P. F. Müller, R. Hackl, I. Tüttő, A. Erb, B. Revaz, E. Walker, H. Berger, and L. Forró, *Carrier relaxation, pseudogap, and superconducting gap in high-T_c cuprates: A Raman scattering study*, Phys. Rev. B **61**, 9752 (2000).

[150] M. Opel, Dissertation, Technische Universität München, 2000.

[151] L. Aslamasov and A. Larkin, , Sov. Phys. Solid State **10**, 875 (1968).

[152] B. R. Patton and L. J. Sham, *Conductivity, Superconductivity, and the Peierls Instability*, Phys. Rev. Lett. **31**, 631 (1973).

[153] S. Takada and E. Sakai, *Fluctuation Conductivity in One-Dimensional Incommensurate Peierls System*, Prog. Theor. Phys. **59**, 1802 (1978).

[154] S. Caprara, C. D. Castro, M. Grilli, and D. Suppa, *Charge-Fluctuation Contribution to the Raman Response in Superconducting Cuprates*, Phys. Rev. Lett. **95**, 117004 (2005).

[155] S. Andergassen, S. Caprara, C. Di Castro, and M. Grilli, *Anomalous Isotopic Effect Near the Charge-Ordering Quantum Criticality*, Phys. Rev. Lett. **87**, 056401 (2001).

[156] G. Grüner, in *Density waves in Solids*, edited by D. Pines (Addison-Wesley, New York, 1994).

[157] M. Rotter, M. Tegel, D. Johrendt, I. Schellenberg, W. Hermes, and R. Pottgen, *Spin-density-wave anomaly at 140 K in the ternary iron arsenide $BaFe_2As_2$*, Phys. Rev. B **78**, 020503 (2008).

[158] V. Brouet, M. Marsi, B. Mansart, A. Nicolaou, A. Taleb-Ibrahimi, P. Le Fèvre, F. Bertran, F. Rullier-Albenque, A. Forget, and D. Colson, *Nesting between hole and electron pockets in $Ba(Fe_{1-x}Co_x)_2As_2$ ($x = 0 - 0.3$) observed with angle-resolved photoemission*, Phys. Rev. B **80**, 165115 (2009).

[159] C. Dhital, Z. Yamani, W. Tian, J. Zeretsky, A. S. Sefat, Z. Wang, R. J. Birgeneau, and S. D. Wilson, *Effect of Uniaxial Strain on the Structural and Magnetic Phase Transitions in* $BaFe_2As_2$, Phys. Rev. Lett. **108**, 087001 (2012).

[160] S. Drotziger, P. Schweiss, K. Grube, T. Wolf, P. Adelmann, C. Meingast, and H. v. Löhneysen, *Pressure versus Concentration Tuning of the Superconductivity in $Ba(Fe_{1-x}Co_x)_2As_2$*, J. Phys. Soc. Jpn **79**, 124705 (2010).

[161] F. Venturini, Dissertation, Technische Universität München, 2003.

[162] R. Rossner, Diplomarbeit, Technische Universität München, 2010.

[163] R. Hackl, Dissertation, Technische Universität München, 1987.

[164] M. Opel, Diplomarbeit, Technische Universität München, 1995.

[165] W. Prestel, Dissertation, Technische Universität München, 2011.

[166] A. Baum, Diplomarbeit, Technische Universität München, 2012.

[167] B. Muschler, W. Prestel, L. Tassini, R. Hackl, M. Lambacher, A. Erb, S. Komiya, Y. Ando, D. Peets, W. Hardy, R. Liang, and D. Bonn, *Electron interactions and charge ordering in CuO_2 compounds*, Eur. Phys. J. ST **188**, 131 (2010).

[168] Y. Machida, K. Tomokuni, T. Isono, K. Izawa, Y. Nakajima, and T. Tamegai, *Possible Sign-Reversing s-Wave Superconductivity in Co-Doped BaFe2As2 Proved by Thermal Transport Measurements*, J. Phys. Soc. Jpn **78**, 073705 (2009).

[169] B. S. Shastry and B. I. Shraiman, *Theory of Raman scattering in Mott-Hubbard systems*, Phys. Rev. Lett. **65**, 1068 (1990).

[170] J. K. Freericks and T. P. Devereaux, *Raman scattering through a metal-insulator transition*, Phys. Rev. B **64**, 125110 (2001).

[171] L. Chauvière, Y. Gallais, M. Cazayous, A. Sacuto, M. A. Measson, D. Colson, and A. Forget, *Doping dependence of the lattice dynamics in $Ba(Fe_{1-x}Co_x)_2As_2$ studied by Raman spectroscopy*, Phys. Rev. B **80**, 094504 (2009).

[172] M. Rahlenbeck, G. L. Sun, D. L. Sun, C. T. Lin, B. Keimer, and C. Ulrich, *Phonon anomalies in pure and underdoped $R_{1-x}K_xFe_2As_2$ (R = Ba, Sr) investigated by Raman light scattering*, Phys. Rev. B **80**, 064509 (2009).

[173] K.-Y. Choi, D. Wulferding, P. Lemmens, N. Ni, S. L. Bud'ko, and P. C. Canfield, *Lattice and electronic anomalies of $CaFe_2As_2$ studied by Raman spectroscopy*, Phys. Rev. B **78**, 212503 (2008).

[174] L. Chauvière, Y. Gallais, M. Cazayous, M. A. Méasson, A. Sacuto, D. Colson, and A. Forget, *Raman scattering study of spin-density-wave order and electron-phonon coupling in $Ba(Fe_{1-x}Co_x)_2As_2$*, Phys. Rev. B **84**, 104508 (2011).

[175] S. Sugai, Y. Mizuno, R. Watanabe, T. Kawaguchi, K. Takenaka, H. Ikuta, Y. Takayanagi, N. Hayamizu, and Y. Sone, *Spin-Density-Wave Gap with Dirac Nodes and Two-Magnon Raman Scattering in $BaFe_2As_2$*, J. Phys. Soc. Jpn **81**, 024718 (2012).

[176] M. Yi, D. Lu, J.-H. Chu, J. G. Analytis, A. P. Sorini, A. F. Kemper, B. Moritz, S.-K. Mo, R. G. Moore, M. Hashimoto, W.-S. Lee, Z. Hussain, T. P. Devereaux, I. R. Fisher, and Z.-X. Shen, *Symmetry-breaking orbital anisotropy observed for detwinned $Ba(Fe_{1-x}Co_x)_2As_2$ above the spin density wave transition*, Proceed. Nat. Acad. Sci. **108**, 6878 (2011).

[177] A. Dusza, A. Lucarelli, F. Pfuner, J.-H. Chu, I. R. Fisher, and L. Degiorgi, *Anisotropic charge dynamics in detwinned $Ba(Fe_{1-x}Co_x)_2As_2$*, Europhys. Lett. **93**, 37002 (2011).

[178] M. Nakajima, T. Liang, S. Ishida, Y. Tomioka, K. Kihou, C. Lee, A. Iyo, H. Eisaki, T. Kakeshita, T. Ito, and S. Uchida, *Unprecedented anisotropic metallic state in undoped iron arsenide BaFe2As2 revealed by optical spectroscopy*, Proc. Natl. Acad. Sci. **108**, 12238 (2011).

[179] R. A. Ewings, T. G. Perring, R. I. Bewley, T. Guidi, M. J. Pitcher, D. R. Parker, S. J. Clarke, and A. T. Boothroyd, *High-energy spin excitations in $BaFe_2As_2$ observed by inelastic neutron scattering*, Phys. Rev. B **78**, 220501 (2008).

[180] A. Heimes, R. Grein, and M. Eschrig, *Electronic Dispersion Anomalies in Iron Pnictide Superconductors*, Phys. Rev. Lett. **106**, 047003 (2011).

[181] B. Moritz, S. Johnston, T. P. Devereaux, B. Muschler, W. Prestel, R. Hackl, M. Lambacher, A. Erb, S. Komiya, and Y. Ando, *Investigation of particle-hole asymmetry in the cuprates via electronic Raman scattering*, Phys. Rev. B **84**, 235114 (2011).

[182] S. Sugai, Y. Mizuno, R.Watanabe, T. Kawaguchi, K. Takenaka, H. Ikuta, K. Kiho, M. Nakajima, C. Lee, A. Iyo, H. Eisaki, and S. Uchida, *The Nodal SDW Gap and the Superconducting Gap in$Ba(Fe_{1-x}Co_x)_2As_2$*, J. Supercond. Nov. Magn. **24**, 1185 (2011).

[183] W. Z. Hu, J. Dong, G. Li, Z. Li, P. Zheng, G. F. Chen, J. L. Luo, and N. L. Wang, *Origin of the Spin Density Wave Instability in AFe_2As_2 (A = Ba,Sr) as Revealed by Optical Spectroscopy*, Phys. Rev. Lett. **101**, 257005 (2008).

[184] S. Sugai, Y. Mizuno, K. Kiho, M. Nakajima, C. H. Lee, A. Iyo, H. Eisaki, and S. Uchida, *Pairing symmetry of the multiorbital pnictide superconductor $BaFe_{1.84}Co_{0.16}As_2$ from Raman scattering*, Phys. Rev. B **82**, 140504 (2010).

[185] S. Sugai, Y. Mizuno, R. Watanabe, T. Kawaguchi, K. Takenaka, H. Ikuta, Y. Takayanagi, N. Hayamizu, and Y. Sone, arXiv:1010.6151v1 (unpublished).

[186] M. D. Lumsden, A. D. Christianson, E. A. Goremychkin, S. E. Nagler, H. A. Mook, M. B. Stone, D. L. Abernathy, T. Guidi, G. J. MacDougall, C. de la Cruz, A. S. Sefat, M. A. McGuire, B. C. Sales, and D. Mandrus, *Evolution of spin excitations into the superconducting state in* $FeTe_{1-x}Se_x$, Nat. Phys. **6**, 182 (2010).

[187] S. Sugai, H. Suzuki, Y. Takayanagi, T. Hosokawa, and N. Hayamizu, *Carrier-density-dependent momentum shift of the coherent peak and the LO phonon mode in p-type high-*T_c *superconductors*, Phys. Rev. B **68**, 184504 (2003).

[188] L. W. Harriger, H. Q. Luo, M. S. Liu, C. Frost, J. P. Hu, M. R. Norman, and P. Dai, *Nematic spin fluid in the tetragonal phase of* $BaFe_2As_2$, Phys. Rev. B **84**, 054544 (2011).

[189] S. O. Diallo, V. P. Antropov, T. G. Perring, C. Broholm, J. J. Pulikkotil, N. Ni, S. L. Bud'ko, P. C. Canfield, A. Kreyssig, A. I. Goldman, and R. J. McQueeney, *Itinerant Magnetic Excitations in Antiferromagnetic* $CaFe_2As_2$, Phys. Rev. Lett. **102**, 187206 (2009).

[190] Z. Yin, K. Haule, and G. Kotliar, *Magnetism and charge dynamics in iron pnictides*, Nat. Phys. **7**, 294 (2011).

[191] M. Nakajima, S. Ishida, K. Kihou, Y. Tomioka, T. Ito, Y. Yoshida, C. H. Lee, H. Kito, A. Iyo, H. Eisaki, K. M. Kojima, and S. Uchida, *Evolution of the optical spectrum with doping in* $Ba(Fe_{1-x}Co_x)_2As_2$, Phys. Rev. B **81**, 104528 (2010).

[192] D. Wu, N. Barišić, N. Drichko, S. Kaiser, A. Faridian, M. Dressel, S. Jiang, Z. Ren, L. J. Li, G. H. Cao, Z. A. Xu, H. S. Jeevan, and P. Gegenwart, *Effects of magnetic ordering on dynamical conductivity: Optical investigations of* $EuFe_2As_2$ *single crystals*, Phys. Rev. B **79**, 155103 (2009).

[193] E. Kaneshita, K. Tsutsui, and T. Tohyama, *Spin and orbital characters of excitations in iron arsenide superconductors revealed by simulated resonant inelastic x-ray scattering*, Phys. Rev. B **84**, 020511 (2011).

[194] D. H. Lu, M. Yi, S.-K. Mo, A. S. Erickson, J. Analytis, J.-H. Chu, D. J. Singh, Z. Hussain, T. H. Geballe, I. R. Fisher, and Z.-X. Shen, *Electronic structure of the iron-based superconductor LaOFeP*, Nature **455**, 81 (2008).

[195] H. Ding, K. Nakayama, P. Richard, S. Souma, T. Sato, T. Takahashi, M. Neupane, Y.-M. Xu, Z.-H. Pan, A. Fedorov, Z. Wang, X. Dai, Z. Fang, G. Chen, J. Luo, and N. Wang, *Electronic structure of optimally doped pnictide* $Ba_{0.6}K_{0.4}Fe_2As_2$*: a comprehensive angle-resolved photoemission spectroscopy investigation* , J. Phys.: Condens. Matter **23**, 135701 (2011).

[196] L. Ortenzi, E. Cappelluti, L. Benfatto, and L. Pietronero, *Fermi-Surface Shrinking and Interband Coupling in Iron-Based Pnictides*, Phys. Rev. Lett. **103**, 046404 (2009).

[197] M. C. Aronson, S. B. Dierker, B. S. Dennis, S.-W. Cheong, and Z. Fisk, *Pressure dependence of the superexchange interaction in antiferromagnetic* La_2CuO_4, Phys. Rev. B **44**, 4657 (1991).

[198] D. Johnston, M. Maki, and G. Gruener, *Influence of charge density wave fluctuations on the magnetic susceptibility of the quasi one-dimensional conductor* $(TaSe_4)_2I$, Solid State Commun. **53**, 5 (1985).

[199] H. Yao, J. A. Robertson, E.-A. Kim, and S. A. Kivelson, *Theory of stripes in quasi-two-dimensional rare-earth tellurides*, Phys. Rev. B **74**, 245126 (2006).

[200] J. Tranquada, B. Sternlieb, J. Axe, Y. Nakamura, and S. Uchida, *Evidence for stripe correlations of spins and holes in copper oxide superconductors*, Nature **375**, 561 (1995).

[201] T. Boehm, private communication, 2011.

[202] L. Tassini, F. Venturini, Q.-M. Zhang, R. Hackl, N. Kikugawa, and T. Fujita, *Dynamical Properties of Charged Stripes in* $La_{2-x}Sr_xCuO_4$, Phys. Rev. Lett. **95**, 117002 (2005).

[203] L. Tassini, W. Prestel, A. Erb, M. Lambacher, and R. Hackl, *First-order-type effects in* $YBa_2Cu_3O_{6+x}$ *at the onset of superconductivity*, Phys. Rev. B **78**, 020511 (2008).

[204] U. Fano, *Effects of Configuration Interaction on Intensities and Phase Shifts*, Phys. Rev. **124**, 1866 (1961).

[205] J. E. Han, O. Gunnarsson, and V. Eyert, *Phonon line shape in disordered* A_3C_{60} (A=K, Rb), Phys. Rev. B **60**, 6495 (1999).

[206] T. P. Devereaux, A. Virosztek, and A. Zawadowski, *Charge-transfer fluctuation, d-wave superconductivity, and the* B_{1g} *Raman phonon in cuprates*, Phys. Rev. B **51**, 505 (1995).

[207] M. Opel, R. Hackl, T. P. Devereaux, A. Virosztek, A. Zawadowski, A. Erb, E. Walker, H. Berger, and L. Forró, *Physical origin of the buckling in* CuO_2*: Electron-phonon coupling and Raman spectra*, Phys. Rev. B **60**, 9836 (1999).

[208] K.-Y. Choi, P. Lemmens, I. Eremin, G. Zwicknagl, H. Berger, G. L. Sun, D. L. Sun, and C. T. Lin, *Self-energy effects and electron-phonon coupling in Fe-As superconductors*, J. Phys. Condens. Matter **22**, 115802 (2010).

[209] A. P. Litvinchuk, B. Lv, and C. W. Chu, *Raman scattering study of electron-doped* $Pr_xCa_{1-x}Fe_2As_2$ *superconductors*, Phys. Rev. B **84**, 092504 (2011).

[210] L. Boeri, M. Calandra, I. I. Mazin, O. V. Dolgov, and F. Mauri, *Effects of magnetism and doping on the electron-phonon coupling in $BaFe_2As_2$*, Phys. Rev. B **82**, 020506 (2010).

[211] L. Chauvière, Y. Gallais, M. Cazayous, M. A. Méasson, A. Sacuto, D. Colson, and A. Forget, *Impact of the spin-density-wave order on the superconducting gap of $Ba(Fe_{1-x}Co_x)_2As_2$*, Phys. Rev. B **82**, 180521 (2010).

[212] G. F. Reiter, *Light scattering from energy fluctuations in magnetic insulators*, Phys. Rev. B **13**, 169 (1976).

[213] A. Zawadowski and M. Cardona, *Theory of Raman scattering on normal metals with impurities*, Phys. Rev. B **42**, 10732 (1990).

[214] S. O. Diallo, D. K. Pratt, R. M. Fernandes, W. Tian, J. L. Zarestky, M. Lumsden, T. G. Perring, C. L. Broholm, N. Ni, S. L. Bud'ko, P. C. Canfield, H.-F. Li, D. Vaknin, A. Kreyssig, A. I. Goldman, and R. J. McQueeney, *Paramagnetic spin correlations in $CaFe_2As_2$ single crystals*, Phys. Rev. B **81**, 214407 (2010).

[215] M. Rahlenbeck, Dissertation, Universität Tübingen, 2010.

[216] N. Barišić, D. Wu, M. Dressel, L. J. Li, G. H. Cao, and Z. A. Xu, *Electrodynamics of electron-doped iron pnictide superconductors: Normal-state properties*, Phys. Rev. B **82**, 054518 (2010).

[217] A. Sanna, F. Bernardini, G. Profeta, S. Sharma, J. K. Dewhurst, A. Lucarelli, L. Degiorgi, E. K. U. Gross, and S. Massidda, *Theoretical investigation of optical conductivity in $Ba(Fe_{1-x}Co_x)_2As_2$*, Phys. Rev. B **83**, 054502 (2011).

[218] R. Hackl, *The Janus face of electrons in superconductors with high transition temperature* (KITP, Santa Barbara, 2010).

[219] H.-H. Kuo, J.-H. Chu, S. C. Riggs, L. Yu, P. L. McMahon, K. De Greve, Y. Yamamoto, J. G. Analytis, and I. R. Fisher, *Possible origin of the nonmonotonic doping dependence of the in-plane resistivity anisotropy of $Ba(Fe_{1-x}T_x)_2As_2$ (T = Co, Ni and Cu)*, Phys. Rev. B **84**, 054540 (2011).

[220] N. Ashcroft and N. Mermin, *Solid State Physics* (Saunder College, Philadelphia, 1976).

[221] A. I. Coldea, C. M. J. Andrew, J. G. Analytis, R. D. McDonald, A. F. Bangura, J.-H. Chu, I. R. Fisher, and A. Carrington, *Topological Change of the Fermi Surface in Ternary Iron Pnictides with Reduced c/a Ratio: A de Haas˘van Alphen Study of $CaFe_2P_2$*, Phys. Rev. Lett. **103**, 026404 (2009).

[222] J. G. Analytis, C. M. J. Andrew, A. I. Coldea, A. McCollam, J.-H. Chu, R. D. McDonald, I. R. Fisher, and A. Carrington, *Fermi Surface of $SrFe_2P_2$ Determined by the de Haas–van Alphen Effect*, Phys. Rev. Lett. **103**, 076401 (2009).

[223] H. Shishido, A. F. Bangura, A. I. Coldea, S. Tonegawa, K. Hashimoto, S. Kasahara, P. M. C. Rourke, H. Ikeda, T. Terashima, R. Settai, Y. Ōnuki, D. Vignolles, C. Proust, B. Vignolle, A. McCollam, Y. Matsuda, T. Shibauchi, and A. Carrington, *Evolution of the Fermi Surface of $BaFe_2(As_{1-x}P_x)_2$ on Entering the Superconducting Dome*, Phys. Rev. Lett. **104**, 057008 (2010).

[224] I. Fisher, L. Degiorgi, and Z. Shen, *In-plane electronic anisotropy of underdoped '122' Fe-arsenide superconductors revealed by measurements of detwinned single crystals*, Rep. Prog. Phys. **74**, 124506 (2011).

[225] D. Wu, N. Barišić, P. Kallina, A. Faridian, B. Gorshunov, N. Drichko, L. J. Li, X. Lin, G. H. Cao, Z. A. Xu, N. L. Wang, and M. Dressel, *Optical investigations of the normal and superconducting states reveal two electronic subsystems in iron pnictides*, Phys. Rev. B **81**, 100512 (2010).

[226] L. Fang, H. Luo, P. Cheng, Z. Wang, Y. Jia, G. Mu, B. Shen, I. I. Mazin, L. Shan, C. Ren, and H.-H. Wen, *Roles of multiband effects and electron-hole asymmetry in the superconductivity and normal-state properties of $Ba(Fe_{1-x}Co_x)_2As_2$*, Phys. Rev. B **80**, 140508 (2009).

[227] A. Damascelli, Z. Hussain, and Z.-X. Shen, *Angle-resolved photoemission studies of the cuprate superconductors*, Rev. Mod. Phys. **75**, 473 (2003).

[228] A. Kemper, private communication, 2011.

[229] M. Kang, G. Blumberg, M. V. Klein, and N. N. Kolesnikov, *Resonance Raman Study of the Superconducting Gap and Low Energy Excitations in $Tl_2Ba_2CuO_{6+\delta}$ Superconductors*, Phys. Rev. Lett. **77**, 4434 (1996).

[230] G. Blumberg, A. Koitzsch, A. Gozar, B. S. Dennis, C. A. Kendziora, P. Fournier, and R. L. Greene, *Nonmonotonic $d_{x^2-y^2}$ Superconducting Order Parameter in $Nd_{2-x}Ce_xCuO_4$*, Phys. Rev. Lett. **88**, 107002 (2002).

[231] S. L. Cooper, M. V. Klein, B. G. Pazol, J. P. Rice, and D. M. Ginsberg, *Raman scattering from superconducting gap excitations in single-crystal $YBa_2Cu_3O_{7-\delta}$*, Phys. Rev. B **37**, 5920 (1988).

[232] D. Einzel and R. Hackl, *Electronic Raman Scattering in Copper Oxide Superconductors*, J. Raman Spectrosc. **27**, 307 (1996).

[233] W. Guyard, M. L. Tacon, M. Cazayous, A. Sacuto, A. Georges, D. Colson, and A. Forget, *Breakpoint in the evolution of the gap through the cuprate phase diagram*, Phys. Rev. B **77**, 024524 (2008).

[234] W. Guyard, A. Sacuto, M. Cazayous, Y. Gallais, M. L. Tacon, D. Colson, and A. Forget, *Temperature Dependence of the Gap Size near the Brillouin-Zone Nodes of $HgBa_2CuO_{4+\delta}$ Superconductors*, Phys. Rev. Lett. **101**, 097003 (2008).

[235] R. Hackl, R. Kaiser, and S. Schicktanz, *Gap mode, superconducting gap and phonon mode in V_3Si and Nb_3Sn*, J. Phys. C: Solid State Phys. **16**, 1729 (1983).

[236] J. Bardeen, L. N. Cooper, and J. R. Schrieffer, *Microscopic Theory of Superconductivity*, Phys. Rev. **106**, 162 (1957).

[237] J. Bardeen, L. N. Cooper, and J. R. Schrieffer, *Theory of Superconductivity*, Phys. Rev. **108**, 1175 (1957).

[238] T. P. Devereaux, *Theory of Electronic Raman Scattering in Disordered Unconventional Superconductors*, Phys. Rev. Lett. **74**, 4313 (1995).

[239] R. Hackl, private communication, 2011.

[240] L. Luan, T. M. Lippman, C. W. Hicks, J. A. Bert, O. M. Auslaender, J.-H. Chu, J. G. Analytis, I. R. Fisher, and K. A. Moler, *Local Measurement of the Superfluid Density in the Pnictide Superconductor $Ba(Fe_{1-x}Co_x)_2As_2$ across the Superconducting Dome*, Phys. Rev. Lett. **106**, 067001 (2011).

[241] N. Munnikes, B. Muschler, F. Venturini, L. Tassini, W. Prestel, S. Ono, Y. Ando, D. C. Peets, W. N. Hardy, R. Liang, D. A. Bonn, A. Damascelli, H. Eisaki, M. Greven, A. Erb, and R. Hackl, *Pair breaking versus symmetry breaking: Origin of the Raman modes in superconducting cuprates*, Phys. Rev. B **84**, 144523 (2011).

[242] V. Mishra, G. Boyd, S. Graser, T. Maier, P. J. Hirschfeld, and D. J. Scalapino, *Lifting of nodes by disorder in extended-s-state superconductors: Application to ferropnictides*, Phys. Rev. B **79**, 094512 (2009).

[243] G. R. Boyd, P. J. Hirschfeld, and T. P. Devereaux, *Effect of disorder on the electronic Raman scattering in the superconducting state of iron pnictides*, Phys. Rev. B **82**, 134506 (2010).

[244] L. Bulaevskii, A. Rusinov, and M. Kulic, *Helical Ordering of Spins in a Superconductor*, J. Low Temp. Phys. **39**, 255 (1980).

[245] D. J. Scalapino and T. P. Devereaux, *Collective d-wave exciton modes in the calculated Raman spectrum of Fe-based superconductors*, Phys. Rev. B **80**, 140512 (2009).

[246] W.-C. Lee, S.-C. Zhang, and C. Wu, *Pairing State with a Time-Reversal Symmetry Breaking in FeAs-Based Superconductors*, Phys. Rev. Lett. **102**, 217002 (2009).

[247] K. Kuroki, H. Usui, S. Onari, R. Arita, and H. Aoki, *Pnictogen height as a possible switch between high-T_c nodeless and low-T_c nodal pairings in the iron-based superconductors*, Phys. Rev. B **79**, 224511 (2009).

[248] F. Wang, H. Zhai, and D.-H. Lee, *Antiferromagnetic correlation and the pairing mechanism of the cuprates and iron pnictides: A view from the functional renormalization group studies*, Europhys. Lett. **85**, 37005 (2009).

[249] T. Tsuneto, *Transverse Collective Excitations in Superconductors and Electromagnetic Absorption*, Phys. Rev. **118**, 1029 (1960).

[250] A. Bardasis and J. R. Schrieffer, *Excitons and Plasmons in Superconductors*, Phys. Rev. **121**, 1050 (1961).

[251] L. Wray, D. Qian, D. Hsieh, Y. Xia, L. Li, J. G. Checkelsky, A. Pasupathy, K. K. Gomes, C. V. Parker, A. V. Fedorov, G. F. Chen, J. L. Luo, A. Yazdani, N. P. Ong, N. L. Wang, and M. Z. Hasan, *Momentum dependence of superconducting gap, strong-coupling dispersion kink, and tightly bound Cooper pairs in the high-T_c $(Sr,Ba)_{1-x}(K,Na)_xFe_2As_2$ superconductors*, Phys. Rev. B **78**, 184508 (2008).

[252] D. V. Evtushinsky, D. S. Inosov, V. B. Zabolotnyy, A. Koitzsch, M. Knupfer, B. Buchner, M. S. Viazovska, G. L. Sun, V. Hinkov, A. V. Boris, C. T. Lin, B. Keimer, A. Varykhalov, A. A. Kordyuk, and S. V. Borisenko, *Momentum dependence of the superconducting gap in $Ba_{1-x}K_xFe_2As_2$*, Phys. Rev. B **79**, 054517 (2009).

[253] T. Kawahara, K. Terashima, Y. Sekiba, J. Bowen, K. Nakayama, T. Sato, P. Richard, Y.-M. Xu, L. Li, G. Cao, Z.-A. Xu, H. Ding, and T. Takahashi, *High-resolution ARPES study of electron-doped Fe-based superconductor $BaFe_{1.85}Co_{0.15}As_2$*, Physica C: Superconductivity **470**, S440 (2010).

[254] K. Nakayama, T. Sato, P. Richard, Y.-M. Xu, T. Kawahara, K. Umezawa, T. Qian, M. Neupane, G. F. Chen, H. Ding, and T. Takahashi, *Universality of superconducting gaps in overdoped $Ba_{0.3}K_{0.7}Fe_2As_2$ observed by angle-resolved photoemission spectroscopy*, Phys. Rev. B **83**, 020501 (2011).

[255] A. Perucchi, L. Baldassarre, S. Lupi, J. Jiang, J.D.Weiss, E. Hellstrom, S. Lee, C. Bark, C. Eom, M. Putti, I. Pallecchi, C. Marini, and P. Dore, *Multi-gap superconductivity in a $BaFe_{1.84}Co_{0.16}As_2$ film from optical measurements at terahertz frequencies*, Eur. Phys. J. B **77**, 25 (2010).

[256] B. Gorshunov, D. Wu, A. A. Voronkov, P. Kallina, K. Iida, S. Haindl, F. Kurth, L. Schultz, B. Holzapfel, and M. Dressel, *Direct observation of the superconducting energy gap in the optical conductivity of the iron pnictide superconductor $Ba(Fe_{0.9}Co_{0.1})_2As_2$*, Phys. Rev. B **81**, 060509 (2010).

[257] K. W. Kim, M. Rössle, A. Dubroka, V. K. Malik, T. Wolf, and C. Bernhard, *Evidence for multiple superconducting gaps in optimally doped $BaFe_{1.87}Co_{0.13}As_2$ from infrared spectroscopy*, Phys. Rev. B **81**, 214508 (2010).

[258] D. Wu, N. Barišić, M. Dressel, G. H. Cao, Z. A. Xu, J. P. Carbotte, and E. Schachinger, *Nodes in the order parameter of superconducting iron pnictides investigated by infrared spectroscopy*, Phys. Rev. B **82**, 184527 (2010).

[259] J. K. Dong, S. Y. Zhou, T. Y. Guan, X. Qiu, C. Zhang, P. Cheng, L. Fang, H. H. Wen, and S. Y. Li, *Thermal conductivity of overdoped $BaFe_{1.73}Co_{0.27}As_2$*

single crystal: Evidence for nodeless multiple superconducting gaps and interband interactions, Phys. Rev. B **81**, 094520 (2010).

[260] M. A. Tanatar, J.-P. Reid, H. Shakeripour, X. G. Luo, N. Doiron-Leyraud, N. Ni, S. L. Bud'ko, P. C. Canfield, R. Prozorov, and L. Taillefer, *Doping Dependence of Heat Transport in the Iron-Arsenide Superconductor* $Ba(Fe_{1-x}Co_x)_2As_2$*: From Isotropic to a Strongly k-Dependent Gap Structure*, Phys. Rev. Lett. **104**, 067002 (2010).

[261] J.-P. Reid, M. A. Tanatar, X. G. Luo, H. Shakeripour, N. Doiron-Leyraud, N. Ni, S. L. Bud'ko, P. C. Canfield, R. Prozorov, and L. Taillefer, *Nodes in the gap structure of the iron arsenide superconductor* $Ba(Fe_{1-x}Co_x)_2As_2$ *from c -axis heat transport measurements*, Phys. Rev. B **82**, 064501 (2010).

[262] F. Hardy, P. Burger, T. Wolf, R. A. Fisher, P. Schweiss, P. Adelmann, R. Heid, R. Fromknecht, R. Eder, D. Ernst, H. v. Löhneysen, and C. Meingast, *Doping evolution of superconducting gaps and electronic densities of states in* $Ba(Fe_{1-x}Co_x)_2As_2$ *iron pnictides* , Europhys. Lett. **91**, 47008 (2010).

[263] K. Gofryk, A. B. Vorontsov, I. Vekhter, A. S. Sefat, T. Imai, E. D. Bauer, J. D. Thompson, and F. Ronning, *Effect of annealing on the specific heat of* $Ba(Fe_{1-x}Co_x)_2As_2$, Phys. Rev. B **83**, 064513 (2011).

[264] G. Mu, J. Tang, Y. Tanabe, J. Xu, S. Heguri, and K. Tanigaki, *Evidence for line nodes in the energy gap of the overdoped* $Ba(Fe_{1-x}Co_x)_2As_2$ *from low-temperature specific heat measurements*, Phys. Rev. B **84**, 054505 (2011).

[265] C. Martin, H. Kim, R. T. Gordon, N. Ni, V. G. Kogan, S. L. Bud'ko, P. C. Canfield, M. A. Tanatar, and R. Prozorov, *Evidence from anisotropic penetration depth for a three-dimensional nodal superconducting gap in single-crystalline* $BaFe_{1-x}Ni_x)_2As_2$, Phys. Rev. B **81**, 060505 (2010).

[266] H. Ikeda, R. Arita, and J. Kuneš, *Phase diagram and gap anisotropy in iron-pnictide superconductors*, Phys. Rev. B **81**, 054502 (2010).

[267] S. Maiti, M. M. Korshunov, T. A. Maier, P. J. Hirschfeld, and A. V. Chubukov, *Evolution of the Superconducting State of Fe-Based Compounds with Doping*, Phys. Rev. Lett. **107**, 147002 (2011).

[268] E. van Heumen, J. Vuorinen, K. Koepernik, F. Massee, Y. Huang, M. Shi, J. Klei, J. Goedkoop, M. Lindroos, J. van den Brink, and M. S. Golden, *Existence, Character, and Origin of Surface-Related Bands in the High Temperature Iron Pnictide Superconductor* $BaFe_{2-x}Co_xAs_2$, Phys. Rev. Lett. **106**, 027002 (2011).

[269] I. I. Mazin, M. D. Johannes, L. Boeri, K. Koepernik, and D. J. Singh, *Problems with reconciling density functional theory calculations with experiment in ferropnictides*, Phys. Rev. B **78**, 085104 (2008).

[270] J. S. Kim, P. J. Hirschfeld, G. R. Stewart, S. Kasahara, T. Shibauchi, T. Terashima, and Y. Matsuda, *Specific heat versus field in the 30 K superconductor* $BaFe_2(As_{0.7}P_{0.3})_2$, Phys. Rev. B **81**, 214507 (2010).

[271] V. Mishra, S. Graser, and P. J. Hirschfeld, *Transport properties of three-dimensional extended s-wave states in Fe-based superconductors*, Phys. Rev. B **84**, 014524 (2011).

Acknowledgment

This work was only possible trough the help of many people. Here, I want to thank all people who contributed to this work, in particular

- *Prof. Dr. Rudolf Gross* for giving me the possibility to work at the WMI, his support during the years and his helpful comments on this thesis
- *Dr. Rudi Hackl* for his enormous encouragement, his advice in any question about the experimental setup, his helpful comments for the interpretation of the data, many fruitful discussions not only about physics and his continuous support during I was writing this thesis
- *Dr. Dietrich Einzel* for many discussion about physics, his great theoretical support and for prove reading this thesis
- *Flo Kretzschmar*, *Andreas Baum*, *Thomas Böhm*, *Peter Jaschke*, *Hans Eiter* and *Wolfgang Prestel* for the good atmosphere in the Raman group and innumerable very helpful discussions about the experimental setup, the Raman experiment, physics and all the fun we had
- *Prof. Dr. Tom Devereaux*, *Dr. Lex Kemper* and *Dr. Brian Moritz* for all the theoretical support during the last years and the continuous and patient explanations of the physics of the FeSCs and cuprates
- *Prof. Dr. Marco Grilli* for valuable discussions and explanations concerning the fluctuations response in the Raman spectra
- *Prof. Dr. Ian Fisher*, *Dr. James Analytis* and *Jun-Haw Chu* for providing me with samples, the resistivity data and giving valuable hints concerning the sample treatment
- Diploma and Doctoral students of other groups for making the last years a great time. In particular *Elisabeth Hoffmann*, *Franz Czechka*, *Johannes Büttner*, *Toni Helm*, *Mathias Weiler*, *Fred Hocke*, *Edwin Menzel*, *Peter Eder*, *Manuel Schwarz*, *Alex Baust* and *Harald Breitkreutz*
- *Dr. Matthias Opel* for the good atmosphere, his help concerning the any computer problem and the experimental setup and his motivating words when things went wrong
- the workshop of the WMI for their help regarding any mechanical problem, especially *Helmut Thiess*, *Robert Müller* and *Christian Reichlmeier*

- *Emel Dönertas* and *Ludwig Ossiander* for organizing the workshops and taking care of any organizational and financial problem
- *Ulrich Guggenberger* for answering any question concerning electronics and making the spectrometer run again and again
- *Joachim Geismann* for always helping and knowing what to find where
- the helium liquidation group *Harald Schwaiger*, *Peter Binkert* and *Jan Naundorf* for providing me with liquid nitrogen and helium although I was late
- my family for their patience when I was complaining about so many things and the support during the years